

**Electronic Structure, Bonding and Properties of
Novel Lanthanide and Actinide Complexes
Involving Various Ligands and Clusters**

By

Debashree Manna

(CHEM 01200904014)

BHABHA ATOMIC RESEARCH CENTRE, MUMBAI

A thesis submitted to the

Board of Studies in Chemical Sciences

In partial fulfillment of requirements

For the Degree of

DOCTOR OF PHILOSOPHY

of

HOMI BHABHA NATIONAL INSTITUTE

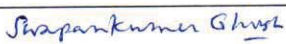


MAY, 2014

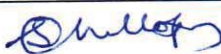
Homi Bhabha National Institute

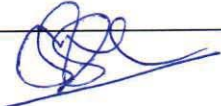
Recommendations of the Viva Voce Committee

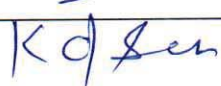
As members of the Viva Voce Committee, we certify that we have read the dissertation prepared by **Debashree Manna** entitled “**Electronic Structure, Bonding and Properties of Novel Lanthanide and Actinide Complexes Involving Various Ligands and Clusters**” and recommend that it may be accepted as fulfilling the thesis requirement for the award of Degree of Doctor of Philosophy.

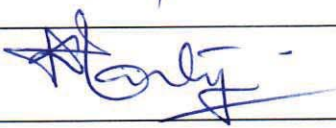
Chairman - Dr. Swapan K Ghosh  Date: 25/2/15

Guide / Convener - Dr. Tapan K Ghanty  Date: 25/02/15

Co-guide - Dr. Subrata Chattopadhyay  Date: 25/2/15

Co-guide - Dr. Sulekha Mukhopadhyay  Date: 25/02/15

External Examiner - Prof. Kalidas Sen  Date: 25/02/2015

Member 1- Dr. Dilip K Maity  Date: 25/02/15

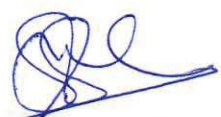
Member 2 - Dr. Chiranjib Majumder Date:

Final approval and acceptance of this thesis is contingent upon the candidate's submission of the final copies of the thesis to HBNI.

I/We hereby certify that I/we have read this thesis prepared under my/our direction and recommend that it may be accepted as fulfilling the thesis requirement.

Date: 25/02/2015

Place: MUMBAI


Dr. S. Mukhopadhyay
Co-guide


Dr. S. Chattopadhyay
Co-guide


Dr. T. K. Ghanty
Guide

STATEMENT BY AUTHOR

This dissertation has been submitted in partial fulfillment of requirements for an advanced degree at Homi Bhabha National Institute (HBNI) and is deposited in the Library to be made available to borrowers under rules of the HBNI.

Brief quotations from this dissertation are allowable without special permission, provided that accurate acknowledgement of source is made. Requests for permission for extended quotation from or reproduction of this manuscript in whole or in part may be granted by the Competent Authority of HBNI when in his or her judgment the proposed use of the material is in the interests of scholarship. In all other instances, however, permission must be obtained from the author.

Debashree Manna

DECLARATION

I, hereby declare that the investigation presented in the thesis has been carried out by me. The work is original and has not been submitted earlier as a whole or in part for a degree / diploma at this or any other Institution / University.

Debashree Manna

List of Publications arising from the thesis

Journal

1. “Complexation behavior of trivalent actinides and lanthanides with 1,10-phenanthroline-2,9-dicarboxylic acid based ligands: Insight from density functional theory.”
D. Manna and T. K. Ghanty, *Phys. Chem. Chem. Phys.* **2012**, *14*, 11060-11069.
2. “Theoretical prediction of icosahedral U@C₂₀ and analogous systems with high HOMO-LUMO gap.”
D. Manna and T. K. Ghanty, *J. Phys. Chem. C* **2012**, *116*, 16716-16725.
3. “Prediction of a new series of thermodynamically stable actinide encapsulated fullerene systems fulfilling the 32-electron principle.”
D. Manna and T. K. Ghanty, *J. Phys. Chem. C* **2012**, *116*, 25630-25641.
4. “Enhancement in the stability of 36-atom fullerene through encapsulation of a uranium atom.”
D. Manna and T. K. Ghanty, *J. Phys. Chem. C* **2013**, *117*, 17859-17869.
5. “Pu@C₂₄: A new example satisfying 32-electron principle.”
D. Manna, A. Sirohiwal and T. K. Ghanty, *J. Phys. Chem. C* **2014**, *118*, 7211–7221.
6. “Actinide selectivity of 1,10-phenanthroline-2,9-dicarboxamide and its derivatives: A theoretical prediction followed by experimental validation.”
D. Manna, S. Mula, A. Bhattacharyya, S. Chattopadhyay and T. K. Ghanty, *Dalton Trans.* **2015**, *44*, 1332-1340.

7. "Complexation of Am³⁺ and Eu³⁺ ions with thiophosphinate ligands involving oxygen and sulphur donors: A density functional investigation."
D. Manna, A. Bhattacharyya, and T. K. Ghanty, *Comput. Theor. Chem.* (Submitted)

Conferences

1. "New series of stable actinide and lanthanide encapsulated fullerene systems"
D. Manna and T. K. Ghanty, Current Trends in Theoretical Chemistry, September 26-28, **2013**, BARC, Mumbai.
2. "Lanthanide/actinide encapsulated icosahedral C₂₀ fullerene system: A density functional prediction"
D. Manna and T. K. Ghanty, Interdisciplinary Symposium on Materials Chemistry December 11-15, **2012**, BARC, Mumbai.
3. "Different spin states of trivalent Americium and Europium complexes with selective sulphur donor ligands"
D. Manna and T. K. Ghanty, Trombay Symposium on Radiation & Photochemistry, January 4-9, **2012**, BARC, Mumbai.
4. "Effect of solvent polarity and spin-orbit interaction on the excited states of uranyl Ion"
D. Manna and T. K. Ghanty, National Symposium on Radiation & Photochemistry, March 10-12, **2011**, JNV University, Jodhpur.
5. "Trivalent actinide and lanthanide complexes with derivatives of 1,10-phenanthroline-2,9-dicarboxylic acid: A density functional investigation"
D. Manna and T. K. Ghanty and S. K. Ghosh, International Symposium on Material Chemistry, Dec 07-11, **2010**, BARC, Mumbai.

Others

1. "Theoretical prediction of XRgCO⁺ ions (X = F, Cl and Rg = Ar, Kr, Xe)."
D. Manna, A. Ghosh and T. K. Ghanty, *J. Phys. Chem. A*, **2013**, *117*, 14282-14292.
2. "Structure and stability of Zn, Cd, and Hg atom doped golden fullerene (Au₃₂)."
D. Manna, T. Jayasekharan and T. K. Ghanty, *J. Phys. Chem. C*, **2013**, *117*, 18777-18788.
3. "Theoretical prediction of rare gas containing hydride cations: HRgBF⁺ (Rg = He, Ar, Kr, and Xe)."
A. Sirohiwal, **D. Manna**, T. Jayasekharan and T. K. Ghanty, *J. Phys. Chem. A*, **2013**, *117*, 10772-10782.
4. "Theoretical prediction of rare gas inserted hydronium ions: HRgOH₂⁺ ions."
A. Ghosh, **D. Manna** and T. K. Ghanty, *J. Chem. Phys.* **2013**, *138*, 194308.
5. "Significant modulation of CO adsorption behaviour on the various sites of Li doped Au₂₀ cluster."
K. Mondal, **D. Manna**, T. K. Ghanty and A. Banerjee, *Chem. Phys.* **2014**, *428*, 75-81.
6. "Thermodynamic study of Eu(III) complexation by pyridine monocarboxylates."
D. R. M. Rao, N. Rawat, R. M. Sawant, **D. Manna**, T. K. Ghanty and B. S. Tomar, *J. Chem. Thermodynamics*, **2012**, *55*, 67-74.

7. "Hindered rotation in a Novel 1,2,4-triazinyl phenanthroline (t-phen) ligand leading to improved separation of Am³⁺ and Eu³⁺ vis-á-vis 1,2,4-triazinyl bipyridine (t-bipy): A computational validation of the experimental results." A. Bhattacharyya, T. Gadly, P. K. Mohapatra, S. K. Ghosh, **D. Manna**, T. K. Ghanty and V. K. Manchanda, *RSC Advances* **2012**, 2, 7066-7073.
8. "Synthesis, characterization, photoluminescence and computational studies of monoorgano - gallium and -indium complexes containing dianionic tridentate ONE (E = O or S) schiff bases." N. Kushwah, M. K. Pal, A. Wadawale, V. Sudarsana, **D. Manna**, T. K. Ghanty and V. K. Jain, *Organometallics*, **2012**, 31, 3836-3843.
9. "Diorgano -gallium and -indium complexes derived from benzoazole ligands: synthesis, characterization, photoluminescence and computational studies." M. K. Pal, N. Kushwah, **D. Manna**, A. Wadawale, V. Sudarsana, T. K. Ghanty and V. K. Jain, *Organometallics* **2013**, 32, 104-111.
10. "Complexation of thorium with pyridine monocarboxylates: a thermodynamic study by experiment and theory." D. R. M. Rao, N. Rawat, R. M. Sawant, **D. Manna**, T. K. Ghanty and B. S. Tomar, *J. Chem. Thermodynamics* **2013**, 58, 432-439.
11. "Complexation of trivalent lanthanides and actinides with several novel diglycolamide functionalized calix[4]arenes: solvent extraction, luminescence and theoretical studies." D. R. Raut, P. K. Mohapatra, S. A. Ansari, S. V. Godbole, M. Iqbal, J. Huskens, **D. Manna**, T. K. Ghanty and W. Verboom, *RSC Advances* **2013**, 3, 9296-9303.
12. "Synthesis, structures and DFT calculations of 2-(4,6-dimethyl pyrimidyl)selenolate complexes of Cu(I), Ag(I) and Au(I) and their conversion into metal selenide nano-crystals."

R. K. Sharma, A. Wadawale, G. Kedarnath, **D. Manna**, T. K. Ghanty, B. Vishwanadh and V. K. Jain, *Dalton Trans.* **2014**, 43, 6525-6535.

13. “Diglycolamide-functionalized task specific ionic liquid (TSIL): Extraction, Luminescence, Theoretical and EPR investigations.”

A. Sengupta, P. K. Mohapatra, R. M. Kadam, **D. Manna**, T. K. Ghanty, M. Iqbal, J. Huskens and W. Verboom, *RSC Adv.* **4**, 46613-46623.

14. “Synthesis, characterization, photoluminescence and computational studies of mono- and diorgano- gallium complexes containing azo linked salicylaldehyde Schiff bases.”

M. Pal, N. Kushwah, A. P. Wadawale, **D.Manna**, V. Sudarsan, T. K. Ghanty, V. K. Jain, *J. of Organomet. Chem.* **2015**, 776, 98-106.

Debashree Manna

Dedicated to

My Parents

ACKNOWLEDGEMENTS

No words of acknowledgment will be sufficient for my family.

Most of all, I acknowledge my debt to Dr. Tapan K Ghanty, who has blended to perfection the roles of mentor, adviser, collaborator and scientist. I have benefited immeasurably from his scientific insight and scholarly attitude. The debt of a student to a great teacher is impossible to quantify. I am deeply indebted to Dr. Subrata Chattopadhyay, for his invaluable guidance, critical comments and constant encouragement during the entire course of this study. It is my pleasure to express my sincere thanks to Dr. Sulekha Mukhopadhyay for her constant help and support. I want to express my gratitude to Dr. B. N. Jagatap and Dr. Swapan K Ghosh for their constant encouragement and support. I would also like to acknowledge my doctoral committee members Dr. Dilip Maity and Dr. Chiranjib Majumder for giving valuable suggestions at all stages of this work. My sincere thanks are also due to all the members of Theoretical Chemistry Section for their unalloyed support. I would like to thank Dr. Arunasis Bhattacharyya and Dr. Soumyaditya Mula for sharing their knowledge and helping me to carry out certain amount of experimental work.

It is my pleasure to express sincere thanks to Mrs. Tuntun Ghanty for her indirect advices and support. Heartiest thanks are due for my friends especially Aparajita, Priyanka, Sumit, Debraj, Dibyendu, Mainak, Ayan, Krishnakanta, and Abhishek for their invaluable help and support.

I earnestly acknowledge the Department of Atomic Energy for providing the fellowship for my research. The supercomputing facility of Bhabha Atomic Research Center is also genuinely acknowledged for providing the computational resources.

.....Debashree

CONTENTS	Page No.
<i>SYNOPSIS</i>	i-viii
<i>LIST OF FIGURES</i>	ix-xi
<i>LIST OF TABLES</i>	xiii-xix

1. Introduction

1.1	Introduction to Coordination Complexes and Clusters	1
1.2	Importance of Selective Complexation from the Viewpoint of Nuclear Waste Management	6
1.3	Selective Encapsulation of Metal Atom/Ion into Fullerenes: Important Applications	11
1.4	Theoretical and Computational Chemistry: A General Introduction	12
1.5	Theoretical Methodologies	14
1.5.1	The Schrödinger Equation	14
1.5.2	Born-Oppenheimer approximation	16
1.5.3	Variational Principle	17
1.5.4	Slater Determinants	18
1.5.5	Wave Function Based Methods	19
1.5.5.1	The Hartree-Fock Approximation	19
1.5.5.2	Correlation Energy and Post-Hartree-Fock methods	21
1.5.6	Density Based Methods: Density Functional Theory	22
1.5.6.1	The Thomas-Fermi Model	22
1.5.6.2	The Hohenberg-Kohn Theorems	23
1.5.6.3	The Kohn-Sham Method	25
1.5.6.4	Solving the Kohn-Sham Equation	27
1.6	Scope of the Present Thesis	28

2. Actinide Selectivity of 1,10-Phenanthroline-2,9-dicarboxylic acid (PDA) Based Ligands: Insight from Density Functional Theory

2.1	Introduction	31
2.1.1	Density Functional Theory Derived Chemical Reactivity Indices	31
2.1.2	Actinide/ Lanthanide Separation: Basic Principle	32
2.1.3	Intra-ligand Synergism: A New Concept	32
2.2	Theoretical Background	36
2.3	Computational Details	37
2.4	Results and Discussions	39
2.4.1	Geometry Optimization and Structural Aspects	39
2.4.2	Energetics	44
2.4.3	Rationalization of Bonding Aspects through HSAB Principle and Fukui Reactivity Indices	45
2.4.4	Charge Distribution in the Complexes	51
2.4.5	Energy Decomposition Analysis	59
2.4.6	Effect of Counter Ions	61
2.4.7	Effect of Oxygen Donor Ligand in Presence of Nitrogen	65
2.5	Concluding Remarks	65

3. Actinide Selectivity of 1,10-Phenanthroline-2,9-dicarboxamide and its Derivatives: A Theoretical Prediction Followed by Experimental Validation

3.1	Introduction	69
3.1.1	Extension from Phenanthroline-diacids to Phenanthroline-dicarboxamide: Why?	69
3.2	Computational Details	71
3.3	Experimental Details	71

3.3.1	Synthetic Procedure	71
3.3.2	Method of Distribution Studies	74
3.4.	Results and Discussions	75
3.4.1	Theoretical Results	75
3.4.2	Experimental Results	83
3.4.2.1	Organic Synthesis	83
3.4.2.2	Results of Distribution Studies	86
3.5	Concluding Remarks	88

4. Theoretical Investigation of Am³⁺/Eu³⁺ Complexes with Cyanex Ligands

4.1	Introduction	91
4.1.1	Cyanex: A Widely Studied Ligand for Actinide Separation	91
4.1.2	Previous Theoretical Studies and our Motivations	91
4.2	Computational Details	94
4.3	Results and Discussions	94
4.3.1	Structural Details of the Metal-Cyanex Complexes	95
4.3.2	Thermodynamics of Extraction	100
4.3.3	Energy Decomposition Analysis	106
4.3.4	Charge Distribution in the Complexes	109
4.4	Concluding Remarks	112

5. Electronic Structure and Stability of the Actinide and Lanthanide Encapsulated Metallofullerenes

5.1	Introduction	115
5.1.1	Smaller Fullerenes: A prologue	115
5.1.2	Stabilization of Smaller Fullerenes and our Objective	116
5.1.3	Previous Studies on C ₂₀ and C ₃₆ Fullerenes	116
5.1.4	Stabilization through Encapsulation of Ln/An Atom or Ion	118

	into the Fullerene Cages	
5.2	Computational Details	118
5.3	Results and Discussions	120
5.3.1	Study of Ln/An Encapsulated C ₂₀ Fullerene	120
5.3.1.1	Structural Analysis	120
5.3.1.2	Molecular Orbital Diagram, Charge Distributions and Energetics	122
5.3.1.3	Study of Aromaticity	133
5.3.1.4	Analysis Including Spin-Orbit Effect	134
5.3.1.5	Analysis of Spectroscopic Data	135
5.3.2	Study of Uranium Encapsulated C ₃₆ Fullerene	139
5.3.2.1	Bare C ₃₆ Isomers	139
5.3.2.2	Structure and Stability of U@C ₃₆ Isomers	141
5.3.2.3	Thermodynamic Analysis	149
5.3.2.4	Molecular Orbital Energy Diagram and Charge Distribution Analysis	151
5.3.2.5	Effect of Spin-Orbit Interaction	160
5.3.2.6	Spectroscopic Study for C ₃₆ and U@C ₃₆ Clusters	161
5.4	Concluding Remarks	164

6. Actinide and Lanthanide Encapsulated Fullerenes: Insight from 32-electron Principle

6.1	Introduction	167
6.1.1	Stability of Clusters: Effect of Electronic Shell Closing	167
6.1.2	Introduction to 32-electron Principle	168
6.2	Computational Details	169
6.3	Results and Discussions	169
6.3.1	Study of Ln/An Encapsulated C ₂₄ Fullerene	169
6.3.1.1	Bare C ₂₄ Isomers	169
6.3.1.2	Structural Analysis of M@C ₂₄ Isomers	172

6.3.1.3	Energetics and Thermodynamics Stability of M@C ₂₄ Isomers	175
6.3.1.4	Molecular Orbital Energy Diagram and Charge Distributions	178
6.3.1.5	Effect of Spin-Orbit Interaction	185
6.3.1.6	Spectroscopic Analysis: C ₂₄ and M@C ₂₄	186
6.3.2	Study of Ln/An Encapsulated C ₂₆ Fullerene	189
6.3.2.1	Bare C ₂₆ Cage	189
6.3.2.2	Optimized Structures of M@C ₂₆ Clusters	190
6.3.2.3	Molecular Orbital Ordering and Charge Distribution Analysis	193
6.3.2.4	Energetics and Thermodynamic Stability	201
6.3.2.5	Effect of Spin-Orbit Interaction	205
6.3.2.6	Spectroscopic Properties of C ₂₆ and M@C ₂₆ Clusters	207
6.4	Concluding Remarks	209
7. Summary and Outlook		213
8. References		217

Synopsis

A rational approach towards designing ligand for selective complexation of metal ions in solution is of potential interests¹ in various fields like medicinal biology, environmental science, hydrometallurgy and nuclear waste management, and hence has important applications in different industries. Similarly, binding of metal ions or atoms with various carbon nano-clusters through endohedral encapsulation has also become the subject of enormous interest due to their diversity and potentials for numerous applications in the field of photovoltaics, electronics, optics, bio-medicine etc.² In recent times computational chemistry has been proven to be a versatile tool in providing meaningful insights to explain the behavior of various chemical systems and processes. Thus, the selectivity of a particular ligand towards a particular metal ion can be rationalized in a better way through theoretical modeling studies. Over the last few decades, *ab initio* density functional theory³ (DFT) based electronic structure calculations have been widely used to study the properties of several materials. DFT based calculations have been highly successful in predicting many ground state properties of several materials. In the present thesis we have attempted to provide theoretical insights towards the selective complexation and encapsulation of important metal ions/atoms with various ligands and clusters using *ab initio* density functional theory based methods. Few experiments have also been performed to validate some of our theoretical predictions.

In recent years, considerable attention has been given to understand the coordination complexes of trivalent lanthanide (Ln) and actinide (An) with various ligands because of its close link with the nuclear waste management steps. This is a challenging and difficult task because of very similar chemical properties of these two

series of ions as they have similar ionic radii and coordination numbers. The hard soft acid base principle (HSAB)⁴ classifies the Ln(III) and An(III) cations as hard Lewis acids, consequently their bonding is primarily ionic and mainly governed by charge density. Despite this, there is a modest enhancement of covalency in the bonding of An(III) with various ligands as compared to that in same Ln(III) complexes due to the larger spatial extent of the 5f shell of actinides as compared to the 4f shell in lanthanides. Because of this, an advantageous discrimination between An(III) and Ln(III) ions is possible while using soft donor atoms like sulfur and nitrogen.⁵ Here in this thesis we have proposed a modified concept related to selective complexation of actinides with either S or N donor ligands. It is important to note that efficiency of complex formation of either Ln(III) or An(III) with oxygen donors is much better as compared to N or S donors because both the set of metal ions are hard Lewis acids, however no selectivity is observed with O donor ligands. Although actinide selective ligands with hard donor atom like O seems highly unusual, in this thesis we have made an attempt to reply to this question affirmatively through the introduction of a new concept, 'intramolecular synergism', where electrostatic interaction predominates between the softer metal ion and hard donor atoms in presence of soft donor centers within the same ligand. Additionally, we have also theoretically investigated some conventional extractants to rationalize the experimentally observed trends.

The present thesis also includes theoretical predictions on new class of stable metallofullerenes with small fullerene cages, through encapsulation of an actinide or lanthanide atom/ion. Smaller fullerenes are of special interest due to the presence of high curvature and huge strain energy owing to the presence of adjacent pentagonal rings, which lead to clusters with unusual intra and inter -molecular bonding and

electronic properties. Among the smaller fullerenes ($n < 60$) only C_{36} have been isolated in solid form,⁶ although other smaller fullerenes have also been identified in various gas phase experiments. The smaller fullerenes, which are formed during the production of stable fullerenes, are difficult to isolate because of their extremely high chemical reactivity. However, encapsulation of proper dopant atom or ion (metal or nonmetal) may lead to the stabilization of smaller fullerenes. Stability of the smaller fullerenes has been shown to be increased considerably through encapsulation of a suitable metal atom or ion so that experimental observation of such smaller size fullerenes may be possible. This stability gain has been rationalized using some fundamental electronic structure principles, viz., electronic shell closing, geometrical shell closing, the concept of magic number etc.

The thesis is organized in the following manner.

Chapter 1: This introductory chapter emphasizes the importance of selective complexation as well as encapsulation of metal ions using different ligands and clusters. Moreover, some rational approaches towards understanding the metal ion selectivity using some basic chemical concepts have been discussed. In particular, problems relevant to selective extraction of actinides from the high level waste has been presented, which is very important in nuclear waste management (NWM). We have also discussed some of the commonly used methods for the separation of actinides from that of the lanthanides including their advantages and drawbacks. It is well known that theoretical modeling studies can provide better insight on the complexation or encapsulation behavior of any particular ligand or cluster towards a specific metal atom or ion. Thus, the importance of computational methods have been

outlined which provides some of the most valuable information that experiments cannot provide. Brief introduction to the existing computational methods have been discussed. Employing these computational methods, the scope of the thesis is to emphasize the complexation or encapsulation behavior of some of the important ligands and clusters towards a specific metal atom or ion.

Chapter 2: In chapter 2 we discuss the complexation behavior of pre-organized 1,10-phenanthroline-2,9-dicarboxylic acid (PDA) based ligands with trivalent lanthanides and actinides using DFT. Through functionalization of the PDA ligand with soft donor atoms such as sulfur, new ligands viz. mono-thio-dicarboxylic acids and di-thio-dicarboxylic acids have been designed. It has been found that selectivity in terms of complexation energy of actinides over lanthanides is the maximum with mono-thio-dicarboxylic acids where the metal-ligand binding is through the O atoms. This unusual aspect where softer actinide metal ion is bonded strongly with hard donor oxygen atoms has been explained using the popular chemical concepts, viz., HSAB principle and the Fukui reactivity indices.⁷ Also, the trends of the calculated metal-ligand bond distances and the corresponding complex formation energies have been rationalized.

Chapter 3: In the previous chapter the unusual selectivity achieved for actinides using hard-soft mixed donor ligands has been rationalized using the concept of “intra-ligand synergism”. Now in this chapter we discuss about theoretical design and prediction of the selectivity of 1,10-phenanthroline-2,9-dicarboxylamide (PDAM) towards Am(III) ion. Here it may be mentioned that the PDA ligand has very low solubility in both

organic and aqueous medium. To improve its organic solubility we switch from PDA to PDAM. Moreover, we further extended our calculation to explore different derivatives of PDAM with long alkyl chains e.g. N,N-di-isobutyl (PDAM-Isobutyl) and N-decyl (PDAM-Decyl). Subsequently, these amide derivatives have been synthesized and solvent extraction experiments have been carried out to validate our theoretical prediction.

Chapter 4: Apart from investigation of some new ligands, we have also theoretically studied complexation behavior of some of the conventional ligands. Chapter 4 deals with the study of the complexation of Am(III) and Eu(III) with Cyanex301 [bis(2,4,4-trimethyl-pentyl) dithiophosphinic acid], Cyanex302 [bis(2,4,4-trimethyl-pentyl) monothiophosphinic acid] and Cyanex272 [bis (2,4,4-trimethylpentyl) phosphinic acid] ligands in an unified and systematic way, to provide an in-depth insight into the experimentally observed selectivity trends.⁸ The structural, energetics, charge distributions and various energy components for all the complexes have been calculated within the framework of DFT. A shorter Am-S bond distance, a higher percentage of orbital interaction energy and a higher degree of metal-ligand charge transfer leading to a greater degree of covalency in Am(Cyanex301)₃ as compared to the Eu(Cyanex301)₃ complex are in agreement with the experimentally observed selectivity trend.

Chapter 5: This chapter deals with the selective encapsulation of metal atom or ions inside the small fullerene cages which may be considered as absorbent materials for radionuclide immobilization. Here we discuss the electronic structures, bonding,

stability and spectroscopic properties of the endohedral metallofullerenes, $M@C_{20}$ ($M = Pr^-, Pa^-, Nd, U, Pm^+, Np^+, Sm^{2+}, Pu^{2+}, Eu^{3+}, Am^{3+}, Gd^{4+}, Cm^{4+}$) and $U@C_{36}$ using DFT and its time-dependent variant.

The bare C_{20} cage with D_{3d} point group transforms to highly symmetrical icosahedral (I_h) structure through encapsulation of an f-block metal atom/ion with 6 valence electrons. The gain in stability of these metal encapsulated clusters can be attributed to the fulfillment of 26 valence electrons criteria corresponding to the fully occupied $2s2p1d$ atomic shells. To explain the experimentally observed⁹ intense $U@C_{36}$ peak in the mass spectrum of $U@C_{2n}$ metallofullerene, we have performed a systematic study on different $U@C_{36}$ isomers. The most stable $U@C_{36}$ isomer is found to be associated with C_{6v} symmetry and closed shell electronic configuration, derived from the open-shell D_{6h} structure of C_{36} .

Chapter 6: In this chapter we discuss two newly predicted series of highly stable metallofullerenes systems viz., $M@C_{26}$ ($M = Pr^-, Pa^-, Nd, U, Pm^+, Np^+, Sm^{2+}, Pu^{2+}, Eu^{3+}, Am^{3+}, Gd^{4+}, Cm^{4+}$) and $M@C_{24}$ (Pu, Cm^{2+}, Sm and Gd^{2+}). In addition to the 8- and 18-electron principles, possibility of 32 valence electron systems had been indicated by Langmuir in 1921.¹⁰ Here, the high stability of these systems have been rationalized through the fulfillment of 32 valence electron principle corresponding to the fully occupied *spdf* atomic shells for the encapsulated central atom. The electronic structures, bonding, stability and spectroscopic properties of these endohedral metallofullerenes, $M@C_{26}$ and $M@C_{24}$ have been investigated systematically using DFT.

The classical bare open shell C_{26} cage with D_{3h} symmetry and ellipsoid shape is transformed to a more spherical closed shell D_{3h} structures on encapsulation of an f-block metal atom/ion with 6 valence electrons. In a similar way, C_{24} fullerene has been found to be stabilized after encapsulation of an actinide/lanthanide atom with 8 valence electrons. Moreover, a transition in point group symmetry from C_2 to D_{6d} in the classical cage isomer of C_{24} cluster is observed after encapsulation of a plutonium atom within it. The encapsulation process leads to highly stable $Pu@C_{24}$ cluster. The high stability of both the $M@C_{26}$ and $M@C_{24}$ systems has been rationalized using the 32 valence electron principle.

Chapter 7: This is the concluding chapter of the thesis. This gives a brief outline about the achievements as well as possible future perspectives that can be explored from the present investigations on different aspects of selective complexation as well as cluster formation using a specific metal atom or ion utilizing various fundamental chemical concepts.

References:

1. Hancock, R. D. *Chem. Rev.* **1989**, *89*, 1875 and references in therein.
2. Popov, A. A.; Yang, S.; Dunsch, L. *Chem. Rev.* **2013**, *113*, 5989 and references in therein.
3. Parr, R. G.; Yang, W. *Density Functional Theory of Atoms and Molecules*, Oxford University Press, New York (**1989**).
4. Parr, R. G.; Pearson, R. G. *J. Am. Chem. Soc.* **1983**, *105*, 7512.
5. Diamond, R. M.; Street, K.; Seaborg, G. T. *J. Am. Chem. Soc.* **1954**, *76*, 1461.
6. Piskoti, C.; Yarger, J.; Zettl, A. *Nature* **1998**, *393*, 771.
7. Parr, R. G.; Yang, W. *J. Am. Chem. Soc.* **1984**, *106*, 4049.
8. Zhu, Y.; Chen, J.; Jiao, R. *Solvent Extr. Ion. Exch.* **1996**, *14*, 61.

9. Dunk, P. W.; Kaiser, N. K.; Mulet-Gas, M.; Rodriguez-Forteza, A.; Poblet, J. M.; Shinohara, H.; Hendrickson, C. L.; Marshall, A. G.; Kroto, H. W. *J. Am. Chem. Soc.* **2012**, *134*, 9380.
10. Langmuir, I. *Science* **1921**, *54*, 59.

LIST OF FIGURES

Figure	Title	Page No.
1.1	Composition of spent nuclear fuel.	7
1.2	Partitioning of minor actinides: Impact on waste management.	7
1.3	Various cycles related to waste management steps.	8
1.4	Different ligands for actinide-lanthanide separation and their separation factors.	10
1.5	Born-Oppenheimer approximation.	16
2.1	Optimized structures of a) bare ligands and b) metal ion-ligand complexes.	39
2.2	Difference in the optimized M-N and M-O/S bond distance values between Am(III) , Eu(III) and U(III), Ce(III) in presence of solvent.	40
2.3	Complexation energies (E/eV) of metal complexes, $[ML]^+$, with various ligands in presence of solvent.	45
2.4	Valence level occupied molecular orbitals of a) metal complexes, $[ML]^+$ and b) $[M-PHEN]^{3+}$ complexes.	55
2.5	Optimized structures of $[M-PDA(H_2O)_4]^+.2H_2O$ and $[M-PDA(NO_3)_3]^{-2}$.	62
2.6	Optimized structure of metal ion-ligand dimer complex, $[ML_2]^-$.	63
3.1	Schematic depictions of structures of 1,10-phenanthroline and it's different derivatives.	69
3.2	Optimized structures of a) $[M-(PDAM)_2]^{3+}$, b) $[M-(PDAM)_2(NO_3)]^{2+}$ and c) $[M-(PDAM)(NO_3)_3]$.	76
3.3	Optimized structures of a) $[M-(PDAM-Isobutyl)_2]^{3+}$ and b) $[M-(PDAM-Decyl)_2]^{3+}$.	83
3.4	a) 1H NMR spectra of 7 in $CDCl_3$ at 25 °C. b) ^{13}C NMR of 7 in $CDCl_3$.	84
3.5	Effect of pH on the distribution and separation behavior of Am^{3+} and Eu^{3+} using the $(PDAM-Decyl)_2$ liand.	87
4.1	Optimized structures of Metal-Cyanex Complex.	95

4.2	Percentage contribution of Pauli repulsion (ΔE_{Pauli}), electrostatic (ΔE_{elec}), steric (ΔE_{steric}) and orbital (ΔE_{orb}) interactions in the total interaction energies (ΔE_{int}) for the different Metal-Cyanex complexes.	108
5.1	Optimized structures of a) bare C_{20} cage and b) $M@C_{20}$ cluster.	120
5.2	Molecular orbital diagram for the $U@C_{20}$ cluster with (right) and without (left) spin-orbit coupling.	123
5.3	Valance molecular orbitals of $U@C_{20}$ cluster.	126
5.4	Bonding energy analysis for the $M@C_{20}$ clusters, where $M=Pr^{-}, Nd, Pm^{+}, Sm^{2+}, Eu^{3+}, Gd^{4+}$.	130
5.5	Bonding energy analysis for the $M@C_{20}$ clusters, where $M=Pa^{-}, U, Np^{+}, Pu^{2+}, Am^{3+}, Cm^{4+}$.	130
5.6	UV-Visible spectra for the C_{20} cage and the $U@C_{20}$ cluster without and with spin-orbit coupling.	137
5.7	Optimized structures of a) bare C_{36} (D_{2d}) cage and b) $U@C_{36}$ (C_{6v}) cluster.	142
5.8	Optimized structures of different $U@C_{36}$ clusters.	143
5.9	Interaction energy analysis for the different $U@C_{36}$ clusters. Inset: Total interaction energy represented in a magnified scale.	145
5.10	Molecular orbital diagram for the $U@C_{36}$ (C_{6v}) cluster without (left) and with (right) spin-orbit coupling.	152
5.11	Valance molecular orbitals of $U@C_{36}$ (C_{6v}) . (Orbital notations within the parentheses refers to the orbitals contributed by pure C_{36} cage.)	154
5.12	Schematic diagrams of the frontier orbital energy levels (in eV) for the U atom, two most stable C_{36} isomers and the corresponding $U@C_{36}$ clusters.	156
5.13	Density of states (DOS) for the a) uranium atom, b) bare C_{36} cage and c) $U@C_{36}$ cluster.	158
5.14	Simulated vibrational spectra of the a) bare C_{36} cage and b)	161

	U@C ₃₆ cluster.	
5.15	UV-visible spectra for the C ₃₆ cage.	163
5.16	UV-visible spectra for the U@C ₃₆ Cluster, a) without and b) with spin-orbit coupling.	164
6.1	Optimized structures of a) bare C ₂₄ and b) M@C ₂₄ clusters.	170
6.2	Binding energy per atom graph for different M@C ₂₄ clusters.	174
6.3	Molecular orbital energy diagram for the Pu@C ₂₄ (D _{6d}) cluster without (left) and with (right) spin-orbit coupling.	179
6.4	Valance molecular orbitals of Pu@C ₂₄ . Orbitals written within the parentheses refers to the orbitals contributed by pure C ₂₄ cage.	180
6.5	Density of states (DOS) for the Pu atom, bare C ₂₄ cage and the Pu@C ₂₄ cluster.	181
6.6	Simulated vibrational spectra of the a) bare C ₂₄ cage and b) Pu@C ₂₄ cluster.	186
6.7	UV-visible spectra for the Pu@C ₂₄ Cluster: a) without and b) with spin-orbit coupling.	188
6.8	UV-visible spectra for the C ₂₄ cage.	189
6.9	Optimized structures of a) bare C ₂₆ cage and b) M@C ₂₆ cluster.	191
6.10	Molecular orbital diagram for the U@C ₂₆ cluster without (left) and with (right) spin-orbit coupling.	194
6.11	Valance molecular orbitals of U@C ₂₆ . Within the parentheses ‘P’ refers to the orbitals contributed by pure C ₂₆ cage only.	195
6.12	Interaction energy analysis for the M@C ₂₆ clusters, where M= Pr ⁻ , Nd, Pm ⁺ , Sm ²⁺ , Eu ³⁺ , Gd ⁴⁺ .	202
6.13	Interaction energy analysis for the M@C ₂₆ clusters, where M= Pa ⁻ , U, Np ⁺ , Pu ²⁺ , Am ³⁺ , Cm ⁴⁺ .	209
6.14	UV-visible spectra for the C ₂₆ cage.	208
6.15	UV-visible spectra for the U@C ₂₆ cluster, a) without and b) with spin-orbit coupling.	208

LIST OF TABLES

Table	Title	Page No.
2.1	Calculated M-L bond distances (Å) and complexation energies (eV) in gas (ΔE_g) and solvent (ΔE_s) phases for Am^{3+} and Eu^{3+} complexes using def-SV(P)/BP86 method.	41
2.2	Calculated M-L bond distances (Å) and complexation energies (eV) in gas (ΔE_g) and solvent (ΔE_s) phases for U^{3+} and Ce^{3+} complexes using def-SV(P)/BP86 method.	41
2.3	Calculated M-L bond distances (Å) and complexation energies (eV) in gas (ΔE_g) and solvent (ΔE_s) phases for Am^{3+} and Eu^{3+} complexes with TZVP/BP86 method.	43
2.4	Calculated bond distances (d in Å) for $[\text{ML}]^+$ complexes obtained from ADF software with TZ2P basis sets and BP86 exchange-correlation functional in the gas phase.	43
2.5	Effect of different exchange correlation functionals (PBE and BLYP) on the M-L bond distance (d in Å) of $[\text{ML}]^+$ complexes calculated using def-SV(P).	43
2.6	Calculated hardness and softness values of the metal ions, dianionic form of the bare ligands and $[\text{M-PHEN}]^{3+}$ complexes in gas and solvent phases using def-SV(P)/BP86 method.	47
2.7	Calculated values of Fukui indices for the nucleophilic attack on the donor site (f_{ei}) and the electrophilic attack on the metal site (f_{nu}) of the free ligands and the $[\text{M-PHEN}]^{3+}$ complexes, respectively, in presence of solvent.	50
2.8	Calculated values of charges on donor center and Fukui indices for the nucleophilic attack on the donor sites in gas and solvent phases for the dianionic form of the bare ligands using def-SV(P)/BP86 method.	50
2.9	Calculated values of Fukui indices for the electrophilic attack on the metal centre of $[\text{M-PHEN}]^{3+}$ complexes in gas and solvent phases using def-SV(P)/BP86 method.	51
2.10	Calculated atomic charges on metal and donor centers of Am^{3+}	52

	and Eu^{3+} complexes in gas and solvent phases using def-SV(P)/BP86 method.	
2.11	Calculated atomic charges on metal and donor centers of U^{3+} and Ce^{3+} complexes in gas and solvent phases using def-SV(P)/BP86 method.	52
2.12	Calculated atomic charges on metal and donor centers of Am^{3+} and Eu^{3+} complexes ($[\text{ML}]^+$ and $[\text{ML}_2]^{-1}$) in gas and solvent phases using TZVP/BP86 method.	53
2.13	Calculated atomic charges at metal centers (q_M) of the complexes $[\text{ML}]^+$ for different exchange correlation functionals (PBE and BLYP) using def-SV(P).	54
2.14	Calculated atomic charges on metal and donor centers of U^{3+} and Ce^{3+} complexes ($[\text{ML}_2]^{-1}$) in gas and solvent phases using TZVP/BP86 method.	54
2.15	Percentage orbital and electrostatic interactions in the total bonding energy as obtained from energy decomposition analysis for Am^{3+} and Eu^{3+} complexes using BP86 functional in the gas phase.	60
2.16	Percentage orbital and electrostatic interactions in the total bonding energy as obtained from energy decomposition analysis for U^{3+} and Ce^{3+} complexes using BP86 functional in the gas phase.	61
2.17	Calculated M-L bond distances (\AA) (in gas phase) and complexation energies (eV) in gas (ΔE_g) and solvent (ΔE_s) phases for Am^{3+} and Eu^{3+} complexes, $[\text{M-PDA}(\text{H}_2\text{O})_4]^+ \cdot 2\text{H}_2\text{O}$ and $[\text{M-PDA}-(\text{NO}_3)_3]^{2-}$ with def-SV(P)/BP86 method.	62
2.18	Calculated M-L bond distances (\AA) and complexation energies (eV) in gas (ΔE_g) and solvent (ΔE_s) phases for Am^{3+} and Eu^{3+} complexes, $[\text{ML}_2]^-$ with TZVP/BP86 method	62
2.19	Calculated M-L bond distances (\AA) and complexation energies (eV) in gas (ΔE_g) and solvent (ΔE_s) phases for U^{3+} and Ce^{3+} complexes, $[\text{ML}_2]^-$ with TZVP/BP86 method	63

3.1	Calculated M-L bond distances (Å) and complexation energies (eV) in gas (ΔE_g) and solvent (ΔE_s) phases for Am^{3+} and Eu^{3+} complexes using BP86/def-SV(P) method.	77
3.2	Calculated M-L bond distances (Å) and complexation energies (eV) in gas (ΔE_g) and solvent (ΔE_s) phases for Am^{3+} and Eu^{3+} complexes using BP86/def-SV(P) method.	78
3.3	Calculated atomic charges on metal and donor centers of Am^{3+} and Eu^{3+} complexes using BP86/def-SV(P) method.	79
3.4	The calculated BCP properties (electron density [ρ], Laplacian of the electron density [$\nabla^2\rho$]) of the M-N and M-O/M-S bonds in Am^{3+} and Eu^{3+} complexes using BP86/TZ2P method.	81
3.5	Distribution and separation behavior of Am^{3+} and Eu^{3+} using PDAM, (PDAM-Isobutyl) ₂ and (PDAM-Decyl) ₂ ligands.	87
4.1	Calculated M-L bond distances (in Å) in gas and solvent Phases for Am^{3+} and Eu^{3+} complexes with Cyanex301, Cyanex302 and Cyanex272 using BP86/def-SV(P) and BP86/TZVP methods and Turbomole program.	96
4.2	Calculated M-L bond distances (in Å) in gas phase for Am^{3+} and Eu^{3+} complexes with Cyanex301, Cyanex302 and Cyanex272 using different GGA functionals in ADF program.	97
4.3	Calculated values of free energy of extraction (in eV) in gas (ΔG_{gas}) and solvent (ΔG_{sol}) (T=298.15 K, P=1 atm) phases for Am^{3+} , Eu^{3+} complexes with Cyanex301, Cyanex302 and Cyanex272 using Turbomole program.	102
4.4	Calculated values of free energy of extraction (in eV) in solvent (ΔG_{sol}) (T=298.15 K, P=1 atm) phase for Am^{3+} , Eu^{3+} complexes with Cyanex301, Cyanex302 and Cyanex272 using BLYP/def-SV(P) method in Turbomole program.	104
4.5	Calculated values of free energy of extraction (in eV) in solvent (ΔG_{sol}) (T=298.15 K, P=1 atm) phase for Am^{3+} , Eu^{3+} complexes with Cyanex301, Cyanex302 and Cyanex272 using BP86/TZVP method in Turbomole Program.	104

4.6	Interaction energies (ΔE_{int}), ligand preparatory energies (ΔE_{prep}) and complexation energies (ΔE_{comp}) for the various Am^{3+} and Eu^{3+} complexes (in eV).	107
4.7	Calculated NPA atomic charges on metal and donor centers of Am^{3+} and Eu^{3+} complexes with Cyanex301, Cyanex302 and Cyanex272 in gas and solvent phases using Turbomole program.	110
4.8	Calculated natural orbital populations at the metal centres for all the complexes using Turbomole program and Mayer bond orders (BOs) for the M-S/O bonds using ADF program.	111
5.1	Calculated values of M-C bond distance ($R_{\text{M-C}}$ in Å) using different functionals with Turbomole and ADF programs for all the $\text{M}@\text{C}_{20}$ clusters.	122
5.2	The calculated values of HOMO-LUMO gap (in eV) obtained using Turbomole and ADF programs for the $\text{M}@\text{C}_{20}$ clusters with different functionals.	124
5.3	Calculated Natural, Löwdin and VDD Charges on metal centers for the $\text{M}@\text{C}_{20}$ clusters using Turbomole and ADF programs with different functionals.	127
5.4	Calculated values of orbital population for the central metal atom in $\text{M}@\text{C}_{20}$ clusters with B3LYP functional using Turbomole program.	129
5.5	Calculated complexation energy (ΔE_{bond}) and the atomization energy (BE) values (in eV) using ADF with B3LYP functional for the $\text{M}@\text{C}_{20}$ clusters.	132
5.6	Calculated harmonic vibrational frequencies (cm^{-1}) for the $\text{M}@\text{C}_{20}$ clusters ($\text{M} = \text{Pr-}, \text{Nd}, \text{Pm}^+, \text{Sm}^{2+}, \text{Eu}^{3+}, \text{Gd}^{4+}$) calculated using B3LYP functional. (Intensities in km/mol are reported in parentheses.)	136
5.7	Calculated harmonic vibrational frequencies (cm^{-1}) for the $\text{M}@\text{C}_{20}$ clusters ($\text{M} = \text{Pa-}, \text{U}, \text{Np}^+, \text{Pu}^{2+}, \text{Am}^{3+}, \text{Cm}^{4+}$) calculated using B3LYP functional. (Intensities in km/mol are reported in	136

	parentheses.)	
5.8	Relative energies (in eV) of different isomers of C ₃₆ cage using def-TZVP basis sets with Turbomole and U@C ₃₆ cluster using def-TZVP and TZ2P basis sets with Turbomole and ADF programs.	140
5.9	Calculated values of average (R _{U-C} (Avg)) and the Shortest (R _{U-C} (Shrt)) U-C bond distances (in Å) using def-TZVP and TZ2P basis sets with Turbomole and ADF programs, and binding energy per atom (BE) in eV using def-TZVP basis sets and B3LYP functional with Turbomole program for all the U@C ₃₆ isomers.	144
5.10	The first-order transition state (TS) symmetries and the energy differences between the minima and the transition states (ΔE in eV) for all the U@C ₃₆ clusters with Turbomole program using B3LYP functional.	148
5.11	The calculated values of change in enthalpy and free energy (in kJ/mol) corresponding to the reaction U + C ₃₆ → U@C ₃₆ as obtained using def-TZVP basis sets and B3LYP Functional with Turbomole program for the different isomers.	149
5.12	The calculated values of HOMO-LUMO gap (in eV) as obtained using def-TZVP and TZ2P basis sets with Turbomole and ADF programs for the U@C ₃₆ isomers using B3LYP functional.	152
5.13	Calculated Mulliken, Hirshfeld and VDD charges on uranium atom in the U@C ₃₆ isomers using TZ2P basis sets and B3LYP functional with ADF program.	158
5.14	Calculated values of orbital population for the central uranium atom in U@C ₃₆ isomers using TZ2P basis sets and B3LYP functional with ADF program.	159
6.1	Calculated values of average X ^a -C and M-C bond lengths for bare and metal encapsulated C ₂₄ systems using PBE functional in Turbomole. Average C-C bond length values are presented in	171

	parenthesis.	
6.2	Calculated relative energy values (in eV) as obtained for the bare C_{24} and $M@C_{24}$ clusters using PBE (B3LYP) functional in Turbomole program and using PBE functional in ADF program within the square bracket.	171
6.3	Calculated values of HOMO-LUMO Gap (in eV) as obtained from Turbomole program for the bare C_{24} and $M@C_{24}$ clusters using PBE (B3LYP) functional.	172
6.4	Calculated enthalpy values (ΔH in kJ mol^{-1}) for the reaction, $M + C_{24} \rightarrow M@C_{24}$. Corresponding values of Gibbs free energies (ΔG in kJ mol^{-1}) are given within the square bracket.	175
6.5	Calculated natural and VDD (in parenthesis) charge values on metal centers for $M@C_{24}$ clusters computed with PBE functional in Turbomole and ADF programs, respectively.	183
6.6	Calculated values of orbital populations for the central metal atom (M) in $M@C_{24}$ clusters using PBE functional in Turbomole.	184
6.7	Calculated values of M-C bond distance (R_{M-C} in \AA) using different functionals with Turbomole and ADF programs and binding energy per atom (BE) in eV with Turbomole program for all the $M@C_{26}$ clusters.	192
6.8	The calculated values of HOMO-LUMO gap (in eV) as obtained using Turbomole and ADF programs for the $M@C_{26}$ clusters with different functionals.	195
6.9	Calculated Natural, Löwdin and VDD charges on metal centers for the $M@C_{26}$ clusters using Turbomole and ADF programs with different functionals.	198
6.10	Calculated values of orbital population for the central metal atom in $M@C_{26}$ clusters with B3LYP functional using Turbomole program.	199
6.11	The percentage contributions of the metal valance orbitals to the hybridized valence MOs as obtained using ADF program.	200

6.12 The calculated values of change in enthalpy (in kJ/mol), 203
entropy (in $\text{Jmol}^{-1}\text{K}^{-1}$) and free energy (in kJ/mol)
corresponding to the reaction $\text{M} + \text{C}_{26} \rightarrow \text{M}@\text{C}_{26}$ as obtained
from Turbomole program using B3LYP functional.

Chapter 1: Introduction

1.1 Introduction to Coordination Complexes and Clusters

Since the discovery of coordination chemistry by the Swiss scientist Alfred Werner (1866-1919), who was awarded the 1913 Nobel Prize in chemistry for his pioneering work on metal complexes, coordination chemistry has become an important branch of chemistry.¹ In honor of Werner, simple coordination compounds are often called *Werner Complexes*. It was not before the end of World War II that coordination chemistry became a popular research field, thanks to the impulse programs for the development of nuclear energy and to the development of theoretical models that allowed explaining the chemical bonding in metal complexes (for instance the Ligand Field Theory).² Coordination chemistry is the chemistry of coordination compounds or metal complexes. A coordination compound consists of a central metal ion surrounded by a certain number of ligands. In general, simple inorganic anions or molecules are considered as ligands, however, large organic molecules can also act as ligands. The ligands are bound via so-called dative or coordinative bonds to the central metal ion. The ligands do not really require the metal to complete their valence shell, but the interaction with the metal ion will result in a coordination compound, which is more stable than the metal ion and the ligands considered separately. Because the central metal ion is very often a d-block element (transition metals) or an f-block element (lanthanides and actinides), for many scientists coordination chemistry is a synonym for the chemistry of the transition metals, lanthanides and actinides. However, s-block and p-block elements can also form coordination compounds. The difference between a coordination compound and an organometallic compound is that in an organometallic compound a direct metal-carbon (M-C) bond is present, whereas

in a coordination compound there is either a heteroatom (O, N, S, P etc.) located between the metal and the carbon atom or no carbon atom at all. Carbonyl compounds (with CO as the ligand) and cyano compounds (with CN⁻ as the ligand) are borderline cases with direct metal-carbon bonds. In general, carbonyl complexes are considered as organometallic compounds and cyano complexes as coordination compounds. Due to the presence of a metal ion with unpaired electrons, coordination compounds can have interesting spectroscopic and magnetic properties. Often, coordination compounds are intensively colored. Although coordination compounds such as the tetrammine copper(II) complex, [Cu(NH₃)₄]²⁺ and 'Berlin blue', Fe₄[Fe(CN)₆]₃ have been known for centuries, coordination chemistry is a branch of chemistry since 1893. These coordination compounds are widely present in mineral, plant and animal worlds and are known to play many important roles in analytical chemistry (environmental), metallurgy, biological systems, industry, medicine etc. Coordination compounds are also used in many qualitative and quantitative chemical analyses. The familiar color reactions given by metal ions with a number of ligands (especially chelating ligands), as a result of formation of coordination entities, form the basis for their detection and estimation by classical and instrumental methods of analysis. Examples of such reagents include ethylene diamine tetra acetic acid (EDTA), dimethylglyoxime (DMG), α-nitroso-β-naphthol, cupron etc. The Ca²⁺ and Mg²⁺ ions form stable complexes with EDTA and the hardness of water is generally estimated by simple titration with Na₂EDTA. Extraction and purification of metals can be achieved through formation and subsequent decomposition of their coordination compounds. Coordination compounds are also of great importance in biological systems. The pigment responsible for photosynthesis, chlorophyll is a coordination compound of

magnesium. Hemoglobin, the red pigment of blood which acts as oxygen carrier is a coordination compound of iron and vitamin B₁₂ is a coordination compound of cobalt. Among the other compounds of biological importance with coordinated metal ions are the enzymes like, carboxypeptidase–A and carbonic anhydrase. Thus, by studying simple coordination compounds, one can gain insight into the mechanism of complex biochemical processes based on the use of a metal ion inside the cell. Moreover, coordination compounds are of importance for medical diagnosis and therapy, for examples, contrast agents for magnetic resonance imaging (MRI), the active compounds in chemotherapy and in photodynamic therapy for the treatment of cancer. Metal complexes are being studied as potential new drugs (metallopharmaceutics). The chelate therapy is used for the treatment of problems caused by the presence of metals in toxic proportions in plants and animal systems. For instances, excess of copper and iron are removed by the chelating ligands D–penicillamine and desferrioxime–B via the formation of coordination compounds. EDTA is used in the treatment of lead poisoning. Some coordination compounds of platinum effectively inhibit the growth of tumors. Apart from medical applications, coordination compounds are also used as catalysts for many industrial processes such as, use of rhodium complex, [(Ph₃P)₃RhCl], a Wilkinson catalyst for the hydrogenation of alkenes. Many dyes and pigments, for instance the blue color of writing ink, are metal coordination complexes. In black and white photography, the developed film is fixed by washing with hypo solution which dissolves the undecomposed AgBr to form a complex ion, [Ag(S₂O₃)₂]³⁻.

In a similar way cluster science is also one of the contemporary and exciting areas of researches in chemistry. Recently, cluster chemistry has become an important

subject in various subfields of chemistry ranging from organometallic chemistry, coordination chemistry, homogeneous and heterogeneous catalysis, and solid-state chemistry. The occurrence of molecular clusters, like fullerene C_{60} , constitutes a fundamental bridging between the chemistry of isolated chemical compounds and that of the solid. Since, clusters especially metal encapsulated clusters exhibit interesting bonding as well as electronic, structural, physical, chemical and catalytic properties, research in metal clusters has become an important enterprise over the past two decades. In chemistry, a cluster is defined as an ensemble of bound atoms or molecules that is of intermediate size in between a molecule and a bulk solid. Clusters exist in diverse stoichiometries and nuclearities. For example, carbon and boron atoms form fullerene and borane clusters, respectively. Transition metals and main group elements form especially robust clusters. Clusters can also consist solely of a certain kind of molecules, such as water clusters. The phrase *cluster* was first invented by F.A. Cotton in the early 1960's to refer to compounds containing metal-metal bonds.³ In another definition, a cluster compound contains a group of two or more metal atoms where direct and substantial metal-metal bonding is present. There are several characteristic features which differentiate a cluster from a molecule and bulk matter. First and foremost difference between clusters and bulk matter is in size; whether three particles bound together constitute a cluster is a matter of choice and convention, but an aggregate of four or more atoms or molecules certainly encompasses a cluster. Such a small cluster would differ markedly from bulk matter in almost all its properties. The variability of the properties of clusters with the number of their constituent particles is the second most significant difference between clusters and bulk matter. The properties of a small cluster vary

significantly and, in general, neither uniformly nor even in the same direction with a change in the number of constituent particles, whereas the properties of bulk matter remain unchanged by the addition or subtraction of a few atoms or molecules. Medium-size clusters have properties that differ smoothly with the number of constituent particles (denoted by N), but their properties, such as the melting point, generally differ significantly from those of the corresponding bulk matter. The properties of large clusters vary smoothly with N and clearly merge into their corresponding bulk counterpart. This distinction is not extremely precise. For small clusters the average binding energies—that is, the average energy per constituent atom or molecule required to separate the particles from each other—vary widely with N . The reason for this wide range is that clusters of certain values of N , known as magic numbers, can acquire unusually stable geometric and electronic structures that yield large binding energies. However, clusters with different values of N may not possess especially stable forms. On the other hand, the manner in which clusters differ from molecules is more of a categorical nature than one of physical properties. Clusters can be made of any number of particles and may have any of several geometries with few exceptions whereas a molecule generally possesses definite composition and geometry. In spite of their multiplicity of structures, small clusters of fixed size, undergoing vibrations of small amplitude around a single geometry, are in most respects indistinguishable from molecules. If such clusters are given energy that is not great enough in magnitude to break them into separate parts, they may assume other geometries, alternating among different structural forms. This phenomenon is rarely seen with conventional molecules; however, few exceptions are there where energized molecules exhibit more than one structure. Thus, small clusters

are much like molecules, while very large clusters are quite similar to bulk matter. The properties of clusters whose size is between these extremes may be like either or like neither. Recently, endohedrally doped metal clusters have become the subject of enormous interest due to their diversity and potentials for numerous applications in the field of photovoltaics, electronics, optics, bio-medicine etc. The physical and chemical properties of an endohedrally doped metal cluster can be easily tuned by altering the nature of the encapsulated species, which in turn can act as a promising functional material.

1.2 Importance of Selective Complexation from the Viewpoint of Nuclear Waste Management

Presently, designing ligands for selective complexation of metal ions in solution is of enormous importance⁴ in various fields like medicinal biology, environmental sciences, hydrometallurgy, and nuclear waste management as well as for different industrial applications. Over the past few decades, considerable attention has been given to design actinide selective ligands due to its close link with the nuclear waste management processes. Spent nuclear fuel (Figure 1.1) consists of unused U, stable fission products, other long-lived fission products, minor actinides, and Cs, Sr, I, Tc and Pu. Almost all fission products decay to negligible level after 1000 yrs except ¹²⁹I, ⁹⁹Tc, and long lived actinides like Np, Am, Cm (very high half lives). These require millions of years to reduce the toxicity level to the recommended level (4000Bq/g) (Figure 1.2).

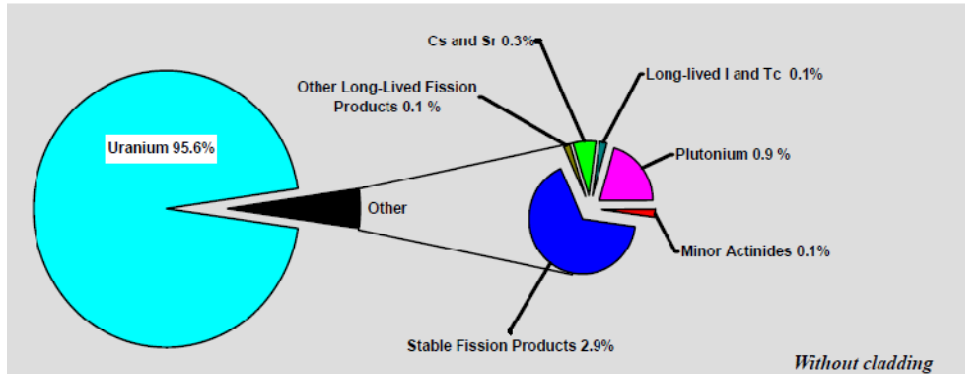


Figure 1.1 Composition of spent nuclear fuel

Removal of long lived α emitting actinides from these wastes under partitioning and transmutation (P&T) option would greatly reduce their long-term radiological hazards and leads to comparatively safer waste. Thus, selective extraction of actinides (An) from the lanthanides (Ln) is one of the most important steps (Figure 1.3) to prevent the long term radiological hazard generated from the nuclear waste. But separation of actinides from lanthanides is a very difficult task due to their similar charge/radius ratio values, and same type of coordinating behavior.

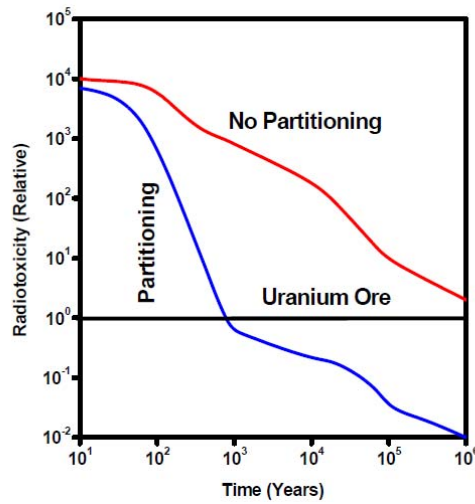


Figure 1.2 Partitioning of minor actinides: Impact on waste management

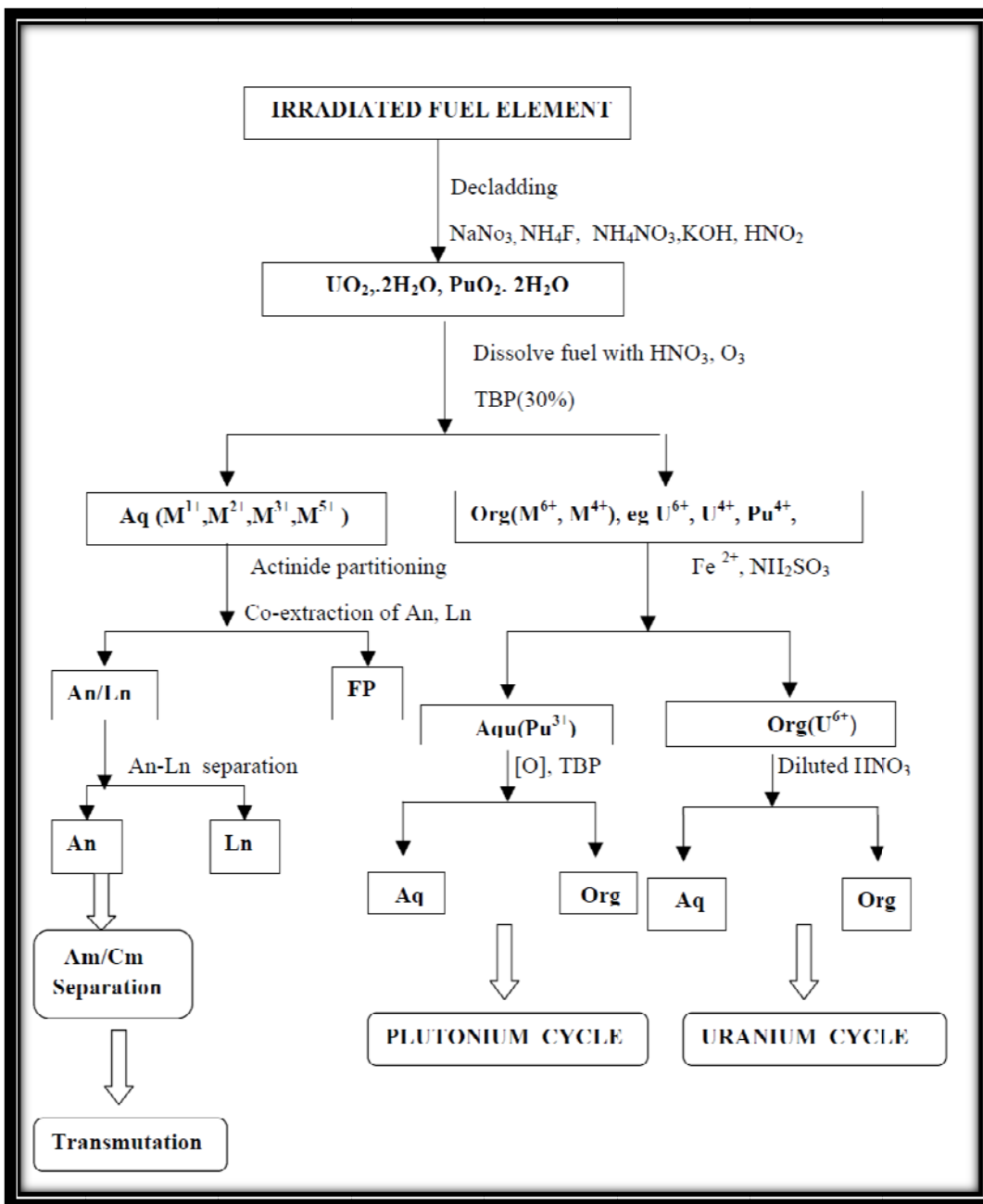


Figure 1.3 Various cycles related to waste management Steps

An(III) and Ln(III) cations are hard Lewis acids, consequently their bonding is primarily ionic and mainly governed by charge density. Despite this, there is a modest enhancement of covalency in the An(III)-ligand bonding compared to that in Ln(III)

complexes due to the larger spatial extent of the 5f shell of actinides as compared to the 4f shell in lanthanides. This results in an advantageous discrimination in bonding between An(III) and Ln(III) ions, using soft donor atoms like sulfur, nitrogen etc. By exploiting this strategy, one can make an attempt to separate actinides from lanthanides. The concept of using soft donor ligands for actinide selectivity was proposed by Glenn Seaborg in 1954,⁵ who received Nobel Prize in chemistry for discoveries of the chemistry of trans-uranium elements in 1951. So far, separation of trivalent actinides from the lanthanides has generally been attempted exploiting the tendency to form the stronger covalent bonding of the trivalent actinides with soft donor ligands as compared to that of the lanthanides.

The separation of An(III) from Ln(III) was first achieved by cation exchange from concentrated chloride media. In general, common processes employed for the Ln(III)/An(III) separation are: (i) Trans Americium Extraction (TRAMEX) process,⁶ where the trivalent actinides are separated selectively from the bulk of lanthanides in presence of a large concentration of chloride ion (11M LiCl) at pH 1-2 using a tertiary amine, viz. 0.6 M alamine-336 (a mixture of octyl and decyl tertiary amines) in diethyl benzene, (ii) Trivalent Actinide Lanthanide Separation by Phosphorus Extractants Aqueous Complexes (TALSPEAK) process,⁷ where trivalent lanthanides are selectively extracted here from the actinides using di-2-ethylhexyl phosphoric acid (D2EHPA), (iii) Selective ActiNide EXtraction (SANEX) processes, where a series of processes have been developed for the Ln(III) / An(III) separation employing 'N' donor heteropolycyclic ligands. These SANEX processes have three different categories, SANEX I, SANEX II and SANEX III.⁸⁻¹² Various other nitrogen donor extractants such as Terpyridyl, Amido-bis pyridyl triazene (ADPTZ), Bis-triazenyl

pyridine (BTP) and bis-triazenyl bipyridine (BTBP) are also used in different processes. Besides the N donor extractants, a number of S donor extractants have also been used in the separation of trivalent actinides from lanthanides, usually at low pH. Thiopyrazolone, aromatic dithiophosphinic acids (SANEX-IV¹³⁻¹⁵ process) and Cyanex ligands are commonly used S donor extractants. All these ligands except Cyanex show a maximum separation factor of ~100, however, in 1996 Zhu et. al. have reported a separation factor of ~5900 with S donor Cyanex301.¹⁶ Commonly used ligands for An/Ln separation and their separation factors are shown in Figure 1.4.

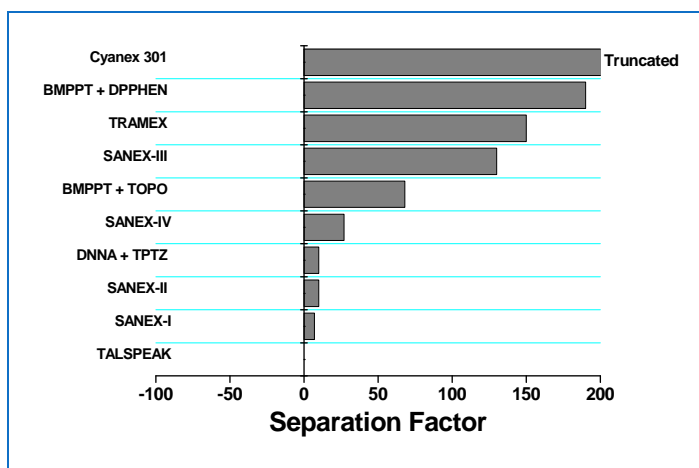


Figure 1.4 Different ligands for actinide-lanthanide separation and their separation factors

Apart from conventional experimental investigations, study of bonding of specific metal ion either through encapsulation in a suitable host molecule or by means of complex formation with a selective ligand using theoretical or computational techniques has received considerable attention among researchers. Indeed, in the present thesis we have attempted to provide theoretical insights towards the selective

complexation and encapsulation of important metal ions/atoms with different ligands using various theoretical and computational techniques.

1.3 Selective Encapsulation of Metal Atom/Ion into Fullerenes: Important Applications

The possibility to use the hollow carbon clusters, known as fullerenes, as robust containers for other species is one of the most attractive properties. For the period of the past two decades endohedral metallofullerenes (fullerenes with metal atom(s) encapsulated), a novel forms of fullerene-based materials have attracted wide interest not only in physics and chemistry but also in interdisciplinary areas such as materials and biological sciences.¹⁷ After the discovery of macroscopic fullerene production¹⁸ in 1990 endohedral metallofullerenes (EMFs) attracted a booming increase of attention although it was first anticipated in 1985.¹⁹ During this period, many new EMF molecules were reported through putting many metal atoms inside fullerenes, and thus the basis for the further advance in the field was grounded.

Endohedral nano-metallofullerenes are of immense interest due to their diversity and potentials for numerous applications. Owing to their unique magnetic, electronic and optical properties the endohedral metallofullerenes play a significant role in emerging nanotechnology, and become the important building blocks for nanoelectronic devices, chemical and biological sensors and nano-composites. The robust carbon cage and large hollow interior of the fullerene can serve as an ideal storage medium for atoms and molecules, as well as a nanometric scale capsule for chemical reaction. The physical and chemical properties of a metallofullerene can be easily tuned by altering the encapsulated species, which in turn can act as a promising functional

material. The radioactive isotopes doped inside the metallofullerenes are used in medical diagnostics purpose, therapy of cancer and immunotherapy, for examples $\text{Gd}@C_{82}$ as MRI contrast agent,²⁰ Lu-encapsulated fullerene as X-Ray imaging agent,²¹ $\text{Ho}@C_n$ in Cancer Therapy.²² Moreover $\text{Lu}_3\text{N}@C_{80}$ is used in photovoltaics and $\text{M}@C_n$ as an electron acceptor in artificial photosynthesis.^{23,24} In endohedral metallofullerenes the encapsulated metal atom can be in different isotopic forms as well as in radioactive form. Therefore, endohedral metallofullerenes attracted considerable attention in the sphere of radiochemistry and materials science since fullerene may act as nanoscale absorbent materials for radionuclide immobilization. Moreover, it may be possible to entrap different actinides into carbon nanostructures, resulting into chemically stable radionuclide encapsulated bio-compatible fullerenes for various applications including safe management of nuclear wastes and designing cluster-assembled novel materials. In the present thesis we have provided in-depth insights into the process of encapsulation of various metal atoms/ions within different fullerene cages using computational techniques.

1.4 Theoretical and Computational Chemistry: A General Introduction

Theoretical chemistry is an exciting, contemporary and broad field, rooted in chemistry. It has tremendous impact on all branches of chemistry and also finds diverse applications in medicine, life science, condensed matter physics, computational materials science, chemical engineering, nuclear science etc. Thus, it straddles the vibrant interfaces between chemistry, physics, materials science and biology, and encompasses any application of mathematical and computational techniques to problems related to chemical systems and related interests. In one

sentence theoretical chemistry seeks to provide explanations to chemical and physical observations by developing concepts or performing computations with the help of the available theoretical, modeling or simulation techniques. Apart from being interpretative, it can be predictive also. The most popular computational techniques are ab-initio, semi-empirical and molecular mechanics. Definitions of these terms are helpful in understanding the use of computational techniques for chemistry:

- a. **Ab-initio**, (Latin for "from scratch") a group of methods in which molecular structures can be calculated using nothing but the Schrödinger equation, the values of the fundamental constants and the atomic numbers of the atoms present.
- b. **Semi-empirical** techniques use approximations from empirical (experimental) data to provide the input into the mathematical models.
- c. **Molecular mechanics** uses classical physics and empirical or semi-empirical (predetermined) force fields to explain and interpret the behavior of atoms and molecules.

In recent times computational chemistry has been proven to be a versatile tool in providing meaningful insights to explain the behavior of various chemical systems and processes. For instance, the selectivity of a particular ligand towards a particular metal ion can be rationalized in a better way through theoretical modeling studies. However, there are also practical limitations in employing theory/computation for these systems as the system of interest can be large and the time scale can be long. Thus, choice of accurate atomistic method is very much challenging. Among the available theoretical methods, the density functional theory (DFT)^{25,26} has become one of the most popular computational methods for large systems because of its computational cost-

effectiveness and reasonably good accuracy. In the following sub-section, we will provide a brief summary of the computational methods.

1.5 Theoretical Methodologies

In this section we will review some of the fundamental aspects of electronic structure theory in terms of elementary quantum mechanics to get an idea about density-functional theory. Here it may be noted that in quantum mechanics we learn that all information we can possibly have about a given system is contained in the system's wave function, Ψ .

1.5.1 The Schrödinger Equation

In quantum mechanics, the ground state properties of many particle systems are described by time-independent Schrödinger Equation,

$$\hat{H}\Psi = E\Psi \quad \dots(1.1)$$

For many body system Schrödinger's equation becomes,

$$\hat{H}\Psi(\vec{x}_1, \vec{x}_2, \dots, \vec{x}_N, \vec{R}_1, \vec{R}_2, \dots, \vec{R}_M) = E\Psi(\vec{x}_1, \vec{x}_2, \dots, \vec{x}_N, \vec{R}_1, \vec{R}_2, \dots, \vec{R}_M) \quad \dots(1.2)$$

where, \hat{H} is the Hamiltonian for a system consisting of M nuclei and N electrons which are described by position vector R_A and r_i , respectively. \hat{H} is a differential operator representing the total energy. \hat{H} can be expanded as:

$$\hat{H} = -\frac{1}{2} \sum_{i=1}^N \nabla_i^2 - \frac{1}{2} \sum_{A=1}^M \frac{1}{M_A} \nabla_A^2 - \sum_{i=1}^N \sum_{A=1}^M \frac{Z_A}{r_{iA}} + \sum_{i=1}^N \sum_{j>i}^N \frac{1}{r_{ij}} + \sum_{A=1}^M \sum_{B>A}^M \frac{Z_A Z_B}{R_{AB}} \quad \dots(1.3)$$

The distance between the i-th electron and the A-th nucleus is $r_{iA} = |r_i - R_{Aj}|$; the distance between the i-th and j-th electron is $r_{ij} = |r_i - r_j|$, and the distance between

the A-th nucleus and B-th nucleus is $R_{AB} = |R_A - R_B|$. In the above equation, the first two terms represent the kinetic energy operators for electrons and nuclei, respectively. Next term represents the interaction between the electrons and nuclei and the last two terms correspond to the repulsive potentials due to electron-electron and nucleus-nucleus interactions, respectively.

The Laplacian operator ∇^2 can be defined as (in Cartesian coordinates):

$$\nabla^2 = \frac{\partial^2}{\partial x^2} + \frac{\partial^2}{\partial y^2} + \frac{\partial^2}{\partial z^2} \quad \dots(1.4)$$

All equations given in this text appear in a very compact form, without any fundamental physical constants. The fundamental physical constants i.e. mass of an electron, m_e , the modulus of its charge, $|e|$, Planck's constant h divided by 2π (\hbar) and $4\pi\epsilon_0$, the permittivity of the vacuum, are all set to unity. Exact solution of the many-body Schrödinger equation (1.2) associated with the full Hamiltonian (1.3) for any realistic system is a formidable task since it requires dealing with $3(N + M)$ degrees of freedom to obtain a desired solution. The complexity arises due to the electrostatic interaction terms which couple the degrees of freedom of the particles among themselves and also with those of others. Thus, one needs to look for reasonable approximations to simplify the complex equation. Fortunately, in this case, we can decouple the nuclear and electronic degrees of freedom using the Born-Oppenheimer approximation and solely focus attention on the Schrödinger equation for the electrons.

1.5.2 Born-Oppenheimer approximation

Since the nuclei are much heavier than the electrons, the Schrödinger equation can be further simplified and it is approximated that electrons move in the field of fixed nuclei which is known as the Born-Oppenheimer approximation.²⁷ By using this approximation, one can neglect the kinetic energy of nuclei from the Hamiltonian. Furthermore, the positions of the nuclei can be treated as parameters and thus the nucleus-nucleus interaction term becomes constant for a fixed set of nuclei.

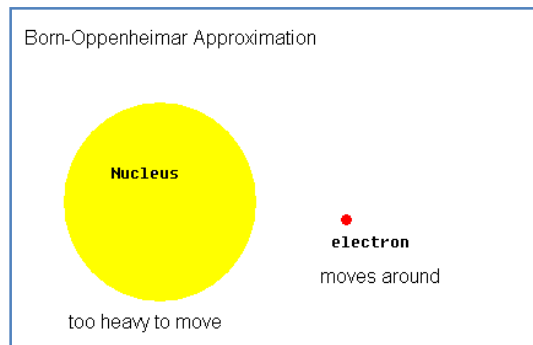


Figure 1.5 Born-Oppenheimer approximation

Thus, the complete Hamiltonian given in equation (2) reduces to the electronic Hamiltonian,

$$\hat{H}_{\text{elec}} = -\frac{1}{2} \sum_{i=1}^N \nabla_i^2 - \sum_{i=1}^N \sum_{A=1}^M \frac{Z_A}{r_{iA}} + \sum_{i=1}^N \sum_{j>i}^N \frac{1}{r_{ij}} = \hat{T} + \hat{V}_{\text{Ne}} + \hat{V}_{\text{ee}} \quad \dots(1.5)$$

and the Schrödinger equation now can be written as,

$$\hat{H}_{\text{elec}} \Psi_{\text{elec}} = E_{\text{elec}} \Psi_{\text{elec}} \quad \dots(1.6)$$

Here Ψ_{elec} depends on the electron coordinates, while the nuclear coordinates enter only parametrically and do not explicitly appear in Ψ_{elec} . Even after introducing the Born-Oppenheimer approximation, solution of the many electron Schrödinger

equation is still a difficult task and the difficulty is due to the second term which couples the electronic coordinates. This term prevents the reduction of a many electron problem to an effective single electron problem.

1.5.3 The Variational Principle

For solving the equation (1.6), one has to find out eigenfunctions Ψ_i which correspond to eigenvalues E_i of \hat{H} . All other properties of the system can be determined invoking the desired operators on the wave functions, once Ψ_i are determined. However, the above equation hardly has any practical relevance. Apart from a few trivial exceptions, no strategy is known to solve the Schrödinger equation exactly for atomic and molecular systems. Nevertheless, the variational principle gives us a way for systematic approaching the ground state eigenfunction Ψ_0 , the state which delivers the lowest energy E_0 as the operator \hat{H} is applied on it. The variational principle states that a guess approximate normalized wave-function will always give an upper bound to the ground-state energy unless of course the guess is exact.

This statement can be written by using the bracket notation as:

$$\langle \Psi_{\text{trial}} | \hat{H} | \Psi_{\text{trial}} \rangle = E_{\text{trial}} \geq E_0 = \langle \Psi_0 | \hat{H} | \Psi_0 \rangle \quad \dots(1.7)$$

Although the variational principle gives us some clue how to approach the ground state eigenfunction and eigenvalue of a particular system, it does not provide any information on how to select the trial wave function, Ψ_{trial} . The difficulties in solving Eq. (1.6) lies in the electron-electron interaction, $\frac{1}{r_{ij}}$, which includes all the quantum effects of the electrons. Despite the intractable nature of these interactions, many approximate methods have been developed to solve Schrödinger-like equations. There

are basically two types of approaches, viz., wave function based methods and density based methods. However, the Slater determinant will be introduced first due to its fundamental role in many aspects of electronic structure theory.

1.5.4 Slater Determinants

Electrons are fermions and obey the Pauli Exclusion Principle. This requires that the wave function of electrons should be antisymmetric with respect to the interchange of the coordinates \mathbf{x} of any two electrons,

$$\Phi(\mathbf{x}_1, \dots, \mathbf{x}_i, \dots, \mathbf{x}_j, \dots, \mathbf{x}_N) = -\Phi(\mathbf{x}_1, \dots, \mathbf{x}_j, \dots, \mathbf{x}_i, \dots, \mathbf{x}_N) \quad \dots(1.8)$$

Slater determinants nicely satisfy this antisymmetric condition through an appropriate linear combination of Hartree products, which are the non-interacting electron wave functions. For example, in a two electron case if we put electron one in X_i and electron two in X_j , we will have,

$$\Phi_{12}(\mathbf{x}_1, \mathbf{x}_2) = \chi_i(\mathbf{x}_1)\chi_j(\mathbf{x}_2) \quad \dots(1.9)$$

On the other hand, if we put the electron one in X_j and electron two in X_i , we will have

$$\Phi_{21}(\mathbf{x}_1, \mathbf{x}_2) = \chi_i(\mathbf{x}_2)\chi_j(\mathbf{x}_1) \quad \dots(1.10)$$

by taking a linear combination of these two products,

$$\Phi(\mathbf{x}_1, \mathbf{x}_2) = 2^{-1/2}(\chi_i(\mathbf{x}_1)\chi_j(\mathbf{x}_2) - \chi_i(\mathbf{x}_2)\chi_j(\mathbf{x}_1)) \quad \dots(1.11)$$

where the factor $2^{-1/2}$ is a normalization factor. It can be seen that the antisymmetry is guaranteed during interchange of the coordinates of electron one and electron two:

$$\Phi(\mathbf{x}_1, \mathbf{x}_2) = -\Phi(\mathbf{x}_2, \mathbf{x}_1) \quad \dots(1.12)$$

The antisymmetric wave function of Eq. (1.11) can be rewritten as a determinant,

$$\Phi(\mathbf{x}_1, \mathbf{x}_2) = 2^{-1/2} \begin{vmatrix} \chi_i(\mathbf{x}_1) & \chi_j(\mathbf{x}_1) \\ \chi_i(\mathbf{x}_2) & \chi_j(\mathbf{x}_2) \end{vmatrix} \quad \dots(1.13)$$

and this is called a Slater determinant.²⁸ For an N-electron system, the Slater determinant becomes,

$$\Phi(\mathbf{x}_1, \mathbf{x}_2, \dots, \mathbf{x}_N) = (N!)^{-1/2} \begin{vmatrix} \chi_i(\mathbf{x}_1) & \chi_j(\mathbf{x}_1) & \dots & \chi_k(\mathbf{x}_1) \\ \chi_i(\mathbf{x}_2) & \chi_j(\mathbf{x}_2) & \dots & \chi_k(\mathbf{x}_2) \\ \vdots & \vdots & & \vdots \\ \chi_i(\mathbf{x}_N) & \chi_j(\mathbf{x}_N) & \dots & \chi_k(\mathbf{x}_N) \end{vmatrix} \quad \dots(1.14)$$

Note that the rows of the N-electron Slater determinant are labeled by electrons: first row (X_1), second row (X_2),..., final row (X_N). The columns are labeled by spin orbitals: first column (X_i), second (X_j),... , final column (X_k). Interchanging the coordinates of two electrons equals to the interchange of two rows of the Slater determinant which will change its sign. Thus the Slater determinant meets the requirement of antisymmetry. Furthermore having two electrons occupying the same spin orbital corresponds to having two columns of the determinant identical which leads to the determinant being zero.

1.5.5 Wave Function Based Methods

1.5.5.1 The Hartree-Fock Theory

The Hartree-Fock (HF) Theory²⁹ is starting point of so called ab initio approaches. It is the simplest wave function-based method and solves the electronic Schrödinger equation for a particular geometric arrangement of nuclei within a molecule. The result of an HF calculation is the electronic structure of a molecule, usually expressed in terms of one-electron wave functions (Molecular orbitals (MOs)) and associated eigenvalues (orbital energies). The MOs are usually broken down into contributions

from atom-based functions, which form part of input to a calculation (the basis set). These basis functions are chosen in such a way that they resemble familiar atomic orbitals (AOs), thereby making the results of HF-SCF calculations more accessible chemically. It relies on the following approximations: the Born-Oppenheimer approximation, the independent electron approximation, the linear combination of atomic orbitals approximation. The expectation value of Hamiltonian operator applied on the Slater determinant will give us HF energy, E_{HF} .

$$E_{\text{HF}} = \langle \Phi | \hat{H} | \Phi \rangle = \sum_i^N (i | \hat{h} | i) + \frac{1}{2} \sum_i^N \sum_j^N (ii | jj) - (ij | ji) \quad \dots(1.15)$$

where

$$(i | \hat{h} | i) = \int \chi_i^*(\vec{x}_1) \left\{ -\frac{1}{2} \nabla^2 - \sum_A^M \frac{Z_A}{r_{1A}} \right\} \chi_i(\vec{x}_1) d\vec{x}_1 \quad \dots(1.16)$$

defines the contribution due to the kinetic energy and the electron-nucleus attraction.

The second term can be expressed as:

$$(ii | jj) = \iint |\chi_i(\vec{x}_1)|^2 \frac{1}{r_{12}} |\chi_j(\vec{x}_2)|^2 d\vec{x}_1 d\vec{x}_2 \quad \dots(1.17)$$

$$(ij | ji) = \iint \chi_i(\vec{x}_1) \chi_j^*(\vec{x}_1) \frac{1}{r_{12}} \chi_j(\vec{x}_2) \chi_i^*(\vec{x}_2) d\vec{x}_1 d\vec{x}_2 \quad \dots(1.18)$$

are the so-called *Coulomb* and *exchange* integrals, respectively. The variational principle is applied for minimizing the E_{HF} , which is a functional of spin orbitals, by choosing an orthonormal set of orbitals. The resulting Hartree-Fock equations can be written as:

$$\hat{f} \chi_i = \varepsilon_i \chi_i, \quad i = 1, 2, \dots, N. \quad \dots(1.19)$$

In the above expression \hat{f} is the Fock operator and ε_i are the Lagrangian multipliers which have the physical representation as the orbital energies.

1.5.5.2 Correlation Energy and Post-Hartree-Fock methods

According to the variational principle, we will always get E_{HF} larger than the exact ground state energy E_0 . The difference between these two energies is called as the correlation energy.

$$E_{\text{corr}} = E_0 - E_{\text{HF}} \quad \dots(1.20)$$

Electron correlation³⁰ is mainly caused by the instantaneous repulsion of the electrons, which is not covered by the effective HF potential, as electrostatic interaction is treated only in an average manner in the HF method. There may be two types of correlations, viz., dynamic and static. The dynamic correlation is due to the movement of electrons and its effect is short range. Dynamic correlation energy is related to $1/r_{12}$ term in the Hamiltonian. The static correlation arises due to the fact that in certain circumstances the ground state Slater determinant is not a good approximation to the true ground state, because there may be other Slater determinants with comparable energies.

The main aim of Post-Hartree-Fock methods in quantum chemistry is to improve the Hartree-Fock energy by taking into account the effect of electron correlation. These methods include configuration interaction (CI), Møller-Plesset perturbation theory, and coupled cluster. For CI methods, a linear combination of Slater determinants rather than one single Slater determinant in Hartree-Fock is used to approximate the wave function. The Møller-Plesset perturbation theory, as the name suggests, treats electron correlation in a perturbative way and in the coupled cluster method, the electron correlation is handled through use of a so-called cluster operator.

1.5.6 Density Based Methods: Density Functional Theory

Density functional theory is an alternative way to study electronic structure of matter in which the ground state electron density of a system is used as a basic variable instead of a many-body wave function. The wave function does not have any physical significance; however, the square of the wave function is an observable quantity. A physical observable that is related to the square of the wave function is called the electron density ($\rho(\vec{r})$) and can be defined as the probability of finding an electron in the volume element $d\vec{r}_1$. It is easy to work with density rather than a many-body wave function since the density is a function of three variables in contrast to the $3N$ variables of the wave function. The calculations based on DFT with these approximate functionals provide a useful balance between accuracy and computational cost.

Mathematically, the probability density can be expressed as,

$$\rho(\vec{r}) = N \int \dots \int |\Psi(\vec{x}_1, \vec{x}_2, \dots, \vec{x}_N)|^2 ds_1 d\vec{x}_2 \dots d\vec{x}_N \quad \dots(1.21)$$

Clearly, $\rho(\vec{r})$ is a non-negative function of only the three spatial variables which vanishes at infinity and integrates to the total number of electrons:

$$\rho(\vec{r} \rightarrow \infty) = 0 \quad \dots(1.22)$$

$$\int \rho(\vec{r}) d\vec{r} = N \quad \dots(1.23)$$

1.5.6.1 The Thomas-Fermi Model

This is the first density-based theory to deal with a many-electron system. In Thomas-Fermi theory,³¹⁻³³ the kinetic energy of electrons are derived from the quantum statistical theory based on the uniform electron gas, but the interaction between electron-nucleus and electron-electron are treated classically. Within this model, the kinetic energy of the electrons is defined as,

$$T[\rho] = C_F \int \rho^{5/3}(\mathbf{r}) d\mathbf{r} \quad \dots(1.24)$$

with

$$C_F = \frac{3}{10}(3\pi^2)^{2/3} = 2.871 \quad \dots(1.25)$$

From the above equation, the approximation is made that the kinetic energy of the electron depends exclusively on the electron density. By adding the interaction between electron-nucleus and electron-electron into Eq. (1.24), a total energy in terms of electron density is obtained,

$$E[\rho] = C_F \int \rho^{5/3}(\mathbf{r}) d\mathbf{r} - Z \int \frac{\rho(\mathbf{r})}{r} d\mathbf{r} + \frac{1}{2} \iint \frac{\rho(\mathbf{r}_1)\rho(\mathbf{r}_2)}{|\mathbf{r}_1 - \mathbf{r}_2|} d\mathbf{r}_1 d\mathbf{r}_2 \quad \dots(1.26)$$

The second and third terms are the electron-nucleus and electron-electron interactions, respectively. The importance of this simple Thomas-Fermi model is not how well it performs in computing the ground state energy and density but more as an illustration that the energy can be determined purely using the electron density. The major shortcomings of the above expression, however, are that the expression of kinetic energy is a very crude approximation to the actual kinetic energy and exchange and correlation effects are neglected completely.

1.5.6.2 The Hohenberg-Kohn Theorems

Density functional theory as we know it today was born in 1964 when a landmark paper by Hohenberg and Kohn²⁵ was published. The theory is based upon the following two theorems.

Theorem 1: *The ground-state energy from Schrödinger's equation is a unique functional of the electron density ($\rho(\mathbf{r})$), in other words a one to one mapping between the external potential and electron density was established.*

Theorem 2: *The electron density that minimizes the energy of the overall functional ($E[\rho(\mathbf{r})]$) is the true electron density corresponding to the full solution of the Schrödinger equation i. e. the ground state density can be found by using a variational principle.*

One of the important outcomes of these theorems is that the ground-state electron density uniquely determines all properties, including the energy and wave function, of the ground state. The energy of any atomic or molecular system can be expressed as:

$$E = \left(F[\rho] + \int \rho(\vec{r}) V_{N_e} d\vec{r} \right) \quad \dots(1.27)$$

And the ground state energy of any atomic or molecular system can be expressed as:

$$E_0 = \min_{\rho \rightarrow N} \left(F[\rho] + \int \rho(\vec{r}) V_{N_e} d\vec{r} \right) \quad \dots(1.28)$$

where the universal functional $F[\rho]$ contains contributions due to the kinetic energy, the classical Coulomb interaction and the non-classical terms as self interaction correction, exchange and electron correlation effects. It is independent of the number of particles as well as the external potential. We have

$$F[\rho(\vec{r})] = T[\rho(\vec{r})] + J[\rho(\vec{r})] + E_{\text{ncI}}[\rho(\vec{r})] \quad \dots(1.29)$$

Out of all the terms present in the above equation, only $J[\rho]$, which accounts for the classical Coulomb interaction, is known explicitly. $E_{\text{ncI}}[\rho]$ is the *non-classical* contribution to the electron-electron interaction containing all the effects of self-interaction correction, exchange and Coulomb correlation. It will come as no surprise that finding explicit expressions for the yet unknown functionals, i. e. $T[\rho]$ and $E_{\text{ncI}}[\rho]$, represents the major challenge in density functional theory.

The HK theorems are non-constructive, since we don't know what the form of the universal functional is. The kinetic energy functionals are particularly problematic as $T[\rho]$ is so large and even a small relative error gives large absolute errors and the

development of approximate functionals that can reasonably model experimental data is still a topic of research in the DFT. Thus, almost all DFT calculations rely on the Kohn-Sham approximation, which avoids the exact kinetic energy functional. Different DFT methods differ in the way they represent exchange and correlation terms.

1.5.6.3 The Kohn-Sham Method

From the Hohenberg-Kohn theorem, we can get the ground-state energy by minimizing the energy functional (equation 1.27),

$$E = \left(F[\rho] + \int \rho(\vec{r}) V_{N_e} d\vec{r} \right) \quad \dots(1.30)$$

Although the Hohenberg-Kohn theorem provided a proof in principle that the total energy could be obtained from the ground state density it was not yet known how to obtain the $\rho(\mathbf{r})$ or $F[\rho]$. In 1965, Kohn and Sham published a paper which transformed density-functional theory into a practical electronic structure theory.²⁶ Kohn and Sham recognized that the failure of Thomas-Fermi theory mainly resulted from the bad description of the kinetic energy. To address this problem they decided to re-introduce the idea of one electron orbitals and approximate the kinetic energy of the system by the kinetic energy of non-interacting electrons. This lead to the central equation in Kohn-Sham DFT which is the one-electron Schrödinger-like equation, expressed as:

$$\left(-\frac{1}{2} \nabla^2 + v(\mathbf{r}) + \int \frac{\rho(\mathbf{r}')}{|\mathbf{r} - \mathbf{r}'|} d\mathbf{r}' + v_{xc}(\mathbf{r}) \right) \phi_i = \varepsilon \phi_i \quad \dots(1.31)$$

Here ϕ_i are the Kohn-Sham orbitals and the electron density is expressed by,

$$\rho(\mathbf{r}) = \sum_i^N |\phi_i|^2 \quad \dots(1.32)$$

The terms on the left side of Eq. (1.30) are the kinetic energy of the non-interacting reference system, the external potential, the Hartree potential, and the exchange-correlation potential, respectively. The ε is the energy of the Kohn-Sham orbital. In addition, the exchange-correlation potential is given by,

$$v_{xc}(\mathbf{r}) = \frac{\delta E_{xc}[\rho]}{\delta \rho(\mathbf{r})} \quad \dots(1.33)$$

and $E_{xc}[\rho]$ is the exchange-correlation functional and effective potential (v_{eff}) can be defined as

$$v_{\text{eff}} = v(\mathbf{r}) + \int \frac{\rho(\mathbf{r}')}{|\mathbf{r} - \mathbf{r}'|} d\mathbf{r}' + v_{xc}(\mathbf{r}) \quad \dots(1.34)$$

Thus Eq. (1.30) can be rewritten in a more compact form,

$$\left(-\frac{1}{2}\nabla^2 + v_{\text{eff}}\right)\phi_i = \varepsilon\phi_i \quad \dots(1.35)$$

Clearly this is a Hartree-Fock like single particle equation which needs to be solved iteratively. Finally, the total energy can be determined from the resulting density through

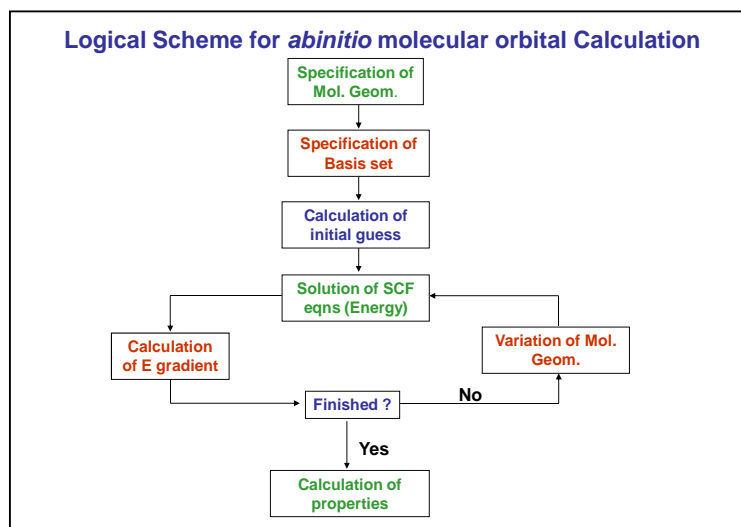
$$E = \sum_i^N \varepsilon_i - \frac{1}{2} \iint \frac{\rho(\mathbf{r})\rho(\mathbf{r}')}{|\mathbf{r} - \mathbf{r}'|} d\mathbf{r}d\mathbf{r}' + E_{xc}[\rho] - \int v_{xc}(\mathbf{r})\rho(\mathbf{r}) d\mathbf{r} \quad \dots(1.36)$$

Equations (1.31), (1.32), and (1.34) are the celebrated Kohn-Sham equations. Note that the v_{eff} depends on $\rho(\mathbf{r})$ through Eq. (1.33). So the Kohn-Sham equation must be solved self-consistently. The general procedure is to begin with an initial guess of the electron density, construct the v_{eff} from Eq. (1.33), and then get the Kohn-Sham orbitals. Based on these orbitals, a new density is obtained from Eq. (1.31) and the process repeated until convergence is achieved. Lastly, the total energy will be calculated from Eq. (1.35) with the final electron density. If each term in the Kohn-

Sham energy functional was known, we would be able to obtain the exact ground state density and total energy. Unfortunately, there is one unknown term, the exchange-correlation (xc) functional (E_{xc}). E_{xc} includes the non-classical aspects of the electron-electron interaction along with the component of the kinetic energy of the real system, which is different from the fictitious non-interacting system. Since E_{xc} is not known exactly, it is necessary to approximate it. Thus, since the birth of DFT, some sorts of approximations for E_{xc} have been used. By now there is an almost endless list of approximations³⁴⁻⁴¹ with varying levels of complexity.

1.5.6.4 Solving the Kohn-Sham Equation

In practice, the Kohn-Sham equation is solved numerically by an iterative procedure called the self-consistent field (SCF) method. The steps involved in the SCF calculations and its corresponding flow chart are given below.



Scheme 1.1 Schematic representations of the flow chart of ab initio MO & DFT calculations

1.6 Scope of the present thesis

Here in this thesis we have proposed a modified concept related to selective complexation of actinides with either S or N donor ligands. It is important to note that efficiency of complex formation of either Ln(III) or An(III) with oxygen donors is much better as compared to N or S donors because both the set of metal ions are hard Lewis acids, however no selectivity is observed with O donor ligands. Although actinide selective ligands with hard donor atom like O seems highly unusual, in this thesis we have made an attempt to reply to this question affirmatively through the introduction of a new concept, 'intramolecular synergism', where electrostatic interaction predominates between the softer metal ion and hard donor atoms in presence of soft donor centers within the same ligand. Syntheses of some of the theoretically designed ligands followed by their solvent extraction study have also been performed to validate our theoretical predictions. Additionally, we have also theoretically investigated some conventional extractants to rationalize the experimentally observed trends.

The present thesis also includes theoretical predictions of a new class of stable metallofullerenes with small fullerene cages, through encapsulation of an actinide or lanthanide atom/ion. Smaller fullerenes are of special interest due to the presence of high curvature and huge strain energy owing to the presence of adjacent pentagonal rings, which lead to clusters with unusual intra and inter -molecular bonding and electronic properties. Among the smaller fullerenes ($n < 60$) only C_{36} have been isolated in solid form,⁴² although other smaller fullerenes have also been identified in various gas phase experiments. The smaller fullerenes, which are formed during the production of stable fullerenes, are difficult to isolate because of their extremely high

chemical reactivity. However, encapsulation of a suitable dopant atom or ion (metal or nonmetal) may lead to the stabilization of smaller fullerenes. Stability of the smaller fullerenes has been shown to be increased considerably through encapsulation of an appropriate metal atom or ion so that experimental observation of such smaller size fullerenes may be possible. This stability gain has been rationalized using some fundamental electronic structure principles, viz., electronic shell closing, geometrical shell closing, the concept of magic number etc.

CHAPTER 2: Actinide Selectivity of 1,10-Phenanthroline-2,9-dicarboxylic acid (PDA) Based Ligands: Insight from Density Functional Theory

2.1 Introduction

2.1.1 Density Functional Theory Derived Chemical Reactivity Indices

Concept of chemical hardness originally introduced by Pearson⁴³ has attracted considerable attention for studying various chemical reactions in different fields like organic, inorganic and biological chemistry.⁴⁴⁻⁴⁶ Softness is defined as the inverse of hardness. Electronegativity⁴⁷, in conjunction with hardness and softness parameters are widely used for a detail understanding of chemical bonding in various systems. Mathematically, electronegativity and hardness can be defined as first⁴⁸ and second⁴⁹ derivative of energy (E) with respect to the number of electrons (N), respectively, at constant external potential. For elucidating chemical reactivity, one of the most important local reactivity indices is the Fukui function, which was introduced by Parr and Yang⁵⁰ in 1984. It can be defined as the derivative of chemical potential against external potential at constant electronic framework or the slope of density against number of electrons, N , at constant perturbation. In the present chapter one of our objectives is to employ all these important concepts in rationalizing the complexation behavior of trivalent actinides vis-à-vis corresponding lanthanides as obtained using density functional calculations.

2.1.2 Actinide/ Lanthanide Separation: Basic Principle

Investigation of bonding of specific metal ion either through encapsulation in a suitable host molecule or by means of complex formation with a selective ligand is of considerable recent interest⁵¹⁻⁵⁶ because of its immense importance both from the fundamental and application point of view. In general, based on the ionic size and the charge on the metal ion, suitable complexing agent (ligand or host molecule) is designed for a particular ion to achieve the selectivity. One instance where selective complexation becomes difficult is the separation of trivalent actinides (An(III)) from trivalent lanthanides (Ln(III)) due to their similar charge/size ratio. This process is very important in nuclear industry from the radioactive waste management point of view.⁵⁷⁻⁵⁹ Lanthanide-actinide separation process is even more complicated due to the presence of partially filled valence *f* orbitals in their trivalent state, which are diffuse in nature. As discussed in the introductory chapter, a number of ligands with soft donor atoms like N and S are exploited for selective complexation of actinide ions as actinides are softer in nature as compared to the lanthanides. However, it is very important to note that efficiency of complex formation of either Ln(III) or An(III) with oxygen donors is much better as compared to N or S donors because both the set of metal ions are hard Lewis acids, however, no selectivity is observed with O donor ligands.

2.1.3 Intra-ligand Synergism: A new Concept

Now one obvious question arises: is it possible to have an actinide selective ligand with hard donor atom like oxygen? Although it seems highly unusual, for the first time we have made an attempt⁶⁰ to reply to this question affirmatively by exploiting

the concept of ‘intramolecular synergism’, where synergistic effects can be achieved through functionalization of the original ligand with suitable soft donor atoms as far as the selectivity is concerned. In fact, intermolecular synergistic agents have been used extensively for an efficient extraction of a particular metal ion in separation chemistry where a second ligand known as co-extractant, works in a synergistic way with the first ligand in presence of each other. In the literature several such investigations are reported where it has been demonstrated that synergistic effect plays an important role for an efficient and selective extraction of a particular metal ion. For instance, a recent experimental report²⁹ has indicated that the role of synergism is significant in the extraction of Am(III) over Eu(III). Several experimental reports related to synergism are also available in the literature involving combinations of hard-soft or soft-soft donors.^{61,62} In this work we use the concept of “intramolecular synergism”,⁶⁰ where electrostatic interaction predominates between a relatively softer metal ion and hard donor atoms (O) in presence of soft donor centers (N) within the same ligand. We have rationalized the selective complex formation of An(III) over Ln(III) with O donor ligands through providing an in-depth insight within the framework of Pearson’s Hard-Soft-Acid-Base (HSAB) principle^{43,49,63,64} and frontier molecular orbital (FMO) theory of chemical reactivity.^{50,65}

Here, 1,10-phenanthroline-2,9-dicarboxylic acid (PDA)^{55,66,67} has been used as the complexing agent. It is important to note that phenanthroline derivatives have been extensively studied experimentally by several reserachers^{55,66-68} for complexation of various metal ions due to their pre-organized framework. Recently, considerable amount of experimental work has been published in the literature dealing with phenanthroline di-alcohol / di-acid / di-amide type ligands.⁶⁶⁻⁶⁹ In these reports it has

been clearly indicated that the 1,10-phenanthroline based ligands with both N and O donor centers would show good selectivity for trivalent actinides over corresponding lanthanides. Hancock and coworkers have already reported complexes of this type of ligands with trivalent lanthanides experimentally (lanthanides with alcohol, amide and acid derivatives of 1,10-phenanthroline). Therefore, we have been motivated to use 1,10-phenanthroline-2,9-dicarboxylic acid and its derivatives for the investigations of complexation behavior of trivalent actinides and corresponding lanthanides theoretically to provide an in-depth insight on their complexation. We have also introduced three other derivatives of PDA through functionalization with soft S atom, viz., 1,10-phenanthroline-2,9-mono-thio-dicarboxylic acid (binding through Oxygen) (TCA1), 1,10-phenanthroline-2,9-mono-thio-dicarboxylic acid (binding through Sulfur) (TCA) and 1,10-phenanthroline-2,9-di-thio-dicarboxylic acid (THIO). Here, it is important to note that complexation of any metal ion with thio derivative of PDA has not been reported in the literature till date. It is well known that soft donor ligands play important role in the selective complexation of actinides, for example, S-donor Cyanex-301, N-donor BTP derivatives etc. are considered as highly selective extractants for trivalent actinides. Consequently, the presence of both N and S in the same ligand can be accomplished by functionalization of PDA ligand with S donors. Also, depending on the number of sulfur atoms (two S atoms in TCA/TCA1 or four S atoms in THIO) overall softness of the ligand can be tuned accordingly. In fact, it has been observed experimentally that lanthanide-actinide separation with S donor ligand can be enhanced to a great extent⁶¹ in presence of auxiliary ligand with N as donor atoms.

It is well known that selective complexation of An(III) in presence of Ln(III) is a difficult and challenging task both experimentally and theoretically because of their comparable charge to radius ratio and similar chemical behavior of these species as stated above. Therefore, in this work our interest is to investigate only the An(III) and Ln(III) complexes using phenanthroline acid type ligands. It is to be noted that 1,10-phenanthroline (PHEN) based nitrogen donor ligands are not very much soluble in water medium due to their inability to form any hydrogen-bond with water molecules,^{67,68} making their study difficult in aqueous medium, whereas Am(III) and Eu(III) are highly hydrophilic in nature. Hence, one can make the ligand hydrophilic by functionalization with carboxylic type groups, and selective extraction of An(III) over Ln(III) is possible in water medium. Indeed, here we demonstrate that in presence of nitrogen donor atoms in the PHEN moiety, harder donor atom like oxygen binds with softer Am(III) in a stronger way than that with Eu(III). To accomplish our objective we have used first-principles density functional theory with three different GGA functionals in the gas and solvent phases for the geometry optimizations and complexation energy calculations. Here we have confined ourselves only to the GGA functionals as it was found that the results obtained using pure GGA functionals are more reliable as compared to that of the hybrid one in predicting the properties of metal-actinide complexes.^{70,71} Finally, all the calculated results are rationalized in the light of HSAB principle^{43,49,63,64} and FMO theory.^{50,65} The details of theoretical background and computational methodologies used are discussed in the subsequent sections.

2.2 Theoretical Background

Parr and Pearson have defined hardness, η of any chemical species as⁴⁹

$$\begin{aligned}\eta &= 1/2(\partial^2 E/\partial N^2)_{v(r)} \\ &= 1/2 (\partial\mu/\partial N)_{v(r)}\end{aligned}\quad \dots(1)$$

where E is the total energy, N is the number of electrons of the chemical species under constant external potential, $v(r)$ and μ is the chemical potential, which is identified as the negative of electronegativity. After applying the finite difference approximation to equation 1, one can get

$$\eta = (\text{IP} - \text{EA}) / 2 \quad \dots(2)$$

where IP and EA denote the ionization potential and electron affinity of the system, respectively. For a particular species M, IP and EA can be calculated by taking the energy values of $(M^+ - M)$ and $(M - M^-)$, respectively.

Fukui function,⁵⁰ denoted as $f(r)$, can be defined as the change in electron density, $\rho(r)$ at a point r with the change in total number of electrons, or sensitivity of chemical potential of a system to an external perturbation at a particular point r .

$$f(r) = (\partial\rho(r)/\partial N)_{v(r)} \quad \dots(3)$$

For a nucleophilic attack,

$$f^+(r) = (\partial\rho(r)/\partial N)_{v(r)}^+ \quad \dots(4)$$

For an electrophilic attack,

$$f^-(r) = (\partial\rho(r)/\partial N)_{v(r)}^- \quad \dots(5)$$

Within the finite difference method, for an N electron system Fukui functions for nucleophilic and electrophilic attack can be defined, respectively, as

$$f^+(r) \approx \rho(r)[N+1] - \rho(r)[N] \quad \dots(6)$$

$$f^-(r) \approx \rho(r)[N] - \rho(r)[N-1] \quad \dots(7)$$

Based on the electronic population Yang et al.⁷² proposed the atom condensed Fukui function to describe the site reactivity or site selectivity. The condensed Fukui function for an atom k , undergoing nucleophilic or electrophilic attack can be defined respectively as

$$f_k^+ \approx q_k(N+1) - q_k(N) \quad \dots (8)$$

$$f_k^- \approx q_k(N) - q_k(N-1) \quad \dots(9)$$

where q_k values are electronic population of the k^{th} atom of a particular species. There are two other terms, relative nucleophilicity index (f_{nu}) and relative electrophilicity index (f_{el}), which can be represented as^{73,74}

$$f_{\text{nu}} = f_k^+ / f_k^-$$

and

$$f_{\text{el}} = f_k^- / f_k^+$$

Relative nucleophilicity and electrophilicity indices are more useful to identify the respective reactive site for a molecular system. A site is favorable for a nucleophilic attack where $f_{\text{nu}} > f_{\text{el}}$. Similarly, a site is favorable toward an electrophilic attack where $f_{\text{el}} > f_{\text{nu}}$.

2.3 Computational Details

All the geometries of the bare ligands and the metal-ligand complexes have been optimized without any symmetry restrictions. Two different program packages have been used, viz., Turbomole 6.0⁷⁵ and ADF2006.01.⁷⁶⁻⁷⁹ For ADF calculations Slater type orbital (STO) basis sets, added with two polarization functions (TZ2P of ADF basis set library) along with frozen core approximations have been used. The frozen cores considered for various atoms are $1s-4d$ for lanthanides, $1s-5d$ for actinides, $1s-2p$ for sulfur and $1s$ for carbon, nitrogen and oxygen. Here we have incorporated the relativistic effects using the zeroth order regular approximation (ZORA) approach,

which is quite successful in predicting the geometries as well as energetics of actinide compounds.⁸⁰⁻⁸³ In Turbomole, 28 (Ce and Eu) and 60 (U and Am) electron core pseudo potentials (ECP) along with the corresponding def-SV(P) Gaussian type orbital (GTO) basis sets have been used.⁸⁴⁻⁹¹ For the lighter atoms, all electron def-SV(P) basis sets have been used, as implemented in the Turbomole program. It may be noted that for the Am and Eu atoms the def-SV(P) basis set as present in the Turbomole basis set library is quite large and consists of (14s13p10d8f1g) functions contracted to [10s9p5d4f1g]. For all the calculations of Am³⁺ and Eu³⁺ ions and their complexes we have considered the open-shell septet state, which is the ground state for these species. To investigate the effect of basis set we have also used TZVP basis along with ECPs for the lanthanide and actinide atoms in Turbomole program. Starting with various initial structures geometries are optimized until vibrational analysis results into all positive frequencies. The partial atomic charges were calculated using the natural population analysis scheme⁹² as implemented in Turbomole. Solvent effect has been considered using COSMO⁹³ approach with water as solvent (epsilon=78.6). The atomic radius values used in the COSMO model are 1.404, 1.989, 1.989, 1.7784, 2.106, 1.820, 2.045, 1.8276 and 2.223 Å for H, C, N, O, S, Eu, Am, Ce and U, respectively.^{75,94,95} The geometries of the bare ligands and all the complexes have been optimized in presence of solvent. To investigate the effect of exchange-correlation functionals, BP86^{36,37}, PBE⁴⁰, and BLYP^{36,39} functionals have been used in all cases. Energy decomposition analysis⁷⁹ has been performed using the ADF software. Interaction energy between the two fragments in the complex is the focus of the bonding analysis. This interaction energy ΔE_{int} can be decomposed into two different components,

$$\Delta E_{\text{int}} = \Delta E_{\text{steric}} + \Delta E_{\text{orb}}$$

ΔE_{steric} is the steric interaction energy between the metal ion and the ligand and it arises from the sum of two contributions, i.e.

$$\Delta E_{\text{steric}} = \Delta E_{\text{elec}} + \Delta E_{\text{Pauli}}$$

where ΔE_{elec} gives the electrostatic interaction energy between the fragments. ΔE_{Pauli} gives the repulsive interactions between the fragments. The stabilizing orbital interaction term, ΔE_{orb} includes polarization term and covalency factor due to metal-ligand orbital overlap.

2.4 Results and Discussions

2.4.1 Geometry Optimization and Structural Aspects

We have optimized the geometries of all the bare ligands and the complexes in their high spin state in both gas and solvent phases using Turbomole program package.⁶⁰ The vibrational frequencies of all the optimized structures have been found to be real. The optimized structures of bare ligand and metal-ligand complex, $[\text{ML}]^+$ are depicted in Figure 2.1. All the metal-complex monomer structures are almost similar irrespective of the metal ions or ligands used. Now onwards we have considered the results obtained using Turbomole program unless otherwise stated.



Figure 2.1 Optimized structures of a) bare ligand and b) metal ion-ligand complexes.

For bare ligands (deprotonated form) the dihedral angles between the PHEN moiety and the functional groups are much larger as compared to the corresponding values in the complex, indicating that the carboxylic acid groups are almost perpendicular with respect to the PHEN moiety. However, after complex formation all these groups reside in the same plane. Now it is interesting to compare the metal-ligand bond distances for the various complexes considered in this work. Therefore, we have reported the M-L bond distances for the $[ML]^+$ complexes in Tables 2.1 and 2.2. From the reported values in the Tables it is evident that the Am-O/S bond distances are shorter than the corresponding Eu-O/S bond distances for all the four ligands considered here although the size of the Am^{3+} ion (ionic radii=0.975 Å) is slightly higher as compared to Eu^{3+} ion (ionic radii=0.95 Å) for coordination number six.⁹⁶ Similar trend is observed for the M-N bond distances also. Metal-nitrogen bond distances are larger when binding is occurring through sulfur center as compared to oxygen center. Difference in M-N bond distance values between Am and Eu complexes are smaller as compared to the difference in M-O bond distance values (Figure 2.2).

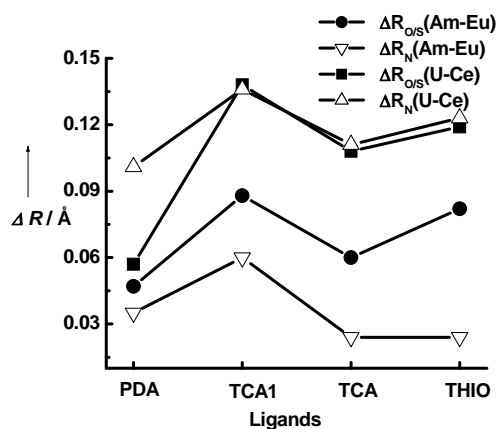


Figure 2.2 Difference in the optimized M-N and M-O/S bond distance values between Am(III), Eu(III) and U(III), Ce(III) in presence of solvent.

Table 2.1 Calculated M-L bond distances (Å) and complexation energies (eV) in gas (ΔE_g) and solvent (ΔE_s) phases for Am³⁺ and Eu³⁺ complexes using def-SV(P)/BP86 method

Complex	M-O/M-S	M-N	M-O/M-S	M-N	ΔE_g	ΔE_s
	Gas	Gas	Solvent	Solvent	Gas	Solvent
[Am-PDA] ⁺	2.179	2.508	2.260	2.527	-41.73	-6.88
[Eu-PDA] ⁺	2.218	2.523	2.307	2.562	-42.76	-4.79
[Am-TCA1] ⁺	2.217	2.501	2.284	2.522	-40.74	-6.25
[Eu-TCA1] ⁺	2.292	2.523	2.372	2.572	-42.13	-4.40
[Am-TCA] ⁺	2.634	2.574	2.708	2.591	-40.25	-5.70
[Eu-TCA] ⁺	2.672	2.571	2.768	2.615	-41.51	-3.80
[Am-THIO] ⁺	2.693	2.554	2.743	2.582	-39.86	-5.30
[Eu-THIO] ⁺	2.766	2.548	2.825	2.606	-41.37	-3.59
[Am-PHEN] ³⁺	-----	2.440	-----	2.410	-15.64	-2.33
[Eu-PHEN] ³⁺	-----	2.500	-----	2.469	-17.52	-1.47

Table 2.2 Calculated M-L bond distances (Å) and complexation energies (eV) in gas (ΔE_g) and solvent (ΔE_s) phases for U³⁺ and Ce³⁺ complexes using def-SV(P)/BP86 method

Complex	M-O/M-S	M-N(Å)	M-O/M-S	M-N	ΔE_g	ΔE_s
	Gas	Gas	Solvent	Solvent	Gas	Solvent
[U-PDA] ⁺	2.148	2.441	2.231	2.460	-40.28	-7.69
[Ce-PDA] ⁺	2.208	2.546	2.288	2.561	-40.26	-3.10
[U-TCA1] ⁺	2.149	2.438	2.222	2.463	-39.19	-7.04
[Ce-TCA1] ⁺	2.217	2.527	2.360	2.599	-39.17	-2.49
[U-TCA] ⁺	2.615	2.416	2.691	2.485	-38.88	-6.63
[Ce-TCA] ⁺	2.660	2.534	2.799	2.596	-38.76	-1.74
[U-THIO] ⁺	2.616	2.400	2.671	2.475	-38.47	-2.97
[Ce-THIO] ⁺	2.672	2.509	2.790	2.598	-38.30	-1.18
[U-PHEN] ³⁺	----	2.308	----	2.391	-13.22	-2.47
[Ce-PHEN] ³⁺	----	2.367	----	2.401	-13.97	-1.35

However, it is important to note that the Am-O bond distances are shorter in case of Am-PDA complex as compared to that in Am-TCA1 complex, where oxygen is the donor atom in both the cases. Similarly, Am-S bond lengths are found to be smaller in case of Am-TCA as compared to that in Am-THIO complex where sulfur is the donor atom in both the cases. Similar trends are observed for Eu complexes in both the cases whether bonding is through oxygen or sulfur atoms. Differences between the Am-O and Eu-O bond distances are increased as we move from PDA to TCA1 ligand. Similarly, moving from TCA to THIO, the differences between the Am-S and Eu-S bond distances are increased. Therefore, binding is stronger for Am^{3+} ion as compared to Eu^{3+} ion as we move from PDA to TCA1 and from TCA to THIO. This may be due to the increase in soft nature of the ligands as we replace the non-coordinating O centers with S atoms. It is interesting to note that the calculated trend is in complete agreement with a recent experimental study⁶¹ where selectivity for Am^{3+} with S-donor ligands is increased in presence of auxiliary N-donor ligands. To investigate the effect of basis sets we have also optimized the geometries of all the complexes using TZVP basis sets in Turbomole. It is interesting to note that irrespective of the basis sets used (def-SV(P) and TZVP in Turbomole) the trends in the calculated M-L bond lengths remain the same (Table 2.1 and 2.3). These trends are similar for all the structures obtained from both ADF and Turbomole packages (Table 2.4). Geometries of the Am^{3+} , Eu^{3+} and U^{3+} , Ce^{3+} complexes are also optimized with two other exchange-correlation functionals, BLYP and PBE and it is to be noted that the bond distance values with these two functionals are also in good agreement with the previous trends (Table 2.5).

Table 2.3 Calculated M-L bond distances (Å) and complexation energies (eV) in gas (ΔE_g) and solvent (ΔE_s) phases for Am³⁺ and Eu³⁺ complexes with TZVP/BP86 method

Complex	M-O/M-S	M-N	M-O/M-S	M-N	(ΔE_g)	(ΔE_s)
	Gas	Gas	Solvent	Solvent		
[Am-PDA] ⁺	2.182	2.506	2.275	2.523	-40.37	-5.62
[Eu-PDA] ⁺	2.227	2.527	2.329	2.562	-41.45	-3.63
[Am-TCA1] ⁺	2.223	2.499	2.299	2.519	-39.52	-5.14
[Eu-TCA1] ⁺	2.305	2.525	2.372	2.572	-40.98	-3.33
[Am-TCA] ⁺	2.638	2.576	-----	-----	-39.17	-----
[Eu-TCA] ⁺	2.679	2.575	-----	-----	-40.47	-----
[Am-THIO] ⁺	2.697	2.553	-----	-----	-38.84	-----
[Eu-THIO] ⁺	2.769	2.550	-----	-----	-40.39	-----

Table 2.4 Calculated bond distances (d in Å) for [ML]⁺ complexes obtained from ADF software with TZ2P basis sets and BP86 exchange-correlation functional in the gas phase

→	Bond Distances							
	PDA		TCA1		TCA		THIO	
↓ Metal	d _{M-O} Å	d _{M-N} Å	d _{M-O} Å	d _{M-N} Å	d _{M-S} Å	d _{M-N} Å	d _{M-S} Å	d _{M-N} Å
Am	2.193	2.506	2.233	2.500	2.579	2.645	2.566	2.688
Eu	2.222	2.508	2.292	2.503	2.556	2.673	2.539	2.739
U	2.152	2.434	2.141	2.407	2.428	2.613	2.418	2.619
Ce	2.206	2.506	2.213	2.493	2.518	2.677	2.495	2.676

Table 2.5 Effect of different Exchange correlation functionals (PBE and BLYP) on the M-L bond distance (d in Å) of [ML]⁺ complexes calculated using def-SV(P)

LIGAND NAME	METAL	B-LYP		PBE	
PDA		d _{M-O}	d _{M-N}	d _{M-O}	d _{M-N}
	Ce	2.223	2.571	2.207	2.545
	Eu	2.233	2.548	2.218	2.531

	U	2.172	2.474	2.147	2.438
	Am	2.198	2.533	2.179	2.508
TCA1	Ce	2.233	2.552	2.217	2.526
	Eu	2.307	2.547	2.292	2.523
	U	2.172	2.469	2.147	2.435
	Am	2.237	2.528	2.217	2.501
TCA	Ce	2.660	2.534	2.654	2.534
	Eu	2.699	5.593	2.669	2.576
	U	2.651	2.459	2.607	2.410
	Am	2.663	2.603	2.629	2.576
THIO	Ce	2.700	2.533	2.682	2.529
	Eu	2.793	2.570	2.753	2.541
	U	2.653	2.439	2.640	2.435
	Am	2.727	2.580	2.688	2.556

2.4.2 Energetics

The calculated metal-ligand complexation energy values in the gas and solvent phases are reported in Tables 2.1-2.3. For all the metal ions, the complex formation energy is decreased along the series PDA > TCA1 > TCA > THIO. This trend is clearly due to the efficiency of the oxygen atoms in forming stronger bonds in $[M\text{-PDA}]^+$ and $[M\text{-TCA1}]^+$ complexes as compared to the sulfur atoms in the corresponding TCA and THIO complexes. It is interesting to note that $[M\text{-TCA1}]^+$ complex is more stable than $[M\text{-TCA}]^+$ complex, although composition of both the ligands are identical, differing only in the binding sites, oxygen and sulfur as donors in TCA1 and TCA, respectively. The complex formation energy is higher in case of Am complexes in comparison with the corresponding Eu complexes in presence of solvent (Figure 2.3). This trend is not consistent with the gas phase complexation energy values. In this context it is interesting to note that the effect of solvent has been found to be quite

significant to explain the experimentally observed higher separation factor for Am(III) with respect to Eu(III) with Cyanex-301 ligand.^{81,94,97,98} In fact, calculated results using merely gas phase data has not been able to provide complete explanation to the experimentally observed results.

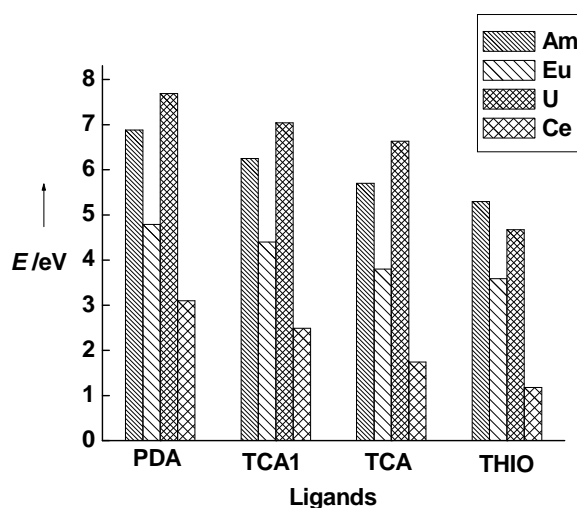


Figure 2.3 Complexation energies (E/eV) of metal complexes, $[ML]^+$, with various ligands in presence of solvent.

2.4.3 Rationalization of Bonding Aspects through HSAB Principle and Fukui Reactivity Indices

From the calculated bond distance and complex formation energy values (in presence of solvent) as reported in Tables 2.1 and 2.3, it is quite clear that Am complex is more stable than the corresponding Eu complex for each of the four ligands considered here. In case of U and Ce complexes similar trend is observed (Table 2.2). This is quite contrary to the conventional wisdom, particularly, with PDA and TCA1 ligands where oxygen atoms act as donor centers (in addition to the nitrogen donors). In fact, since last two decades it is being believed^{80,81,94,97-104} that actinide ions prefer to bind to soft

donor ligands like N and S as compared to the corresponding lanthanide ion because of the more diffuse $5f$ orbitals of actinides (as compared to the $4f$ orbitals in lanthanide), by virtue of which, actinides generally favor covalent interactions with soft donor ligands than the corresponding lanthanides. However, reported results in Tables 2.1, 2.2 and 2.3, shows that separation may also be achieved with hard donor ligand center in presence of soft atoms (with PDA and TCA1). To explain this anomaly and also to explain the observed trends as presented in the Tables, we have invoked the concepts of Pearson's Hard-Soft-Acid-Base principle and the frontier molecular orbital theory of chemical reactivity as proposed by Fukui. For calculations we have adopted the definition of hardness, η as $(IP-EA)/2$ as proposed⁴⁹ by Parr and Pearson within the framework of density functional theory, where IP and EA denotes ionization potential and electron affinity of the species, respectively. Softness, S is defined as the reciprocal of hardness. The gas phase (aqueous phase) calculated values of η are found to be 0.682 au (0.395 au) and 0.526 au (0.270 au) for the Eu^{3+} and Am^{3+} ions, respectively. Therefore, softer nature of Am^{3+} is evident from these values. Now we have calculated the η values of Eu and Am complexes with PHEN, and the corresponding gas phase (aqueous phase) values are found to be 0.179 au (0.072 au) and 0.176 au (0.077 au) for $[\text{Eu-PHEN}]^{3+}$ and $[\text{Am-PHEN}]^{3+}$ complexes (Table 2.6). Therefore, it is quite clear that the nature of the metal ion is changed dramatically after coordination with nitrogen donors present in the PHEN moiety. Indeed, now the hardness values of the two complexes are quite close to each other, in contrast to the situation corresponding to the bare metal ions.

Table 2.6 Calculated Hardness and Softness values of the metal ions, dianionic form of the bare ligands and [M-PHEN]³⁺ complexes in gas and solvent phases using def-SV(P)/BP86 method

COMPLEX NAME	HARDNESS		SOFTNESS	
	Gas	Solv	Gas	Solv
Am ³⁺	0.526	0.270	1.901	3.708
Eu ³⁺	0.682	0.395	1.466	2.533
U ³⁺	0.497	0.258	2.013	3.869
Ce ³⁺	0.630	0.383	1.588	2.609
[PDA] ²⁻	0.196	0.126	5.097	7.914
[TCA/TCA1] ²⁻	0.187	0.095	5.352	10.571
[THIO] ²⁻	0.179	0.099	5.581	10.062
PHEN	0.305	0.177	3.282	5.654
[Am-PHEN] ³⁺	0.176	0.077	5.680	12.943
[Eu-PHEN] ³⁺	0.179	0.072	5.596	13.964
[U-PHEN] ³⁺	0.237	0.135	4.216	7.429
[Ce-PHEN] ³⁺	0.231	0.119	4.324	8.435

In fact, η value of [Am-PHEN]³⁺ complex is slightly larger as compared to the corresponding [Eu-PHEN]³⁺ complex in presence of solvent. In other words, [Am-PHEN]³⁺ complex is calculated to be slightly harder than the [Eu-PHEN]³⁺ complex, which is in contrast to the hardness values of the respective bare metal ions. Consequently, Am³⁺ in [Am-PHEN]³⁺ may bind to harder donor atoms in a stronger way. Thus, it could rationalize the shorter Am-O bond distance as compared to the corresponding Eu-O bond length in PDA and TCA1 complexes. Shorter Am-N bond length in the PHEN complex (Table 2.1) is clearly due to the softer Am³⁺ ion as compared to Eu³⁺ ion. However, this is an idealistic picture, where it is assumed that in the first step complexation occurs through the N donors of the PHEN moiety of the

ligand followed by interaction with other donor centers. It can explain only the interactions when both soft and hard donor centers are present in the same ligand but is not able to explain the shorter Am-S bond distances in case of TCA and THIO complexes where both the donor centers are soft in nature. Definitely, covalency may play a major role in these complexes (see discussion in Section 2.4.4). Also, from Table 2.1 it is evident that metal-N bond distances are increased quite a bit in going from PHEN complexes to the other complexes and the effect is more pronounced in case of Am³⁺ complexes.

In general, global reactivity indices such as electronegativity and hardness parameters have been quite valuable in providing in-depth insight in rationalizing various aspects of chemical binding and reactivity in molecular systems.^{105,106} For explaining different trends in chemical reactivity in difficult situations several local reactivity descriptors are proposed from time to time in chemistry. One such reactivity index, Fukui function,⁵⁰ which was proposed within the framework of density functional theory have been found to be quite valuable in rationalizing competing reactive sites^{73,74,107-109} in a molecule towards a nucleophile or an electrophile. Afterwards, several variants of this reactivity index are proposed to explain various experimentally observed results. In the recent past, Roy et al^{73,74} demonstrated that instead of only f_k^+ and f_k^- , the ratios, f_{nu} and f_{el} behave as better reactivity descriptors for nucleophilic and electrophilic attack, respectively.

Very recently, these descriptors have been used extensively for a successful rationalization of favorable and competing reactive sites in a molecule or cluster.¹⁰⁹ However, to the best of our knowledge these concepts have never been exploited for the interpretation of metal-ligand complexation process involving trivalent lanthanides

and actinides. Therefore, we have been motivated to use Fukui reactivity indices for the rationalization of complexation behavior of metal ions with the four ligands considered here. Initially we investigate the effect of nitrogen donors present in the PHEN moiety towards the reactivity of metal ion. The calculated values of the various parameters reported in Table 2.7 reveal that the f_{nu} value for Am in the $[Am-PHEN]^{3+}$ complex is higher than that in Eu in the corresponding $[Eu-PHEN]^{3+}$ complex.

It indicates that Am in $[Am-PHEN]^{3+}$ complex should act as a better electrophile in comparison with the Eu in $[Eu-PHEN]^{3+}$ complex towards a particular nucleophile. In other words, between $[Am-PHEN]^{3+}$ and $[Eu-PHEN]^{3+}$ complexes nucleophilic attack will be more favorable on the Am center. This trend is evident from the calculated values of Am-O/S and Eu-O/S bond distances reported in Table 2.1, where it is clear that Am-O/S bond distance is shorter than the Eu-O/S bond distance for each of the four ligands, PDA, TCA1, TCA and THIO.

The calculated f_{el} values of the donor atoms in each of the four ligands in presence of solvent reported in Table 2.7 reveal that the calculated M-O/S bond distances trend is consistent with the f_{el} values. For instance, f_{el} value is higher for the oxygen atom in PDA than that in TCA1 suggesting stronger complex formation ability of PDA with a particular metal ion, which is in agreement with the calculated bond length and complexation energy values. Similarly, a higher value of f_{el} for sulfur atom in TCA than that in THIO indicates a stronger complex formation ability of TCA than THIO. Thus, all the trends resulting from the calculated density functional based reactivity descriptors values are in excellent agreement with the variations in the calculated bond distance and complex formation energy values. All the trends

observed in the calculated values of Fukui reactivity indices in the gas phase are found to remain the same in the solvent phase as well (Tables 2.8 and 2.9).

Table 2.7 Calculated values of Fukui indices for the nucleophilic attack on the donor site (f_{el}) and the electrophilic attack on the metal site (f_{nu}) of the free ligand and the [M-PHEN]³⁺ complexes, respectively, in presence of solvent

Free Ligand	f_{el} (O/S)	f_{el} (N)	PHEN Complex	f_{nu} (M)
[PDA] ²⁻	6.039	0.679	[Am-PHEN] ³⁺	3.967
[TCA1] ²⁻	1.784	0.786	[Eu-PHEN] ³⁺	2.718
[TCA] ²⁻	4.126	0.786	[U-PHEN] ³⁺	6.529
[THIO] ²⁻	2.752	0.308	[Ce-PHEN] ³⁺	3.452

Table 2.8 Calculated values of charges on donor center and Fukui indices for the nucleophilic attack on the donor sites in gas and solvent phases for the dianionic form of the bare ligands using def-SV(P)/BP86 method

Gas Phase						
LIGAND NAME	q _N	q _O /q _S	f_{-k}^- (O) or f_{-k}^- (S)	f_{-k}^- (N)	f_{el} (O or S)	f_{el} (N)
[PDA] ²⁻	-0.446	-0.691	0.142	0.040	3.017	3.137
[TCA1] ²⁻	-0.445	-0.589	0.068	0.024	1.623	0.933
[TCA] ²⁻	-0.445	-0.450	0.290	0.024	2.273	0.933
[THIO] ²⁻	-0.439	-0.196	0.202	0.010	2.335	1.189
Solvent Phase						
[PDA] ²⁻	-0.496	-0.756	0.129	0.061	---	---
[TCA1] ²⁻	-0.493	-0.639	0.061	0.028	---	---
[TCA] ²⁻	-0.493	-0.491	0.331	0.028	---	---
[THIO] ²⁻	-0.496	-0.227	0.203	0.024	---	---

Table 2.9 Calculated values of Fukui indices for the electrophilic attack on the metal centre of [M-PHEN]³⁺ complexes in gas and solvent phases using def-SV(P)/BP86 method

COMPLEX NAME	f_k^+ (M)		f_{nu} (M)
	Gas Phase	Solvent phase	Gas Phase
[Am-PHEN] ³⁺	0.280	0.531	1.456
[Eu-PHEN] ³⁺	0.152	0.307	1.029
[U-PHEN] ³⁺	0.607	0.905	3.529
[Ce-PHEN] ³⁺	0.327	0.511	1.741

2.4.4 Charge Distribution in the Complexes

Now, it would be interesting to compare the charge on the metal ion in various complexes for the analysis of nature of metal-ligand interactions. For this purpose we have reported the partial atomic charges on the metal and donor centers in Tables 2.10 and 2.11. For the [Am-L]⁺ complexes, charge on the metal ion and the donor centers decreases monotonically from PDA to THIO, however, atomic charge on nitrogen centers virtually remains the same irrespective of the ligand. Similar trends are observed for the other metal complexes also. Shorter actinide-ligand bond length along with higher charges on metal and donor centers in PDA and TCA1 complexes indicate that electrostatic interaction is dominating in these complexes, in contrary to that in other well known actinide complexes with Cyanex and BTP,^{80,81,94} where charges on the metal center are very low. The calculated charges on actinide ions are found to be higher for PDA and TCA1 complexes whereas for TCA and THIO complexes charges are higher on lanthanides, which reveal that with PDA and TCA1 ligands electrostatic interaction is more for actinide complexes as compared to the corresponding lanthanide complexes. On the other hand, electrostatic interaction is

slightly less for actinide complexes involving TCA and THIO ligands. Similar trend is maintained with $[ML_2]^+$ complexes, TZVP basis set and also with different functionals (Tables 2.12, 2.13 and 2.14). In presence of solvent, charges on metal centers are found to be slightly higher as compared to corresponding gas phase values; however, overall trend remains the same.

Table 2.10 Calculated atomic charges on metal and donor centers of Am^{3+} and Eu^{3+} complexes in gas and solvent phases using def-SV(P)/BP86 method

Complex	q_M	q_N	q_O/q_S	q_M	q_N	q_O/q_S
	Gas	Gas	Gas	Solvent	Solvent	Solvent
$[Am-PDA]^+$	2.013	-0.606	-0.805	2.277	-0.581	-0.809
$[Eu-PDA]^+$	1.924	-0.596	-0.785	2.236	-0.561	-0.777
$[Am-TCA1]^+$	1.967	-0.617	-0.757	2.264	-0.588	-0.739
$[Eu-TCA1]^+$	1.843	-0.603	-0.747	2.174	-0.565	-0.709
$[Am-TCA]^+$	1.590	-0.592	-0.263	1.962	-0.572	-0.327
$[Eu-TCA]^+$	1.558	-0.587	-0.231	1.963	-0.557	-0.290
$[Am-THIO]^+$	1.567	-0.602	-0.150	1.950	-0.581	-0.178
$[Eu-THIO]^+$	1.581	-0.595	-0.156	1.942	-0.563	-0.165
Am-Phen	2.050	-0.704	-----	2.567	-0.655	-----
Eu-Phen	2.441	-0.615	-----	2.216	-0.639	-----

Table 2.11 Calculated atomic charges on metal and donor centers of U^{3+} and Ce^{3+} complexes in gas and solvent phases using def-SV(P)/BP86 method

Complex	q_M	q_N	q_O/q_S	q_M	q_N	q_O/q_S
	Gas	Gas	Gas	Solvent	Solvent	Solvent
$[U-PDA]^+$	2.120	-0.637	-0.799	2.420	-0.615	-0.817
$[Ce-PDA]^+$	2.065	-0.603	-0.832	2.293	-0.582	-0.830
$[U-TCA1]^+$	2.117	-0.644	-0.753	2.438	-0.617	-0.756

[Ce-TCA1] ⁺	2.047	-0.616	-0.779	2.466	-0.577	-0.754
[U-TCA] ⁺	1.495	-0.594	-0.216	1.939	-0.594	-0.335
[Ce-TCA] ⁺	1.616	-0.587	-0.287	2.225	-0.575	-0.406
[U-THIO] ⁺	1.479	-0.604	-0.089	1.921	-0.599	-0.167
[Ce-THIO] ⁺	1.611	-0.600	-0.164	2.174	-0.573	-0.266
U-Phen	2.419	-0.684	-----	2.748	-0.704	-----
Ce-Phen	2.316	-0.743	-----	2.653	-0.685	-----

Table 2.12 Calculated atomic charges on metal and donor centers of Am³⁺ and Eu³⁺ complexes ([ML]⁺ and [ML₂]⁻¹) in Gas and Solvent phases using TZVP/BP86 method

Complex	q _M	q _N	q _O /q _S	q _M	q _N	q _O /q _S
	Gas	Gas	Gas	Solvent	Solvent	Solvent
[Am-PDA] ⁺	2.049	-0.502	-0.758	2.325	-0.476	-0.759
[Eu-PDA] ⁺	1.960	-0.490	-0.738	2.284	-0.453	-0.729
[Am-TCA1] ⁺	2.008	-0.517	-0.726	2.309	-0.485	-0.702
[Eu-TCA1] ⁺	1.882	-0.504	-0.717	2.174	-0.565	-0.709
[Am-(PDA) ₂] ⁻	1.724	-0.409	-0.677	1.722	-0.424	-0.701
[Eu-(PDA) ₂] ⁻	1.640	-0.394	-0.667	1.647	-0.410	-0.690
[Am-(TCA1) ₂] ⁻	1.806	-0.433	-0.634	1.838	-0.451	-0.646
[Eu-(TCA1) ₂] ⁻	1.663	-0.449	-0.594	1.657	-0.460	-0.618
[Am-(TCA) ₂] ⁻	0.835	-0.396	-0.153	0.901	-0.405	-0.230
[Eu-(TCA) ₂] ⁻	0.878	-0.477	-0.184	0.886	-0.489	-0.237
[Am-(THIO) ₂] ⁻	0.888	-0.441	0.025	0.910	-0.445	-0.033
[Eu-(THIO) ₂] ⁻	0.946	-0.429	0.009	0.975	-0.432	-0.051

Table 2.13 Calculated atomic charges at metal centers (q_M) of the complexes $[ML]^+$ for different exchange correlation functionals (PBE and BLYP) using def-SV(P)

→ Ligand	q_M							
	PDA		TCA1		TCA		THIO	
↓ Metal	BLYP	PBE	B-LYP	PBE	BLYP	PBE	BLYP	PBE
Am	2.011	2.010	1.958	1.965	1.596	1.590	1.563	1.568
Eu	1.920	1.918	1.834	1.843	1.564	1.557	1.554	1.542
U	2.116	2.118	2.109	2.116	1.526	1.484	1.508	1.479
Ce	2.065	2.059	2.043	2.042	1.616	1.607	1.620	1.606

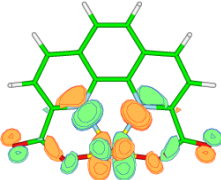
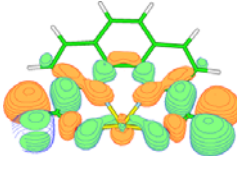
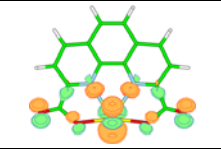
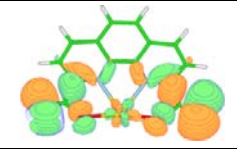
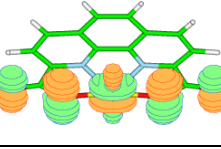
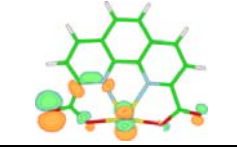
Table 2.14 Calculated atomic charges on metal and donor centers of U^{3+} and Ce^{3+} complexes ($[ML_2]^{-1}$) in Gas and Solvent phases using TZVP/BP86 method

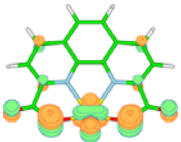
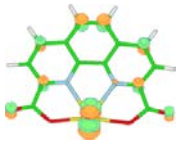
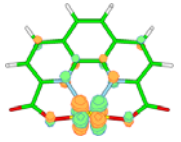
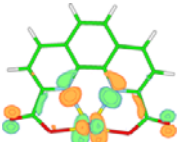
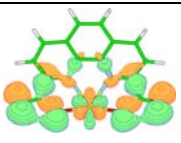
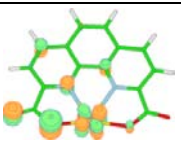
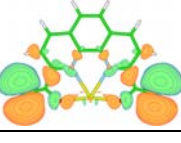
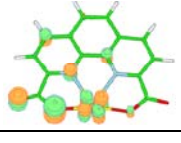
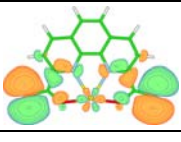
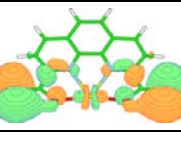
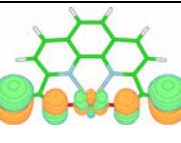
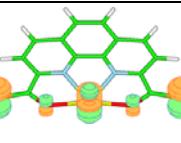
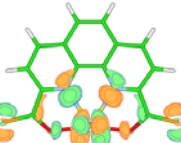
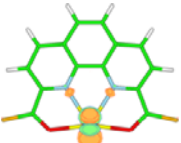
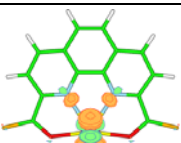
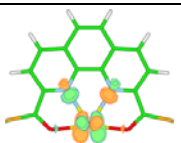
Complex	q_M	q_N	q_O/q_S	q_M	q_N	q_O/q_S
	Gas	Gas	Gas	Solvent	Solvent	Solvent
$[U-(PDA)_2]^-$	1.547	-0.386	-0.604	1.570	-0.400	-0.633
$[Ce-(PDA)_2]^-$	1.696	-0.396	-0.668	1.697	-0.413	-0.698
$[U-(TCA1)_2]^-$	1.566	-0.396	-0.572	1.571	-0.407	-0.587
$[Ce-(TCA1)_2]^-$	1.718	-0.413	-0.619	1.717	-0.424	-0.640
$[U-(TCA)_2]^-$	0.253	-0.381	0.002	0.472	-0.403	-0.118
$[Ce-(TCA)_2]^-$	0.920	-0.400	-0.174	0.987	-0.407	-0.283
$[U-(THIO)_2]^-$	0.342	-0.400	0.130	0.391	-0.404	0.080
$[Ce-(THIO)_2]^-$	0.871	-0.406	0.007	0.958	-0.415	-0.087

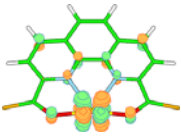
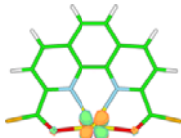
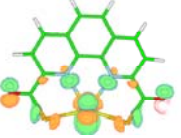
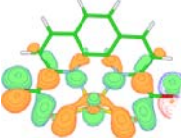
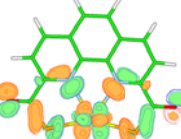
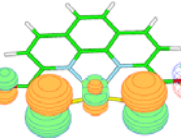
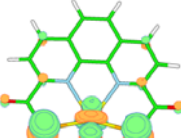
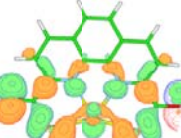
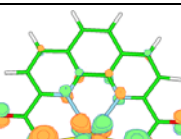
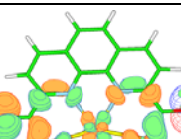
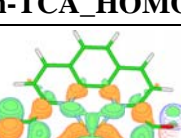
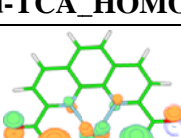
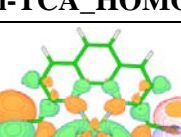
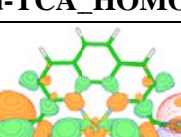
Valence orbitals pictures (Figure 2.4) also indicate that metal-ligand interaction in $[ML]^+$ complexes (M=Am, Eu) is mostly ionic in nature with virtually no overlap between metal and ligand orbitals except in one or two molecular orbitals involving S donor ligands. Particularly, for the complexes with O-donor ligands (PDA and TCA1)

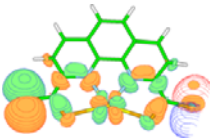
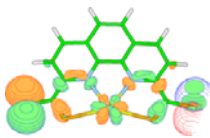
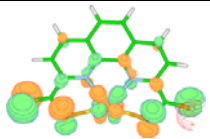
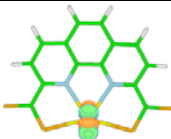
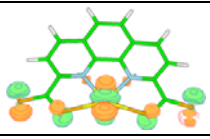
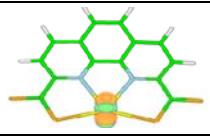
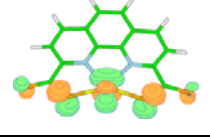
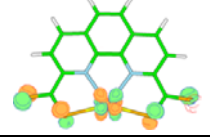
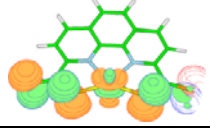
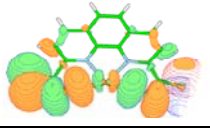
no metal-ligand orbital overlap has been found. However, for $[\text{Am-PHEN}]^{3+}$ complex substantial amount of overlap has been found between the Am^{3+} and PHEN orbitals. Also, considerable amount of overlap for all the U complexes indicates that covalent interaction plays an important role here. Although, among the four metal ions, charge on U(III) ion is highest for PDA and TCA1 ligands, but, it is not entirely due to more electrostatic interaction. Significant amount of metal–ligand orbitals overlap indicate that metal-ligand back donation is responsible for maximum charge on U atom among all the $[\text{ML}]^+$ complexes considered here. This aspect for U(III) complex with N-donor ligand has already been demonstrated earlier.^{80,104} It is also interesting to note that metal-nitrogen orbital overlap in $[\text{Am-PHEN}]^{3+}$ complex vanishes completely in $[\text{Am-PDA}]^+$ and $[\text{Am-TCA1}]^+$ complexes indicating the dominating nature of electrostatic interaction with oxygen donor ligands in presence of softer nitrogen donor site.

a)

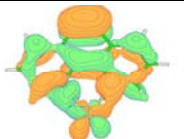
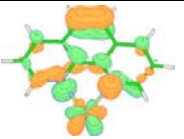
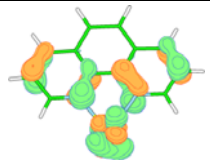
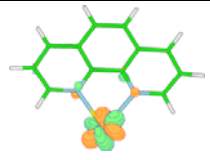
Americium	Europium
	
Am-PDA-HOMO	Eu-PDA-HOMO
	
Am-PDA_HOMO-1	Eu-PDA_HOMO-1
	
Am-PDA_HOMO-2	Eu-PDA_HOMO-2

	
Am-PDA_HOMO-3	Eu-PDA_HOMO-3
	
Am-PDA_HOMO-4	Eu-PDA_HOMO-4
	
Am-PDA_HOMO-5	Eu-PDA_HOMO-5
	
Am-TCA1_HOMO	Eu-TCA1_HOMO
	
Am-TCA1_HOMO-1	Eu-TCA1_HOMO-1
	
Am-TCA1_HOMO-2	Eu-TCA1_HOMO-2
	
Am-TCA1_HOMO-3	Eu-TCA1_HOMO-3
	
Am-TCA1_HOMO-4	Eu-TCA1_HOMO-4

	
Am-TCA1_HOMO-5	Eu-TCA1_HOMO-5
	
Am-TCA_HOMO	Eu-TCA_HOMO
	
Am-TCA_HOMO-1	Eu-TCA_HOMO-1
	
Am-TCA_HOMO-2	Eu-TCA_HOMO-2
	
Am-TCA_HOMO-3	Eu-TCA_HOMO-3
	
Am-TCA_HOMO-4	Eu-TCA_HOMO-4
	
Am-TCA_HOMO-5	Eu-TCA_HOMO-5
	
Am-THIO_HOMO	Eu-THIO_HOMO

	
Am-THIO_HOMO-1	Eu-THIO_HOMO-1
	
Am-THIO_HOMO-2	Eu-THIO_HOMO-2
	
Am-THIO_HOMO-3	Eu-THIO_HOMO-3
	
Am-THIO_HOMO-4	Eu-THIO_HOMO-4
	
Am-THIO_HOMO-5	Eu-THIO_HOMO-5

b)

	
Am-PHEN_HOMO	Eu-PHEN_HOMO
	
Am-PHEN_HOMO-1	Eu-PHEN_HOMO-1

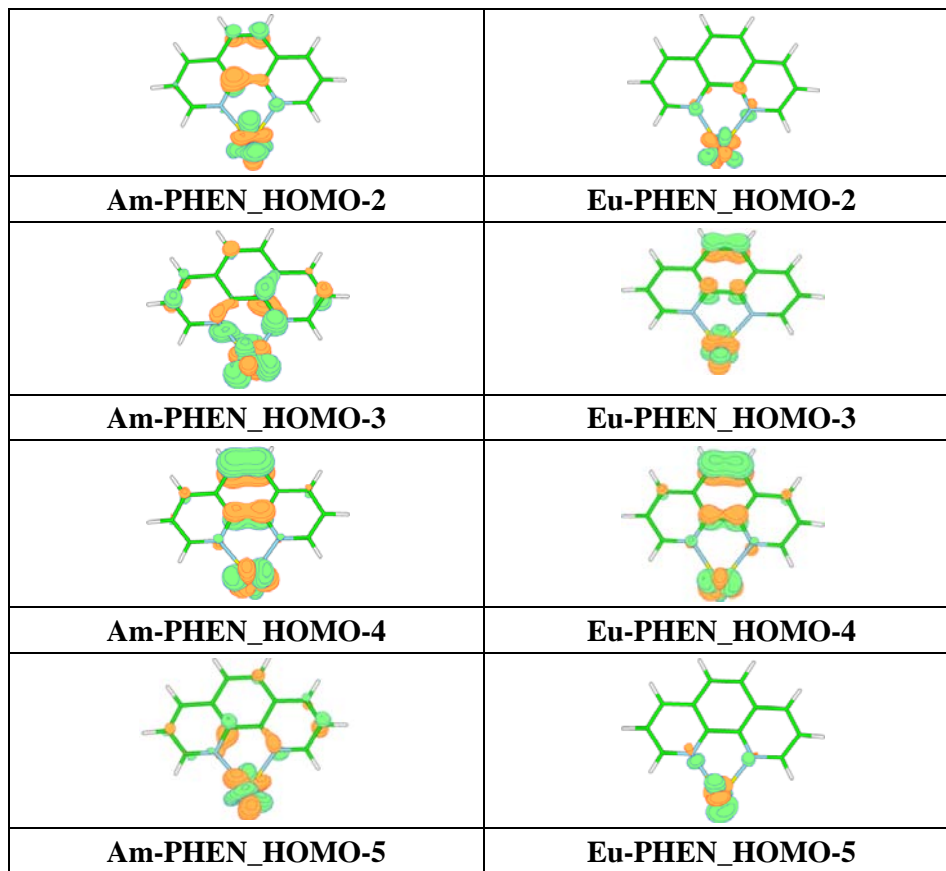


Figure 2.4 Valence level occupied molecular orbitals of a) metal complexes, $[ML]^+$ and b) $[M-PHEN]^{3+}$ complexes.

2.4.5 Energy Decomposition Analysis

Energy decomposition analysis is also performed using the ADF software. It is important to note that both repulsive Pauli and attractive electrostatic components are responsible for the overall Coulombic interaction. Therefore, it is interesting to combine these two components and compare the variation of this resulting component (steric component) from PDA to THIO complexes. From Table 2.15 it is clear that steric interaction, which is electrostatic in nature, is minimum for the $[Am-THIO]^+$ complex.

Table 2.15 Percentage orbital and electrostatic interactions in the total bonding energy as obtained from energy decomposition analysis for Am³⁺ and Eu³⁺ complexes using BP86 exchange-correlation functional in the gas phase

Complex Name	% Electrostatic Interaction	% Steric Interaction	% Orbital Interaction
[Am-PDA] ⁺	83.44	57.21	42.79
[Eu-PDA] ⁺	77.88	58.99	41.01
[Am-TCA1] ⁺	78.33	54.30	45.70
[Eu-TCA1] ⁺	71.97	55.70	44.30
[Am-TCA] ⁺	80.77	54.71	45.29
[Eu-TCA] ⁺	75.00	55.45	44.55
[Am-THIO] ⁺	76.73	52.38	47.62
[Eu-THIO] ⁺	70.73	53.01	46.99

On the other hand for [Eu-PDA]⁺ complex its contribution is maximum. Orbital interaction component differs the most for PDA complexes although absolute values of this component are the highest for THIO complexes. Thus, it is evident that among all the complexes considered in this work, a minimum value of steric component, which is electrostatic in nature and a maximum value of orbital component that is mostly covalent in nature for [Am-THIO]⁺ complex are found, which in turn leads to a stronger covalency in Am-S bond. This picture is consistent with a shorter Am-S bond distance than the corresponding Eu-S bond distance for THIO complexes. Similar trend in the variation of metal-ligand bond distance has been found in the Cyanex301 complexes of Am³⁺ and Eu³⁺ ions where the experimentally observed separation factor has been found to be very high.⁸¹ Thus, it is natural to expect that the THIO ligand is likely to be highly Am³⁺ selective. Various energy components for the U and Ce complexes reported in Table 2.16 reveal that the orbital interaction component is

higher for all the U complexes. This trend is consistent with the N-donor complexes of U and Ce investigated earlier.^{80,82}

Table 2.16 Percentage orbital and electrostatic interactions in the total bonding energy as obtained from energy decomposition analysis for U³⁺ and Ce³⁺ complexes using BP86 exchange-correlation functional in the gas phase

Complex Name	% Electrostatic Interaction	% Steric Interaction	% Orbital Interaction
[U-PDA] ⁺	87.37	51.67	48.33
[Ce-PDA] ⁺	83.97	57.56	42.43
[U-TCA1] ⁺	84.25	53.11	46.89
[Ce-TCA1] ⁺	81.12	54.54	45.46
[U-TCA] ⁺	86.45	50.53	49.46
[Ce-TCA] ⁺	82.96	55.22	44.78
[U-THIO] ⁺	84.60	46.64	53.35
[Ce-THIO] ⁺	80.41	51.87	48.13

2.4.6 Effect of Counter Ions

Now, one may argue that for [ML]⁺ complexes all the coordination sites of the metal ions may not be fulfilled, therefore, we have performed calculations of the metal ion complexes using one PDA ligand along with six water molecules ([M(PDA)(H₂O)₄]⁺.2H₂O) and also [M(PDA)(NO₃)₃]²⁻ complexes. In the case of ([M(PDA)(H₂O)₄]⁺.2H₂O) it has been observed that four water molecules are in close proximity (within the bonding distance with the metal ion), however, other two water molecules are not directly connected with the metal ion. Calculated results (Table 2.17) indicate that all the trends observed in the case of [ML]⁺ complexes are maintained in the [M-PDA(H₂O)₄]⁺.2H₂O and [M-PDA(NO₃)₃]²⁻ complexes (Figure 2.5) as well. Details results are reported in the Table 2.18 and 2.19.

Table 2.17 Calculated M-L bond distances (Å) (in gas phase) and complexation energies (eV) in gas (ΔE_g) and solvent (ΔE_s) phases for Am^{3+} and Eu^{3+} complexes, $[\text{M-PDA}(\text{H}_2\text{O})_4]^+ \cdot 2\text{H}_2\text{O}$ and $[\text{M-PDA}(\text{NO}_3)_3]^{2-}$ with def-SV(P)/BP86 method

Complex	M-O	M-N	ΔE_g	ΔE_s
$[\text{Am-PDA}(\text{H}_2\text{O})_4]^+ \cdot 2\text{H}_2\text{O}$	2.398	2.585	-48.65	-10.66
$[\text{Eu-PDA}(\text{H}_2\text{O})_4]^+ \cdot 2\text{H}_2\text{O}$	2.470	2.595	-49.12	-7.15
$[\text{Am-PDA}(\text{NO}_3)_3]^{2-}$	2.417	2.643	-50.94	-10.55
$[\text{Eu-PDA}(\text{NO}_3)_3]^{2-}$	2.453	2.685	-51.45	-7.15

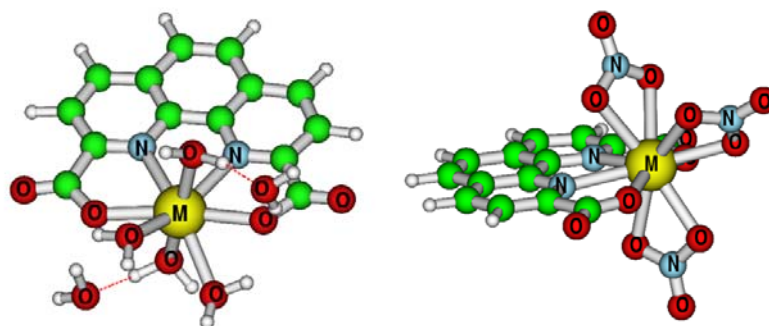


Figure 2.5 Optimized structures of $[\text{M-PDA}(\text{H}_2\text{O})_4]^+ \cdot 2\text{H}_2\text{O}$ and $[\text{M-PDA}(\text{NO}_3)_3]^{2-}$.

Table 2.18 Calculated M-L bond distances (Å) and complexation energies (eV) in gas (ΔE_g) and solvent (ΔE_s) phases for Am^{3+} and Eu^{3+} complexes, $[\text{ML}_2]^-$ with TZVP/BP86 method

Complex	M-O/M-S	M-N	M-O/M-S	M-N	ΔE_g	ΔE_s
	Gas	Gas	Solvent	Solvent		
$[\text{Am}(\text{PDA})_2]^-$	2.373	2.579	2.398	2.577	-51.80	-8.45
$[\text{Eu}(\text{PDA})_2]^-$	2.393	2.601	2.400	2.593	-52.58	-5.37
$[\text{Am}(\text{TCA}1)_2]^-$	2.414	2.578	2.429	2.550	-49.76	-7.65
$[\text{Eu}(\text{TCA}1)_2]^-$	2.477	2.584	2.481	2.597	-49.15	-4.06
$[\text{Am}(\text{TCA})_2]^-$	2.802	2.613	2.814	2.631	-49.77	-6.28
$[\text{Eu}(\text{TCA})_2]^-$	2.839	2.634	2.820	2.647	-49.89	-3.35
$[\text{Am}(\text{THIO})_2]^-$	2.817	2.578	2.812	2.562	-47.74	-5.16
$[\text{Eu}(\text{THIO})_2]^-$	2.863	2.601	2.866	2.596	-48.63	-2.29

Table 2.19 Calculated M-L bond distances (Å) and complexation energies (eV) in gas (ΔE_g) and solvent (ΔE_s) phases for U^{3+} and Ce^{3+} complexes, $[ML_2]^-$ with TZVP/BP86 method

Complex	M-O/M-S	M-N	M-O/M-S	M-N	ΔE_g	ΔE_s
	Gas	Gas	Solvent	Solvent		
$[U-(PDA)_2]^-$	2.244	2.555	2.275	2.555	-51.98	-10.59
$[Ce-(PDA)_2]^-$	2.377	2.645	2.420	2.643	-50.69	-3.45
$[U-(TCA1)_2]^-$	2.235	2.533	2.259	2.536	-50.40	-9.94
$[Ce-(TCA1)_2]^-$	2.388	2.636	2.423	2.630	-49.01	-2.51
$[U-(TCA)_2]^-$	2.714	2.505	2.782	2.517	-49.45	-9.34
$[Ce-(TCA)_2]^-$	2.843	2.613	2.859	2.619	-48.32	-1.82
$[U-(THIO)_2]^-$	2.720	2.530	2.728	2.526	-48.84	-8.79
$[Ce-(THIO)_2]^-$	2.816	2.611	2.859	2.616	-47.61	-1.56

Here, it is interesting to note that irrespective of the overall charge on the complex and the composition, the trend in the calculated complexation energy values remains the same. We have also examined the $[ML_2]^-$ type complexes (Figure 2.6) where two phenanthroline-based ligands are involved and the metal ion is octa-coordinated.

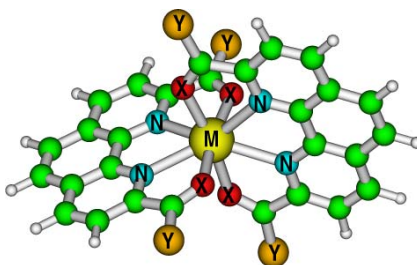


Figure 2.6 Optimized structure of metal ion-ligand dimer complex, $[ML_2]^-$.

In all the four types of complexes considered here, viz., $[ML]^+$, $[M-PDA(H_2O)_4]^+ \cdot 2H_2O$, $[M-PDA(NO_3)_3]^{2-}$ and $[ML_2]^-$, the trends in the calculated metal-ligand bond distances and complexation energies are found to be the same. In fact,

from the values reported in Tables 2.1 and 2.18 it is clearly evident that the percentage difference in the complexation energy between Am and Eu complexes (in presence of solvent) is increased from $[ML]^+$ complexes to $[ML_2]^-$ complexes. It is to be noted that similar type of complexes with other metal ions have already been investigated experimentally by Hancock and co-workers.^{67,68} Apart from the M-L bond distances and the complexation energy values, the calculated partial atomic charge values on the metal as well as donor centers for the $[ML_2]^-$ complexes follow the similar trend as observed in $[ML]^+$.

Here the gas phase calculated values of basis set super position error (BSSE) for the complexation energy have been found to be ~ 0.3 eV for both $[Am(PDA)_2]^-$ and $[Eu(PDA)_2]^-$ complexes, which are rather negligible in comparison to the computed ΔE values of ~ 52 eV. Similar trend in the calculated values of BSSE has been found earlier by Petit et al.⁸⁰

It may be interesting to compare the M-N and M-O bond lengths of metal complexes with other N and O donor ligands like DTPA, te-tpyda etc.^{110,111} with the present ones. For the $[Eu-DTPA]^{2-}$ complex, the Eu-N bond lengths reported in the literature are found to be 2.761-2.893 Å and Eu-O bond lengths are varied from 2.365 to 2.505 Å,¹¹⁰ which are quite larger than the corresponding Eu-O and Eu-N bond lengths calculated for the complexes considered in this work. For te-tpyda complexes Nd-O and Dy-O bond distances are already reported and the values are 2.53 and 2.39 Å,¹¹¹ respectively. In this context it may be noted that DTPA (consists of N and O donors) is used as a complexing agent in the TALSPEAK process.¹¹²

2.4.7 Effect of Oxygen Donor Ligand in Presence of Nitrogen

Now, to investigate the effect of N atoms on the coordinating behavior of O/S donors present in phenanthroline derivatives further, we have considered the ligand PDA with N-atoms replaced with -CH groups (denoted as NRC). With this modification one can investigate the behavior of the oxygen binding towards the metal ion in absence of N donors. For $[M(\text{NRC})_2]^-$ and $M(\text{NO}_3)_3$ complexes ($M=\text{Am}$ and Eu) we have noticed that bond lengths remain almost the same for Am and Eu complexes (M-O bond distances are 2.278 and 2.279 Å, where, $M = \text{Am}$ and Eu , respectively for $[M(\text{NRC})_2]^-$ complexes) and (M-O bond distances are 2.388 and 2.391 Å, where, $M = \text{Am}$ and Eu , respectively for $[M(\text{NO}_3)_3]$ complexes). All these calculated values indicate that in these two cases there are essentially no difference in M-O bond distances and hence no selectivity. However, in presence of nitrogen atom as another donor center, the ligand becomes selective towards actinides as compared to lanthanides as far as the calculated bond distances and complexation energies are concerned. This is certainly due to the intra-ligand synergistic effect as evident from all the calculated results reported here.

2.5 Concluding Remarks

In summary, two valence isoelectronic metal ions, viz., Am(III) and Eu(III) along with two other metal ions i.e U(III) and Ce(III) have been considered to investigate the complex formation process with different ligands derived from 1,10-phenanthroline-2,9-dicarboxylic acid through functionalization with soft donor atoms such as sulfur. In addition to the selectivity of Am with S donor ligands (TCA and THIO), the bonding ability of Am(III) is found to be significant with PDA and TCA1 ligands also

as compared to Eu(III), where the metal-ligand binding is through the O atoms. Similar trend is also observed for U(III) and Ce(III). It is quite unusual that the hard donor oxygen atoms bind strongly with the softer actinide metal ions as compared to harder lanthanide ions. Pearson's Hard-Soft-Acid-Base (HSAB) principle and the frontier orbital theory of chemical reactivity as proposed by Fukui have been employed to rationalize these unusual features. Detail analysis within the framework of HSAB principle indicate that the presence of softer nitrogen atoms in the PHEN moiety (which also act as donors to the metal ion) has profound influence in changing the hard-soft character of the actinide ions, which in turn bounds with the hard oxygen atoms in a stronger way as compared to the valence isoelectronic lanthanide ion. Although, among all the complexes investigated here, the interaction of metal ion is stronger with O-center than with N-center, the role of N donor is quite significant. Particularly, for TCA1 complexes presence of S atoms in the same ligand also helps in tuning the interactions between the metal ion and donor centers. The calculated values of the Fukui indices corresponding to the nucleophilic and electrophilic attack have been able to enlighten the trends in the variation of calculated values of the metal-ligand bond distances and the corresponding complex formation energies. The "intra-ligand synergistic effect" demonstrated here through stepwise analysis, particularly for PDA or TCA1 with soft and hard donor centers might be very important in designing new ligands for selective extraction of various metal ions in a competitive environment. In case of TCA and THIO complexes, along with intra-ligand synergism, a shorter Am-S bond distance, lower metal ion charge and a higher percentage of orbital interaction energy confirm the presence of a higher degree of

covalency in Am-S bonds, which in turn may be responsible for selectivity towards Am^{3+} .

Chapter 3: Actinide Selectivity of 1,10-Phenanthroline-2,9-dicarboxamide and its Derivatives: A Theoretical Prediction Followed by Experimental Validation

3.1 Introduction

3.1.1 Extension from Phenanthroline-diacids to Phenanthroline-dicarboxamide: Why?

In the previous chapter we theoretically rationalized the selective complex formation of An(III) over Ln(III) with O donor ligands, 1,10-phenanthroline-2,9-dicarboxylic acid (PDA, **2**) (Figure 3.1).⁶⁰

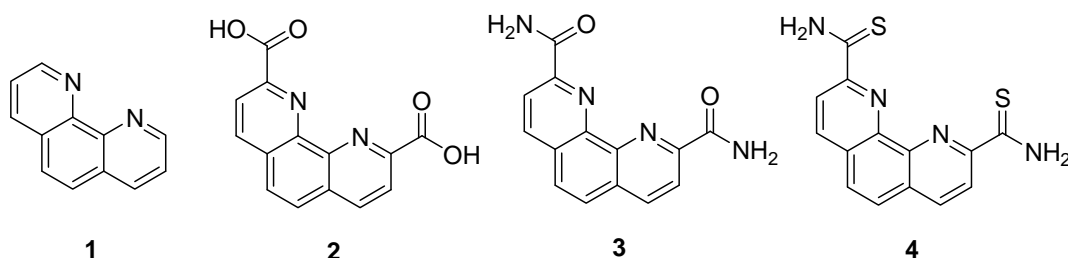


Figure 3.1 Schematic depiction of structures of 1,10-phenanthroline and its different derivatives.

We explained this unconventional complexation affirmatively by exploiting the concept of “intramolecular synergism”. We established that the synergistic effects can be achieved through functionalization of the original ligand with suitable donor atoms as far as the selectivity is concerned by providing an in-depth insight within the framework of Pearson’s Hard-Soft-Acid-Base (HSAB) principle^{49,63,64} and frontier molecular orbital (FMO) theory^{50,65} of chemical reactivity. Detail analysis within the framework of HSAB principle indicates that the presence of softer

nitrogen atoms in the 1,10-phenanthroline moiety has profound influence in changing the hard-soft character of the actinide ions. Subsequently two reports are published, which have provided further support to our conjecture. In one of the reports, authors have not only supported our “intramolecular synergism” concept but also reproduced this effect with a well-established system DTPA⁵⁻,¹¹³ and in the second report Nash and co-workers have claimed that PDA has the ability to replace DTPA in TALSPEAK type separations.¹¹⁴ They have also mentioned that the selectivity of PDA for Am³⁺ over Nd³⁺ can be used to effectively separate one from the other using solvent extraction methods. Although PDA may be considered as a promising ligand for the purpose of An/Ln separation, it is limited by its low solubility in aqueous solutions ($\sim 10^{-4}$ mol L⁻¹ in alkaline solution) as well as in organic medium due to the presence of aromatic nitrogen heterocyclic backbone. However, it has been emphasized that solubility of PDA in aqueous or in organic medium can be enhanced through sulfonation of the phenanthroline backbone of PDA or conversion of carboxylate groups into carboxyamides, respectively, to make it suitable for An/Ln separation.

In the earlier chapter we have used anionic ligand (di-carboxylate) for investigating the “intramolecular synergism”. However, it will be interesting to evaluate the performance of neutral ligand (amide and thio-amide) with higher lipophilicity for the selectivity of An(III) over Ln(III).¹¹⁵ Very recently, Galletta et al. have also reported the extraction and separation behavior of Am³⁺ and Eu³⁺ employing 2,9-dicarbonyl-1,10-phenanthroline derivatives experimentally in presence of additional synergistic agent.¹¹⁶ Consequently, it is interesting to investigate theoretically whether neutral ligand also shows “intramolecular synergism” or not. Therefore, the objective of this work is twofold: (i) theoretical

study of the complexation behavior of different amide and thio-amide derivatives of PDA with Am^{3+} and Eu^{3+} metal ions and (ii) experimental validation of our theoretical findings through synthesis of optimized PDA derivatives followed by solvent extraction study to know the selectivity trends without using any additional synergistic agent.¹¹⁵

3.2 Computational Details

Most of the computational methodologies are same as mentioned before in Chapter 2, section 2.3. Here additionally we have calculated bond critical point (BCP) properties (electron density $[\rho]$, Laplacian of the electron density $[\nabla^2\rho]$) using ADF program within the framework of quantum theory of atoms-in-molecule (AIM) approach.^{117,118}

3.3 Experimental Details

3.3.1 Synthetic Procedure

General experimental details: 1,10-phenanthroline-2,9-dicarboxylic acid (PDA) (from *AlfaAesar*) has been used without any further purification. All the chemicals and solvents has been purchased from Aldrich, Merck or Sigma and used without any further purification. The ^1H and ^{13}C NMR spectra have been recorded with a Bruker 200 FT-spectrometer or a Bruker 500 FT-spectrometer in CDCl_3 if not mentioned otherwise. The high resolution mass spectra have been recorded with an Agilent make instrument (Model: 1290 Infinity UHPLC System, 1260 infinity Nano HPLC with Chipcube, 6550 iFunnel Q-TOF). Melting points has been determined using a Fisher-Johns Melting Point Apparatus.

2,9-dicarbomethoxy-1,10-phenanthroline (5): A solution of 1,10-phenanthroline-2,9-dicarboxylic acid (PDA) (**1**) (400 mg, 1.49 mmol) in MeOH (100 mL), has been saturated with dry HCl and heated under reflux for 2.5 hours. Then MeOH has been evaporated and CH₂Cl₂ (100 mL) has been added to it. The solution has been washed with H₂O (2 x 50 mL), saturated NaHCO₃ solution (2 x 50 mL) and brine (2 x 50 mL). The organic phase has been dried and concentrated *in vacuo*. The solid residue has been recrystallized from ethanol to furnish **2** (as the monohydrate). Yield: 290 mg (65 %); yellow plates; Mp: 212 °C (lit.¹ Mp: 213-214 °C); ¹H NMR (200 MHz, CDCl₃, 25 °C, TMS): δ = 4.13 (s, 6H), 7.97 (s, 2H), 8.42 (d, *J* = 8.2 Hz, 2H), 8.49 (d, *J* = 8.2 Hz, 2H); ¹³C NMR (50 MHz, CDCl₃, 25 °C, TMS): δ = 53.1, 123.8, 128.3, 130.7, 137.5, 145.4, 148.1, 165.9 ppm; EI-MS: *m/z* (%): 296.1 (100) [*M*]⁺. elemental analysis calculated (%) for C₁₆H₁₂N₂O₄.H₂O: C 61.14, H 4.49, N 8.91; found: C 61.29, H 4.17, N 9.13.¹¹⁹

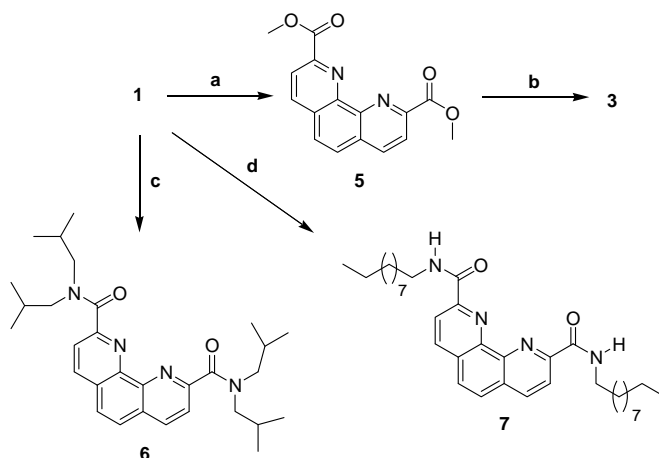
2,9-Dicarbamoyl-1,10-phenanthroline (PDAM) (3): A mixture of **5** (296 mg, 1 mmol), conc. NH₃ (aq., 7 mL) and NH₄Cl (20 mg) has been stirred at 25 °C for 15 h. The precipitate has been filtered, washed with H₂O (3 x 10 mL) and dried under *vacuo* to furnish **3**. Yield: 200 mg (75%); light yellow solid; Mp: >300 °C (lit.² Mp: >300 °C); ¹H NMR (200 MHz, (CD₃)₂SO, 25 °C, TMS): δ = 7.87 (br s, 2H), 8.15 (s, 2H), 8.42 (d, *J* = 8.2 Hz, 2H), 8.67 (d, *J* = 8.3 Hz, 2H), 8.95 (br s, 2H); ¹³C NMR (50 MHz, (CD₃)₂SO, 25 °C, TMS): δ = 121.0, 127.7, 130.2, 137.8, 144.0, 150.1, 166.0 ppm; elemental analysis calcd (%) for C₁₄H₁₀N₄O₂.H₂O: C 59.15, H 4.25, N 19.71; found: C 58.85, H 4.02, N 20.01.¹²⁰

2,9-bis(N,N-di(2-methyl-1-propanamine)carbonyl)-1,10-phenanthroline (6) and 2,9-bis(N-decylaminocarbonyl)-1,10-phenanthroline (7): 1,10-phenanthroline-2,9-dicarboxylic acid (PDA) (1) (250 mg, 0.93 mmol) has been refluxed in excess thionyl chloride (5 mL, 69.7 mmol) for 24 h, and then the residual thionyl chloride has been removed at a reduced pressure. Without isolation and purification, the resulting 1,10-phenanthroline-2,9-dicarbonyl chloride has been used in the subsequent step. The crude product has been dissolved in DMF (4.0 mL) at 25 °C, and diisobutylamine or decylamine (4.65 mmol) has been added into it. Then the mixture has been stirred for 24 h at 25 °C. The reaction mixture has been concentrated under reduced pressure and then dissolved in chloroform (60 mL). The chloroform solution has been washed with 1.0 M NaOH (3 × 60 mL) and H₂O (3 × 60 mL). The organic phase has been dried and concentrated in *vacuo*, and the residue has been subjected to column chromatography (silica gel, MeOH/CHCl₃) to furnish **6** and **7**, respectively.

Compound 6: Yield: 250 mg (54%); light yellow solid; Mp: 164 °C; ¹H NMR (200 MHz, CDCl₃, 25 °C, TMS): δ = 0.64 (d, J = 6.6 Hz, 12H), 1.05 (d, J = 6.6 Hz, 12H), 1.58-1.75 (m, 2H), 2.13-2.34 (m, 2H), 3.44 (d, J = 7.6 Hz, 4H), 3.78 (d, J = 7.4 Hz, 4H), 7.84 (s, 2H), 7.98 (d, J = 8.2 Hz, 2H), 8.29 (d, J = 8.2 Hz, 2H); ¹³C NMR (50 MHz, CDCl₃, 25 °C, TMS): δ = 19.8, 20.1, 26.6, 27.8, 53.9, 56.5, 123.2, 126.9, 128.5, 136.5, 144.0, 154.5, 169.0 ppm; HRMS: m/z : 491.3308 [$M + 1$]⁺; Exact Mass: 490.3308.

Compound 7: Yield: 330 mg (65%); light yellow solid; Mp: 142 °C; ¹H NMR (200 MHz, CDCl₃, 25 °C, TMS): δ = 0.85 (t, J = 6.6 Hz, 6H), 1.22-1.48 (m, 24H), 1.64-

1.74 (m, 8H), 3.53 (q, $J = 6.2$ Hz, 4H), 7.92 (s, 2H), 8.42 (d, $J = 8.2$ Hz, 2H), 8.58 (d, $J = 8.2$ Hz, 2H), 8.65 (t, $J = 5.6$ Hz, 2H); ^{13}C NMR (50 MHz, CDCl_3 , 25 °C, TMS): $\delta = 13.9, 22.5, 26.8, 29.0, 29.1, 29.3, 31.7, 39.5, 122.0, 127.7, 130.3, 137.8, 144.0, 150.2, 163.6$ ppm; HRMS: m/z : 547.3931 [$M + 1$] $^+$ Exact Mass: 546.3934.



Scheme 3.1 Synthesis of **3**, **6** and **7**: a) MeOH, dry HCl, reflux, 2.5 h; b) NH_3 , NH_4Cl , 25 °C, 15 h; c) i. SOCl_2 , reflux, 24 h. ii. Diisobutylamine, DMF, 25 °C, 24 h; d) i. SOCl_2 , reflux, 24 h. ii. Decylamine, DMF, 25 °C, 24 h.

3.3.2 Method of Distribution Studies

Distribution studies have been carried out using ^{241}Am and $^{152,154}\text{Eu}$ tracers under varying experimental conditions. Different concentration of **3** and **6** in a mixture of 1 M 2-bromo-octanoic acid and *n*-dodecane has been used as the organic phase while in case of **7**, a mixture of *n*-octanol and *n*-dodecane has been used as the organic phase. The dilute nitric acid at pH 2.0 has been used as aqueous phase for the ligands **3** and **6** and a mixture of HClO_4 and 2M LiClO_4 at different pH has been used in case of ligand **7**. Equal volumes (0.5 mL) of the organic and aqueous phases containing the required tracer have been kept for equilibration in a thermostated water bath at $25 \pm 0.1^\circ\text{C}$ for 60 minutes. The two phases have been then centrifuged

and assayed by taking suitable aliquots (100-200 μL) from both the phases. The gamma activities have been measured using a high purity germanium detector procured from Baltic Scientific Instruments. The distribution ratio (D_M) has been calculated as the ratio of counts per minute per unit volume in the organic phase to that in the aqueous phase. Mass balance has been found to be within the experimental error limits ($\pm 5\%$). The separation factor (S.F.) has been calculated as the ratio of D_{Am} to D_{Eu} .

3.4. Results and Discussions

3.4.1 Theoretical Results

In the previous chapter we showed that the softer actinide metal ion is bonded strongly with hard donor oxygen atoms through a computational study on the interaction of the Am^{3+} ion with the PDA ligand (O and N donors)⁶⁰ and that was possible due to the “intra-ligand synergistic” effect due to which the hard-soft character of the metal ion is changed, and consequently Am^{3+} interacts strongly with the carbonyl oxygen atoms. Detail analysis within the framework of HSAB principle implies that the presence of softer nitrogen atoms in PHEN has significant influence in modulating the hard-soft nature of the actinide ions. In the present study we have extended our investigation to the 1,10-phenanthroline-2,9-dicarboxamide (PDAM, **3**) (Figure 3.1) where carboxylate groups of PDA are replaced with the carboxamides. It would be interesting to check the complexation behavior of PDAM as it is a neutral ligand as compared to the anionic PDA.

For the purpose of comparison, we have also performed theoretical calculations of the Am^{3+} and Eu^{3+} complexes with 1,10-phenanthroline-2,9-dithiocarboxamide (THIOAM, **4**) (Figure 3.1) ligand where two soft donor centers, viz.,

and Am-O bond lengths are slightly shorter as compared to the corresponding Eu-N and Eu-O bond lengths. It is also interesting to note that there are considerable differences in metal-ligand bond length values between the Am³⁺ and Eu³⁺ complexes for the [M(PDAM)₂NO₃]²⁺ and [M(PDAM)(NO₃)₃] compositions. The difference in bond length values are more significant for the [M-(THIOAM)₂]³⁺ complexes and both Am-S and Am-N bond distance values are shorter as compared to the corresponding Eu-S and Eu-N bond distances. Apart from the structural analysis we have also calculated the complexation energies corresponding to the formation of various complexes considered here, and reported in Table 3.1. From the reported values it is evident that the gas phase complexation energies are not able provide the expected selectivity trends. Similar situation was found for other Am³⁺ complexes reported previously.^{60,81}

Table 3.1 Calculated M-L bond distances (Å) and complexation energies (eV) in gas (ΔE_g) and solvent (ΔE_s) phases for Am³⁺ and Eu³⁺ complexes using BP86/def-SV(P) method

Complexes	M-N	M-O/M-S	ΔE_g	ΔE_s
[Am-(PDAM) ₂] ³⁺	2.605	2.408	-29.64	40.10
[Eu-(PDAM) ₂] ³⁺	2.612	2.402	-30.33	29.84
[Am-(THIOAM) ₂] ³⁺	2.621	2.826	-28.26	41.46
[Eu-(THIOAM) ₂] ³⁺	2.635	2.859	-29.09	31.06
[Am-(PDAM-Isobutyl) ₂] ³⁺	2.604	2.371	-28.97	41.27
[Eu-(PDAM-Isobutyl) ₂] ³⁺	2.603	2.363	-29.91	30.75
[Am-(PDAM-Decyl) ₂] ³⁺	2.615	2.409	-30.32	40.13
[Eu-(PDAM-Decyl) ₂] ³⁺	2.681	2.449	-31.46	29.76
[Am-(PDAM) ₂ (NO ₃) ₂] ²⁺	2.648	2.527	-38.98	35.90
[Eu-(PDAM) ₂ (NO ₃) ₂] ²⁺	2.677	2.520	-39.72	25.60
[Am-(PDAM)(NO ₃) ₃]	2.657	2.496	-48.38	33.51

[Eu-(PDAM)(NO ₃) ₃]	2.713	2.537	-48.96	23.33
[Am-PHEN] ³⁺	2.440	---		
[Eu-PHEN] ³⁺	2.500	---		

However, incorporating the effect of solvent within the continuum solvation model does show the selectivity of the Am³⁺ ion with the amides considered in the present work, which is also in agreement with the earlier works.^{60,81} In addition to the complexation energy values, we have also performed energy decomposition analysis using ADF program. Various energy components obtained after performing the energy decomposition analysis are given in Table 3.2. It is important to note that both repulsive Pauli and attractive electrostatic components are responsible for the overall Coulomb interaction. Therefore, it is interesting to combine these two components and compare the variation of this resulting component (steric component) for [M-PDAM]³⁺ and [M-THIOAM]³⁺ complexes.

Table 3.2 Calculated M-L bond distances (Å) and complexation energies (eV) in gas (ΔE_g) and solvent (ΔE_s) phases for Am³⁺ and Eu³⁺ complexes using BP86/def-SV(P) method

Complex Name	% electrostatic interaction	% steric interaction	% orbital interaction
[Am-PDAM] ³⁺	77.40	36.87	63.12
[Eu-PDAM] ³⁺	70.05	39.05	63.95
[Am-THIOAM] ³⁺	65.84	23.00	76.99
[Eu-THIOAM] ³⁺	65.97	30.02	69.97

From Table 3.2 it is evident that the steric interaction, which is electrostatic in nature, is minimum for the [Am-THIOAM]³⁺ complex. On the other hand for [Eu-

PDAM]³⁺ complex, its contribution is maximum. For the complexes with THIOAM ligand percentage of electrostatic contribution is almost the same for both the Am³⁺ and Eu³⁺ complexes, while [Am-PDAM]³⁺ is associated with much higher percentage of electrostatic interaction as compared to [Eu-PDAM]³⁺. Orbital interaction components are considerably higher for complexes with THIOAM ligand as compared to the PDAM ligand. The percentage of orbital contribution is almost the same for the [Am-PDAM]³⁺ and [Eu-PDAM]³⁺ complexes, however [Am-THIOAM]³⁺ complex is having reasonably higher percentage of orbital contribution as compared to the corresponding Eu³⁺ complex. Therefore, it is clear that the higher percentage of the electrostatic interaction is responsible for the selectivity of the Am³⁺ ion with the amide ligands whereas, selectivity of Am³⁺ ion with the thio-amide ligand is mainly dominated by higher percentage of orbital interaction.

Calculation of charges on the metal centre is another important exercise for obtaining an insight into the nature of M-L bonding in a metal complex. For this purpose we have reported the calculated partial atomic charges in Table 3.3, as obtained using natural population analysis (NPA) scheme.

Table 3.3 Calculated atomic charges on metal and donor centers of Am³⁺ and Eu³⁺ complexes using BP86/def-SV(P) method

Complexes	q _M	q _{O/S}	q _N
[Am-(PDAM) ₂] ³⁺	1.734	-0.659	-0.522
[Eu-(PDAM) ₂] ³⁺	1.659	-0.649	-0.507
[Am-(THIOAM) ₂] ³⁺	0.936	-0.002	-0.506
[Eu-(THIOAM) ₂] ³⁺	0.964	-0.005	-0.497
[Am-(PDAM-Isobutyl) ₂] ³⁺	1.693	-0.680	-0.518

[Eu-(PDAM-Isobutyl) ₂] ³⁺	1.619	-0.666	-0.508
[Am-(PDAM-Decyl) ₂] ³⁺	1.669	-0.674	-0.516
[Eu-(PDAM-Decyl) ₂] ³⁺	1.573	-0.672	-0.499
[Am-(PDAM) ₂ (NO ₃) ₂] ²⁺	1.492	-0.613	-0.471
[Eu-(PDAM) ₂ (NO ₃) ₂] ²⁺	1.428	-0.615	-0.468
[Am-(PDAM)(NO ₃) ₃]	1.463	-0.590	-0.457
[Eu-(PDAM)(NO ₃) ₃]	1.380	-0.577	-0.435

The partial atomic charge on the Am center is found to be always higher than that on the Eu atom in all the complexes with amide derivatives considered here whereas for the complexes with thio-amide ligand, charge on the Am center is found to be less as compared to the Eu centre. It clearly indicates that electrostatic interaction is rather higher in Am³⁺ complexes as compared to the corresponding Eu³⁺ complexes with amide ligands, which is also consistent with the results obtained from the energy decomposition analysis.

In addition to the charge distribution analysis we have also calculated the bond critical point (BCP) properties corresponding to the metal-ligand bonds within the framework of quantum theory of atoms-in-molecule (AIM) approach.^{117,118} To understand the nature of a chemical bond, electron density based topological parameters, such as the electron density [ρ] and Laplacian of the electron density [$\nabla^2\rho$] obtained from AIM calculations have been shown to be highly successful.^{123,124} in rationalizing the complexation behavior of actinide and lanthanide ions. Thus we have calculated these parameters for the M-N and M-O/M-S bonds present in the [M-PDAM]³⁺ and [M-THIOAM]³⁺ complexes and the corresponding BCP values are reported in Table 3.4. The reported values in the Table suggest that the M-N and M-O/M-S bonds are mostly ionic in nature with a

positive value of the $\nabla^2\rho$ at the BCPs. It is noticeable that the absolute values of the ρ for the Am systems are consistently larger than the Eu analogues although the differences between the values are higher for the complexes with the amide ligands as compared to the thio-amide ligand. This suggests a better extraction capability of the PDAM than THIOAM. This supports the previously observed experimental results that the separation with the amide ligands should be better than the separation of the thio-amide ligand.¹¹⁶ The M-O bonds are found to be more ionic in nature as compared to the M-N, while, M-S bonds shows more covalent character as compared to the M-N bond.

Table 3.4 The calculated BCP properties (electron density [ρ], Laplacian of the electron density [$\nabla^2\rho$]) of the M-N and M-O/M-S bonds in Am^{3+} and Eu^{3+} complexes using BP86/TZ2P method

Bond	M-N		M-O/M-S	
	ρ ($e a_0^{-3}$)	$(-1/4)\nabla^2\rho$ ($e a_0^{-5}$)	ρ ($e a_0^{-3}$)	$(-1/4)\nabla^2\rho$ ($e a_0^{-5}$)
[Am-PDAM] ³⁺	0.0315	-0.0239	0.0461	-0.0410
[Eu-PDAM] ³⁺	0.0237	-0.0184	0.0340	-0.0337
[Am-THIOAM] ³⁺	0.0288	-0.0227	0.0309	-0.0119
[Eu-THIOAM] ³⁺	0.0241	-0.0186	0.0226	-0.0099
[Am-PHEN] ³⁺	0.0359	-0.0261	---	---
[Eu-PHEN] ³⁺	0.0270	-0.0192	---	---

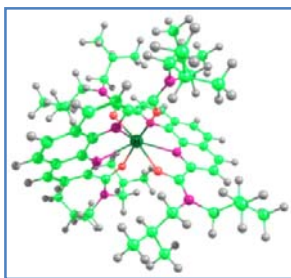
One of the most interesting points to be noted here is that the BCP ρ and $\nabla^2\rho$ values for the Am-O bonds are significantly higher as compared to that for the corresponding Eu-O bonds in the [M-PDAM]³⁺ complexes. It clearly indicates that the Am-O bond is stronger than the corresponding Eu-O bonds in the complexes

considered here. For the sake of comparison we have also calculated the ρ and $\nabla^2\rho$ for the M-N bonds in the $[\text{M-PHEN}]^{3+}$ complexes. The calculated BCP ρ and $\nabla^2\rho$ values for the M-N bonds are found to decrease from that in the $[\text{M-PHEN}]^{3+}$ complexes to that in the $[\text{M-PDAM}]^{3+}$ complexes, however, the extent of decrease is smaller in the case of Eu-N bond. This trend is also reflected in the calculated bond distances in the two sets of complexes, as reported in Table 3.1. All the trends obtained from the AIM analysis imply that the Am-O/N interactions are stronger as compared to the corresponding Eu-O/N interactions in the $[\text{M-PDAM}]^{3+}$ complexes, which in turn are responsible for the selectivity of the PDAM based ligands towards Am^{3+} ion. The calculated charge distribution values and the AIM properties are also found to be consistent with the data obtained from the energy decomposition analysis.

According to our theoretical analysis, the PDAM ligand is more efficient for An extraction, therefore, we have extended our calculation further to explore different derivatives of PDAM. Anticipating a lower solubility of the PDAM in the nonpolar extraction conditions because of the absence of large alkyl group, we have selected N,N-di-isobutyl (PDAM-Isobutyl, **6**) and N-decyl (PDAM-Decyl, **7**) derivatives (Scheme 3.1). These will also help to understand whether there is any effect of the bulkier alkyl groups on the complexation behaviour at the N centre. The optimized structures of the metal-ligand complexes with PDAM-Isobutyl and PDAM-Decyl are shown in Figure 3.3. From the calculated metal-ligand bond distances (M-O and M-N) it is clear that the difference in bond distances are negligible between the Am^{3+} and the Eu^{3+} complexes with PDAM-Isobutyl ligand. As discussed earlier, the differences between the Am-O/N and Eu-O/N bond distances are rather smaller in

the case of $[M-(PDAM)_2]^{3+}$ complexes, although Am-O/N bond distances are found to be always shorter. However, there is a considerable difference between the Am-O/N and Eu-O/N bond lengths in $[Am-(PDAM-Decyl)_2]^{3+}$ and $[Eu-(PDAM-Decyl)_2]^{3+}$ complexes though the size of the Am^{3+} ion (ionic radii = 0.975 Å) is slightly higher as compared to Eu^{3+} ion (ionic radii = 0.95 Å) for coordination number six.⁹⁶

a)



b)

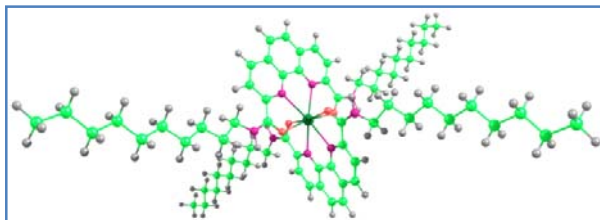


Fig. 3.3 Optimized structures of a) $[M-(PDAM-Isobutyl)_2]^{3+}$ and b) $[M-(PDAM-Decyl)_2]^{3+}$.

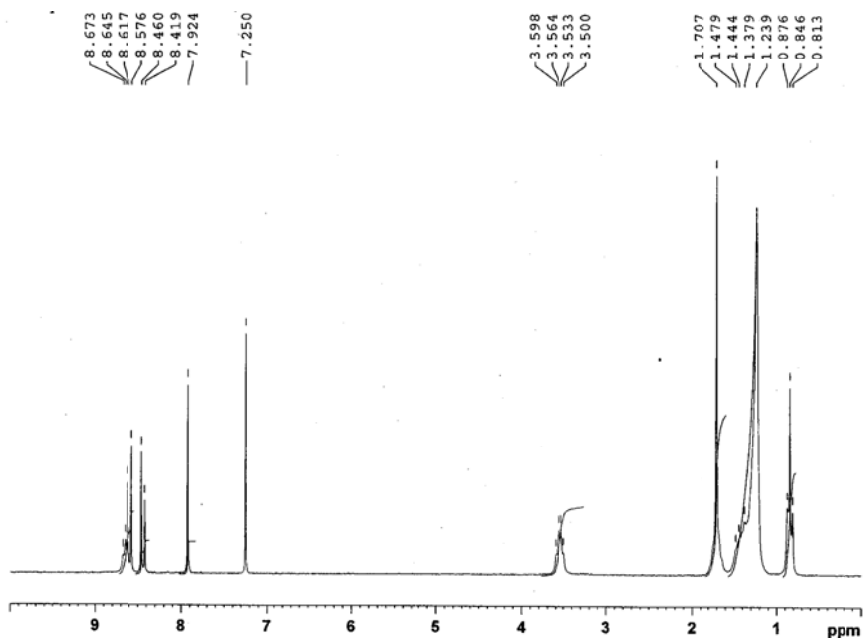
3.4.2 Experimental Results

3.4.2.1 Organic Synthesis

As PDAM (**3**), PDAM-Isobutyl (**6**) and PDAM-Decyl (**7**) ligands are promising for the Am^{3+}/Eu^{3+} selectivity; we have synthesized them to check their metal extraction ability. All the compounds have been synthesized starting from commercially available PDA (**2**) (Scheme 1). At first, PDA has been converted to **5** via the acid

catalyzed reaction with MeOH. Then the subsequent reaction of **5** with conc. NH₃ and NH₄Cl has furnished PDAM (Scheme 3.1). In another experiment, PDA has been reacted with excess thionyl chloride to furnish 1,10-phenanthroline-2,9-diacyl chloride which has been immediately reacted with diisobutylamine and decylamine separately to get **6** and **7**, respectively (Scheme 3.1). All the compounds have been purified by flash chromatography and unambiguously characterized by NMR spectroscopy, giving well-defined spectra. A typical example is depicted in Figure 3.4 giving a first order spectrum of **7** in which aromatic protons show two different types of signal. Protons of the central aromatic ring resonate as a singlet at 7.92 ppm (Figure 3.4a) whereas the other aromatic protons exhibit two doublets. CH (6 signals). The amide signal is found at 163.6 ppm (Figure 3.4b).

a)



b)

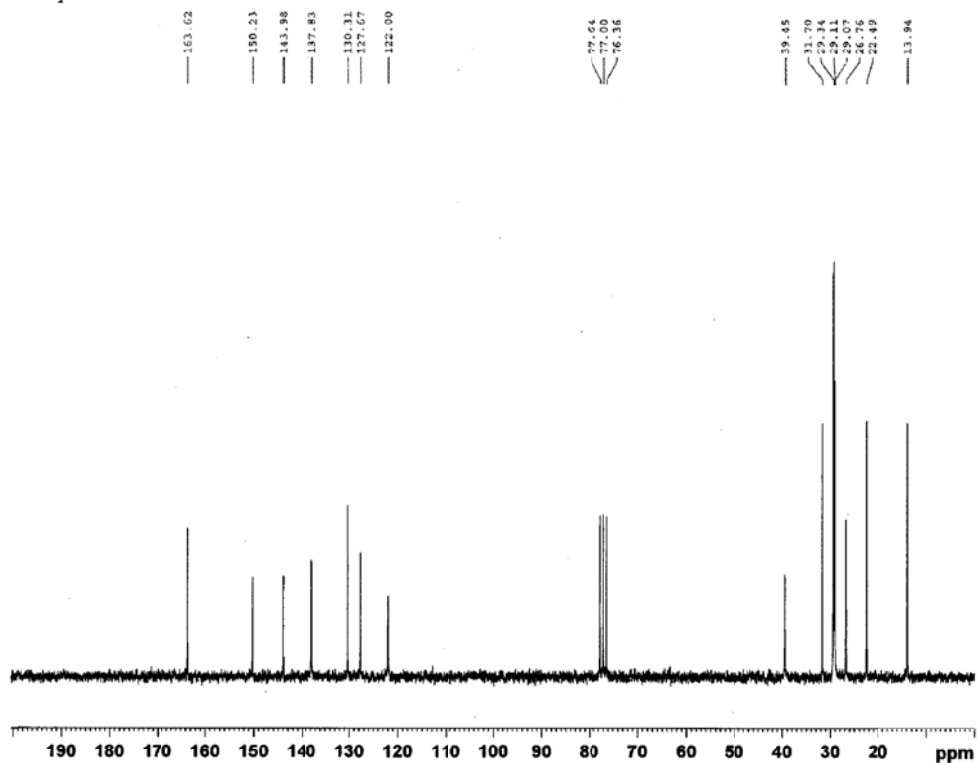


Fig. 3.4 a) ^1H NMR spectra of **7** in CDCl_3 at 25°C . b) ^{13}C NMR of **7** in CDCl_3 .

Diagnostic signals are provided by the N- CH_2 and N-H protons at 3.53 (q) and 8.65 (t) ppm, respectively. The terminal methyl groups of the alkyl chains resonate as a triplet at 0.85 ppm. Other alkyl protons are found as multiplets at 1.22-1.48 and 1.64-1.74 ppm with the expected 24 and 8 protons integration for each signal respectively. The carbon spectra present the expected 7 signals for the alkyl atoms, the N- CH_2 signal at 39.5 ppm and the expected aromatic

3.4.2.2 Results of Distribution Studies

The extraction studies of Am^{3+} and Eu^{3+} from 0.01M HNO_3 medium have been carried out using 2.7×10^{-3} M of the ligand **3** in a mixture of 1M 2-bromo-octanoic acid and n-dodecane. The results have not been promising since selectivity was found to be poor (separation factor (S.F.) = 7.4) (Table 3.5). Both the extraction and selectivity of Am^{3+} and Eu^{3+} have been found to be even poorer in case of the ligand **6**. Poor extractability of the ligand **6** is probably due to the presence of four bulky branched alkyl (isobutyl) groups adjacent to the two donor carbonyl 'O' atoms. The presence of 'O' donor synergist, viz. 2-bromo-octanoic acid is probably, responsible for such a poor selectivity. However, these ligands have been found to be rather insoluble in the organic phase in absence of 2-bromo-octanoic acid. Galletta et al.¹¹⁶ however, evaluated 2,9-dicarbonyl-1,10-phenanthroline derivatives along with the synergist, viz. Br-cosan in NPHE medium. Therefore more lipophilic ligand, **7** with only two straight chain alkyl (n-decyl) substitutions was synthesized and evaluated for the $\text{Am}^{3+}/\text{Eu}^{3+}$ separation study in a solvent mixture of n-dodecane and n-octanol in absence of any synergist from perchlorate medium. The extraction as well as selectivity for Am^{3+} over Eu^{3+} has been found to be enhanced with increasing the perchlorate ion concentration in the aqueous phase (Table 3.5). Significantly high selectivity (S.F. ~51) with the distribution ratio (D_{Am}) value of 10.3 has been achieved with this ligand when the extraction has been carried out from the perchlorate medium (Figure 3.5). It is to be noted that the separation factor is increased with decrease in pH. This observation is interesting since extraction of Am^{3+} ion is considered to be important from highly acidic conditions from the nuclear waste management point of view.

Table 3.5 Distribution and separation behavior of Am³⁺ and Eu³⁺ using PDAM, (PDAM-Isobutyl)₂ and (PDAM-Decyl)₂ ligands

Ligand	D _{Am}	D _{Eu}	S.F.
3 ^a	21.4	2.9	7.4
6 ^b	4.62	1.05	4.4
7 ^c	0.489	0.017	29.6
7 ^d	10.3	0.2	51

^aOrg.Phase: Ligand **3** (2.7×10^{-3} M) + 2Br-octanoic acid in n-dodecane; Aq. Phase: 0.01M HNO₃; ^bOrg.Phase: Ligand **6** (4.0×10^{-3} M) + 2Br-octanoic acid in n-dodecane; Aq. Phase: 0.01M HNO₃; ^cOrg.Phase: Ligand **7** (8.0×10^{-3} M) in n-dodecane/n-octanol (5:1); Aq. Phase: 0.1M HClO₄+1M LiClO₄; ^dOrg.Phase: Ligand **7** (8.0×10^{-3} M) in n-dodecane/n-octanol (5:1); Aq. Phase: 0.1M HClO₄+2M LiClO₄

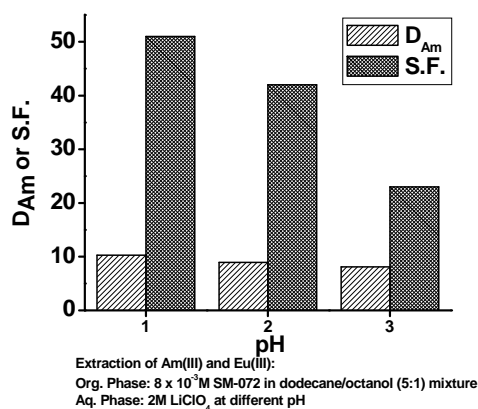


Fig. 3.5 Effect of pH on the distribution and separation behavior of Am³⁺ and Eu³⁺ using the (PDAM-Decyl)₂ ligand.

Very poor separation factor has been observed when this ligand has been used for the extraction of metal ions from the nitrate medium, which may be due to strong complexation of the nitrate ion with the water molecules in the aqueous medium. Therefore, more work is required to make these ligands actinide selective in the nitrate medium, through suitable modification.

3.5 Concluding Remarks

In a nutshell, in the present work, two valence isoelectronic metal ions, viz., Am(III) and Eu(III) have been considered to investigate the complex formation process with different amide based ligands, derived from 1,10-phenanthroline-2,9-dicarboxylic acid. For the comparison purpose we have also compared the complexation behavior of the 1,10-phenanthroline-2,9-dithio-carboxamide ligand with Am³⁺ and Eu³⁺ ions. It is quite unusual that the hard donor oxygen atoms bind strongly with the softer actinide metal ion as compared to harder lanthanide ion. In the earlier chapter,⁶⁰ we have rationalized these unusual features using Pearson's Hard-Soft-Acid-Base principle and the frontier orbital theory of chemical reactivity as proposed by Fukui. Stronger 'Am-N or Am-O/Am-S' bond as compared to 'Eu-N or Eu-O/Eu-S' bond has also been reflected in shorter bond lengths associated with the Am³⁺ complexes as compared to the corresponding Eu³⁺ complexes in spite of larger size of Am³⁺ ion. Larger charge on the Am centre, higher percentage of electrostatic interaction and higher values of BCP ρ and $\nabla^2\rho$ values indicate that the Am³⁺ complexes with amide based ligands are more ionic in nature as compared to the corresponding Eu³⁺ complexes, and this larger electrostatic interaction is responsible for the selectivity of the Am³⁺ ion with the amide ligands. On the other hand, selectivity of Am³⁺ ion with the thio-amide ligand is mainly dominated by higher covalency.

Due to the solubility problem of the PDAM ligand in the organic diluents, we have alkylated the amide groups of PDAM through which its solubility in organic medium has been enhanced. Therefore, three amide ligands viz, PDAM (**3**), PDAM-Isobutyl (**6**) and PDAM-Decyl (**7**) have been synthesized. Subsequently, the extraction efficiency of these ligands have been investigated using solvent

extraction technique and it has been found that all the alkyl derivatives of PDAM ligand are Am^{3+} selective. A maximum extraction efficiency and separation of Am^{3+} over Eu^{3+} has been observed experimentally using the ligand PDAM-Decyl as compared to the other ligands investigated here. All the experimental results reported here on the selectivity of hard donor containing ligands towards Am^{3+} ion confirm our theoretical predictions.

Chapter 4: Theoretical Investigation of Am³⁺/Eu³⁺ Complexes with Cyanex Ligands

4.1 Introduction

4.1.1 Cyanex: A Widely Studied Ligand for Actinide Separation

Cyanex ligands are commonly used sulfur donor extractants for actinide lanthanide separation. Except Cyanex the other commonly known ligands for actinide lanthanide separation show a maximum separation factor of ~100. In 1996 Zhu et. al. have reported a separation factor of ~5900 with sulfur donor Cyanex301 ligand.¹⁶ Subsequently, numerous investigations^{81,94,98,103,125-131} have been carried out using Cyanex ligands.

4.1.2 Previous Theoretical Studies and our Motivations

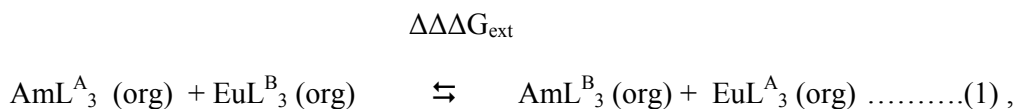
Due to enormous developments in the computational field, in recent years various groups are involved in theoretical investigations of lanthanide and actinide complexes. In spite of extensive studies, origin of selectivity of a Cyanex ligand towards trivalent actinides is still not very clear.^{81,94} Jensen et. al.¹⁰³ emphasized a stronger covalency in An-L bonds to explain the selectivity of Cyanex301 towards actinides, although no structural differences were found in XAFS experiment. In a recent computational study involving complexation of actinide and lanthanide ions with Terpy and Me-BTP ligands, it has been reported by Guillaumont that An-L bond distances are shorter as compared to Ln-L bond distances, which clearly indicates the presence of higher amount of covalency in An-L bonds.¹³² It is consistent with the opinion expressed by Nash that the origin of ligand selectivity is due to greater covalent nature of An-L

bonds.¹³³ However, in one of the recent reports it has been computationally demonstrated⁹⁴ that the effect of solvation is of prime importance in rationalizing the experimentally observed selectivity of Am³⁺ ion in presence of Eu³⁺ ion with Cyanex301 ligand. On the other hand, in one of the recent works, it has been found that the calculated bond distances are shorter for Am-S bonds as compared to the corresponding Eu-S bonds in the complexes using modified Cyanex301 ligand.⁸¹ In this report the bis(2,4,4-trimethylpentyl) groups in each Cyanex ligand was replaced with dimethyl groups to reduce the computational cost. Therefore, it is not very clear whether the presence of bulkier bis(2,4,4-trimethylpentyl) groups have any effect on the calculated metal-ligand bond distances due to steric crowding or inductive effects. Also, it may be noted that Cao et. al.⁹⁴ have used f-in-core basis^{90,134-136} sets for the lanthanide and the actinide atoms in their calculations. Consequently, it is not possible to consider the spin-multiplicity of the complexes, although it is known that trivalent actinide and lanthanide complexes generally exist in high spin state with unpaired f electrons.⁵⁶

Therefore, in the present work¹³⁷ we have used small core pseudo potentials in conjunction with f-in-valence basis sets for actinides and lanthanides. Also, we have considered the entire Cyanex ligand instead of the smaller size modified Cyanex ligand used in one of the earlier works.⁸¹ Moreover, for the first time we have considered three different phosphinate ligands, viz., Cyanex301, Cyanex302, and Cyanex272 with donor atoms as sulfur, sulfur and oxygen, and oxygen, respectively. To the best of our knowledge, there is no theoretical report on the complexation of Eu³⁺ and Am³⁺ ions with Cyanex272 and Cyanex302 ligands. The computational cost involved to investigate the actinide and lanthanide complexes with Cyanex ligands

(inclusive of all atoms) using small-core pseudopotential along with def-SV(P) or TZVP basis sets without any symmetry constraint is rather challenging. Moreover, we have used various functionals to assess their performance in predicting the metal-ligand bond distances and other quantities. We have also optimized¹³⁷ the geometries of all the complexes in presence of solvent using COSMO approach. Partial atomic charges have been calculated for all the complexes using natural population analysis (NPA).

Recently it has been conjectured¹³⁸ that free energy of extraction ($\Delta\Delta\Delta G_{\text{ext}}$) is one of the important factors in deciding the selectivity of Am^{3+} over Eu^{3+} in presence of dithiophosphinic acid based S donor ligands, where $\Delta\Delta\Delta G_{\text{ext}}$ was calculated according to the following equation:



where Am^{3+} is selective with the ligand L^{B} . The quantity, $\Delta\Delta\Delta G_{\text{ext}}$ can also be calculated by considering the free energy changes for the various steps involved in the complexation process, where it is possible to take into account the solvation effects with different approaches. It has also been emphasized that the quantity $\Delta\Delta\Delta G_{\text{ext}}$ is independent on the method of solvation used or any environmental effect. The quantity, $\Delta\Delta\Delta G_{\text{ext}}$ seems to be quite appealing since it does not involve most of the uncertainties in determining the free energy of extraction. Therefore, to assess the predictive ability of $\Delta\Delta\Delta G_{\text{ext}}$, detail thermodynamic analysis has been performed in this work through calculation of this quantity for various possible complexes of Am^{3+} and Eu^{3+} with three Cyanex ligands, which are structurally similar but differ in the donor centres (S or O).

4.2 Computational Details

Computational methodologies used are almost the same as mentioned before in Chapter 2, section 2.3. To investigate the effect of basis set, in addition to def-SV(P) here we have also used TZVP basis sets in Turbomole program. The total number of cartesian basis functions generated using TZVP basis sets are 1898 for Eu(Cyanex301)₃ complex. In addition to BP86, here we have also used PBE,⁴⁰ BLYP^{36,39} and PW91¹³⁹ functionals for the geometry optimization of all the complexes. In addition to COSMO⁹³ approach we have also considered explicit solvent molecules and counter ions for the calculation of free energy values for the various steps involved in the extraction processes.

4.3 Results and Discussions

The Cyanex ligands are bidentate and chelating in nature while coordinating with a metal ion. Both the coordinating sites are same for the Cyanex301 and Cyanex272, viz, S and O atoms, respectively. On the other hand, O and S atoms act as donors in Cyanex302 ligand. In the recent past Jensen and Bond¹⁰³ reported that trivalent f-elements form M(Cyanex301)₃ complex as deduced from EXAFS and absorption spectroscopy. In one recent paper it has been demonstrated⁸¹ that Am³⁺ and Eu³⁺ ions form mainly ML₃ type complexes with Cyanex301 ligand through distribution studies at various concentration of the ligand. Moreover, in a very recent study, Keith and Batista considered¹³⁸ ML₃ type complexes while investigating the complexation of Am³⁺ and Eu³⁺ ions with dithiophosphinic acid based ligands. Consequently, here we have considered only ML₃ type of complexes. Results of theoretical calculations are discussed below.

4.3.1 Structural Details of the Metal-Cyanex complexes

As mentioned earlier, the structures of all the complexes have been optimized in both gas and solvent phases using Turbomole program package. The vibrational frequencies are calculated to be almost real for all the complexes (in few cases small imaginary frequencies ($5\text{-}10\text{ cm}^{-1}$) are observed). The optimized structures of bare ligands and metal-ligand complexes, $[\text{ML}_3]$ are depicted in Figure 4.1.

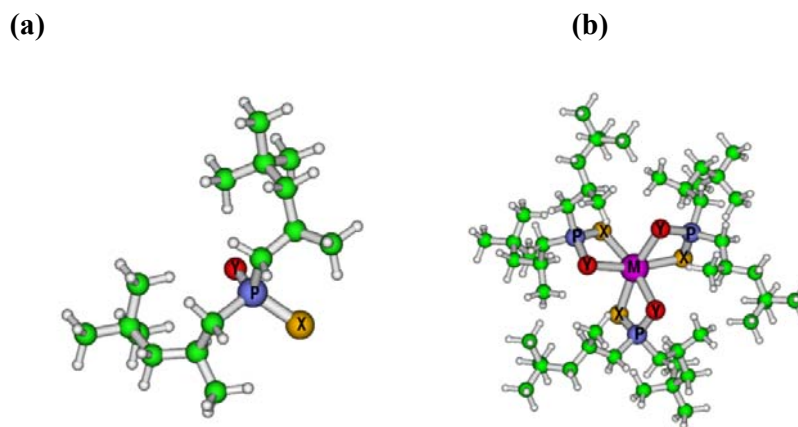


Figure 4.1 Optimized structures of metal-Cyanex complex.

The structures of all the metal complexes are almost similar irrespective of the metal ions or ligands used. All the metal-ligand bond distances calculated using Turbomole and ADF programs have been reported in Tables 4.1 and 4.2.

Table 4.1 Calculated M-L bond distances (in Å) in gas and solvent phases for Am³⁺ and Eu³⁺ complexes with Cyanex301, Cyanex302 and Cyanex272 using BP86/def-SV(P) and BP86/TZVP methods and Turbomole program

Complex	Gas Phase		Solvent Phase
	d _(M-S) / d _(M-O)	d _(M-S) (Literature Value)	d _(M-S) / d _(M-O)
Am-(Cyanex301)₃	2.846 (2.841) ^a	(2.918, 2.900) ^b [2.829] ^c	2.847 (2.843) ^a
Eu-(Cyanex301)₃	2.887 (2.871) ^a	(2.863, 2.841) ^b [2.860] ^c	2.878 (2.872) ^a
Cm-(Cyanex301)₃	2.837	(2.900, 2.883) ^b 2.826 ± 0.008 ^d	2.836
Am-(Cyanex302)₃	2.935 / 2.329		2.935 / 2.328 (2.924 / 2.338) ^a
Eu-(Cyanex302)₃	2.968 / 2.326		2.967 / 2.326 (2.958 / 2.335) ^a
Am -(Cyanex272)₃	2.400		2.401 (2.407) ^a
Eu -(Cyanex272)₃	2.385		2.383 (2.392) ^a

^aCalculated bond distances with TZVP basis sets are given within parenthesis.

^bBond distance values reported by Dolg and co-workers⁹⁴ using f-in-core basis for lanthanides and actinides and def-SV(P), def2-TZVP basis sets for other elements

^cCalculated bond distances reported by Bhattacharyya et. al.⁸¹ using modified Cyanex301 ligand and def-SV(P) basis are given within square bracket.

^dExperimentally observed Cm-S bond distance as reported by Jensen et. al.¹⁰³

Table 4.2 Calculated M-L bond distances (in Å) in gas phase for Am³⁺ and Eu³⁺ complexes with Cyanex301, Cyanex302 and Cyanex272 using different GGA functionals in ADF program

Complex	d _(M-S) / d _(M-O)			
	(BP86)	(PW91)	(BLYP)	(PBE)
Am-(Cyanex301)₃	2.853	2.842	2.893 (2.895) ^a	2.846
Eu-(Cyanex301)₃	2.871	2.856	2.922 (2.929) ^a	2.863
Am-(Cyanex302)₃	2.929 / 2.347	2.909 / 2.352	2.987 / 2.372 (2.989 / 2.349) ^a	2.894 / 2.346
Eu-(Cyanex302)₃	2.949 / 2.343	2.933 / 2.345	3.006 / 2.368 (3.015 / 2.348) ^a	2.913 / 2.350
Am-(Cyanex272)₃	2.406	2.402	2.433 (2.425) ^a	2.405
Eu-(Cyanex272)₃	2.396	2.392	2.422 (2.405) ^a	2.395

^aCalculated bond distances in solvent phase using BLYP functional and Turbomole program are given within parenthesis.

For the sake of comparison, some of the recently reported literature values are also included in Table 4.1. From the calculated values it is clear that the M-S bond distances in Am-(Cyanex301)₃ are smaller as compared to the same in the corresponding Eu³⁺ complex, although the size of the Am³⁺ ion (ionic radii=0.975 Å) is slightly higher as compared to that of the Eu³⁺ ion (ionic radii=0.95 Å).⁹⁶ It may be due to the preference of Am³⁺ ion to bind with soft donor ligands. Experimentally observed separation factor (SF_{Am/Eu}) of ~5900 by Zhu et. al.⁹⁷ is consistent with the calculated bond distance values. The presently calculated metal-ligand bond distances are also in complete agreement with one of the recently published combined experimental and theoretical reports,⁸¹ where dimethyl dithiophosphinic acid ligand has been used in place of Cyanex301 for the calculations, although all the bond

distance values are slightly smaller. This is because of the replacement of the bulkier bis(2,4,4-trimethylpentyl) with the smaller methyl group so that the steric crowding becomes less with the latter ligand, which in turn reduces the M-L bond distances. It is interesting to note that in the recently reported¹⁴⁰ $M[N(EPH_2)_2]_3$ (M=Eu and Am, and E=O/S/Se/Te) complexes ‘Am-S’ (2.835 Å) bond length is shorter than the ‘Eu-S’ (2.873 Å) bond length whereas ‘Am-O’ bond distance (2.358 Å) is larger than the ‘Eu-O’ bond distance (2.335 Å) indicating a higher covalence in the ‘Am-S’ bond as compared to that in the ‘Eu-S’ bond. In that report the authors also observed that the difference between the ‘Eu-S’ and the ‘Am-S’ bond length increases from 0.038 Å to 0.051 Å as the donor atom was changed from ‘S’ to ‘Te’, indicating enhancement in selectivity for Am^{3+} over Eu^{3+} . This observation is in agreement with the trends observed in the present work involving metal-Cyanex complexes.

Since experimental value of Cm-S bond distance is available in the literature, we have been motivated to calculate the structure of Cm-(Cyanex301)₃ using Turbomole for the purpose of comparison. It is interesting to notice that the experimentally observed Cm-S bond distance value of 2.826 ± 0.008 ¹⁰³ in Cm-(Cyanex301)₃ complex is closer to our theoretically obtained bond distance value of 2.837 Å.

In the case of Cyanex272 as the complexing agent, Am-O bond distances are slightly longer than the Eu-O bond distances. Naturally, Cyanex272 is not expected to bind Am^{3+} ion preferentially as compared to the Eu^{3+} ion. In fact, experimentally observed separation factor, $SF_{Am/Eu}$ has been found to be 0.08¹⁴¹ with Cyanex272 by Zhu et. al. It clearly indicates that the extraction of Eu^{3+} ion is slightly preferable with Cyanex272 ligand. Thus, variations in the calculated M-L bond distance trends can be

correlated nicely with the experimentally observed results. Cyanex302, possesses one 'S' and one 'O' donor site, and expected to show intermediate behavior between Cyanex301 and Cyanex272. From Table 4.1 it is clear that Am-S bond distances are shorter than the corresponding Eu-S bond distances, however, Am-O bond distances are slightly longer as compared to the Eu-O bond distances in case of $M(\text{Cyanex302})_3$ complexes. Stronger 'Eu-O bond as compared to 'Am-O' bond makes this ligand less selective for Am^{3+} over Eu^{3+} as compared to Cyanex301. However, to the best of our knowledge there is no experimental or theoretical report available on the Cyanex302 complexes with Am^{3+} and Eu^{3+} ions to establish this view.

The trends in the calculated bond distances using ADF program have also been found to be the same as found using Turbomole. All the M-L bond distances calculated by replacing the bulkier bis(2,4,4-trimethylpentyl) groups present in Cyanex ligands with the dimethyl groups as reported⁸¹ earlier have been found to be shorter as compared to the present ones obtained from ADF. The effect on the calculated bond distances using different GGA functionals (BP86, PW91, BLYP and PBE) has been reported in Table 4.2. Since GGA functionals are found to be more reliable in predicting the bond distance values,^{142,143} we have investigated only the effect of GGA functionals here. It is important to note that the results obtained using different functionals have been found to be mutually consistent.

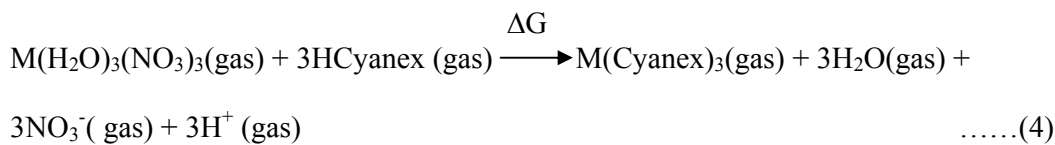
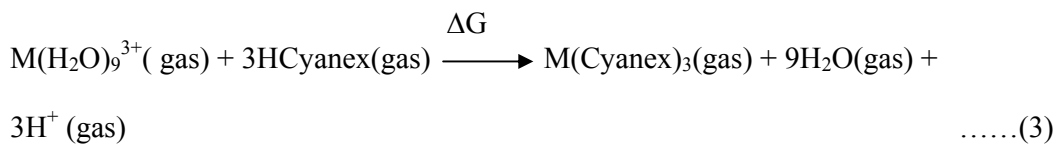
In the presence of solvent, the M-L bond distances for all these complexes virtually remain the same as in the gas phase results (Table 4.1). From the calculated values reported in Table 4.1 it is evident that the bond distances for all the complexes are quite close for two different basis sets, viz., def-SV(P) and TZVP. Moreover, the calculated bond distance values of 2.827, 2.869 and 2.816 Å for Am-S, Eu-S and Cm-

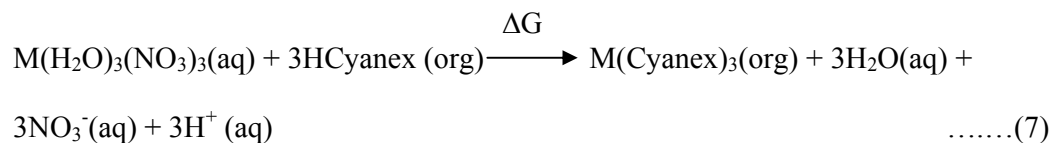
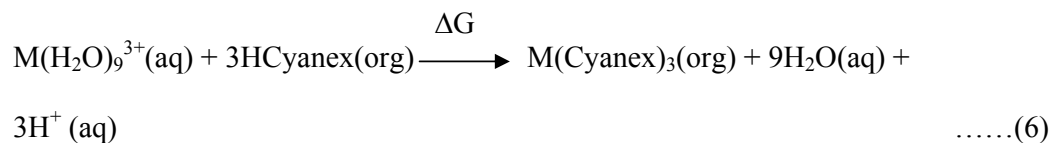
S bonds, respectively, with the hybrid PBE0 functional¹⁴⁴ are found to be very close to the corresponding BP86 values as obtained using Turbomole.

4.3.2 Thermodynamics of Extraction

In the spirit of very recent work reported by Keith and Batista¹³⁸ we have analyzed the complexation process through calculations of changes in free energies (ΔG) for various steps involved in the complexation of Am^{3+} and Eu^{3+} ions with Cyanex301, Cyanex302 and Cyanex272, and presented the results in Table 4.3. The Gibbs free energies of all the species (except H^+ ion) have been calculated from their respective total electronic energies, zero-point energies and thermal corrections by using the ideal gas model with temperature =298.15 K and pressure=0.1 MPa. The free energy of the proton in the gas phase ($\Delta G_{\text{gas}}[\text{H}^+]=-6.28$ kcal/mol) and aqueous phase ($\Delta G_{\text{sol}}[\text{H}^+]=-264.0$ kcal/mol) has been taken from the literature.¹³⁸

We have adopted three approaches for the calculations of ΔG in solution, viz., method-1, method-2 and method-3 corresponding to Equations (2), (3), (4) and (5), (6), (7) in gas and solvent -phase, respectively.





(M=Am and Eu)

Bare metal ion in the gas and aqueous phases has been considered in method-1. In method-2 explicit solvent molecules (9 water molecules) are considered to treat the M^{3+} ions, i.e., M^{3+} is replaced with $M(H_2O)_9^{3+}$. In addition to explicit solvent molecules, COSMO approach has also been taken into account for the solution phase calculations. The effect of counter ion has been taken care of by incorporating NO_3^- ion in case of method-3. In the gas phase, ΔG values are calculated to be negative (< 0) for method-1, while for the other two methods ΔG values are found to be positive. This is due to the requirement of extra energy to remove the explicit water molecules and nitrate ions from the inner sphere coordination of metal ion in method-2 and method-3 as compared to the method-1, both in gas and solvent phases. For all the three methods calculated gas phase values of $\Delta\Delta G^{Am/Eu}$ are positive, which indicate that Eu^{3+} forms a stronger complex than Am^{3+} with all the three ligands (Table 4.3). (Here the quantity, $\Delta\Delta G^{Am/Eu}$ refers to the difference in the free energy of complexation between the Am^{3+} and Eu^{3+} complexes, and also represented as $\Delta G[Am] - \Delta G[Eu]$).

Table 4.3 Calculated values of free energy of extraction (in eV) in Gas (ΔG_{gas}) and solvent (ΔG_{sol}) (T=298.15 K, P=1 atm) phases for Am^{3+} , Eu^{3+} complexes with Cyanex301, Cyanex302 and Cyanex272 using Turbomole program ^a

Complexes	ΔG_{gas}^1	$\Delta\Delta G_{\text{gas}}^1$	$\Delta\Delta\Delta G_{\text{gas}}^1$	ΔG_{gas}^2	$\Delta\Delta G_{\text{gas}}^2$	$\Delta\Delta\Delta G_{\text{gas}}^2$	ΔG_{gas}^3	$\Delta\Delta G_{\text{gas}}^3$	$\Delta\Delta\Delta G_{\text{gas}}^3$
Am-(Cyanex301)₃	-1.952	0.844	0.005	23.248	0.277	0.005	44.169	0.061	0.005
Eu-(Cyanex301)₃	-2.796			22.971			44.108		
Am-(Cyanex302)₃	-2.151	0.856		23.050	0.289		43.970	0.073	
Eu-(Cyanex302)₃	-3.007			22.761			43.897		
Am-(Cyanex272)₃	-2.290	0.839		22.911	0.272		43.831	0.056	
Eu-(Cyanex272)₃	-3.129			22.639			43.775		

Complexes	ΔG_{sol}^1	$\Delta\Delta G_{\text{sol}}^1$	$\Delta\Delta\Delta G_{\text{sol}}^1$	ΔG_{sol}^2	$\Delta\Delta G_{\text{sol}}^2$	$\Delta\Delta\Delta G_{\text{sol}}^2$	ΔG_{sol}^3	$\Delta\Delta G_{\text{sol}}^3$	$\Delta\Delta\Delta G_{\text{sol}}^3$
Am-(Cyanex301)₃	-4.215	-3.017	0.044	3.232	0.232	0.044	2.331	0.083	0.044
Eu-(Cyanex301)₃	-1.198			3.000			2.248		
Am-(Cyanex302)₃	-4.373	-3.014		3.074	0.234		2.173	0.085	
Eu-(Cyanex302)₃	-1.359			2.840			2.088		
Am-(Cyanex272)₃	-4.460	-3.061		2.987	0.188		2.086	0.039	
Eu-(Cyanex272)₃	-1.399			2.799			2.047		

^aEquations (2)-(7) are used to calculate the ΔG values.

¹, ² and ³ refer to the method-1, method-2 and method-3.

$$\Delta\Delta G = \Delta G [\text{Am}] - \Delta G [\text{Eu}]; \Delta\Delta\Delta G_{\text{ext}} = \Delta\Delta G [\text{Cyanex301}] - \Delta\Delta G [\text{Cyanex272}]$$

In contrast to the experimental observations, the calculated trends found in the present work are similar to the earlier results reported by Dolg and co-workers⁹⁴ and also by Keith and Batista.¹³⁸ In the solution phase the ΔG values (< 0) calculated using method-1 for the $\text{Am}-(\text{Cyanex301})_3$ and $\text{Eu}-(\text{Cyanex301})_3$ complexes correctly predict the experimentally observed higher selectivity for Am^{3+} with Cyanex301 ligand. This trend is also consistent with the work reported by Dolg and co-workers⁹⁴ as well as Keith and Batista.¹³⁸ The reason was suggested as the high dehydration energy requirement for Eu^{3+} complexation as compared to that of Am^{3+} due to smaller ionic

radius of Eu^{3+} , and ligand has no role in controlling the selectivity. Therefore, the calculated ΔG values obtained using method-1 always favour Am^{3+} complex to be more stable as compared to the Eu^{3+} complex for the other two ligands, viz., Cyanex302 and Cyanex272 as well, which is in contrary to the experimental observations. The trends in the calculated free energy of complexation values using other two methods in solution phase are found to be similar to the gas phase results. Methods 2 and 3 show more selectivity for Eu^{3+} over Am^{3+} irrespective of the ligand and thus cannot explain the experimentally observed trends.

In view of very recent work¹³⁸ on the complexation of two metal ions in presence of two ligands, we have calculated the free energy of extraction, $\Delta\Delta\Delta G_{\text{ext}}^{\text{Am/Eu}}$ for Am^{3+} and Eu^{3+} ions in presence of Cyanex301 and Cyanex272 ligands ($\Delta\Delta\Delta G_{\text{ext}}^{\text{Am/Eu}} = \Delta\Delta G^{\text{Am/Eu}} [\text{Cyanex301}] - \Delta\Delta G^{\text{Am/Eu}} [\text{Cyanex272}]$) using Equation (1). The positive values of $\Delta\Delta\Delta G_{\text{ext}}^{\text{Am/Eu}}$ reported in Table 4.3 clearly indicate that extraction of Eu^{3+} is more favourable with Cyanex301 ligand. Similar argument holds good for the Cyanex301 and Cyanex302 ligand pair. We have also performed similar thermodynamic analysis with BLYP functional, as the differences in bond length values are maximum between this functional and the BP86 functional, and results are reported in the Table 4.4. Indeed, the calculated trends remain the same in both the cases. In addition to the effect of exchange-correlation functionals, we have also investigated the effect of TZVP basis sets on the calculated thermodynamic parameters and reported in Table 4.5. It is clear that most of the earlier trends obtained using def-SV(P) basis sets remain the same. However, the complexes with Cyanex301 become more stable as compared to the Cyanex272 complexes (Table 4.5) for both the metal ions as far as ΔG values are concerned.

Table 4.4 Calculated values of free energy of extraction (in eV) in solvent (ΔG_{sol}) (T=298.15 K, P=1 atm) phases for Am^{3+} , Eu^{3+} complexes with Cyanex301, Cyanex302 and Cyanex272 using BLYP/def-SV(P) method in Turbomole Program ^a

Complexes	ΔG_{sol}^1	$\Delta\Delta G_{\text{sol}}^1$	$\Delta\Delta\Delta G_{\text{sol}}^1$	ΔG_{sol}^2	$\Delta\Delta G_{\text{sol}}^2$	$\Delta\Delta\Delta G_{\text{sol}}^2$	ΔG_{sol}^3	$\Delta\Delta G_{\text{sol}}^3$	$\Delta\Delta\Delta G_{\text{sol}}^3$
Am-(Cyanex301)₃	-3.607	-2.82	0.14	4.124	0.310	0.14	3.406	0.235	0.14
Eu-(Cyanex301)₃	-0.786			3.814			3.171		
Am-(Cyanex302)₃	-4.028	-2.90		3.703	0.224		2.984	0.148	
Eu-(Cyanex302)₃	-1.121			3.479			2.836		
Am-(Cyanex272)₃	-4.236	-2.96		3.495	0.168		2.777	0.093	
Eu-(Cyanex272)₃	-1.274			3.327			2.684		

^aEquations (5)-(7) are used to calculate the ΔG values

¹, ² and ³ refer to the method-1, method-2 and method-3.

$$\Delta\Delta G = \Delta G [\text{Am}] - \Delta G [\text{Eu}]; \Delta\Delta\Delta G_{\text{ext}} = \Delta\Delta G [\text{Cyanex301}] - \Delta\Delta G [\text{Cyanex272}]$$

Table 4.5 Calculated values of free energy of extraction (in eV) in solvent (ΔG_{sol}) (T=298.15 K, P=1 atm) phases for Am^{3+} , Eu^{3+} complexes with Cyanex301, Cyanex302 and Cyanex272 using BP86/TZVP method in Turbomole program ^a

Complexes	ΔG_{sol}^1	$\Delta\Delta G_{\text{sol}}^1$	$\Delta\Delta\Delta G_{\text{sol}}^1$	ΔG_{sol}^2	$\Delta\Delta G_{\text{sol}}^2$	$\Delta\Delta\Delta G_{\text{sol}}^2$	ΔG_{sol}^3	$\Delta\Delta G_{\text{sol}}^3$	$\Delta\Delta\Delta G_{\text{sol}}^3$
Am-(Cyanex301)₃	-3.196	-2.945	0.053	1.110	0.162	0.053	0.606	0.071	0.053
Eu-(Cyanex301)₃	-0.251			0.948			0.535		
Am-(Cyanex302)₃	-2.832	-2.955		1.474	0.152		0.970	0.061	
Eu-(Cyanex302)₃	0.123			1.322			0.909		
Am-(Cyanex272)₃	-2.755	-2.998		1.551	0.109		1.047	0.018	
Eu-(Cyanex272)₃	0.243			1.442			1.029		

^aEquations (5)-(7) are used to calculate the ΔG values.

¹, ² and ³ refer to the method-1, method-2 and method-3.

$$\Delta\Delta G = \Delta G [\text{Am}] - \Delta G [\text{Eu}]; \Delta\Delta\Delta G_{\text{ext}} = \Delta\Delta G [\text{Cyanex301}] - \Delta\Delta G [\text{Cyanex272}]$$

Therefore, the calculated $\Delta\Delta\Delta G_{\text{ext}}^{\text{Am/Eu}}$ values cannot rationalize the experimentally observed high selectivity of Cyanex301 ligand towards Am^{3+} ion. Now, it would be

interesting to perform a comparative analysis between the results as reported by Keith and Batista¹³⁸ with the present ones. In their work, solvation Method C (which is equivalent to method-1 in the present manuscript) fails to predict a higher selectivity of the ligand L^1 towards Eu^{3+} ion in presence of Am^{3+} ion. Moreover, ΔG (complexation) values for Am^{3+} is always higher for both L^1 and L^2 ligands as predicted by COSMO based Methods C and D, which are considered to be more sophisticated as compared to the PCM based Methods A and B. Thus, the selectivity of Am^{3+} is always higher for any of the two ligands considered by Keith and Batista if one considers only the ΔG (complexation) values. This result is similar to the trend obtained in the present work and also by Dolg and co-workers, who have considered only the Cyanex301 ligand. Hence, it is clear that even if the level of sophistication of a solvation method is improved, predictive ability of a continuum solvation based approach may not necessarily be better as far as agreement with experimentally observed selectivity trends involving valence isoelectronic trivalent lanthanide and actinide are concerned. Unlike the results of Keith and Batista, thermodynamic analyses performed on the present systems do not agree with the observed selectivity trends as far as the calculated $\Delta\Delta\Delta G_{\text{ext}}$ values are concerned. Thus, the scope of the approach put forward by them is rather limited to certain class of systems. In their work, ligands are considered with same donor atoms, viz., sulfur donors. On the other hand, in the present work we are concerned with ligands where donor atoms are different (oxygen and sulfur) and that may be the reason for the failure of the $\Delta\Delta\Delta G_{\text{ext}}$ term in explaining the selectivity trends. It is important to note that in the present work we obtained $\Delta\Delta\Delta G_{\text{ext}}$ values in the range of 0.1 to 3.2 kcal/mol, but with different sign. It is difficult to draw any meaningful conclusion from such small energy values,

which are dependent on the basis sets or exchange-correlation functionals, and sometimes lie within the computational accuracy. On the other hand, geometrical parameters, in particular, calculated trends in the metal-ligand bond distances are found to be rather consistent for different exchange-correlation functionals or basis sets used, as discussed in Section 4.3.1.

4.3.3 Energy Decomposition Analysis

Now, we focus our attention to the energy decomposition analysis, which has been quite successful in providing a quantitative interpretation of chemical bonds in terms of various energy components.¹⁴⁵⁻¹⁴⁸ Therefore, bonding analysis has been performed to obtain an insight into the nature of the metal-ligand bonds present in various complexes investigated in this work. The total complexation energies of all the complexes obtained from the gas phase ADF calculations reported in Table 4.6 reveal that Eu^{3+} complex is more stable as compared to the corresponding Am^{3+} complex irrespective of the ligand, which is in agreement with the gas phase results obtained from Turbomole. Various energy components contributing to the total complexation energy are presented in the form of bar diagrams in Figure 4.2. First we discuss the variations of various energy components corresponding to a particular metal ion with three different ligands considered here. Figure 4.2 reveals that Pauli, electrostatic and steric components are increased upon going from Cyanex301 to Cyanex272, although extent of increase in Pauli repulsion is not significant. However, for a particular metal ion, orbital interaction component is found to decrease while going from Cyanex301 to Cyanex272 complexes. All these trends are clearly due to the change in the nature of donor atoms involved in these three ligands, viz., soft 'S' donor to hard 'O' donor.

These trends are observed for both Am³⁺ and Eu³⁺ complexes. Now it is interesting to compare the various energy components between Am³⁺ and Eu³⁺ complexes with the Cyanex ligands. From Figure 4.2 it is evident that for all the ligands, the percentage of orbital interaction and electrostatic interaction energies are higher for the Am³⁺ complexes as compared to the corresponding Eu³⁺ complexes. On the other hand, higher percentage of Pauli repulsion energies are calculated for the Eu³⁺ complexes, although contributions are negative towards total interaction energy. Differences in the Pauli repulsion energies between Am³⁺ and Eu³⁺ complexes are almost remain the same while going from Cyanex301 to Cyanex272.

Table 4.6 Interaction energies (ΔE_{int}), ligand preparatory energies (ΔE_{prep}) and complexation energies (ΔE_{comp}) for the various Am³⁺ and Eu³⁺ complexes (in eV)

Complex name	ΔE_{int}	ΔE_{prep}	ΔE_{comp}
Am-(Cyanex301) ₃	-50.09	9.25	-40.86
Eu-(Cyanex301) ₃	-51.92	9.31	-42.61
Am-(Cyanex302) ₃	-52.41	9.80	-42.61
Eu-(Cyanex302) ₃	-53.52	9.96	-43.56
Am-(Cyanex272) ₃	-53.98	10.86	-43.13
Eu-(Cyanex272) ₃	-55.32	11.13	-44.19

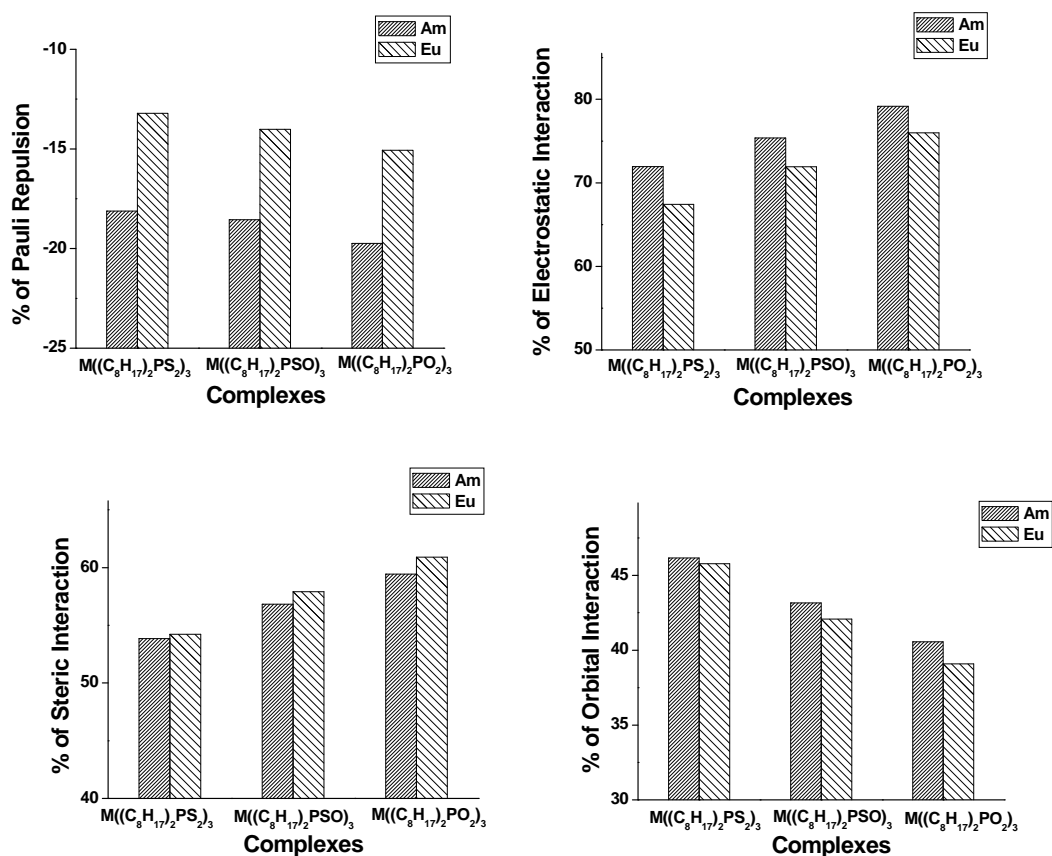


Figure 4.2 Percentage contribution of Pauli repulsion (ΔE_{Pauli}), electrostatic (ΔE_{elec}), steric (ΔE_{steric}) and orbital (ΔE_{orb}) interactions in the total interaction energies (ΔE_{int}) for the different metal-Cyanex complex.

However, variation of electrostatic component is quite significant as we are moving from one complex to another complex. Difference in the electrostatic energy is the maximum for the Cyanex301 complexes, though for Cyanex272 complexes the magnitude of this component is maximum for both Am^{3+} and Eu^{3+} . Nevertheless, it is important to note that both repulsive Pauli and attractive electrostatic components are responsible for the overall Coulomb interaction. Therefore, it is interesting to combine these two components (steric component) and compare the variation of this component from Cyanex301 to Cyanex272 complexes. The steric interaction, which is

electrostatic in nature, is found to be minimum for the Am-(Cyanex301)₃ and maximum for the Eu-(Cyanex272)₃ complexes. Orbital interaction component differs most for Cyanex272 complexes although absolute values of this component are the largest for Cyanex301 complexes. Thus, it is evident that among all the complexes considered in this work, a minimum value of steric component, which is electrostatic in nature and a maximum value of orbital component that is mostly covalent in nature¹⁴⁵⁻¹⁴⁸ are found for Am-(Cyanex301)₃ complex, which in turn lead to a more covalent nature in Am-S bond. A comparatively smaller atomic charge on Am in Am-(Cyanex301)₃ complex supports this view (Section 4.3.4). Consequently, covalency in Am-S bonds in Am-(Cyanex301)₃ complex may be considered as one of the factors for higher selectivity of Am³⁺ with Cyanex301 ligand as compared to Eu³⁺ ion. This picture is consistent with a shorter Am-S bond distance than the corresponding Eu-S bond distance for the Cyanex301 complexes.

4.3.4 Charge Distribution in the Complexes

Natural population analysis shows (Table 4.7) that charges on the metal centers gradually decrease from [Metal-(Cyanex272)₃] to [Metal-(Cyanex301)₃] complexes. It indicates that with increasing softness of the ligand (due to presence of soft donor ‘S’ atoms), covalent nature of the metal-ligand bonds increase. The charge distributions in Am-(Cyanex301)₃ and Eu-(Cyanex301)₃ complexes reveal that metal-ligand charge transfer is more in case of Am³⁺ complex with a q_M value of 0.729. On the other hand, q_{Eu} value is calculated to be 0.896 for Eu-(Cyanex301)₃ complex. Once again it may be correlated with a higher degree of covalency present in the Am-S bonds as compared to the Eu-S bonds for the Cyanex301 complexes. However, an

opposite trend is found for [Metal-(Cyanex272)₃] complexes where q_{Am} charge is higher than q_{Eu} (Table 4.7). Gradual variation of charge from Cyanex301 - Cyanex302 – Cyanex272 complexes indicates a subtle change in the nature of M-L bonding from covalent to electrostatic, which in turn implies a stronger complexation of Eu^{3+} with Cyanex272, and Am^{3+} with Cyanex301. All these trends are found to be consistent in presence of solvent as well.

Table 4.7 Calculated NPA atomic charges on metal and donor centers of Am^{3+} and Eu^{3+} complexes with Cyanex301, Cyanex302 and Cyanex272 in gas and solvent phases using Turbomole program

Complex	q_M	q_S / q_O	q_M	q_S / q_O
	Gas	Gas	Solvent	Solvent
Am-(Cyanex301)₃	0.729	-0.486	0.735	-0.504
Eu-(Cyanex301)₃	0.896	-0.522	0.894	-0.524
Cm-(Cyanex301)₃	0.824	-0.505	0.811	-0.520
Am-(Cyanex302)₃	1.308	-0.570 / -1.039	1.309	-0.580 / -1.040
Eu-(Cyanex302)₃	1.370	-0.578 / -1.042	1.374	-0.588 / -1.043
Am-(Cyanex272)₃	1.684	-1.062	1.684	-1.064
Eu-(Cyanex272)₃	1.660	-1.055	1.659	-1.052

Now, it is interesting to discuss the NPA derived orbital wise population distribution for the valence orbitals of the metal ion for all the complexes (Table 4.8). The population in the metal centered 's', 'p', 'd' and 'f' orbitals are consistently higher in case of Am^{3+} complex as compared to the corresponding Eu^{3+} complex. Ingram et. al.,¹⁴⁰ however, observed high 's' and 'd' population for Am^{3+} complex as compared to Eu^{3+} complex. Also, 'f' orbital population was higher in the Eu^{3+} complex as compared to the Am^{3+} complex. In the present work, the reported results indicate that

the difference in the metal d orbital population between the Am³⁺ and Eu³⁺ complexes is more for Cyanex301 ligand as compared to the Cyanex272 ligand. In fact, this difference is almost negligible between the Cyanex272 complexes. Difference in the f-orbital population between Am(Cyanex301)₃ and Eu(Cyanex301)₃ complexes is found to be small as compared to the corresponding d-orbital population difference. Detail analysis of the MO coefficients also reveals that f-orbital based covalency is quite less and d-orbital based covalency is rather more for all the complexes considered here. All these trends are clearly due to transfer of more electron density from the ligand to the metal 6d/5d orbital in comparison to the 5f/4f orbital, especially for the Cyanex301 complexes.

The total population (s+d+f) on the metal atom, M, decreases from M-(Cyanex301)₃ to M-(Cyanex272)₃ and this may be taken as evidence that covalency decreases in the same manner.¹²³ Moreover, for a particular Eu(III) complex, total M population (s+d+f) is less than the corresponding Am(III) complex. This is consistent with the bond lengths and energy decomposition analysis trends as discussed earlier.

Table 4.8 Calculated natural orbital populations at the metal centres for all the complexes using Turbomole program and Mayer bond orders (BOs) for the M-S/O bonds using ADF program

Complex	n(s)	n(p)	n(d)	n(f)
Am-(Cyanex301) ₃	4.406	12.006	11.422	6.436
Eu-(Cyanex301) ₃	4.355	12.008	11.219	6.523
Am-(Cyanex302) ₃	4.287	11.999	11.047	6.358
Eu-(Cyanex302) ₃	4.239	12.000	10.945	6.445
Am-(Cyanex272) ₃	4.189	11.993	10.805	6.331
Eu-(Cyanex272) ₃	4.158	11.993	10.835	6.353

4.4 Concluding Remarks

In this chapter we have reported the relative complex-forming ability of Am(III) and Eu(III) ions with Cyanex272, Cyanex302 and Cyanex301 ligands within the framework of density functional theory in an unified way. The geometrical parameters, metal-ligand complex formation energies, charge distributions and various energy components have been calculated and compared with each other and related literature values. We have optimized the geometries for all the complexes of Am³⁺ and Eu³⁺ ions using small core pseudopotentials for the actinide and lanthanide atoms. Detailed thermodynamic analysis including continuum solvation model correctly predicts a higher stability of Am(Cyanex301)₃ as compared to the Eu(Cyanex301)₃ complex, which is in agreement with the experimentally observed results. However, from the calculated ΔG (complexation) values, a higher stability of Am³⁺ complex is obtained using both Cyanex302 and Cyanex272 ligands. Thus, it is rather unable to explain the experimentally observed higher selectivity of Am³⁺ with only Cyanex301 and Eu³⁺ with Cyanex272. A similar trend of higher selectivity of Am³⁺ is also evident from the previously reported ΔG (complexation) values, which were obtained using analogous solvation models. Although, recently proposed $\Delta\Delta G_{\text{ext}}^{\text{Am/Eu}}$ values could explain the relative separation abilities of two ligands where both the donor centres involve sulfur atom only, in the present work it fails to produce the experimentally observed trends where both oxygen and sulfur atoms are involved as donors. Nevertheless, here it is important to note that it is difficult to draw any meaningful conclusion from the calculated $\Delta\Delta G_{\text{ext}}^{\text{Am/Eu}}$ values, which lie in the range of 0.1 to 3.2 kcal/mol, and are dependent on the basis sets or exchange-correlation functionals. On the other hand, a shorter Am-S bond distance in conjunction with higher degree of

metal-ligand charge transfer and a higher percentage of orbital interaction energy indicate a greater degree of covalency in $\text{Am}(\text{Cyanex301})_3$ as compared to the $\text{Eu}(\text{Cyanex301})_3$ complex, which in turn can be implicated as one of the factors for higher selectivity of Am^{3+} with Cyanex301 ligand. Moreover, a comparatively higher selectivity of Cyanex272 towards Eu^{3+} ion can be correlated with a shorter Eu-O bond distance and a higher percentage of steric interaction (overall metal-ligand electrostatic interaction).

Chapter 5: Electronic Structure and Stability of the Actinide and Lanthanide Encapsulated Metallofullerenes

5.1 Introduction:

5.1.1 Smaller Fullerenes: A prologue

Since the discovery of C_{60} ,^{18,19} carbon based materials have attracted considerable interest as possible new stable cluster or super atom. Consequently, fullerene and its derivatives are considered to provide a group of potential materials with novel structural and electronic properties, such as covalent bonding, high chemical reactivity, large steric strain, superconductivity etc.¹⁴⁹⁻¹⁵¹ Gas phase experiments indicate the possible existence of a broad range of fullerene clusters, however, beyond C_{60} only a very few number of isolated fullerenes have been obtained so far in the bulk scale. Smaller fullerenes are of special interest due to the presence of high curvature and huge strain energy owing to the presence of adjacent pentagonal rings, which lead to clusters with unusual intra and inter -molecular bonding and electronic properties. Fully hydrogenated form of C_{20} , viz., $C_{20}H_{20}$ ^{51,152} has been found to be highly stable and synthesized experimentally long back. Starting from $C_{20}H_{20}$, synthesis of various isomers of C_{20} , viz., bowl, cage and ring structures has been carried out by Prinzbach et. al.¹⁵³ in 2000 in the gas phase. However, among the smaller fullerenes only C_{36} have been isolated in solid form.⁴² Other smaller fullerenes have also been identified in various gas phase experiments.^{42,51,153,154} Solid C_{36} has been obtained using arc-discharge method by Piskoti et. al.⁴² and is the first smaller fullerene than C_{60} that has been produced in a large scale. Chemically the C_{36} molecule is more reactive than C_{60} . The smaller fullerenes, which are formed during

the production of stable fullerenes, are difficult to isolate because of their extremely high chemical reactivity.

5.1.2 Stabilization of Smaller Fullerenes and our Objectives

Encapsulation of proper dopant atom or ion (metal or nonmetal) into the smaller fullerenes may lead to highly stable clusters with fascinating properties. Examples of some of the recently reported important metal encapsulated smaller fullerene (C_n for $n < 60$) magic clusters are $U@C_{36}$,¹⁵⁴ $U@C_{44}$,¹⁵⁴ $U@C_{28}$,^{51,154,155} $Ti@C_{28}$,¹⁵⁴ $Zr@C_{28}$,¹⁵⁴ etc. It may be noted that for any magic cluster, pronounced intensity peak can be observed as compared to the neighboring peaks in mass spectra. In some of the experimental reports it has been shown that the $U@C_{36}$ peak is significantly strong as compared to the adjacent peaks, in the FT-ICR mass spectrum of cluster cations formed from the vaporization of a UO_2 -graphite target.^{51,154} In the present chapter we have considered two smaller fullerenes, viz., C_{20} and C_{36} and study their possible stabilization through doping with proper lanthanide or actinide atom/ion.^{156,157}

5.1.3 Previous Studies on C_{20} and C_{36} Fullerenes

Energy orderings of the C_{20} isomers are found to be somewhat different depending upon the method of calculation.^{158,159} Here we consider only the cage structure of C_{20} consisting of twelve pentagon rings, where each carbon atom binds with other three carbon atoms forming a 108° bond angle. Due to the absence of any hexagon ring, curvature is extreme in C_{20} cage and bond angle is also considerably deformed as compared to the 120° corresponding to normal sp^2 graphite system.⁵¹ The highest possible symmetry for C_{20} is I_h , which corresponds to a triplet state with a fourfold

degenerate HOMO. Therefore, I_h structure of C_{20} is distorted to D_{5d} or C_{5v} structures according to Jahn-Teller distortion. However, once again these structures are reduced to lower symmetry because of the presence of two-fold degenerate triplet state.¹⁵⁹ Eventually, a non-degenerate singlet state with either D_{3d} or D_{2h} or C_{2h} symmetry becomes the ground state structure for the C_{20} cage.¹⁵⁸⁻¹⁶⁰ Ground state structure of C_{20} cage differs from one symmetry to another depending on the method of calculation and is still a matter of controversy.¹⁶⁰ Recently, neutral $Ce@C_{20}$ and $Gd@C_{20}$ clusters have been studied theoretically.¹⁶¹ These clusters are associated with much lower than I_h symmetry (C_{2h} symmetry), which may be due the absence of any magic number electron configuration.

First theoretical study on C_{36} has been reported by Grossman and co-workers,¹⁶² which revealed that the energetically most favorable structures of C_{36} fullerene are associated with D_{6h} and D_{2d} symmetry using density functional calculation with local density approximation (LDA) and generalized gradient approximation (GGA) methods. Subsequently, considerable amount of theoretical work has been published in the literature dealing with C_{36} fullerene system.¹⁶³⁻¹⁸² Depending on the method of calculation, ground state structure of C_{36} cage is found to be either D_{2d} or D_{6h} structure, however, in most of the reports it is clearly stated that the D_{2d} singlet state, D_{6h} singlet state, and D_{6h} triplet state are almost isoenergetic.^{162,164,167,179,180} Apart from $U@C_{36}$, which is detected in FT-ICR mass spectrum, there is no experimental evidence available for any other endohedral C_{36} derivative. Even for $U@C_{36}$ system no further theoretical or experimental information is available on its structure and characterization. Nevertheless, recently some of the

endohedral C_{36} systems $X@C_{36}$ ($X = \text{He, N, C, H, Li, Na, K}$) are investigated theoretically.^{176,177,180,183}

5.1.4 Stabilization through Encapsulation of Ln/An Atoms or Ions into the Fullerene Cages

In the present chapter one of our objectives is to investigate the possibility of stabilizing C_{20} cage in the I_h symmetry through encapsulation of suitable metal atom/ion from the f-block elements so that the total number of valence electrons correspond to certain magic numbers with closed shell configuration as demonstrated earlier for other systems.^{53,54,83,163,184-194} Here we report a series of $M@C_{20}$ clusters ($M = \text{Pr}^-, \text{Pa}^-, \text{Nd, U, Pm}^+, \text{Np}^+, \text{Sm}^{2+}, \text{Pu}^{2+}, \text{Eu}^{3+}, \text{Am}^{3+}, \text{Gd}^{4+}, \text{Cm}^{4+}$) with I_h symmetry and try to explain theoretically the high stability of these compounds. Further, we analyze bonding aspects, stabilities and also electronic and spectral properties of these clusters from theoretical viewpoint.

Another aim is to elucidate the structure and stability of $U@C_{36}$ cluster to provide an in-depth insight into the origin of the experimentally observed strong peak in the mass spectra, which has been reported earlier⁵¹ and very recently as well.¹⁵⁴ We have also analyzed bonding aspects, thermodynamic stabilities and also electronic and spectral properties of $U@C_{36}$ clusters from theoretical viewpoint.

5.2 Computational Details

Computational methodologies are same as mentioned before in Chapter 2, section 2.3. Here, the partial atomic charges were calculated using the natural population analysis (NPA) and Löwdin schemes as implemented in Turbomole. Also, the Voronoi deformation density (VDD)¹⁹⁵ charges have been calculated using ADF program.

Here we have also calculated the binding energy per atom (BE) of a complex corresponding to the atomic dissociation channel,

$$BE = -E(M@C_n) - E(M) - nE(C)/m.$$

Here $E(M@C_n)$, $E(M)$ and $E(C)$ denote the energy of the complex, metal atom/ion and the carbon atom, respectively and m is the total number of atoms present in the cluster.

Vibrational frequency calculations have also been performed to get the structures with true energy minima. Using these vibrational frequency values and standard statistical thermodynamics, various thermodynamic parameters viz. enthalpy, entropy and free energy values have been calculated for the reaction, $M + C_n \rightarrow M@C_n$.

Because of the correct asymptotic behavior, we have used the the statistical average of orbital potentials (SAOP)^{196,197} model potentials in ADF for the calculations of absorption spectra of bare and metal encapsulated clusters within the framework of time dependent density functional theory (TDDFT). In fact, exchange-correlation functionals possessing correct asymptotic behavior is generally used¹⁹⁸⁻²⁰¹ for the calculations of the excited states and the response properties using TDDFT. For the purpose of comparison we have also employed PBE functional for the calculations of absorption spectra. All-electron calculations have been performed while using SAOP functional.

5.3 Results and Discussions

5.3.1 Study of Ln/An Encapsulated C₂₀ Fullerene

5.3.1.1 Structural Analysis

The geometries of the bare cage like C₂₀ and all the M@C₂₀ clusters have been optimized using Turbomole and ADF programs. For each cluster, all the calculated vibrational frequencies have been found to be real, which indicates that all the structures are true minima on their respective potential energy surfaces. Geometries of M@C₂₀ clusters are optimized starting from various initial cage structures; however, in all the cases geometry optimization leads to highly symmetric closed shell I_h structure. The optimized structures of bare C₂₀ and M@C₂₀ clusters are depicted in Figure 5.1. The structures of all the M@C₂₀ clusters are almost similar irrespective of the encapsulated metal atom or ion. Now onwards we have considered the results obtained using Turbomole program unless otherwise stated.

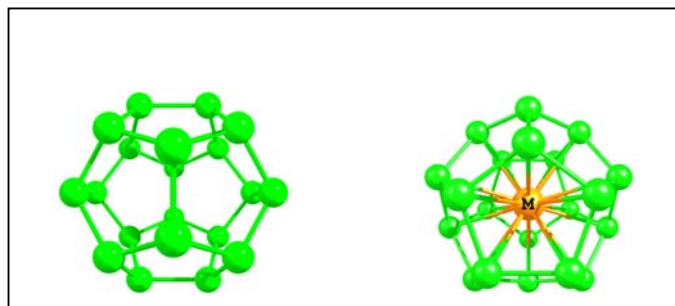


Figure 5.1 Optimized structures of a) bare C₂₀ cage and b) M@C₂₀ cluster.

Bare C₂₀ with D_{3d}, D_{2h} and C_{2h} symmetric structures have been reported¹⁵⁸⁻¹⁶⁰ earlier by Zeng and co-workers, Paulus, and Zhang et. al. using various level of theory. In the present work, D_{3d} structure has been found to be the lowest energy geometry, which corresponds to ¹A_{1g} state with 4a_{1u} as the HOMO. However, energy differences

between the D_{3d} , D_{2h} and C_{2h} structures, calculated using B3LYP functional with both ADF and Turbomole program packages, are found to be almost negligible (~ 0.1 kcal/mol with). After incorporation of metal atom/ion with 6 valence electrons, all the systems are found to be highly symmetrical I_h structure with either $3g_u$ or $5t_{1u}$ as the HOMO. The C-C bond distances in C_{20} cage have been calculated using B3LYP functional and found to lie in the range, 1.440 - 1.516 Å. Encapsulation of metal atom/ion within the C_{20} cage leads to an overall increase in cage size, and as a result C-C bond lengths corresponding to D_{3d} structure increase to 1.53-1.58 Å in $I_h M@C_{20}$. Also, the extent of increase is smaller for the positively charged metal ions. To investigate the effect of different functionals, we have optimized the geometries using PBE, B3LYP, B3LYP and PBE0 functionals in Turbomole. On the other hand we have used BP86 and PBE functionals in ADF. The M-C bond lengths obtained from Turbomole and ADF using different functionals are reported in Table 5.1. For a particular metal atom/ion the bond lengths calculated using different functionals are found to be almost the same. The trends in the variation of the M-C bond lengths along the lanthanide and the actinide series also remain the same. In general, M-C bond length has been found to decrease from Pr to Eu in the lanthanide series and from Pa to Am in the actinide series. It is due to the increase in positive charge of the encapsulated metal atom/ion in going down the series. The M-C bond lengths obtained from ADF and Turbomole, using the same PBE functional, are in good agreement with each other.

Table 5.1 Calculated values of M-C bond distance (R_{M-C} in Å) using different functionals with Turbomole and ADF programs for all the $M@C_{20}$ clusters

Metal Atom/Ion (M)	R_{M-C} in Å (Turbomole)					R_{M-C} in Å (ADF)	
	B3LYP	PBE	BHLYP	PBE0	HF	BP86	PBE
Pr ⁻	2.187	2.183	2.162	2.166	2.158	2.191	2.186
Pa ⁻	2.221	2.223	2.202	2.204	2.199	2.230	2.225
Nd	2.169	2.173	2.146	2.151	2.139	2.176	2.172
U	2.197	2.200	2.177	2.180	2.173	2.206	2.200
Pm ⁺	2.161	2.166	2.138	2.144	2.129	2.168	2.164
Np ⁺	2.183	2.186	2.162	2.166	2.156	2.191	2.187
Sm ²⁺	2.158	2.163	2.136	2.142	2.128	2.166	2.162
Pu ²⁺	2.177	2.181	2.155	2.160	2.146	2.184	2.179
Eu ³⁺	2.162	2.166	2.140	2.146	2.134	2.168	2.164
Am ³⁺	2.175	2.179	2.154	2.159	2.146	2.184	2.180
Gd ⁴⁺	2.133	--- ^a	2.150	2.152	2.148	--- ^a	--- ^a
Cm ⁴⁺	2.184	--- ^a	2.163	2.167	2.157	--- ^a	--- ^a

^aValues are not reported because of poor geometry convergence using PBE and BP86 functionals.

5.3.1.2 Molecular Orbital Diagram, Charge Distributions and Energetics

Molecular orbital energy diagram for the $U@C_{20}$ system with I_h symmetry as calculated using B3LYP functional with ADF program is presented in Figure 5.2. Here $3g_u$ and $3t_{2u}$ molecular orbitals (MOs) are the HOMO and the LUMO, respectively. However, it is to be noted that either $3g_u$ or $5t_{1u}$ can be HOMO depending on the encapsulated metal atom/ion, although ordering of the other occupied MOs remains the same. However, LUMO is found to be either $3t_{2u}$ or $4g_u$ depending on the encapsulated species.

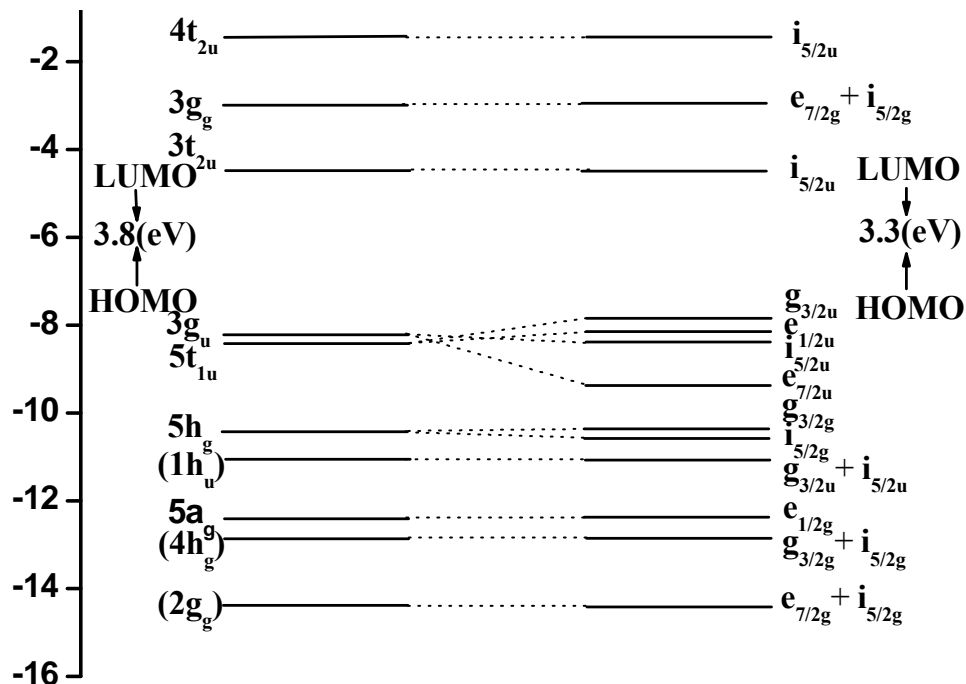


Figure 5.2 Molecular orbital diagram for the $U@C_{20}$ cluster with (right) and without (left) spin-orbit coupling.

Now, the stabilities of the systems can be explained with respect to HOMO-LUMO gaps. The calculated values of HOMO-LUMO gaps are presented in Table 5.2. For a particular cluster, the HF calculated gap value is the largest among all. The HOMO-LUMO gap for the bare C_{20} cage with D_{3d} symmetry is found to be 1.94 eV with B3LYP functional using both Turbomole and ADF program, which is very close to the previously calculated value of 1.93 eV.¹⁵⁸ We have also calculated the HOMO-LUMO gaps by using different functionals and the corresponding values are reported in Table 5.2. The calculated value of HOMO-LUMO energy gap for all the $M@C_{20}$ systems are found to be significantly higher (e.g., 2.4-5 eV with B3LYP functional) as compared to the bare C_{20} (1.94 eV at the same level).

Table 5.2 The calculated values of HOMO-LUMO gap (in eV) obtained using Turbomole and ADF programs for the M@C₂₀ clusters with different functionals

Metal Atom/Ion (M)	(Turbomole)				(ADF)
	BHLYP	B3LYP	PBE	HF	B3LYP
Pr ⁻	5.55	3.30	1.79	8.95	3.35
Pa ⁻	5.43	3.26	1.82	8.80	3.35
Nd	6.18	3.68	1.79	9.89	3.66
U	6.02	3.69	2.12	9.61	3.78
Pm ⁺	6.86	4.08	1.60	10.91	3.95
Np ⁺	6.58	3.88	1.87	10.53	3.88
Sm ²⁺	7.36	4.56	1.40	11.41	4.30
Pu ²⁺	6.73	3.64	1.25	11.39	3.60
Eu ³⁺	7.14	4.93	1.47	10.76	4.73
Am ³⁺	6.64	3.18	1.21	11.47	3.10
Gd ⁴⁺	6.74	4.70	--- ^a	10.07	4.54
Cm ⁴⁺	6.47	2.48	--- ^a	10.99	2.41
C ₂₀ (D3d)	3.74	1.94	0.75	6.75	1.94

^aValues are not reported because of poor geometry convergence using PBE and BP86 functionals.

This trend is found to be valid for all the functionals considered in this work. It confirms the extra chemical stability gain after incorporation of metal atom/ion into the C₂₀ cage. Similar trend in the calculated HOMO-LUMO gap for some of the highly stable systems has been found in the recently reported literature.^{53,54,83,155,184-186,189-191} Among all the DFT functionals, the BHLYP calculated HOMO-LUMO gap values are found to be rather very high due to 50% contribution of HF exchange in this hybrid functional.

Pictorial representation of the valence molecular orbitals (MOs) depicted in Figure 5.3 reveals that the atomic orbitals (AOs) from both metal atom/ion and carbon

atoms are combined to form the $3g_u$, $5t_{1u}$, $5h_g$ and $5a_g$ orbitals, with a cumulative valence electron count of 26. The 26 valence electrons are contributed by metal atom/ion (6 f electrons) and the C_{20} cage (20 π electrons). For these MOs substantial amount of overlapping has been found to be present between the metal and C_{20} cage orbitals. On the other hand, it is evident from Figure 5.3 that the $1h_u$, $4h_g$ and $2g_g$ MOs correspond to pure carbon orbitals of C_{20} . The energy gap between the $4h_g$ and $2g_g$ MOs is also found to be fairly large, and a total number of 46 electrons up to the $4h_g$ MOs correspond to the cumulative number of electrons occupied by $3g_u$, $5t_{1u}$, $5h_g$ and $5a_g$ metal-carbon hybrid MOs (26 electron), and $1h_u$ and $4h_g$ pure carbon MOs (20 electrons). The energy gap between the inner and the $2g_g$ MOs is also found to be very high. From Figure 5.2 it can be noticed that a total number of 54 electrons can be accommodated from the $2g_g$ to HOMO, which include 26 electrons from the metal-carbon hybrid MOs ($3g_u$, $5t_{1u}$, $5h_g$, $5a_g$) along with (in parentheses) 28 electrons from pure carbon MOs ($1h_u$, $4h_g$, $2g_g$). Thus, it is quite clear that the lanthanide and actinide atoms/ions corresponding to 6 valence electrons have been able to elevate the D_{3d} symmetry of the C_{20} cage to the I_h symmetry through fulfilling the 26-electron principle for the central metal atom/ion. In fact, so far only two chemical systems with 26 valence electrons have been predicted^{149,193,194} to be highly stable through experiment and theory.

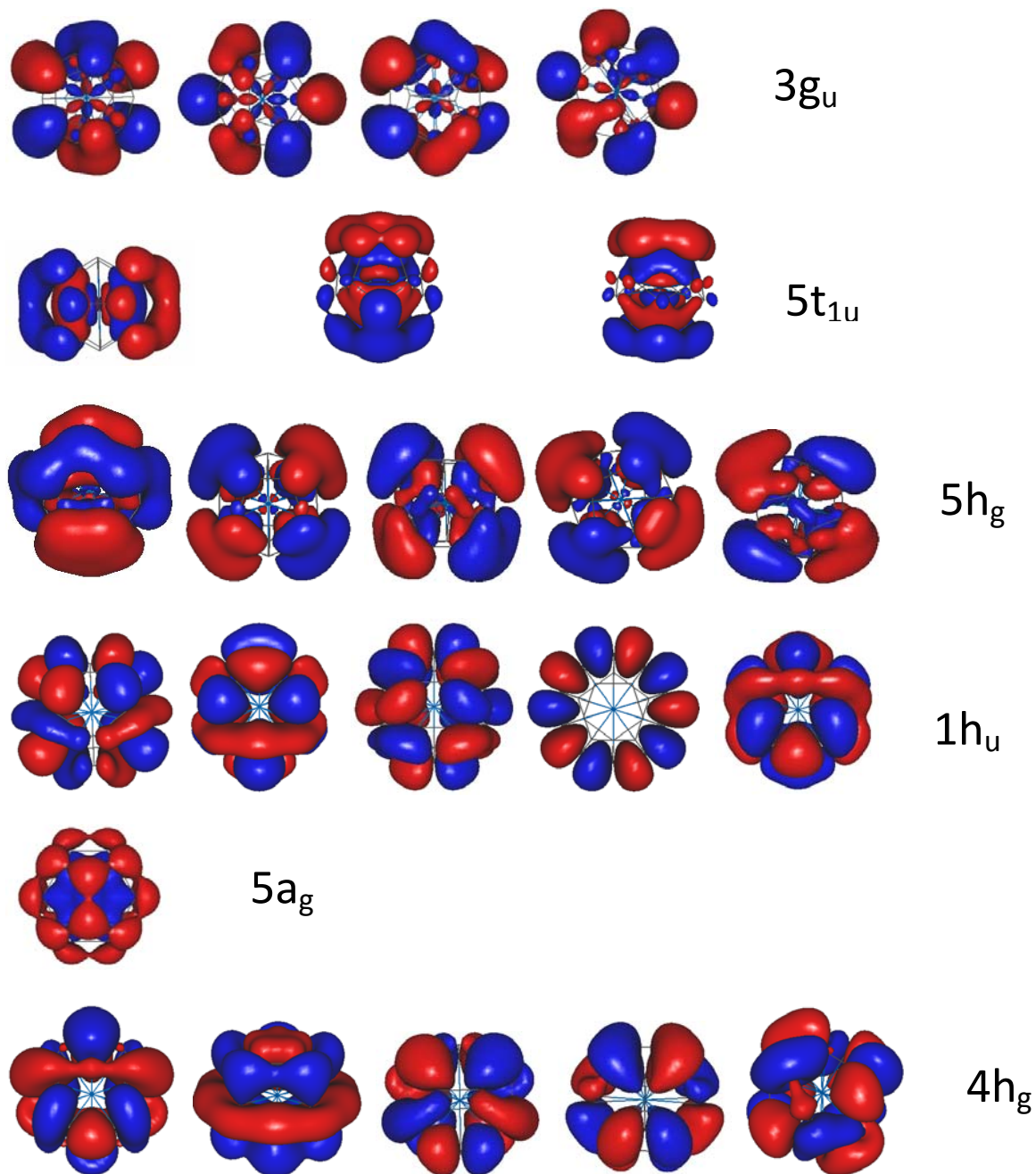


Figure 5.3 Valence molecular orbitals of $U@C_{20}$.

Now we discuss the charge distributions in the $M@C_{20}$ clusters. High negative charges are obtained on the metal centers from both natural population analysis (NPA) and Löwdin charge (Table 5.3) analysis. The negative charge on the metal center in

M@C₂₀ decreases almost monotonically with increase in the positive charge on the bare metal ion, except for Pu²⁺ and Gd⁴⁺. However, high negative values of atomic charges on the metal centers as obtained from the orbital based population analysis schemes, viz., NPA and Löwdin, particularly, for the positively charged clusters are somewhat unrealistic. Similar improbable atomic charges are obtained for WAu₁₂ system by using orbital-based Mulliken population analysis scheme where the atomic charge for the W atom was found to be –15 using B3LYP/SVP level, however, VDD analysis have been found to yield realistic charges.¹⁸⁶ Therefore, apart from NPA and Löwdin schemes we have also calculated the charges as obtained from VDD analysis (Table 5.3). VDD method is based on the calculated amount of electronic density that flows to or from a certain atom due to bond formation through spatial integration of the deformation density over the atomic Voronoi cell, and thus is not explicitly dependent on the basis functions involved in a calculation. Consequently, VDD derived charges are considered to yield chemically meaningful charge distributions in a chemical system. The calculated VDD charges (Table 5.3) lie in the range of 0.25-0.58 and provide chemically meaningful values.^{186,195}

Table 5.3 Calculated natural, Löwdin and VDD charges on metal centers for the M@C₂₀ clusters using Turbomole and ADF programs with different functional

Metal Atom/Ion (M)	(Turbomole)						(ADF)	
	(Natural Charges)			(Löwdin Charges)			(VDD)	
	BP86	B3LYP	PBE	BP86	B3LYP	PBE	BP86	PBE
Pr ⁻	-3.362	-3.227	-3.404	-2.451	-2.393	-2.506	0.285	0.286
Pa ⁻	-2.762	-2.577	-2.781	-3.677	-3.594	-3.748	0.247	0.248
Nd	-3.126	-3.029	-3.166	-2.357	-2.410	-2.323	0.273	0.276
U	-3.689	-3.526	-3.717	-3.292	-3.217	-3.354	0.286	0.288

Pm ⁺	-2.786	-2.706	-2.822	-2.251	-2.233	-2.299	0.268	0.271
Np ⁺	-3.438	-3.309	-3.472	-3.077	-3.019	-3.132	0.287	0.292
Sm ²⁺	-2.384	-2.307	-2.420	-2.168	-2.163	-2.214	0.260	0.265
Pu ²⁺	-3.417	-3.309	-3.477	-4.407	-4.383	-4.470	0.584	0.590
Eu ³⁺	-1.736	-1.640	-1.767	-2.066	-2.066	-2.109	0.254	0.259
Am ³⁺	-2.002	-1.871	-2.042	-2.307	-2.277	-2.352	0.569	0.576
Gd ⁴⁺	--- ^a	-2.427	--- ^a	--- ^a	-2.483	--- ^a	--- ^a	--- ^a
Cm ⁴⁺	--- ^a	-1.254	--- ^a	--- ^a	-2.123	--- ^a	--- ^a	--- ^a

^aValues are not reported because of poor geometry convergence using PBE and BP86 functionals.

To obtain an idea about the distribution of electrons, in Table 5.4 we have reported the NPA calculated values of s, p, d, and f occupations for the metal center in M@C₂₀ clusters. Occupations corresponding to the s and p orbitals remain almost the same for the lanthanide and the actinide containing species. On the other hand d orbital occupation, n(d) has been found to be higher for a lanthanide as compared to the corresponding isoelectronic actinide system. Conversely, f orbital population denoted as n(f) is higher for a particular actinide system as compared to the corresponding lanthanide system. It is clearly due a larger spatial extent of the 5f orbital of actinides as compared to the 4f orbital of lanthanides. It has been found that the 7s, 7p, 6d, 5f orbitals for actinides and 6s, 6p, 5d, 4f orbitals of lanthanides participate in the hybridization with the C₂₀ cage. Symmetrized fragment orbitals analysis through ADF calculations shows that participation of 5f/4f atomic orbitals are maximum (23-80%) for 3g_u molecular orbital except in Pr⁻ and Pa⁻ clusters, where the percentage contribution is rather less (15% and 21%, respectively). The 5t_{1u}, 5h_g and 5a_g MOs correspond to 7p/6p, 6d/5d, 7s/6s orbitals of actinide/lanthanide, respectively. It has

been noticed that the contribution of metal s, d and f character increases from Pr^- to Gd^{4+} and Pa^- to Cm^{4+} , although this trend is opposite for the percentage p character.

Table 5.4 Calculated values of orbital population for the central metal atom in $\text{M}@C_{20}$ clusters with B3LYP functional using Turbomole program

Metal Atom/Ion (M)	n(s)	n(p)	n(d)	n(f)
Pr^-	4.31	12.01	12.63	5.27
Pa^-	4.33	12.00	11.88	5.12
Nd	4.32	12.00	12.71	5.99
U	4.34	12.00	12.07	7.12
Pm^+	4.33	12.00	12.77	6.60
Np^+	4.36	12.00	12.02	7.86
Sm^{2+}	4.34	12.00	12.82	7.15
Pu^{2+}	4.37	12.00	12.20	8.80
Eu^{3+}	4.35	12.00	12.64	7.64
Am^{3+}	4.36	12.00	12.09	8.42
Gd^{4+}	4.37	12.00	12.74	7.91
Cm^{4+}	4.37	12.00	12.12	8.76

Now we focus our attention to the energetics of the clusters. A graphical presentation of different energy components and also the total bonding energy corresponding to the dissociation of $\text{M}@C_{20}$ into $(\text{M} + \text{C}_{20})$ are given in Figures 5.4 and 5.5 for the actinide and lanthanide ions, respectively. Here negative sign is used to represent the total interaction energy term, which is stabilizing in nature according to the bonding energy analysis implemented in ADF. Interaction energies are calculated using ADF software and the corresponding energy range is in between 4 to 87 eV. From the figures one can see that the total interaction energy becomes more negative with increase in positive charge for both actinide and lanthanide containing systems. The natures of

plots are almost the same for both, although the trends in the variations of various energy components contributing to total interaction energy differ widely for the actinide and lanthanide series. Steric energy is the summation of electrostatic and Pauli repulsion terms. Steric term is the minimum for $\text{Pu}^{2+}@C_{20}$ and $\text{Sm}^{2+}@C_{20}$ among the actinides and lanthanides, respectively. Orbital stabilization energy term is also found to be the minimum for Pu^{2+} .

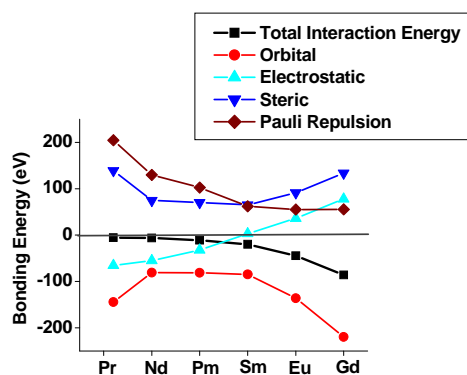


Figure 5.4 Bonding energy analysis for the $M@C_{20}$ clusters, where $M= \text{Pr}^{-}, \text{Nd}, \text{Pm}^{+}, \text{Sm}^{2+}, \text{Eu}^{3+}, \text{Gd}^{4+}$.

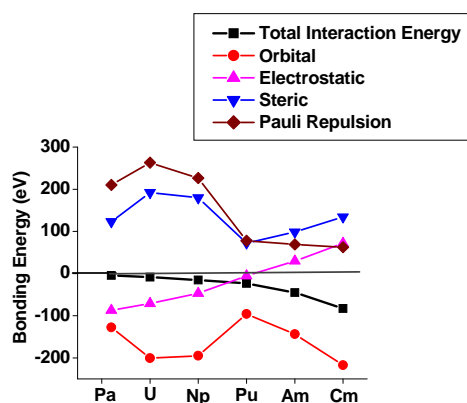


Figure 5.5 Bonding energy analysis for the $M@C_{20}$ clusters, where $M= \text{Pa}^{-}, \text{U}, \text{Np}^{+}, \text{Pu}^{2+}, \text{Am}^{3+}, \text{Cm}^{4+}$.

Here it is to be noted that the energy decomposition analysis involves the structures of the fragments corresponding to the complex geometries. Therefore, deformation energies of the fragments in going to the complex geometries from their respective equilibrium geometries have to be considered to obtain the bonding energies. Thus, for an $M@C_{20}$ cluster the net bonding energy (ΔE_{bond}) for the complex can be calculated as

$$\Delta E_{\text{bond}} = \Delta E_{\text{int}} - \Delta E_{\text{def}} ,$$

where ΔE_{def} denotes the deformation energy for the C_{20} fragment. Thus, ΔE_{bond} essentially refers to the following equation:

$$\Delta E_{\text{bond}} = E(M@C_{20}) - E(C_{20}) - E(M),$$

where $E(M@C_{20})$ and $E(C_{20})$ denote the total energy of the complex and the C_{20} cluster at their respective equilibrium geometries. $E(M)$ is the energy of the metal atom/ion. The calculated values of the ΔE_{int} , ΔE_{def} , and ΔE_{bond} are reported in Table 5.5. Here ΔE_{int} refers to the net bonding interaction between the fragments in their respective complex geometries. However, deformation energies corresponding to the structural deformation of the C_{20} fragment in the complex geometries from its equilibrium geometry has to be considered to obtain the complexation energy (ΔE_{bond}) for the process, $M + C_{20} \rightarrow M@C_{20}$. Here we have used the convention of positive sign for the binding to take place. It is contrary to the sign convention used in Figures 5.4 and 5.5, where negative sign is used for the interaction energy term as per the bonding energy analysis implemented in ADF. From Table 5.5 it is clear that formation of all the $M@C_{20}$ complexes are energetically favorable with positive bonding energy, except the Pa^- , Pm^+ , Sm^{2+} and Pu^{2+} complexes. In these four complexes, the deformation energy is found to be higher as compared to the

corresponding interaction energy leading to a negative bonding energy, as a consequence, the net complexation energies are found to be negative. In general, bonding energy is found to increase with increase in the overall charge of the clusters. Also, the bonding energy for a particular lanthanide encapsulated cluster is higher as compared to that for the corresponding isoelectronic actinide-containing cluster. This trend is due to the higher deformation energy for an actinide-encapsulated cluster as compared to the corresponding lanthanide ones.

Table 5.5 Calculated complexation energy (ΔE_{bond}) and the atomization energy (BE) values (in eV) using ADF with B3LYP functional for the $M@C_{20}$ clusters

Metal (M)	Atom/Ion	ΔE_{int}	ΔE_{def}	ΔE_{bond}	BE
Pr ⁻		5.55	4.39	1.15	6.75
Pa ⁻		4.39	7.08	-2.68	6.55
Nd		6.33	5.91	0.42	6.62
U		8.52	7.84	0.69	6.72
Pm ⁺		10.99	12.04	-1.05	6.43
Np ⁺		15.34	13.48	1.85	5.99
Sm ²⁺		20.00	22.81	-2.81	6.23
Pu ²⁺		23.36	24.03	-0.67	6.45
Eu ³⁺		44.66	41.54	3.11	6.46
Am ³⁺		44.90	42.58	2.32	6.56
Gd ⁴⁺		86.18	63.58	22.60	7.36
Cm ⁴⁺		82.69	66.31	16.38	7.22

Experimentally, these types of clusters are generally formed from the constituent atomic fragments (obtained by laser ablation of the corresponding solid materials),^{51,53,185} therefore, it is interesting to know the binding energies of the

clusters with respect to atomic fragments. Thus, apart from complexation energy, we have calculated the binding energy per atom of a metal encapsulated cluster with respect to its atomic fragments and reported the values in Table 5.5. All the complexes are found to be highly stable with respect to their dissociation into constituent atomic fragments with a binding energy range of 5.99 to 7.36 eV. Among the actinide containing species, $U@C_{20}$, $Pu^{2+}@C_{20}$, and $Am^{3+}@C_{20}$ are found to be more stable than the corresponding lanthanide encapsulated clusters.

5.3.1.3 Study of Aromaticity

In order to get an idea about the aromatic nature of the bare C_{20} cluster and metal encapsulated C_{20} , we have calculated the NICS²⁰²⁻²⁰⁵ values at different positions. We choose three different centers viz. cage center, surface of the cage and 1 Å above the cage, and calculated the NICS values for the bare C_{20} cluster. The calculated NICS values of -16.1, 6.9 and -9.6 ppm at the center, surface and outside the cage, respectively, indicate that the diatropic current dominates over paratropic current within and outside the cage. Previously reported NICS value of -24.0 ppm at the cage center is found to be rather close to the corresponding present value although differs quantitatively, which may be due to the different symmetry of the C_{20} cage as well as different exchange correlation functional used previously.¹⁶⁰ For the $U@C_{20}$ system NICS values are calculated almost at the same positions similar to the bare C_{20} cage except the center one. Instead of center position here we have taken the midpoint between the cage center and the center of a pentagon located on the cage surface. The calculated NICS values of 111.2, -7.1 and 1.3 ppm for the positions inside the cage, on the surface of the cage and above the cage, respectively, have been found to be

significantly different for the metal encapsulated C_{20} cage as compared to the bare C_{20} cage. It indicates that the diatropic current dominates over paratropic current only on the cage surface. This type of drastic change in the NICS values have also been observed for the sandwiched complex of actinides with two cyclooctatetraenes as compared to the bare cyclooctatetraene, although the qualitative trend was similar.²⁰⁶

5.3.1.4 Analysis Including Spin-Orbit Effect

In general, for heavy elements inclusion of spin-orbit effect is very important. To evaluate the influence of spin-orbit interaction we have taken $U@C_{20}$ complex and made a systematic investigation. The geometry optimization considering spin-orbit effect leads to almost no change in bond length values as obtained using relativistic scalar ZORA calculations. Bonding energy analysis reveals that there is an increase of 0.08 % in the steric component and 0.31 % in orbital component after inclusion of spin-orbit interaction, which leads to an overall increase of 2.01 eV in absolute bonding energy value for the $U@C_{20}$ complex.

Now, it is interesting to assess the effect of spin-orbit interaction on the orbital energy diagram. The calculated spin-orbit splittings for all the valence orbitals are reported in Figure 5.2. It can be noticed that the HOMO-LUMO gap for the $U@C_{20}$ cluster calculated using scalar relativistic approach is decreased from 3.8 to 3.3 eV after inclusion of spin-orbit interaction, and thus not affected significantly. In general, the splittings are found to be small, however, for $3g_u$ and $5t_{1u}$ states significant splittings (0.40 and 1.05 eV, respectively) are observed. These states correspond to a mixing of $5f/4f$ and $7p/6p$ orbitals of actinides/lanthanides with $2p$ orbitals of C_{20} cage. Thus, except for the $3g_u$ and $5t_{1u}$ states, spin-orbit coupling effect is not that

important. It may be due to the presence of C_{20} cage, which reduces this effect. Effect of spin-orbit interaction on the NICS values for the $U@C_{20}$ cluster are calculated to be rather small and the corresponding values of 104.3, -7.0 and 1.6 ppm at the positions, inside the cage, on the surface of the cage and above the cage, respectively. Consequently, ground state molecular properties are not likely to be much affected by spin-orbit coupling. Similar kind of trend is observed for $M@C_{28}$ systems.¹⁵⁵

5.3.1.5 Analysis of Spectroscopic Data

Harmonic vibrational frequencies of $M@C_{20}$ clusters are given in Tables 5.6 and 5.7. In the tables, the IR active modes correspond to non-zero intensity value. In general, for a particular lanthanide species the value of the lowest vibrational frequency is larger as compared to the corresponding actinide system. It may be due to slightly larger M-C bond length in actinide systems as compared to the corresponding lanthanide ones. The calculated frequency values for the bare C_{20} cage lie in the range, 84-1427 cm^{-1} . From the tables it is clear that the frequency range decreases on encapsulation of a metal atom/ion into the C_{20} cage. Here it is important to note that the lowest vibrational frequency for each of the $M@C_{20}$ clusters is much higher as compared to the same for the C_{20} cage. This difference in the lowest vibrational frequency between the C_{28} cage and the $M@C_{28}$ cluster has been found to be rather small.¹⁵⁵ Combined motions of the cage atoms and the central metal atom/ion contribute to the high intensity peaks near 300 cm^{-1} and 800 cm^{-1} , respectively, for the lighter and heavier actinides/lanthanides.

Table 5.6 Calculated harmonic vibrational frequencies (cm^{-1}) for the $\text{M}@\text{C}_{20}$ clusters ($\text{M} = \text{Pr}^-$, Nd , Pm^+ , Sm^{2+} , Eu^{3+} , Gd^{4+}) calculated using B3LYP functional (Intensities in km/mol are reported in parentheses)

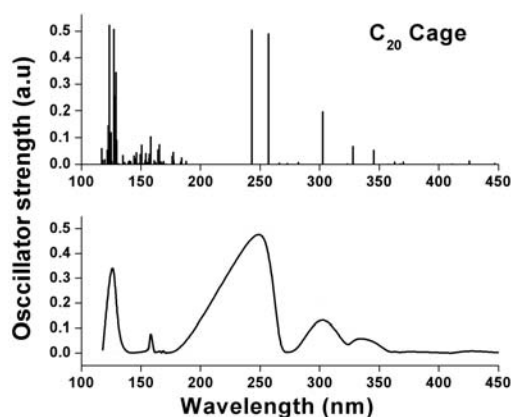
$\text{Pr}^-@\text{C}_{20}$	$\text{Nd}@\text{C}_{20}$	$\text{Pm}^+@\text{C}_{20}$	$\text{Sm}^{2+}@\text{C}_{20}$	$\text{Eu}^{3+}@\text{C}_{20}$	$\text{Gd}^{4+}@\text{C}_{20}$
400.65 (31.5)	423.00 (38.2)	435.57 (45.6)	438.41 (52.0)	433.20 (56.7)	411.06 (60.1)
552.85 (0.0)	563.72 (0.0)	563.24 (0.0)	553.93 (0.0)	534.14 (0.0)	510.42 (0.0)
630.30 (0.0)	632.31 (0.0)	630.70 (0.0)	633.86 (0.0)	639.05 (0.0)	633.01 (0.0)
745.87 (0.0)	752.91 (0.0)	755.97 (0.0)	756.18 (0.0)	753.53 (0.0)	749.80 (0.0)
751.67 (0.0)	768.68 (0.0)	765.78 (0.0)	771.57 (0.0)	776.42 (0.0)	771.25 (0.0)
771.90 (0.0)	780.58 (0.0)	803.35 (0.0)	820.68 (0.0)	813.87 (0.0)	802.63 (0.0)
785.66 (0.0)	815.82 (0.0)	821.33 (0.0)	820.73 (0.0)	829.47 (0.0)	825.92 (0.0)
802.37 (0.0)	822.58 (0.0)	830.11 (0.0)	833.56 (0.0)	833.34 (0.0)	832.96 (0.0)
809.87 (0.0)	862.01 (0.0)	898.62 (0.0)	895.18 (0.0)	892.76 (0.0)	874.88 (125.7)
815.07 (0.0)	878.67 (0.0)	912.49 (4.3)	910.46 (28.4)	900.58 (73.8)	895.47 (0.0)
870.68 (0.0)	892.50 (0.0)	913.19 (0.0)	945.86 (0.0)	962.33 (0.0)	961.62 (0.0)
889.85 (20.4)	905.43 (1.6)	926.21 (0.0)	956.23 (0.0)	968.81 (0.0)	966.41(0.0)
967.90 (0.0)	996.51 (0.0)	1007.09 (0.0)	1004.07 (0.0)	987.20 (0.0)	966.87 (0.0)
969.23 (0.0)	997.75 (0.0)	1014.57 (0.0)	1020.38 (0.0)	1014.47 (0.0)	1001.83 (0.0)
1034.89 (0.0)	1057.61 (0.0)	1068.54 (0.0)	1072.20 (0.0)	1069.80 (0.0)	1065.20 (0.0)

Table 5.7 Calculated harmonic vibrational frequencies (cm^{-1}) for the $\text{M}@\text{C}_{20}$ clusters ($\text{M} = \text{Pa}^-$, U , Np^+ , Pu^{2+} , Am^{3+} , Cm^{4+}) calculated using B3LYP functional (Intensities in km/mol are reported in parentheses)

$\text{Pa}^-@\text{C}_{20}$	$\text{U}@\text{C}_{20}$	$\text{Np}^+@\text{C}_{20}$	$\text{Pu}^{2+}@\text{C}_{20}$	$\text{Am}^{3+}@\text{C}_{20}$	$\text{Cm}^{4+}@\text{C}_{20}$
320.44 (20.4)	348.57 (23.4)	362.48 (29.6)	368.13 (37.2)	351.79 (43.7)	314.96 (46.7)
505.57 (0.0)	537.79 (0.0)	548.89 (0.0)	562.08 (0.0)	531.72 (0.0)	491.01 (0.0)
561.86 (0.0)	603.76 (0.0)	615.73 (0.0)	631.54 (0.0)	611.57 (0.0)	584.01(0.0)
657.68 (0.0)	726.43 (0.0)	749.64 (0.0)	761.12 (0.0)	742.46 (0.0)	722.49 (0.0)
688.52 (0.0)	738.62 (0.0)	752.11 (0.0)	766.55 (0.0)	752.39 (0.0)	745.37 (0.0)
731.87 (0.0)	745.45 (0.0)	761.80 (0.0)	800.42 (0.0)	794.54 (0.0)	786.29 (0.0)

764.84 (0.0)	820.09 (0.0)	833.56 (0.0)	836.32 (0.0)	829.36 (0.0)	811.80 (0.0)
789.76 (0.0)	832.95 (0.0)	837.45 (0.0)	838.47 (0.0)	831.97 (0.0)	823.88 (0.0)
812.56 (0.0)	842.85 (0.0)	894.53 (0.4)	900.80 (11.2)	887.99 (44.5)	866.58 (98.1)
817.53 (0.0)	866.39 (0.0)	898.38 (0.0)	913.91 (0.0)	893.29 (0.0)	871.47 (0.0)
857.39 (22.4)	880.86 (5.1)	901.38 (0.0)	953.09 (0.0)	953.69 (0.0)	944.66 (0.0)
859.86 (0.0)	887.73 (0.0)	910.82 (0.0)	962.88 (0.0)	956.41 (0.0)	949.75 (0.0)
902.88 (0.0)	949.20 (0.0)	975.15 (0.0)	1008.10 (0.0)	976.72 (0.0)	952.83 (0.0)
913.33 (0.0)	960.56 (0.0)	989.91 (0.0)	1022.88 (0.0)	1004.43 (0.0)	984.44 (0.0)
973.17 (0.0)	1015.35 (0.0)	1040.73 (0.0)	1075.42 (0.0)	1057.75 (0.0)	1041.94 (0.0)

Vertical electronic excited states for the $U@C_{20}$ cluster have been calculated using time-dependent density functional theory as implemented in ADF program. Here SAOP functional has been employed to obtain the excitation energies corresponding to the singlet-excited states. According to the selection rule, only the transitions from the ground state I_h structure of $U@C_{20}$ cluster to the t_{1u} states (a_{2u} and e_{1u} states corresponding to D_{5d} symmetry in ADF) have been found to be the allowed ones. The calculated spectra using scalar relativistic approach within the framework of ZORA as well as spin-orbit interaction are given in Figure 5.6.



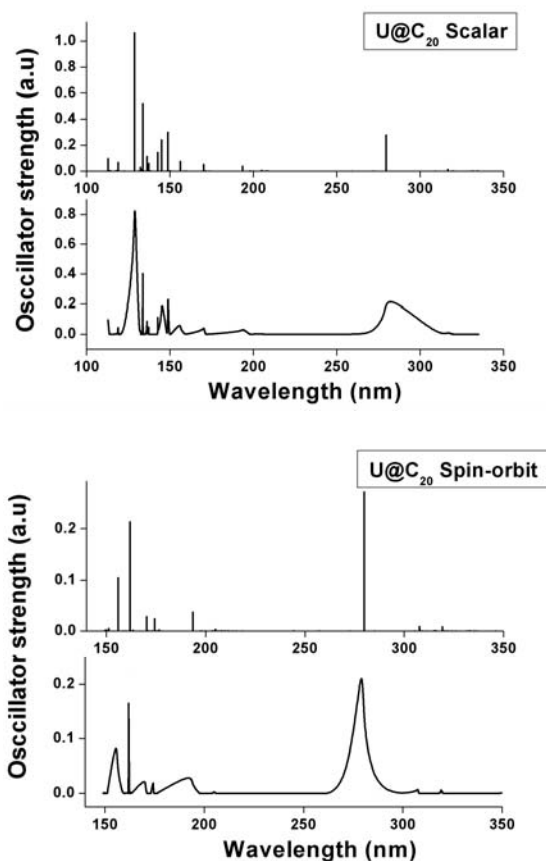


Figure 5.6 UV-visible spectra for the C_{20} Cage, and $U@C_{20}$ cluster without and with spin-orbit coupling.

For the purpose of comparison we have also included the similar spectrum for the bare C_{20} cage as obtained using scalar relativistic approach. From the figure it is clear that the low intensity absorption maxima found at the UV region corresponding to the C_{20} cage (~ 300 nm) is shifted slightly towards higher energy region (~ 280 nm) for $U@C_{20}$ cluster. On the other hand, position of the high intensity absorption maxima found in the UV region (~ 250 nm) is also shifted towards ~ 280 nm region after encapsulation of metal atom. Highly intense absorption peak observed at around 125 nm for C_{20} cluster remains almost unaffected in $U@C_{20}$ cluster. After inclusion of spin-orbit

interaction in the $U@C_{20}$ cluster, the absorption peak observed at around 125 nm is found to be slightly red shifted, whereas the peak at around 280 nm almost remains at the same position. We have also considered LB94²⁰⁷ and PBE functionals for the purpose of comparison. With the LB94 and PBE functionals the peak positions for the bare C_{20} cage almost remain the same. On the other hand, for the $U@C_{20}$ cluster, the position of the absorption maxima (~ 280 nm) calculated using SAOP functional is shifted to 295 and 270 nm with LB94 and PBE functionals, respectively, using both scalar relativistic and spin-orbit methods. It is quite likely that the metal-cage interaction would be changed depending on the nature of the encapsulated metal atom/ion. Consequently, spectrum nature may be influenced strongly by the metal species involved in the encapsulation process.

5.3.2 Study of Uranium Encapsulated C_{36} Fullerene

5.3.2.1 Bare C_{36} Isomers

There are fifteen possible different symmetry isomers available for classical C_{36} fullerene cage.^{162,178} Among all these isomers closed shell D_{2d} symmetry structure is the most stable one, which is also isoenergetic with the triplet D_{6h} isomer. Both these structures are having same number of pentagon and hexagon rings. Singlet D_{6h} isomer is slightly higher in energy as compared to the most stable structures. All these findings are similar to the results previously reported using DFT.^{167,179,180} However, it may be noted that the ground state structure of the C_{36} cage differs from one symmetry to another depending on the method of calculation.^{162,164,167,179,180} The D_{6h} and D_{2d} symmetry isomers have a minimal number of adjacent pentagon units, which may be the reason for higher stability of these two isomers. Apart from the cage

structures, bowl and ring isomers are also possible for the C₃₆ fullerene. We have found that the cage C₃₆ fullerenes are substantially more stable than the bowl and the ring, which is in agreement with the previous theoretical report.¹⁶² The C-C bond distances in D_{2d} symmetry C₃₆ cage have been calculated with B3LYP functional using Turbomole program and found to be 1.382, 1.420, 1.422, 1.434, 1.444, 1.459, 1.480 and 1.481 Å and the calculated average C-C bond distance is 1.4384 Å. The HOMO-LUMO gap for the bare C₃₆ cage with D_{2d} symmetry is found to be 1.38 eV and the molecular orbitals 12b₁ and 27e are the HOMO and LUMO, respectively. In the case of triplet D_{6h} symmetry C₃₆ cage the C-C bond distances are 1.407, 1.428, 1.442 and 1.487 Å with an average value of 1.4383 Å. Although individual C-C bond distances are different in the two structures, the average bond distances are found to be the same. The HOMO-LUMO gap for this isomer is found to be 1.34 eV using the same functional with Turbomole program. Here, 5b_{2g} and 5b_{1u} are the HOMO and LUMO, respectively. The relative energy ordering of all the fifteen C₃₆ isomers considered in this work, as calculated using B3LYP functional, are given in the Table 5.8.

Table 5.8 Relative energies^a (in eV) of different isomers of C₃₆ cage using def-TZVP basis sets with Turbomole and U@C₃₆ cluster using def-TZVP and TZ2P basis sets with Turbomole and ADF programs

C ₃₆ Structures	ΔE	U@C ₃₆ Structures	ΔE (B3-LYP)	ΔE (B3-LYP)	ΔE (PBE)	ΔE (PBE with dispersion correction)
Str-01-D _{6h}	0.107	Str-01-C _{6v}	0	0	0	0
Str-01-D _{6h} (triplet)	0					
Str-02-C ₂	3.80	Str-02-C ₁	4.06	4.11	3.59	3.61

Str-03-D ₂	4.78	Str-03-C ₂	7.22	7.26	6.61	6.64
Str-04-C ₁	2.59	Str-04-C ₁	3.40	3.46	3.14	3.15
Str-05-C _S	3.38	Str-05-C _S	3.97	3.95	3.55	3.57
Str-06-D ₂	5.41	Str-06-C ₂	6.59	6.65	6.13	6.15
Str-07-D _{2d}	1.37	Str-07-C _{2v}	1.85	1.90	1.51	1.52
Str-08-C ₁	1.62	Str-08-C ₁	2.38	2.41	2.18	2.18
Str-09-C _S	2.13	Str-09-C _S	2.33	2.44	2.14	2.15
Str-10-C _{2v}	0.54	Str-10-C _S	1.33	1.34	1.25	1.26
Str-11-C ₂	2.10	Str-11-C ₁	3.23	3.30	3.04	3.04
Str-12-C ₂	0.57	Str-12-C ₁	1.45	1.46	1.27	1.27
Str-13-C ₂	0.30	Str-13-C ₁	1.27	1.29	1.15	1.16
Str-14-D _{3h}	1.76	Str-14-C _{2v}	3.15	3.12	3.07	3.08
Str-15-D _{2d}	0	Str-15-C _S	0.89	0.91	0.81	0.81

^aAll the structures reported here are of singlet state unless specified.

5.3.2.2 Structure and Stability of U@C₃₆ Isomers

Geometry optimizations starting from fifteen different symmetry C₃₆ cage isomers, each encapsulated with a uranium atom, lead to various closed shell U@C₃₆ clusters. The geometry optimizations have been performed using both Turbomole and ADF programs with B3LYP functional. For all the clusters, the calculated vibrational frequencies have been found to be real, which indicate that all the structures are true minima on their respective potential energy surfaces. The relative energies for all the bare C₃₆ and U@C₃₆ isomers are reported in the Table 5.8. Additionally, dispersion-correction²⁰⁸⁻²¹⁰ (DFT-D3) has also been considered for the U@C₃₆ clusters using the PBE functional in Turbomole.

The optimized most stable structures of bare C₃₆ (singlet D_{2d}) isomer and U@C₃₆ (singlet C_{6v} symmetry isomer) cluster are depicted in Figure 5.7.

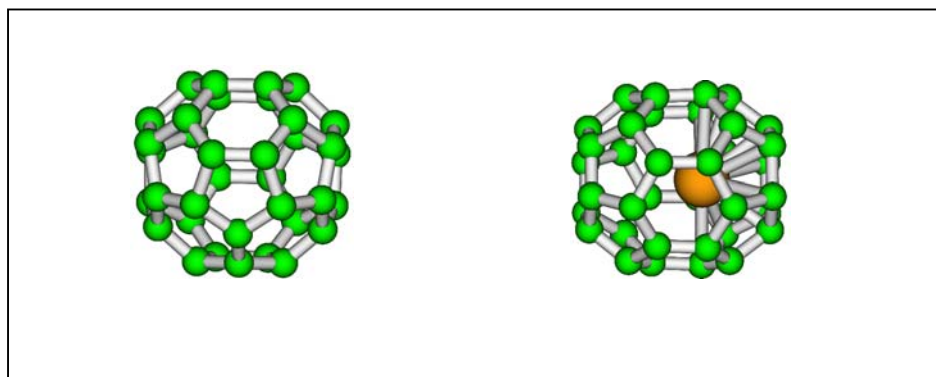


Figure 5.7 Optimized structures of a) bare C_{36} (D_{2d}) cage and b) $U@C_{36}$ (C_{6v}) cluster.

Here it is interesting to note that although singlet D_{2d} and triplet D_{6h} structures of C_{36} cluster are found to be isoenergetic, however, introduction of uranium atom into these C_{36} cages leads to different symmetry isomers (C_{6v} derived from D_{6h} and C_s from D_{2d} isomer) with considerable energy difference (20.5 kcal/mol). Among all the $U@C_{36}$ isomers the highest symmetry isomer is associated with C_{6v} symmetry followed by the C_{2v} symmetry, while other isomers are of either C_s or C_2 or C_1 symmetry indicating that the uranium atom is displaced from the cage center for all these isomers. The optimized structures for rest of the isomers are given in Figure 5.8. Encapsulation of metal atom/ion within the C_{36} cage leads to an overall increase in cage size, and as a result most of the C-C bond lengths are found to increase (except the largest one). For example, the calculated C-C bond lengths for the C_{6v} symmetry $U@C_{36}$ cluster are found to be 1.426, 1.436, 1.438, 1.454, 1.456, 1.458 and 1.468 Å with an average value of 1.451 Å. It is worthwhile to note that this average C-C bond length value is only slightly higher as compared to the same in the bare C_{36} cage. The shortest and the average U-C bond lengths ($R_{U-C}(Shrt)$ and $R_{U-C}(Avg)$), respectively, obtained using

def-TZVP and TZ2P basis sets are reported in Table 5.9. The trends of $R_{U-C}(\text{Shrt})$ and $R_{U-C}(\text{Avg})$ obtained from these two different programs for different isomers are almost the same.

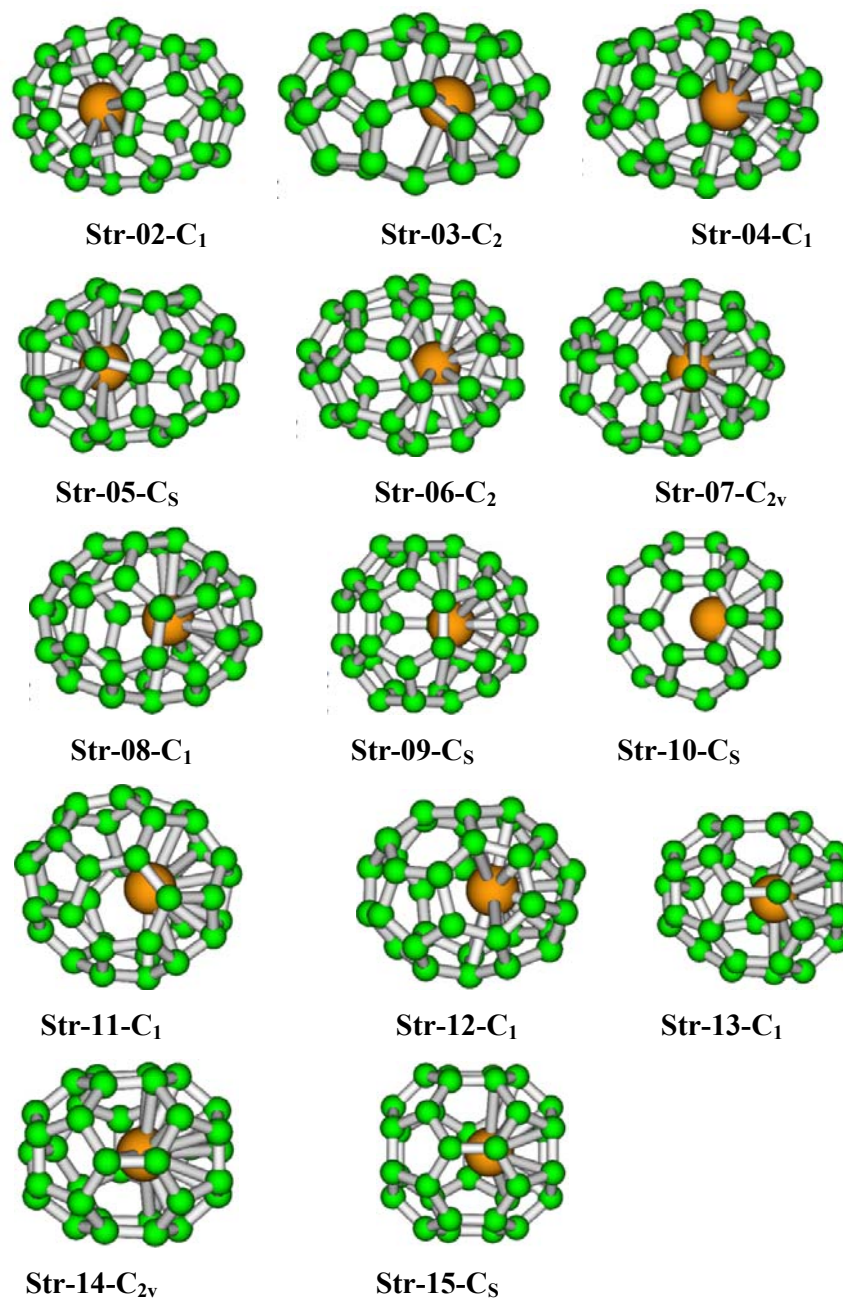


Figure 5.8 Optimized structures of different $U@C_{36}$ clusters.

Table 5.9 Calculated values of average (R_{U-C} (Avg)) and the shortest (R_{U-C} (Shrt)) U-C bond distances (in Å) using def-TZVP and TZ2P basis sets with Turbomole and ADF programs, and binding energy per atom (BE) in eV using def-TZVP basis sets and B3LYP functional with Turbomole program for all the $U@C_{36}$ isomers

Structures	R_{U-C} (Avg)	R_{U-C} (Shrt)	R_{U-C} (Avg)	R_{U-C} (Shrt)	BE
	def-TZVP		TZ2P		def-TZVP
Str-01- C_{6v}	2.823	2.412	2.827	2.438	6.55
Str-02- C_1	2.879	2.370	2.883	2.390	6.44
Str-03- C_2	2.924	2.331	2.928	2.350	6.36
Str-04- C_1	2.857	2.343	2.861	2.362	6.46
Str-05- C_5	2.858	2.388	2.862	2.407	6.44
Str-06- C_2	2.876	2.335	2.883	2.349	6.37
Str-07- C_{2v}	2.853	2.382	2.858	2.402	6.50
Str-08- C_1	2.843	2.376	2.847	2.397	6.49
Str-09- C_5	2.839	2.399	2.843	2.418	6.49
Str-10- C_5	2.809	2.391	2.813	2.409	6.51
Str-11- C_1	2.841	2.356	2.847	2.374	6.46
Str-12- C_1	2.834	2.405	2.839	2.428	6.51
Str-13- C_1	2.822	2.368	2.827	2.388	6.52
Str-14- C_{2v}	2.816	2.411	2.820	2.426	6.47
Str-15- C_5	2.808	2.372	2.812	2.395	6.53

The chemical stability of the $U@C_{36}$ cluster can be presumed by the observation of significantly strong peak as compared to the adjacent peaks in the FT-ICR mass spectrum of cluster cations formed from the vaporization of a UO_2 -graphite target.^{51,154} Therefore, it is interesting to analyze the stability of different isomers of the $U@C_{36}$ system in terms of binding energy values. For this purpose we have calculated the binding energy per atom (BE) values for the $U@C_{36}$ clusters and reported in Table 5.9. The BE values for different $U@C_{36}$ isomers vary from 6.37 to

6.55 eV. Among all the isomers, the C_{6v} symmetry isomer has the highest BE value. It is important to note that the BE value for the bare C_{36} cage is 6.53 eV. Hence only the C_{6v} symmetry isomer has the higher BE value as compared to the bare C_{36} cage. Here, it can be noted that for the binding energy and relative energy quantities we have used standard convention: higher binding energy refers to more stability whereas higher relative energy indicates less stability. In the present work, the stability trends as obtained from the BE and relative energy values are the same.

It is also interesting to analyze the different energy components for a comprehensive study of the nature of interactions involved after the formation of the $U@C_{36}$ complex from its constituent fragments. For this purpose graphical presentation of the various energy components and also the total interaction energy corresponding to the dissociation of $U@C_{36}$ into $(U + C_{36})$ have been depicted in Figure 5.9.

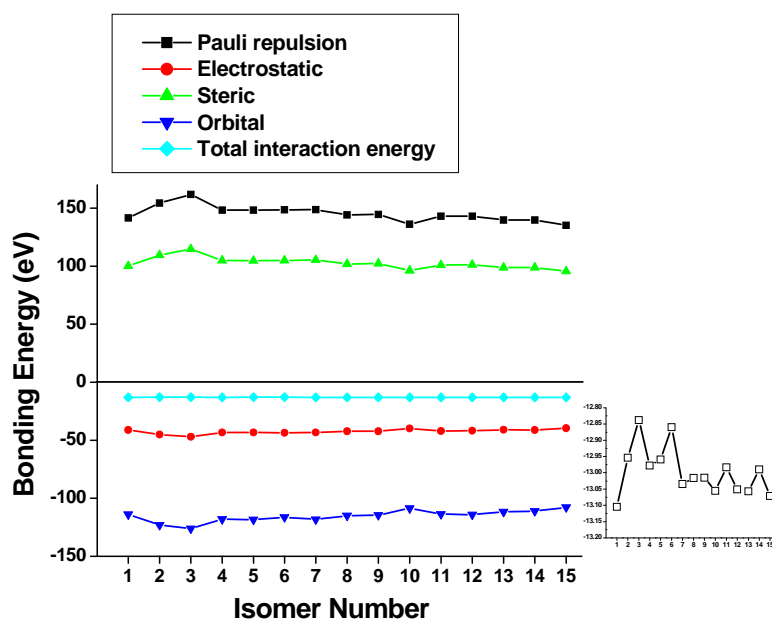


Figure 5.9 Interaction energy analysis for the different $U@C_{36}$ clusters. Inset: Total interaction energy represented in a magnified scale.

The calculated interaction energies for various isomers are found to lie in the range of -13.104 to -12.837 eV, using the ADF software, which indicates that all the isomer studied here are of almost comparable energy. However, the other energy components differ considerably for the different isomers. The relative energy ordering for different isomers obtained using TZ2P and def-TZVP basis sets with ADF and Turbomole programs, respectively, is almost the same.

For the sake of comparison we have also investigated the open-shell $U@C_{36}$ clusters (triplet and quintet) for both Str-01- C_{6v} and Str-15- C_s , which are derived, respectively, from D_{6h} and D_{2d} isomers of bare C_{36} cage. However, the triplet Str-01- C_{6v} and Str-15- C_s isomers are found to be energetically less stable by 7.5 and 28.5 kcal/mol, respectively, as compared to the most stable singlet Str-01- C_{6v} $U@C_{36}$ cluster. Similarly, the corresponding quintet structures are found to be energetically higher by 50.3 and 94.0 kcal/mol. The uranium incorporated C_{36} bowl and ring structures have also been investigated. They are also found to be substantially higher in energy (236 and 323 kcal/mol for bowl and ring isomer, respectively) as compared to the most stable isomer.

We have re-optimized all the $U@C_{36}$ structures using PBE (GGA) functional and the frequency calculations have also been performed. The choice of PBE functional is based on some previous reports.²¹¹⁻²¹⁴ The structural and energy trends obtained using PBE functional are found to be the same as obtained using B3LYP functional, with a slight decrease in the total energy values in case of PBE functional as compared to the B3LYP functional. The relative energy trends using PBE functional are reported in Table 5.8. We have also calculated the $U@C_{36}$ systems incorporating dispersion correction using PBE functional. Inclusion of this correction

term leads to slight decrease in the total energy values for all the systems. However, the relative energy trend is found to be the same as obtained from the calculations, which do not include the dispersion correction term. In fact, dispersion-corrected relative energy values remain almost the same with negligible changes. We have also optimized triplet and quintet states of the most stable $U@C_{36}$ clusters using PBE functional. The triplet and quintet Str-01- C_{6v} isomers are found to be energetically less stable by 14.1 and 71.7 kcal/mol, respectively, as compared to the most stable singlet Str-01- C_{6v} $U@C_{36}$ cluster (*cf.* 7.5 and 50.3 kcal/mol with B3LYP functional).

Now it is interesting to investigate the structural transitions of the C_{36} cage during encapsulation of a U atom, the way it is done for the $Ti@C_{28}$ ²¹⁵ system in a recent theoretical report. For that purpose we have started geometry optimization process by placing the U atom on the center position of the various bare C_{36} cages, associated with different symmetries. In order to locate the different stationary points on the potential energy surface, we have characterized various transition states involved during the encapsulation process. The most stable $U@C_{36}$ isomer is associated with C_{6v} symmetry and it is derived through the encapsulation of U atom into the D_{6h} symmetric C_{36} cage, as mentioned before. Initially we have placed the U atom into the central position of the cage. The endohedral complex with the U atom at the origin is the third-order saddle point on the potential energy surface and associated with three imaginary frequencies. This point is 61.6 kcal/mol higher in energy as compared to the minimum energy structure. However, during optimization it is moved to off-center position along the vertical C_6 axis (principal axis) resulting into C_{6v} symmetric $U@C_{36}$ structure with all real frequencies. The first-order transition state is found to be of C_{2v} symmetry, which is arrived through horizontal movement of the central U atom along

the C_2 axis, perpendicular to the C_6 axis of D_{6h} symmetric $U@C_{36}$ structure. This point is found to be 45.6 kcal/mol above the minimum energy point. The transition state symmetries for rest of the $U@C_{36}$ isomers and the energy differences of these transition state structures as compared to the corresponding minimum energy isomers are given in the Table 5.10.

Table 5.10 The first-order Transition state (TS) symmetries and the energy differences between the minima and the transition states (ΔE in eV) for all the $U@C_{36}$ clusters with Turbomole program using B3LYP functional

$U@C_{36}$ Isomers	TS Symmetry	ΔE
Str-01- C_{6v}	C_{2v}	1.976
Str-02- C_1	C_2	1.477
Str-03- C_2	C_2	1.687
Str-04- C_1	-- ^a	-- ^a
Str-05- C_s	C_2	1.118
Str-06- C_2	D_2	2.374
Str-07- C_{2v}	D_{2d}	1.810
Str-08- C_1	C_2	1.476
Str-09- C_s	-- ^a	-- ^a
Str-10- C_s	C_{2v}	0.134
Str-11- C_1	C_2	1.110
Str-12- C_1	C_2	1.398
Str-13- C_1	C_2	1.729
Str-14- C_{2v}	-- ^a	-- ^a
Str-15- C_s	C_{2v}	1.189

^aValues are not reported because of poor convergence in transition-state geometry optimization

5.3.2.3 Thermodynamic Analysis

In addition to the BE calculations, thermodynamic analysis have also been carried out using Turbomole program. Thermodynamic parameters (Gibb's free energy (Δ_rG), enthalpy (Δ_rH) and entropy (Δ_rS)) for the reaction, $U + C_{36} \rightarrow U@C_{36}$ are calculated using the B3LYP functional (T = 298.15 K, P = 0.1 MPa) and are reported in Table 5.11.

Table 5.11 The calculated values of change in enthalpy and free energy (in kJ/mol) corresponding to the reaction $U + C_{36} \rightarrow U@C_{36}$ as obtained using def-TZVP basis sets and B3LYP functional with Turbomole program for the different isomers

Structures	Δ_rH	Δ_rG
Str-01- C_{6v}	-668	-618
Str-02- C_1	-283	-238
Str-03- C_2	14	60
Str-04- C_1	-345	-301
Str-05- C_s	-291	-247
Str-06- C_2	-44	-1
Str-07- C_{2v}	-495	-448
Str-08- C_1	-442	-398
Str-09- C_s	-449	-405
Str-10- C_s	-542	-500
Str-11- C_1	-362	-318
Str-12- C_1	-531	-487
Str-13- C_1	-549	-505
Str-14- C_{2v}	-371	-326
Str-15- C_s	-583	-540

The calculated Δ_rG and Δ_rH values are found to be negative for all the structures except for the isomer Str-03- C_2 . Negative Δ_rG values suggest the spontaneity of the

encapsulation process of uranium atom into the C_{36} cage. Similar to the BE value, the thermodynamic stability is also highest for the Str-01- C_{6v} isomer. For most of the clusters, the calculated Δ_rH values are negative, indicating the exothermic nature of the encapsulation process. It is interesting to note that the calculated ΔG and ΔH values of some of the experimentally observed^{51,154,155} endohedral metallofullerene systems such as $U@C_{28}$ and $Ti@C_{28}$ are found to be comparable with that of the $U@C_{36}$ cluster using the same level of theory. Thus, the calculated ΔG (ΔH) values are found to be -673 (-722) and -541 (-548) kJ/mol for $U@C_{28}$ and $Ti@C_{28}$ systems, respectively. These values are comparable with the ΔG and ΔH values reported in the present work for the most stable $U@C_{36}$ system. Consequently, the results reported in this work clearly indicate the feasibility of the possible existence of the $U@C_{36}$ cluster. Moreover, origin of the higher intensity peak in the experimentally observed FT-ICR mass spectrum of $U@C_{36}$ cluster is most likely due to the highly stable Str-01- C_{6v} isomer. The next competitive structure, Str-15- C_s , which is 20.5 kcal/mol less stable, is unlikely to contribute to the experimentally observed spectra, although it depends on the experimental conditions.

In one very recent experimental and theoretical reports¹⁵⁴ on smallest stable fullerene, it has been clearly stated that $U@C_{28}$ is the initial product and forms directly from the carbon vapor during laser vaporization of UO_2 –graphite target under increasing helium pressure. It has also been mentioned that the formation of $U@C_{28}$ is not due to fragmentation of larger magic number uranofullerenes like $U@C_{36}$ or $U@C_{44}$. Moreover, it has been demonstrated that the larger uranofullerenes form only after the formation of $U@C_{28}$ through closed network growth mechanism^{154,216} either by assimilation of atomic carbon or C_2 molecule i.e., $U@C_{28}$ is the precursor to larger

uranofullerenes. Therefore, in this context it is also interesting to consider the reaction, $U@C_{28} + 4C_2 \rightarrow U@C_{36}$, which is found to be associated with a very high negative Δ_rG value (-3270 kJ/mol), indicating that this process is energetically favorable.

5.3.2.4 Molecular Orbital Energy Diagram and Charge Distribution Analysis

For the detail investigations of the different properties, now onwards we have considered only the most stable $U@C_{36}$ isomer (Str-01- C_{6v}) unless otherwise specified. The molecular orbital energy diagram for the $U@C_{36}$ cluster as calculated using B3LYP functional and TZ2P basis sets is represented in Figure 5.10. The HOMO and the LUMO for this particular isomer have been found to be $14a_1$ and $6b_2$ molecular orbitals (MOs), respectively. The calculated HOMO-LUMO gaps for all the isomers using B3LYP functional have been reported in Table 5.12 using TZ2P and def-TZVP basis sets. For almost all the isomers, the calculated HOMO-LUMO energy gap values are found to be reasonably higher (e.g., 1.42-2.48 eV with B3LYP functional) as compared to that for the bare C_{36} cage using the same level of theory. Here it may be important to note that some of the recently reported, highly stable clusters, have been found to be associated with high HOMO-LUMO gaps.^{53,54,83,155,184-186,189-191} Consequently, the calculated high HOMO-LUMO gaps for $U@C_{36}$ isomers can be correlated with the chemical stability gain after incorporation of the metal atom into the C_{36} cage.

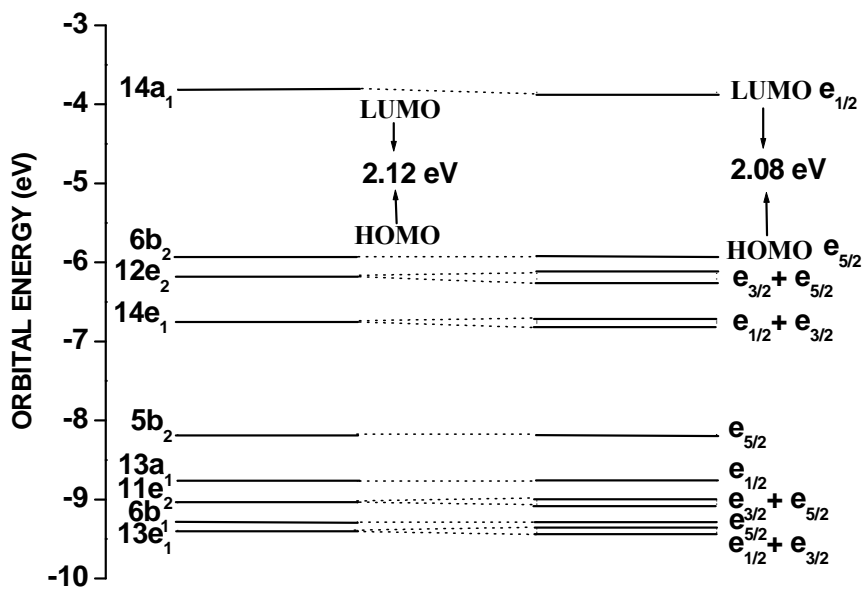


Figure 5.10 Molecular orbital diagram for the $U@C_{36}$ (C_{6v}) cluster without (left) and with (right) spin-orbit coupling.

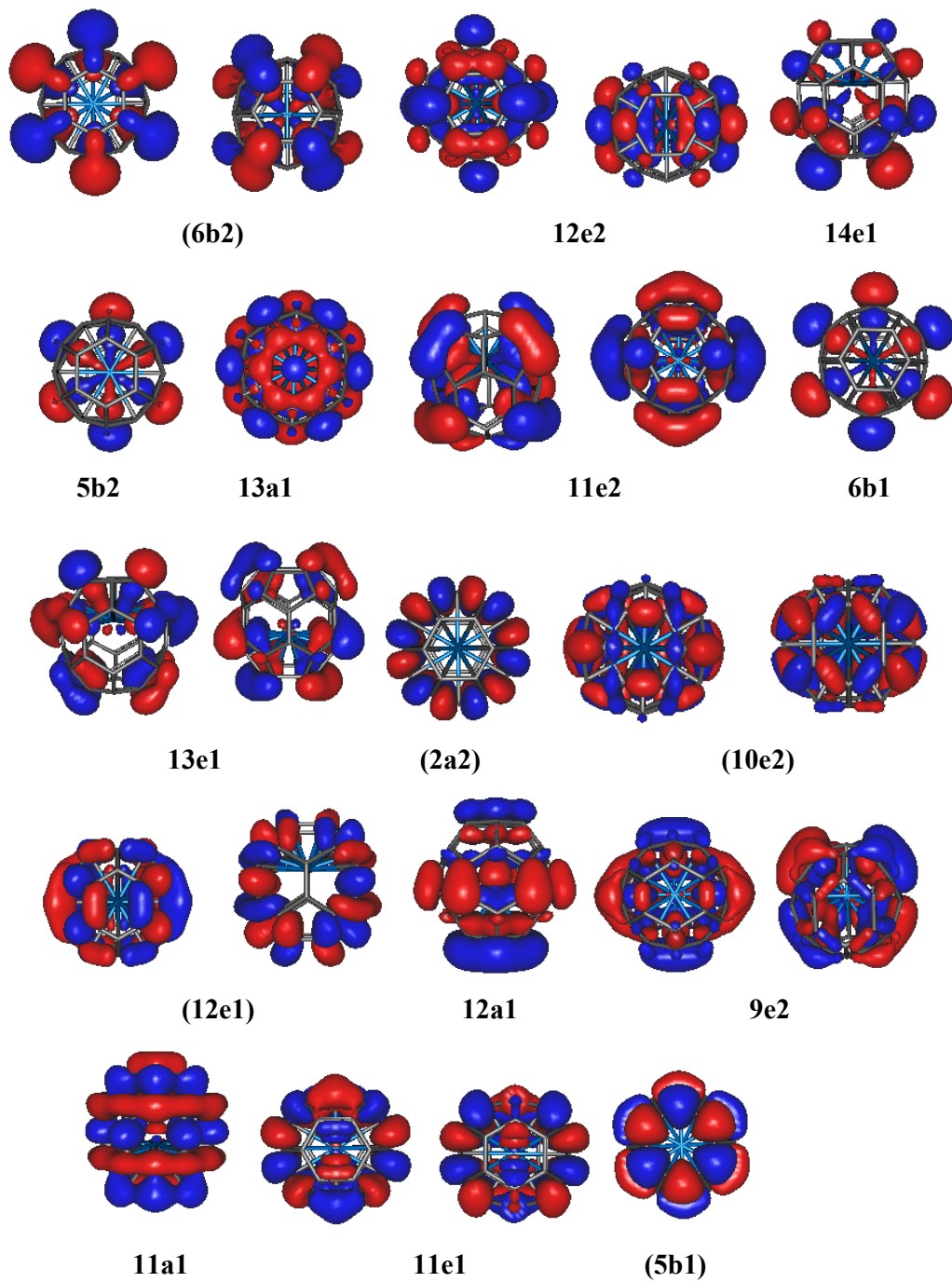
Table 5.12 The calculated values of HOMO-LUMO gap (in eV) as obtained using def-TZVP and TZ2P basis sets with Turbomole and ADF programs for the $U@C_{36}$ isomers using B3LYP functional

Structures	HOMO-LUMO gap	
	Turbomole	ADF
Str-01- C_{6v}	2.00	2.12
Str-02- C_1	2.21	2.25
Str-03- C_2	1.96	1.97
Str-04- C_1	1.94	1.92
Str-05- C_5	2.13	2.19
Str-06- C_2	1.77	1.74
Str-07- C_{2v}	2.48	2.22
Str-08- C_1	1.87	1.89
Str-09- C_5	1.42	1.35
Str-10- C_5	1.73	1.79
Str-11- C_1	1.89	1.82

Str-12-C ₁	1.83	1.86
Str-13-C ₁	1.88	1.93
Str-14-C _{2v}	1.67	1.72
Str-15-C _s	2.21	2.27

The valence MOs of the C_{6v} symmetric U@C₃₆ cluster are depicted in Figure 5.11. On analysis of the contributions of symmetrized fragment orbitals (SFOs) towards valence MOs, and from the orbital pictures of the U@C₃₆ cluster, it has been found that a reasonable amount of overlap is present between the uranium atom and carbon atoms in 12e₂, 14e₁, 5b₂, 13a₁, 11e₂, 6b₁, 13e₁, 12a₁, 9e₂, 11a₁, 11e₁, 10e₁, 8e₂, 9e₁, 10a₁ and 9a₁ MOs, with a total valence electron count of 50, which corresponds to a magic electron number. The origin of this 50-electron may be interpreted as a cumulative contribution from the 14 electrons of the uranium atom and the 36 π electrons of the C₃₆ cage. On the other hand, the 6b₂, 2a₂, 10e₂, 12e₁, 5b₁, 1a₂, 4b₂, 8e₁, 4b₁, 7e₂, 7e₁, 8a₁ and 3b₂ MOs correspond to pure carbon orbitals that do not overlap with the metal center and altogether account for 36 electrons. SFOs have also been used for the analysis of the characters of the metal-cage hybrid MOs. Here our interest is to see the contributions of various atomic orbitals corresponding to the uranium atom towards these hybrid orbitals. In general, SFO contributions from the uranium atom are found to be the largest from the 5f atomic orbitals. In case of 12e₂, 14e₁, 5b₂, 13a₁, 11e₂ and 6b₁ hybrid orbitals, contribution of uranium atom is mainly from 5f orbital, whereas for the 13e₁ and 12a₁ orbitals, along with f orbital, small contributions from p and d orbitals are also observed. However, for the other hybrid orbitals i.e., 9e₂, 11a₁, 11e₁, 10e₁, 8e₂, 9e₁, 10a₁ and 9a₁, no f orbital contribution is found. For the

$9e_2$, $11a_1$, $11e_1$, $10e_1$, $8e_2$, $9e_1$ and $10a_1$ orbitals, main contributions are from p and d orbitals whereas for $9a_1$ orbital only contribution is from uranium s orbital.



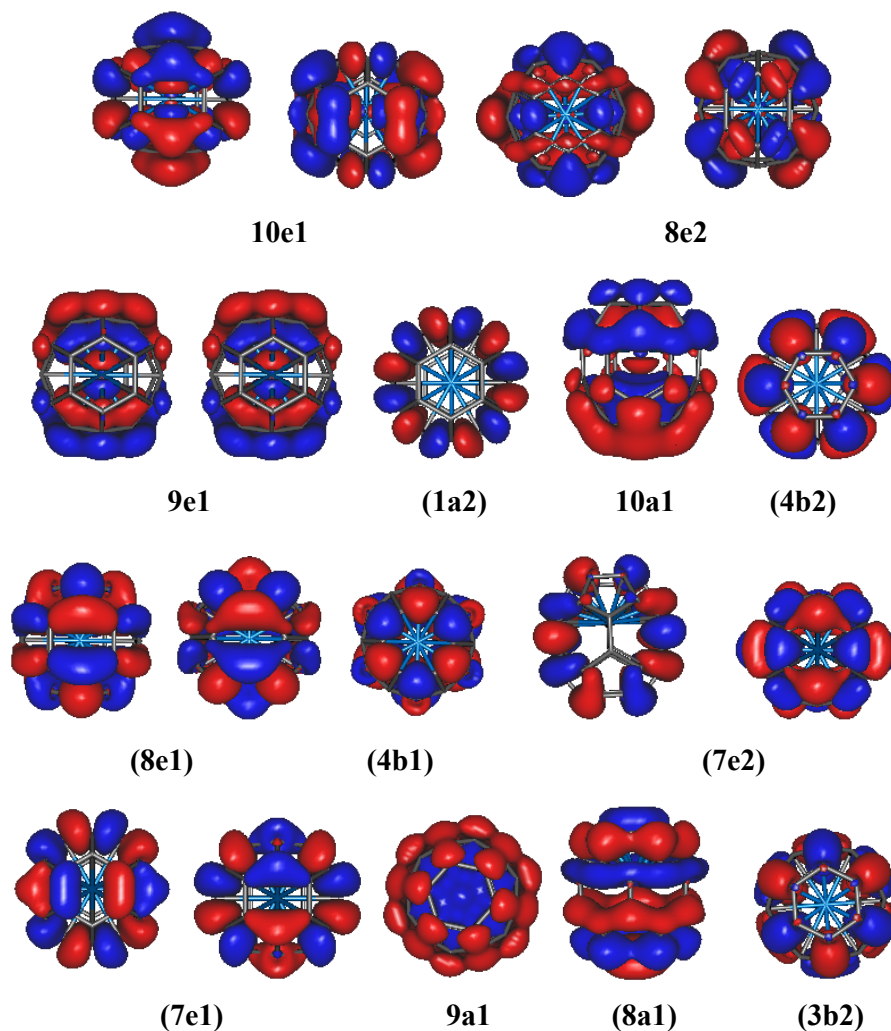
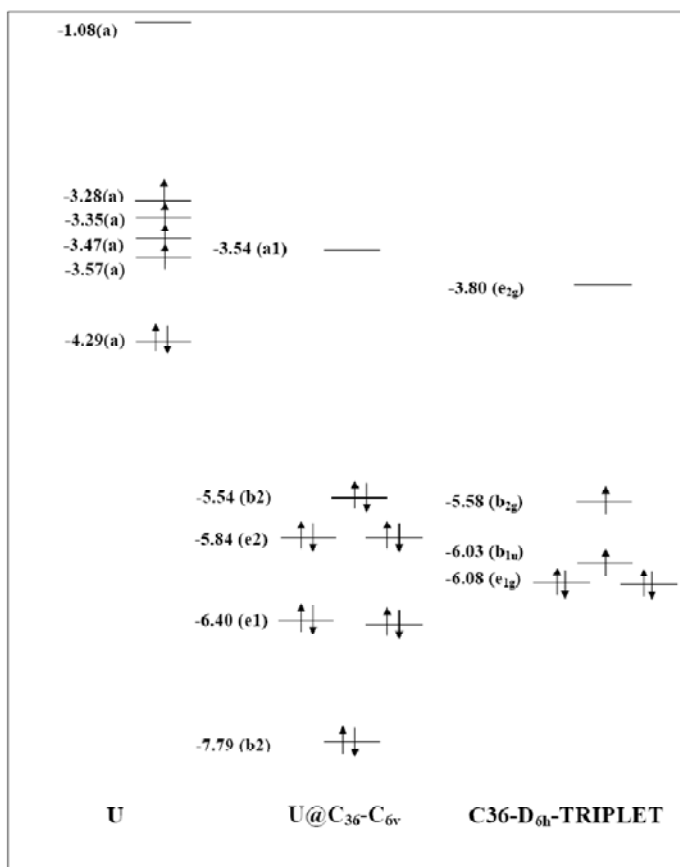


Figure 5.11 Valence molecular orbitals of $U@C_{36}$ (C_{6v}). (Orbital Notations within the parentheses refers to the orbitals contributed by pure C_{36} cage.)

The most stable C_{36} structure is associated with either D_{6h} or D_{2d} symmetry. The ground state of D_{6h} isomer is triplet, whereas D_{2d} isomer is singlet. However, incorporation of U atom into the C_{36} cage leads to closed shell structures for both the isomers. D_{6h} and D_{2d} isomers are transformed to C_{6v} and C_s symmetry, respectively, after introduction of the U atom. Here it is important to note that although the bare D_{6h} -triplet C_{36} and the D_{2d} -singlet C_{36} are of same energy, the corresponding $U@C_{36}$ isomers differ quite a bit as far as stability is concerned. To analyze this aspect, the schematic diagrams of the frontier

orbital energy levels involved for the two most stable $U@C_{36}$ structures, U atom and the corresponding C_{36} cages, are depicted in the Figure 5.12. We have considered 6 valence electrons for all the starting species (U, D_{6h} -triplet C_{36} and D_{2d} -Singlet C_{36}), and 12 electrons for the $U@C_{36}$ (both C_{6v} and C_s isomers). From the Figure 5.12 it is clear that the cumulative energy of the outermost 6 valence electrons is lower (more stable) in the case of D_{2d} -Singlet C_{36} isomer, as compared to that of the D_{6h} -triplet C_{36} isomer. Moreover, open-shell D_{6h} - C_{36} isomer is converted into a closed-shell species after encapsulation of the U atom. Consequently, valence electrons of D_{6h} -triplet C_{36} isomer are stabilized more after formation of the singlet C_{6v} $U@C_{36}$ cluster as compared to the stability gain during the transformation of D_{2d} -singlet C_{36} isomer into the C_s $U@C_{36}$ isomer.

a)



b)

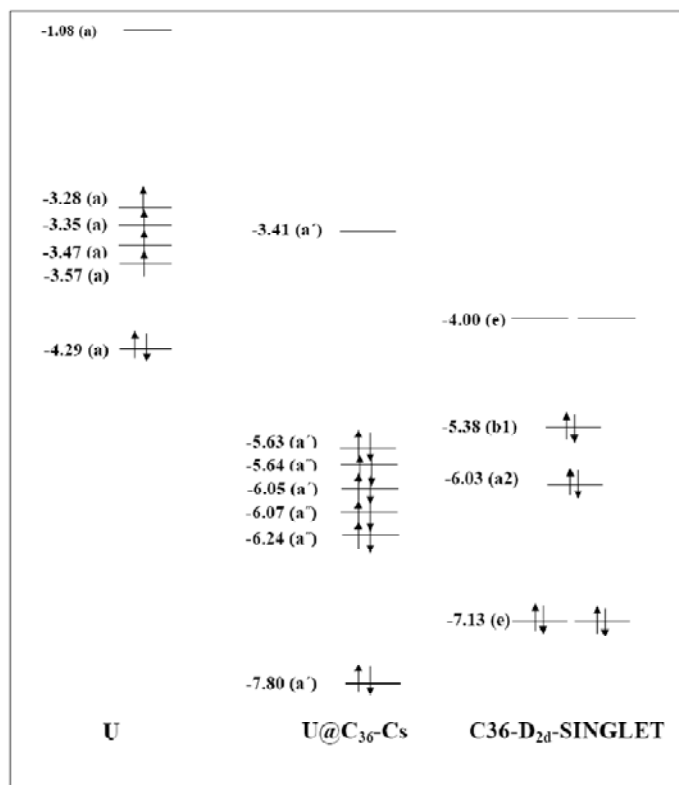


Figure 5.12 Schematic diagrams of the frontier orbital energy levels (in eV) for the U atom, two most stable C₃₆ isomers and the corresponding U@C₃₆ clusters

The densities of states (DOS) of the uranium atom, bare C₃₆ cage and the U@C₃₆ cluster are plotted in Figure 5.13. The HOMO energies for these three systems are -2.36, -5.62 and -5.93 eV respectively. From the figure, it is clear that the DOS curve for the U@C₃₆ cluster shifted slightly towards more negative energy as compared to the DOS curve for the C₃₆ cage. It is clearly due to the bonding between the uranium atom and the C₃₆ cage orbitals. Moreover, DOS corresponding to the U@C₃₆ cluster is quite different from that of the C₃₆ cluster, which indicates significant mixing between the orbitals of the uranium atom and the fullerene cage.

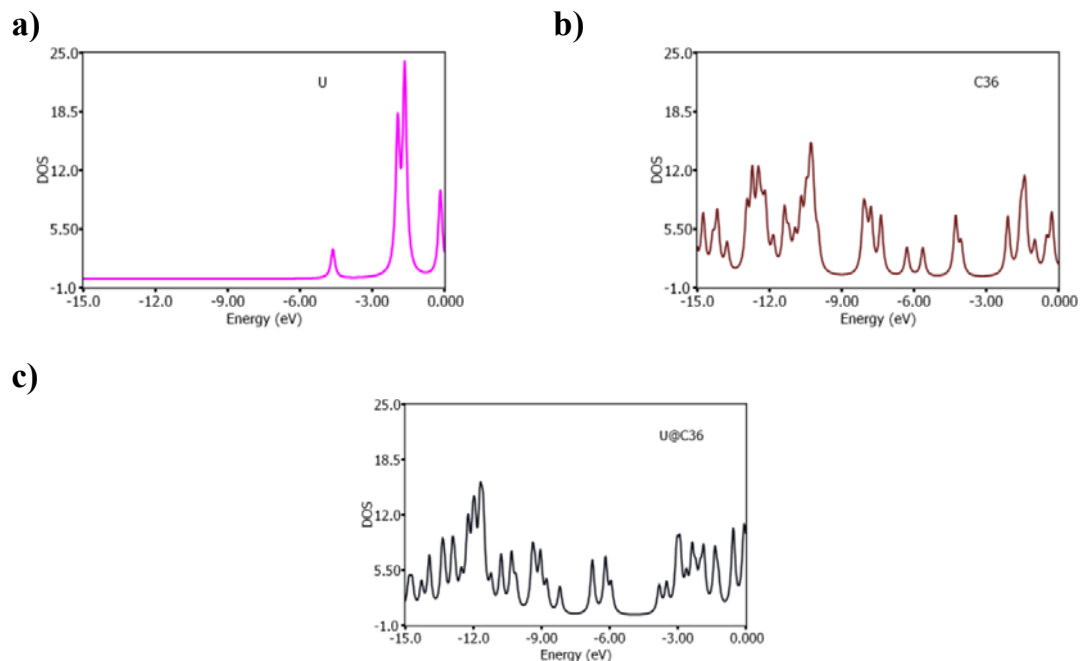


Figure 5.13 Density of states (DOS) for the a) uranium atom, b) bare C_{36} cage and c) $U@C_{36}$.

To understand the charge rearrangements due to the formation of the $U@C_{36}$ clusters from its constituent fragments, we have calculated the VDD, Hirshfeld and Mulliken charges as implemented in ADF program. The calculated VDD, Hirshfeld and Mulliken charges on the uranium atom for different structures are reported in Table 5.13.

Table 5.13 Calculated Mulliken, Hirshfeld and VDD charges on uranium atom in the $U@C_{36}$ isomers using TZ2P basis sets and B3LYP Functional with ADF program

Structures	Mulliken	Hirshfeld	VDD
Str-01- C_{6v}	0.840	0.738	0.555
Str-02- C_1	0.949	0.655	0.482
Str-03- C_2	1.062	0.634	0.471
Str-04- C_1	0.944	0.680	0.505
Str-05- C_s	0.897	0.675	0.499
Str-06- C_2	0.947	0.664	0.493

Str-07-C _{2v}	0.913	0.678	0.500
Str-08-C ₁	0.906	0.706	0.528
Str-09-C _S	0.924	0.701	0.518
Str-10-C _S	0.830	0.761	0.578
Str-11-C ₁	0.903	0.700	0.520
Str-12-C ₁	0.865	0.716	0.535
Str-13-C ₁	0.870	0.738	0.557
Str-14-C _{2v}	0.934	0.748	0.570
Str-15-C _S	0.829	0.769	0.588

From the reported results it is evident that the VDD charges lie in the range of 0.47 - 0.55. To get an idea about the distribution of electrons corresponding to the s, p, d, and f orbital occupations for the metal center in the cluster, we have reported the Mulliken orbital-wise population values for the uranium centre in U@C₃₆ isomers in Table 5.14.

Table 5.14 Calculated values of orbital population for the central uranium atom in U@C₃₆ isomers using TZ2P basis sets and B3LYP functional with ADF program

Structures	n(s)	n(p)	n(d)	n(f)
Str-01-C _{6v}	2.03	5.95	2.06	3.10
Str-02-C ₁	1.92	5.96	1.98	3.17
Str-03-C ₂	1.90	5.95	1.96	3.11
Str-04-C ₁	1.96	5.95	2.00	3.13
Str-05-C _S	1.94	5.96	1.99	3.19
Str-06-C ₂	1.96	5.93	1.95	3.19
Str-07-C _{2v}	1.96	5.95	1.98	3.18
Str-08-C ₁	1.97	5.95	2.02	3.13
Str-09-C _S	1.99	5.94	2.02	3.10
Str-10-C _S	2.02	5.95	2.06	3.11
Str-11-C ₁	1.97	5.94	2.00	3.16

Str-12-C ₁	1.98	5.96	2.04	3.15
Str-13-C ₁	2.01	5.95	2.04	3.12
Str-14-C _{2v}	1.99	5.95	2.03	3.07
Str-15-C _s	2.03	5.93	2.04	3.15

For all the isomers, 5f orbital occupations are around 3.1. This value is very close to the 5f metal occupation, which is 3. The total occupation corresponding to two s orbitals (6s and 7s) decreases to ~2 from the ideal value of 4, however, d orbital occupation (6d) increases to ~2 from the ideal value of 1 in the isolated atom.

5.3.2.5 Effect of Spin-Orbit Interaction

In general, spin-orbit interaction is very important for any molecular system that contains a heavy element. Therefore, we have systematically investigated the effect of spin-orbit interaction on the U@C₃₆ complex including geometry optimization and detail bonding energy analysis using ADF program. Changes in the structural parameters are found to be negligible after inclusion of the spin-orbit coupling. As far as the total interaction energy corresponding to atomic dissociation is concerned, an overall increase in stability by 1.98 eV (0.054 eV in terms of BE) is found after inclusion of spin-orbit effect. Detail bonding energy analysis considering spin-orbit effects leads to an increase of 0.008 % in the steric component and 0.11 % in the orbital component. It indicates that the spin-orbit effect tends to increase the contribution of the orbital interaction, which is stabilizing in nature.

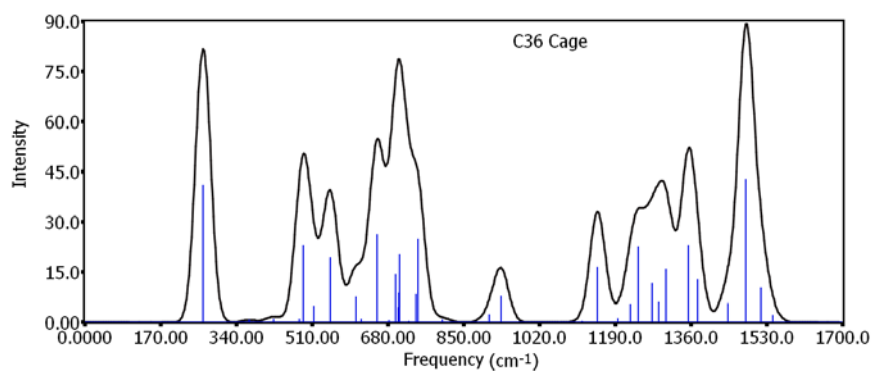
Although the effect of spin-orbit interaction is found to be insignificant in the energetics, still, it is interesting to assess its effect on the molecular orbital energy levels. The splitted molecular orbital levels after considering the spin-orbit effect are depicted in Figure 5.10. The splittings of the molecular orbital energy levels are found to be very

small (<0.05 eV) here, unlike $U@C_{20}$ case. A slight change is observed in the HOMO-LUMO gap for the $U@C_{36}$ cluster after inclusion of spin-orbit interaction. Thus, spin-orbit interaction has no major effect in case of $U@C_{36}$ cluster. This may be due to the presence of the C_{36} cage, which reduces this effect. Consequently, spin-orbit coupling does not affect the ground state molecular properties for the $U@C_{36}$ systems.

5.3.2.6 Spectroscopic Study for C_{36} and $U@C_{36}$ Clusters

Vibrational Spectra: The calculated vibrational spectra for the bare C_{36} cage and the $U@C_{36}$ cluster have been reported in Figure 5.14.

a)



b)

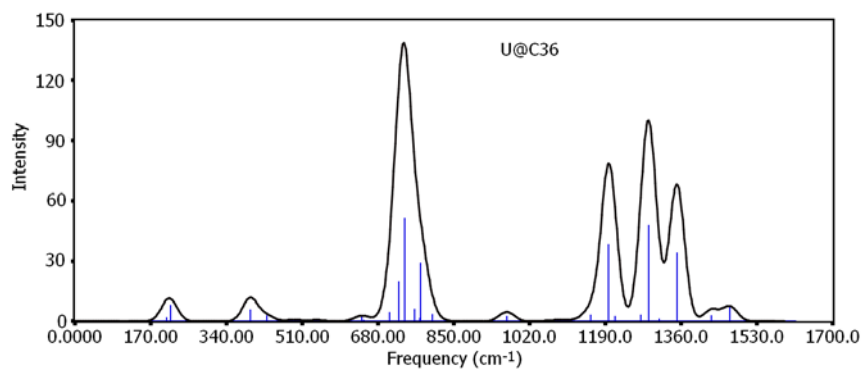


Figure 5.14 Simulated vibrational spectra of the a) bare C_{36} cage and b) $U@C_{36}$ cluster.

In case of bare C_{36} cage with D_{2d} point group, only the frequency values corresponding to the B_2 and E symmetries are IR-active, whereas, for the $U@C_{36}$ cluster (C_{6v} symmetry) frequencies with A_1 and E_1 symmetries are IR-active. The uranium atom has strong influence on the spectrum of the $U@C_{36}$ cluster. As a result, the peak positions and the corresponding intensities are changed drastically for the uranium encapsulated C_{36} clusters as compared to that in the bare C_{36} cage. One of the interesting features observed is that the lowest and highest frequency peaks in the C_{36} cage are shifted towards blue and red regions, respectively. In the case of $U@C_{36}$ system, the most intense peak is observed at 741 cm^{-1} and three other moderately intense peaks lie at 1198, 1287 and 1351 cm^{-1} . All these peaks arise due to combined motions of the central uranium atom and the cage except the 1287 cm^{-1} peak, which is the result of the motion of the cage only. It may be interesting to note that all these high intensity peaks are doubly degenerate i.e. these are arising from the frequency corresponding to the E_1 symmetry.

Electronic Spectra: Time-dependent density functional theory within the framework of ZORA has been used for the calculations of the electronic excited states of the bare C_{36} cage and the $U@C_{36}$ cluster in ADF. To obtain the excitation energies corresponding to the singlet-excited states, SAOP model functional has been employed here. In case of bare D_{2d} symmetric C_{36} cage the transitions from the ground state to the B_2 and E levels have been found to be allowed whereas for the $U@C_{36}$ cluster as the symmetry is C_{6v} , only the excitations having the symmetry E_1 and A_1 are allowed as far as selection rule is concerned. The scalar relativistic approach has been used for the calculation of the absorption spectra of the C_{36} cage. On the other hand, for the $U@C_{36}$ cluster, both scalar as well as spin-orbit methods have been adopted. All these results are displayed in

Figures 5.15 and 5.16. For the bare C_{36} cluster two main absorption peaks are observed at 5.35 and 5.75 eV along with some small humps at around 3.2, 3.95, 4.15, 4.6, 4.8 and 4.95 eV. After encapsulation of uranium atom, the absorption peaks are shifted slightly towards the lower energy i.e. higher wavelength region. The first absorption peak is observed at around 2.95 eV for the $U@C_{36}$ cluster using scalar relativistic approach. However, introduction of spin-orbit effect does not make significant changes in the UV-Vis spectra of the $U@C_{36}$ cluster, and the nature of the spectra is found to be almost similar to that obtained using the scalar approach.

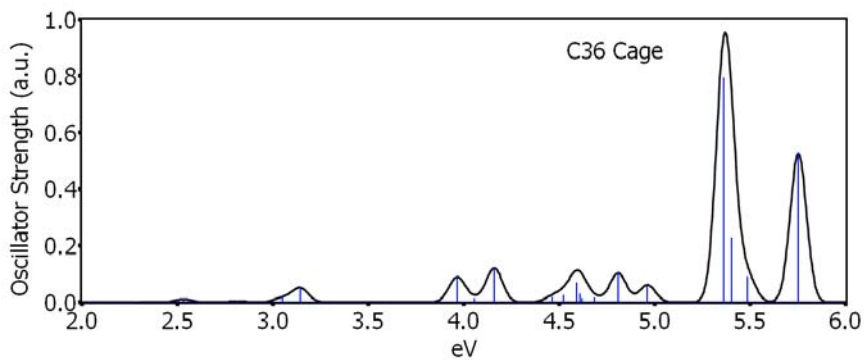
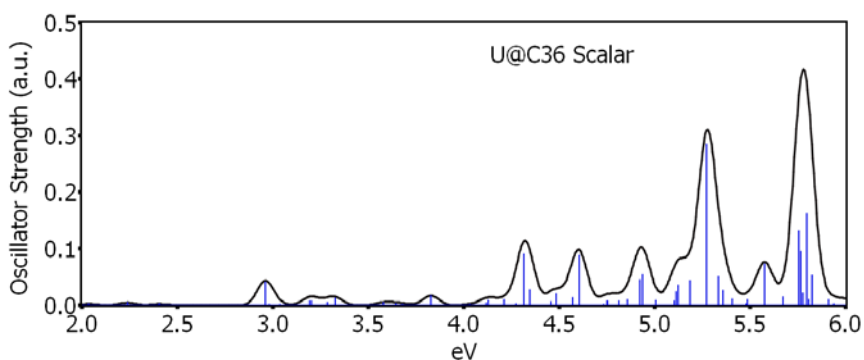


Figure 5.15 UV-visible spectra for the C_{36} cage.

a)



b)

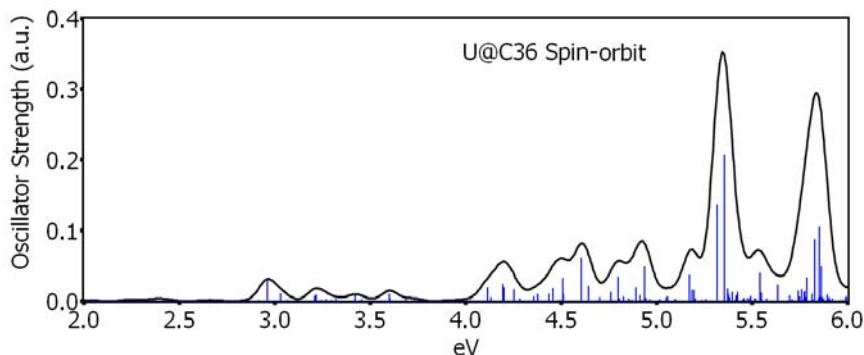


Figure 5.16 UV-visible spectra for U@C₃₆ cluster, a) without and b) with spin-orbit coupling.

Here it may be noted that the HOMO-LUMO gap of any chemical species is likely to correlate well with its excitation energy. In the present work, the HOMO-LUMO energy gap values for the U@C₃₆ system is found to be higher as compared to that of the bare C₃₆ cage. However, in the case of U@C₃₆, the first absorption peak is observed at lower energy (2.95 eV) as compared to that of the bare C₃₆ cage (3.2 eV). This may be due to the presence of uranium atom as it has been found that the first excitation peak for the free uranium atom appears at around 3 eV. Moreover, from the detail analysis of the low intense first excitation peak of U@C₃₆, involvement of uranium atom orbitals has been found to be significant.

5.4 Concluding Remarks

In this chapter, we have presented the results predicting a new class of closed shell species with smallest fullerene cages, viz., C₂₀ and C₃₆, through encapsulation of an actinide or lanthanide atom/ion, using density functional calculations. Structural,

electronic, bonding and spectroscopic properties for the clusters have been calculated and discussed.

Highly symmetric icosahedral structure along with large HOMO-LUMO gap indicates that the $M@C_{20}$ clusters are associated with high stability as compared to the bare C_{20} cage with D_{3d} symmetry. Similar to Pb_{12}^{2-} and Sn_{12}^{2-} species, all the predicted organometallic icosahedral $M@C_{20}$ systems with 26 valence electrons occupying the metal-carbon hybrid orbitals, can be considered as highly stable clusters with “intermediate magic numbers”. Preparation of the $M@C_{20}$ clusters using laser ablation techniques may be one of the possible ways of detecting the elusive I_h structure of C_{20} cage by mass spectroscopy or photoelectron spectroscopy as reported earlier for $U@C_n$ ¹⁵⁴ and $M@Sn_{12}^{-}$ ¹⁶⁷ clusters.

In case of C_{36} , we have considered different classical cage structures of C_{36} fullerene with an objective to investigate the possibility of enhancing the stability of the C_{36} cage through encapsulation of a uranium atom. We have studied fifteen $U@C_{36}$ isomers associated with various symmetries. Two competitive isomers are found to exist for the C_{36} cage, viz., D_{2d} and D_{6h} , whereas, for the $U@C_{36}$ cluster, the C_{6v} isomer, which is derived from the D_{6h} cage, is the most stable one and significantly lower in energy as compared to the other isomers. The stability of the most stable $U@C_{36}$ cluster has been rationalized through geometric and energetic criteria. Thus, the stability of the $U@C_{36}$ cluster has been explained in terms of larger HOMO-LUMO gap as compared to the bare C_{36} cage, higher binding energy per atom and calculated high negative values of free energy and enthalpy of reaction for the $U@C_{36}$ cluster during its formation from uranium and C_{36} species. Thus, the origin of the higher intensity peak corresponding to the $U@C_{36}$ cluster in the experimentally observed^{154,155} mass spectra of $U@C_{2n}$ clusters may be

attributed to the highly stable Str-01-C_{6V} structure, derived from the C₃₆ cage with D_{6h} symmetry. The stability and the magic nature of the uranium encapsulated 36-atom fullerene cage, as evident from the reported results, clearly indicate a possibility of formation of cluster-assembled material consisting of U@C₃₆ cluster as building block, although formation of metal encapsulated fullerene systems with varying number of carbon atoms may differ widely depending on the experimental conditions.^{51,154,217,218} Nevertheless, it may be noted that the significantly strong U@C₃₆ peak as compared to the adjacent peaks in the FT-ICR mass spectrum of cluster cations formed from the vaporization of a UO₂-graphite target also corroborate our inferences.

Chapter 6: Actinide and Lanthanide Encapsulated Metallofullerenes: Insight from 32-electron Principle

6.1 Introduction

6.1.1 Stability of Clusters: Effect of Electronic Shell Closing

In the past two decades cluster science has attracted enormous interest because of its applications in the design of novel materials with fascinating properties. In particular, just after the experimental identification of C_{60} by Kroto et. al^{18,19} in 1985, search for highly stable new clusters gained tremendous momentum. The origin of the stability of a particular cluster with respect to its neighboring ones can be considered as a manifestation of electronic or geometric shell closing.^{184,219,220} The effect of shell closing in atomic systems is responsible for the variation in chemical properties of the elements across the periodic table. Similarly, the geometrically and electronically closed shell structure can be regarded as one of the important factors to attain high stability for a particular cluster. Through encapsulation of a proper impurity atom (metallic or non-metallic), stability of a particular cluster can be enhanced^{51,184-187} drastically. These highly stable clusters show pronounced stability in the mass spectrum, and the exceptional stability of some of these clusters can be followed directly from a specific number of electrons corresponding to electronic shell closings. For instances, the Lewis octets and the Langmuir 18-electron (18e) rule²²¹ are well recognized. These correspond to fully occupied ns^2np^6 and $ns^2np^6(n-1)d^{10}$ orbitals, respectively. The numbers 8 and 18 are called magic numbers, a term borrowed from the same concept in nuclear physics. In the recent past, the actual interpretation of the 18-electron rule has been discussed by Pyykkö.²²² $W@Au_{12}$,¹⁸⁴⁻¹⁸⁶ $An@C_{28}$,^{53,155}

(where An stands for actinide atoms/ions) Au_{20} ,¹⁸⁹ Au_{32} ,¹⁹⁰ Au_{42} ,¹⁹¹ Au_{72} ,¹⁹² Pb_{12}^{2-} ,¹⁹³ Sn_{12}^{2-} ,¹⁹⁴ $M@Sn_{12}^{-}$,⁵³ $Pu@Pb_{12}$,^{54,83} $[U@Si_{20}]^{6-}$,²²³ $M@C_{20}$ (M = lanthanide/actinide atoms or ions),²²⁰ $U@C_{36}$ ^{51,154,157} etc. are some of the examples of recently reported important magic clusters.

6.1.2 Introduction to 32-electron Principle

In addition to the 8- and 18-electron principles, possibility of 32 valence electron systems had been indicated by Langmuir in 1921.²²¹ The first predicted metal encapsulated 32-electron system is $Pu@Pb_{12}$,^{54,83} where central Pu atom is attached to 12 Pb atoms, resulting into 32 valence electrons and corresponds to the fully occupied *spdf* shells. Here, 6 valence electrons from Pu^{2+} ion along with 26 valence electrons from Pb_{12}^{2-} collectively make an electron count of 32. Second example of such a system, $An@C_{28}$, has been predicted¹⁵⁵ later on, where An is an actinide atom/ion with 4 valence electrons. Here 32-electron criterion is satisfied cumulatively using the 4 valence electrons from an actinide atom/ion and 28 π electrons from the C_{28} cage. Subsequently, importance of 32-electron system is further emphasized in two news articles.^{224,225} The high stability of Au_{32} cluster can also be explained in terms of 32-electron principle. Recently, A new example of 32 electron system, $[U@Si_{20}]^{6-}$ is reported by Dognon et. al.²²³

In the present work our main objective is to explore the possibility of stabilization of small size fullerene through encapsulation of a suitable actinide/lanthanide metal atom or ion which will satisfy valence 32 electron counts for the central metal atom/ion.^{226,227} It can be achieved by varying the number of π and

valence electrons corresponding to the fullerene and the encapsulated metal atom, respectively.

For this purpose, we have taken 8-valence and 6-valence actinide or lanthanide atom/ion and encapsulated into C_{24} (24 π electrons) and C_{26} (26 π electrons) cages, respectively, with the objective to design new 32-electron system, followed by their systematic investigations.^{226,227}

6.2 Computational Details

In this present work, computational methodologies are same as discussed previously in Chapter 5, section 5.2. The software package CaGe²²⁸ developed by Brinkmann and McKay has been used to generate different isomeric structures of the fullerene.

6.3 Results and Discussions

6.3.1 Study of Ln/An encapsulated C_{24} fullerene

6.3.1.1 Bare C_{24} Isomers

We have considered here five lowest lying cage isomers of bare C_{24} , which are depicted in Figure 6.1. In the case of bare C_{24} fullerene only one classical isomer (STR01) exists and the other isomers are non-classical ones as reported earlier by An et. al. in 2008²²⁹. The four low energy non-classical isomers considered here are associated with one or two 4-membered ring(s) but no 7-membered ring. STR02, STR03, STR04 and STR05 consist of two 4-membered rings located far apart, only one 4-membered ring, two 4-membered rings separated by one 6-membered ring and two 4-membered rings widely separated, respectively. Other non-classical isomers of C_{24} are not considered as they are significantly higher in energy.

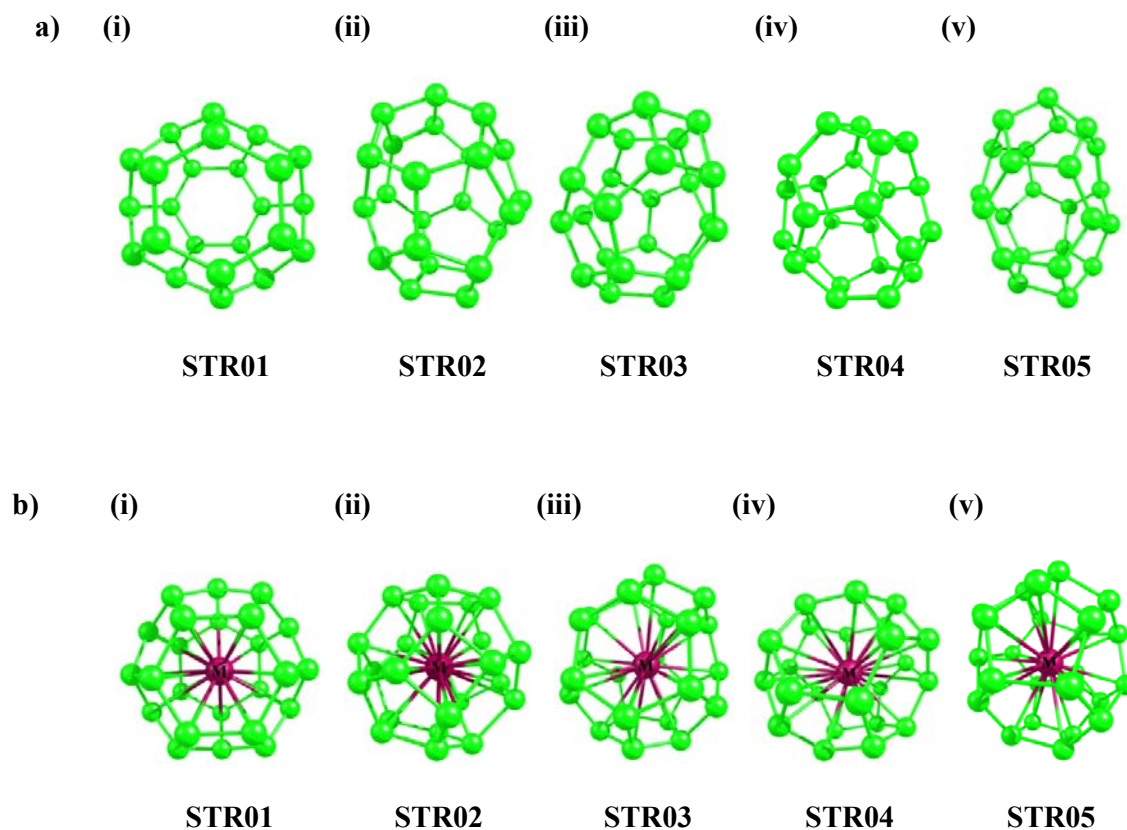


Figure 6.1 Optimized structures of a) bare C_{24} and b) $M@C_{24}$ clusters.

After optimization, the STR01 (classical isomer) was found to be associated with C_2 symmetry and the non-classical isomers STR02, STR03, STR04 and STR05 are of C_2 , C_s , C_s and C_1 symmetry, respectively. For all the bare C_{24} isomers average C-C and C-X (X is a centrally located dummy atom) bond lengths are reported in Table 6.1. Relative energy ordering and HOMO-LUMO gap for all the bare structures using PBE functional are reported in Tables 6.2 and 6.3, respectively. Among all the isomers considered here, the non-classical STR02 with C_2 symmetry is the most stable one and solitary classical isomer (STR01) is found to be the third most stable isomer, which is 0.15 eV higher in energy from the most stable structure at the PBE level of theory. However, energy ordering obtained using B3LYP functional is slightly different than

that obtained using the PBE functional (Table 6.2), and the classical isomer is found to be isoenergetic with the non-classical STR02.

Table 6.1 Calculated values of average X^a-C and M-C bond lengths for bare and metal encapsulated C₂₄ systems using PBE functional in Turbomole. Average C-C Bond lengths values are presented within the square bracket.

Isomers	Bare C ₂₄	Pu@C ₂₄	Sm@C ₂₄	Gd ⁺² @C ₂₄	Cm ⁺² @C ₂₄
STR01	2.256 [1.456]	2.315 [1.496]	2.311 [1.475]	2.302 [1.465]	2.304 [1.489]
STR02	2.213 [1.464]	2.328 [1.505]	2.335 [1.504]	2.332 [1.499]	2.329 [1.488]
STR03	2.253 [1.453]	2.334 [1.501]	2.333 [1.493]	2.321 [1.489]	2.321 [1.489]
STR04	2.262 [1.451]	2.332 [1.502]	2.329 [1.496]	2.326 [1.493]	2.328 [1.493]
STR05	2.273 [1.452]	2.349 [1.507]	2.349 [1.513]	2.341 [1.511]	2.340 [1.501]

^a X is a dummy atom, which is placed at the origin of the bare C₂₄ structures.

Table 6.2 Calculated relative energy values (in eV) as obtained for the bare C₂₄ and M@C₂₄ clusters using PBE (B3LYP) functional in Turbomole program and using PBE functional in ADF program within the square bracket

Isomers	Bare C ₂₄	Pu@C ₂₄	Sm@C ₂₄	Gd ⁺² @C ₂₄	Cm ⁺² @C ₂₄
STR01	0.15 (0) [0.15]	0.0 (0) [0]	0.0 (0) [0]	0.0 (0) [0]	0.0 (0) [0]
STR02	0.0 (0.02) [0]	3.61 (4.24) [3.37]	3.18 (2.33) [2.76]	2.91 (1.50) [3.59]	3.35 (3.18) [3.17]
STR03	0.04 (0.24)	2.15 (2.32)	2.07 (1.62)	2.02 (1.91)	2.21 (2.26)

	[0.06]	[2.23]	[2.00]	[2.15]	[2.11]
STR04	0.17 (0.17) [0.17]	1.86 (1.96) [1.72]	1.58 (1.02) [1.36]	1.50 (0.31) [1.84]	1.71 (1.66) [1.59]
STR05	0.44 (0.60) [0.46]	5.98 (6.23) [6.04]	5.67 (2.33) [5.53]	5.54 (4.62) [5.97]	5.99 (6.07) [5.71]

Table 6.3 Calculated values of HOMO-LUMO Gap (in eV) as obtained from Turbomole program for the bare C_{24} and $M@C_{24}$ clusters using PBE (B3LYP) functional

Isomers	Bare C_{24}	$Pu@C_{24}$	$Sm@C_{24}$	$Gd^{+2}@C_{24}$	$Cm^{+2}@C_{24}$
STR01	0.47 (1.83)	1.47 (3.26)	0.39 (3.57)	1.22 (3.42)	1.37 (3.99)
STR02	1.27 (2.52)	1.03 (1.49)	0.26 (3.07)	0.55 (2.51)	1.18 (3.44)
STR03	0.83 (1.89)	1.49 (3.05)	0.48 (3.12)	0.54 (2.07)	1.49 (3.74)
STR04	0.99 (2.16)	1.39 (3.03)	0.56 (3.07)	0.86 (2.73)	1.53 (3.78)
STR05	1.48 (2.66)	0.97 (2.45)	0.22 (1.92)	0.35 (2.31)	1.16 (3.14)

6.3.1.2 Structural Analysis of $M@C_{24}$ Isomers

Here our main idea is to find out systems with 32 valence electron count involving C_{24} fullerene. For this purpose we have used atoms or ions with 8 valence electrons (Pu , Cm^{2+} , Sm and Gd^{2+}) for encapsulation into above mentioned optimized classical and non-classical bare C_{24} isomers. Both PBE and B3LYP functionals have been used for the optimization purpose in Turbomole. Now onwards we have considered the results

obtained using Turbomole program, unless otherwise stated. All real frequencies for the $M@C_{24}$ structures reported here simply suggest that these complexes are true minima on their respective potential energy surfaces. It is mentioned above that the non-classical isomer with C_2 symmetry has been the most stable bare C_{24} cluster, however, after encapsulation either of the Pu, Cm^{2+} , Sm and Gd^{2+} metal atom or ion, the classical isomer attained D_{6d} symmetry and becomes the most stable structure using both PBE and B3LYP functionals. This transformation from low to high symmetry is an indication of stability gain after incorporation of a suitable actinide or lanthanide atom or ion. The optimized structures for all the plutonium based complexes are presented in the Figure 6.1. In any particular C_{24} isomer, the structures of Cm^{2+} , Sm and Gd^{2+} doped C_{24} cluster are almost the same irrespective of the encapsulated metal atom or ion. We find that the classical $M@C_{24}$ isomer (STR01) is the most stable one irrespective of the encapsulated species considered here. Moreover, $Pu@C_{24}$ (STR01) is found to be energetically the most stable among all the classical $M@C_{24}$ (STR01) isomers, as far as the binding energy per atom is concerned (Figure 6.2). Thus, classical $Pu@C_{24}$ is used as a representative for further studies beyond the structure and stability aspects, i.e. for the analysis of molecular orbital energy diagram, vibrational and UV-Vis spectra, effect of spin-orbit interactions etc. Average C-C and M-C bond lengths for all the metal encapsulated C_{24} clusters are reported in Table 6.1. Encapsulation of metal atom/ion within the C_{24} cage leads to an overall increase in cage size, and as a result average M-C and C-C bond lengths are found to be increased in $M@C_{24}$ as compared to the average X-C and C-C bond lengths in the bare C_{24} clusters. It may be noted that there are three categories of C-C bonds and two classes of M-C bonds present in the most stable $M@C_{24}$ classical

isomer (STR01), with 12 bonds in each category or class. However, for the bare C_{24} -STR01 (C_2 symmetry), there are seven categories of bond lengths present for each of the C-C and X-C bonds. Nevertheless, for the purpose of comparison it is better to take the average C-C and M-C (X-C for the bare) bond lengths. Thus, the average C-C bond length varies from 1.456 to 1.496 Å from bare C_{24} -STR01 to $Pu@C_{24}$ (STR01). Similarly, for other encapsulated species also C-C bond length values are increased as compared to the corresponding bare C_{24} cage. It is also to be noted that the average X-C bond length lies in the range, 2.213-2.273 Å for the bare C_{24} cage isomers, whereas average Pu-C bond length varies from 2.315 to 2.349 Å in the case of $Pu@C_{24}$ isomers. This trend is similar for the other encapsulated structures also. Among all the $M@C_{24}$ -STR01 species, $Pu@C_{24}$ -STR01 has the largest average C-C and M-C bond lengths, although the differences are small from that of the other metal species encapsulated clusters.

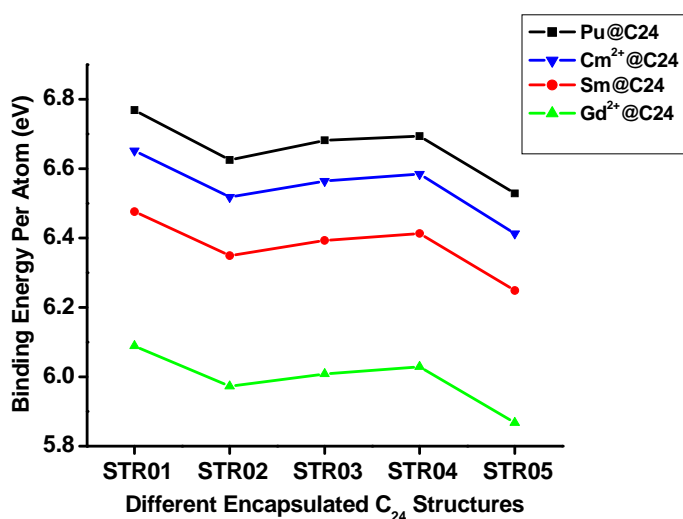


Figure 6.2 Binding energy per atom graph for different $M@C_{24}$ clusters.

6.3.1.3 Energetics and Thermodynamics Stability of M@C₂₄ Isomers

The relative energy ordering of the bare as well as encapsulated structures are calculated and reported in Table 6.2 using both PBE and B3LYP functionals. It has already been mentioned that the non-classical STR02 isomer is the most stable for the bare C₂₄ as obtained using PBE functional, and the classical STR01 is found to be the most stable for the M@C₂₄ clusters. Therefore, STR02 is taken as a reference for predicting the stability of other bare C₂₄ isomers and STR01 is taken as reference for the other metal encapsulated C₂₄ clusters (for any particular metal atom/ion). According to the relative energy values, STR05 is found to be the least stable among all the encapsulated species irrespective of the encapsulated atom/ion. There are slight differences in energy ordering using B3LYP functional, and STR01 becomes the most stable for the bare C₂₄ structure, however, the energy ordering remains the same for the encapsulated structures. Moreover, the relative energy ordering is exactly the same using the PBE functional as obtained from Turbomole and ADF programs.

Thermodynamic parameters i.e. enthalpy change (ΔH) and Gibbs free energy change (ΔG) for the encapsulation reaction ($M + C_{24} \rightarrow M@C_{24}$) have been calculated for all the lanthanide/actinide encapsulated complexes and reported in Table 6.4.

Table 6.4 Calculated enthalpy values (ΔH in kJmol^{-1}) for the reaction, $M + C_{24} \rightarrow M@C_{24}$. Corresponding values of Gibbs free energies (ΔG in kJmol^{-1}) are given within the square bracket

Isomers	Pu@C ₂₄	Sm@C ₂₄	Gd ⁺² @C ₂₄	Cm ⁺² @C ₂₄
STR01	-620.1 [-549.2]	71.3 [154.1]	1027.2 [1098.7]	-335.8 [-262.8]
STR02	-272.6 [-219.1]	390.8 [443.7]	1303.7 [1358.1]	-8.4 [48.1]

STR03	-299.4 [-352.3]	394.9 [341.0]	1333.7 [1281.5]	-10.3 [-61.2]
STR04	-446.8 [-500.8]	229.3 [174.5]	1165 [1111.8]	-177.2 [-229]
STR05	-88.6 [-37.2]	582.6 [633.8]	1514.7 [1568.9]	195.4 [250.5]

The calculated thermodynamic parameters provide consistent trends with the relative energy orderings. The results suggest that the classical encapsulated fullerenes are more stable than the non-classical metal encapsulated fullerenes. Similar trend has been found with the binding energy per atom values (Figure 6.2). Moreover, Pu@C₂₄ (STR01) with largest negative ΔH (-620.1 kJ mol⁻¹) and ΔG (-549.2 kJ mol⁻¹) values is found to be the most stable, and accordingly the encapsulation process is also highly feasible. The Sm and Gd²⁺ encapsulated C₂₄ complexes are rather less stable energetically as compared to the Pu and Cm²⁺ encapsulated C₂₄ complexes (except for Cm²⁺@C₂₄ STR05). The ΔH value varies from -620.1 to -88.6 kJ mol⁻¹ for Pu encapsulated structures. The negative values for the enthalpy change suggest that these encapsulation processes are exothermic in nature. For the Pu and Cm²⁺ encapsulated fullerenes ΔH values are negative, however, the same is positive for the Sm and Gd²⁺ containing species. Similarly for the Pu@C₂₄ isomers, ΔG varies from -549.2 to -37.2 kJ mol⁻¹, which also indicate the feasibility of the encapsulation of Pu atom inside the C₂₄ cage. Change in Gibbs free energy values is found to be negative for both the actinide containing species (except Cm²⁺-STR02 and Cm²⁺-STR05), however ΔG values are positive for Sm and Gd²⁺ encapsulated isomers. To examine the feasibility of the encapsulation process we have compared the stability of Pu@C₂₄

systems with some of the experimentally observed endohedral metallofullerene systems such as $U@C_{28}$ ^{51,154} and $Ti@C_{28}$.¹⁵⁴ The calculated ΔG and ΔH values are found to be -673, -722 for $U@C_{28}$ and -541, -548 kJ/mol for $Ti@C_{28}$ system using the same level of theory. These ΔG and ΔH values are comparable with the presently reported ΔG and ΔH values (-549 and -620 kJ/mol) for the most stable D_{6d} symmetric $Pu@C_{24}$ system. This supports the possible formation of the $Pu@C_{24}$ cluster through proper experimental technique.

In general, these types of clusters are usually formed from the constituent atomic components (obtained by laser ablation of the precursor solid materials),^{51,53,154,185} therefore, it is interesting to know the binding energy per atom (BE) of the clusters with respect to the atomic fragments. Thus, apart from the thermodynamic parameter and relative energy calculations, we have calculated the binding energy of a metal encapsulated cluster with respect to its atomic fragments using the following equation:

$$BE = - [E (M@C_{24}) - E (M) - 24E(C)]/n$$

Figure 6.2 represents the trends in the variation of BE for the different $M@C_{24}$ isomers with varying the trapped species. Here BE denotes the dissociation energy of a complex into its atomic fragments and refers to the process, $M + 24 C \rightarrow M@C_{24}$. All the clusters are found to be highly stable with respect to their dissociation into constituent atomic fragments with a BE range of 5.87 to 6.77 eV. As far as the BE results are concerned, for all the encapsulated species STR01 is the most stable and STR05 is the least stable isomer irrespective of the central metal atom/ion present. The stability ordering for a particular isomer of $M@C_{24}$ decreases in the order $Pu-Cm^{2+}$ - $Sm-Gd^{2+}$. Results obtained from the BE calculations are also in exact agreement with the calculated values of thermodynamic parameters and the relative energy

trends. Moreover, the calculated BE value for the most stable D_{6d} symmetric $\text{Pu}@C_{24}$ (6.77 eV) system is found to be slightly higher as compared to the previously predicted $\text{U}@C_{20}$ and $\text{U}@C_{26}$ systems (6.72 and 6.28 eV, respectively). It is interesting to note that the calculated BE value is 6.39 eV for the experimentally observed $\text{U}@C_{28}$ system. Thus, through proper tuning of the experimental parameters it may be possible to observe the $\text{Pu}@C_{24}$ system experimentally.

6.3.1.4 Molecular Orbital Energy Diagram and Charge Distributions

Apart from the above energy criteria a large HOMO-LUMO gap in the encapsulated structures is also a criterion of stability. The HOMO-LUMO gap values for these metallofullerenes are presented in Table 6.3 using both PBE and B3LYP functionals. For a particular C_{24} isomer the HOMO-LUMO gap for the encapsulated complexes differ depending upon the metal species trapped inside it. The most stable bare C_{24} STR02 isomer has sufficiently high HOMO-LUMO gap of 2.52 eV calculated using B3LYP functional. In case of STR01 although bare isomer has low HOMO-LUMO gap (1.83 eV), however, after encapsulation of a eight valance metal atom/ion the HOMO-LUMO gap increases significantly (3.26 eV). The HOMO-LUMO gap values can also be correlated well with the binding or encapsulation energy ordering of the metal encapsulated structures. Actinide encapsulated isomers have larger HOMO-LUMO gap values as compared to the corresponding lanthanide encapsulated species. Molecular orbital energy diagram as calculated using the PBE functional with ADF program is depicted in Figure 6.3 for the $\text{Pu}@C_{24}$ (STR01) system with D_{6d} symmetry. Molecular orbitals (MOs) $5b_2$ and $5e_4$ are the HOMO and the LUMO, respectively, for the D_{6d} $\text{Pu}@C_{24}$ isomer. The MOs $5b_2$, $4e_4$, $4e_3$, $6e_1$, $4b_2$, $5e_1$, $4e_5$, $4e_2$, $5a_1$ and $4a_1$

have the contribution from both the metal atom/ion and carbon atoms, with a cumulative valence electron count of 32.

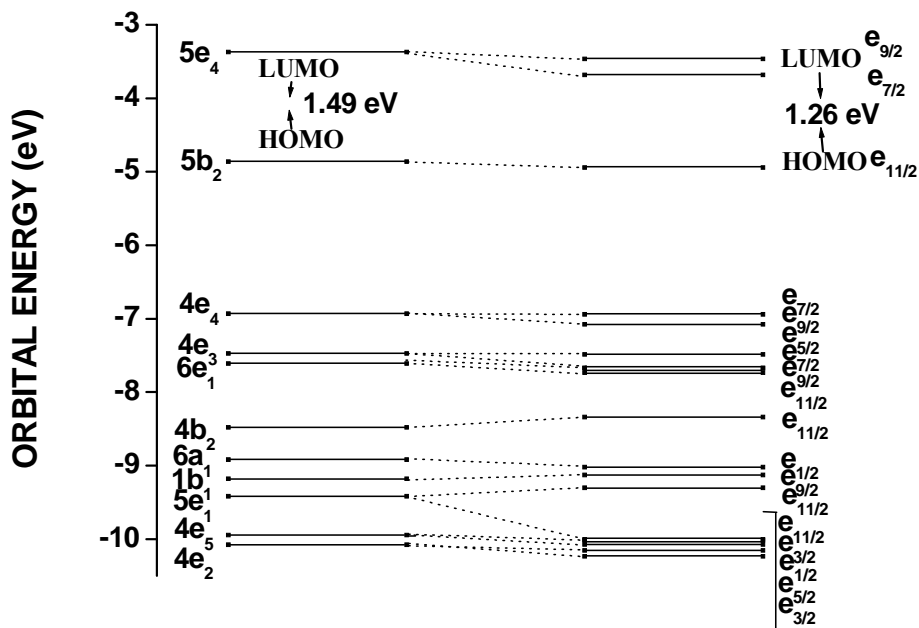


Figure 6.3 Molecular orbital energy diagram for the Pu@C₂₄ (D_{6d}) cluster without (left) and with (right) spin-orbit coupling.

The pictures of the valence MOs have been depicted in Figure 6.4. The metal atom/ion contributes 8 valence electrons and remaining 24 electrons come from the C₂₄ cage (24 π electrons). Significant amount of overlap has been found to be present between the metal and the C₂₄ cage orbitals for these MOs. However, 6a₁, 1b₁, 3e₂, 3e₄, 4e₁, 3e₅ and 3e₃ MOs correspond to pure carbon orbitals of C₂₄. The energy gap between the 4a₁ and 2e₅ MOs is also found to be fairly large, and a total number of 56 electrons up to the 4a₁ MOs correspond to the cumulative number of electrons occupied by the metal-carbon hybrid MOs (32 electron), and pure carbon MOs (24 electrons) mentioned above.

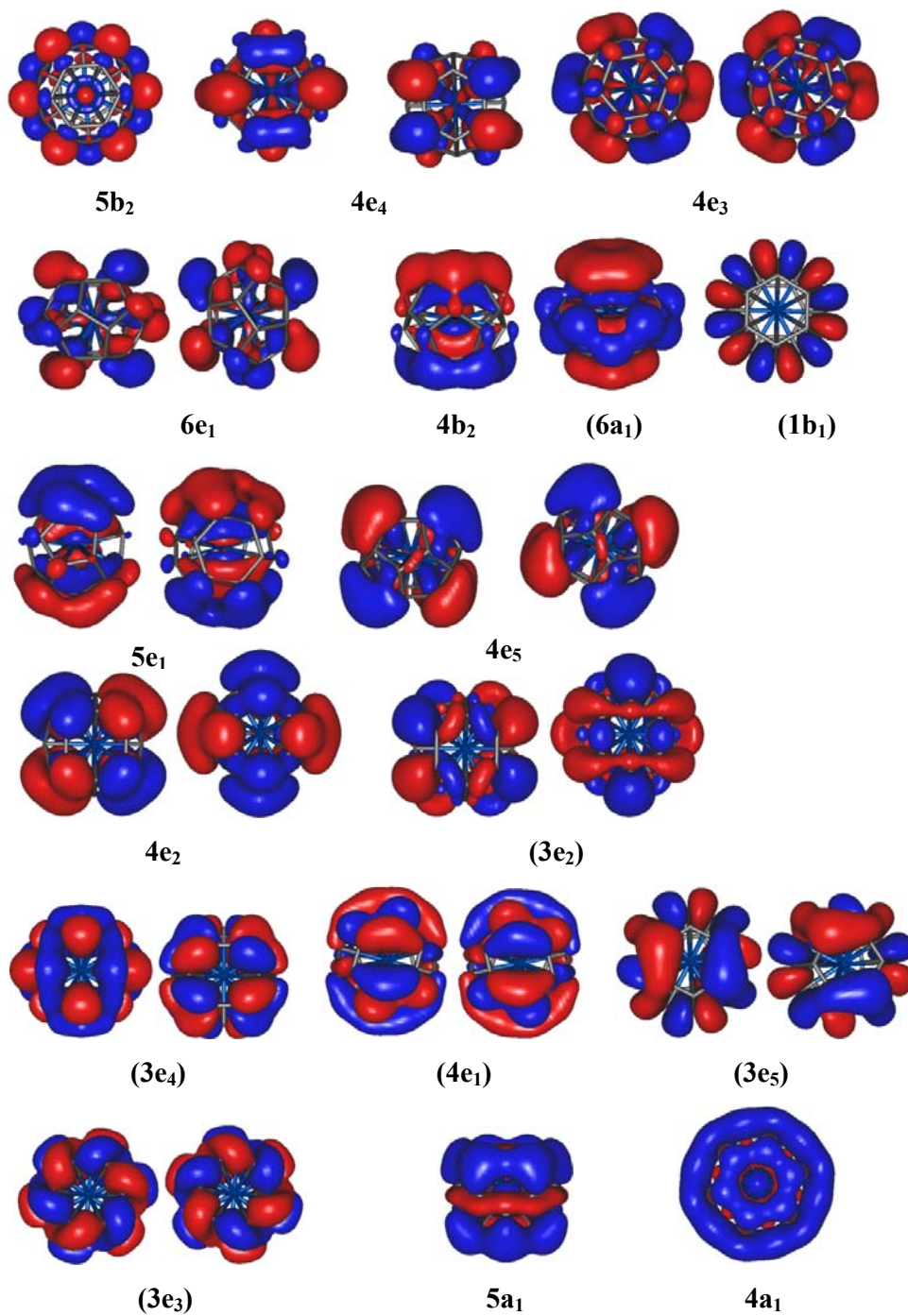
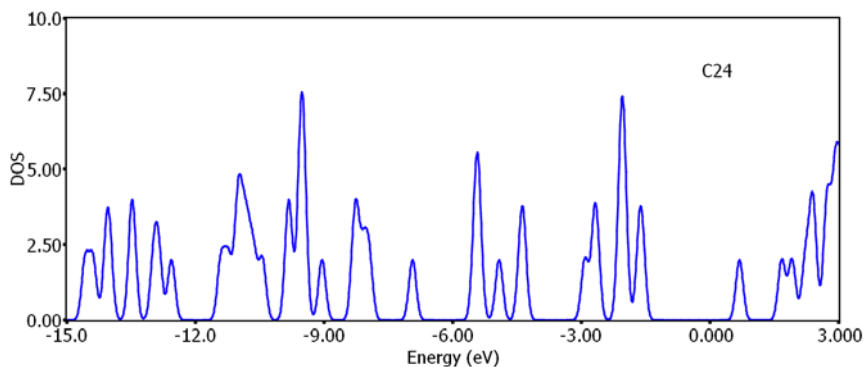


Figure 6.4. Valence molecular orbitals of $\text{Pu}@C_{24}$. Orbitals written within the parentheses refers to the orbitals contributed by pure C_{24} cage.

Thus, it is evident that the plutonium atom corresponding to 8 valence electrons has been able to elevate the C_2 symmetry of the C_{24} cage to the D_{6d} symmetry through fulfilling the 32-electron principle corresponding to the *spdf* shells of the central metal atom. Here, it may be noted that as per group theoretical analysis, for a D_{6d} symmetric system the molecular orbitals a_1 , $(b_2 \oplus e_1)$, $(a_1 \oplus e_2 \oplus e_5)$, $(b_2 \oplus e_1 \oplus e_3 \oplus e_4)$ can be assigned in terms of the central metal atomic orbitals *s*, *p*, *d* and *f*, respectively. Now, it is interesting to analyze the valence MOs to get the contributions of the centred metal orbitals from symmetrized fragment orbitals (SFOs) analysis. From this analysis it has been found that the hybrid $5b_2$ orbital is primarily of *f* character (~64% contribution from the Pu f_{xyz} orbital). All the other hybridized orbitals are associated with smaller *f* character (<40%). If an MO with more than 50% 5*f* contribution is assumed as a pure 5*f* then Pu remains in $5f^2$ configuration in the Pu@ C_{24} system. The contribution of the metal *f* orbitals towards MOs $4e_4$, $4e_3$ and $6e_1$ are found to be 36%, 30% and 27%, respectively. Remaining valence hybrid orbitals consist mainly of Pu *p* and *d* characters, without any *f* orbital contribution. The densities of states (DOS) of the bare C_{24} cage and the Pu@ C_{24} (STR01) cluster are plotted in Figure 6.5.

(a)



(b)

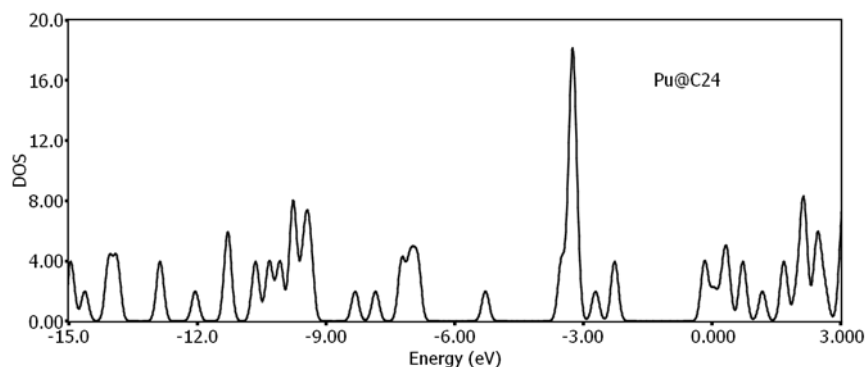


Figure 6.5 Density of states (DOS) for the (a) bare C₂₄ cage and (b) the Pu@C₂₄ cluster.

DOS corresponding to the Pu@C₂₄ cluster is quite different from that of the bare C₂₄ cluster, which indicates significant mixing between the orbitals of the plutonium atom and the fullerene cage. The HOMO energies for these two systems are -5.39 and -4.55 eV, respectively.

Now it will be interesting to discuss the charge distributions in the M@C₂₄ clusters. Natural population analysis (NPA) method has been employed to study the charge distribution on the atoms in the clusters. The charge distribution and the relative stability of the species follow a good agreement for the neutral clusters (Pu@C₂₄ and Sm@C₂₄) i.e. for the most stable cluster the charge value is the largest and then it gradually decreases following the same stability trend. This observation is not exactly matched with the charged species. High negative charge values are obtained on the metal centers in the M@C₂₄ structures, irrespective of the initial charges located on the metal atom. This is to some extent unrealistic, particularly for the Cm²⁺ and Gd²⁺ encapsulated structures. In view of this, additionally we have calculated the Voronoi deformation density (VDD) charges (Table 6.5).¹⁹⁵

Table 6.5 Calculated natural and VDD (in parenthesis) charge values on metal centers for M@C₂₄ clusters computed with PBE functional in Turbomole and ADF programs, respectively

Isomers	Pu	Sm	Gd	Cm
STR01	-3.526 (0.474)	-2.784 (0.219)	-2.254 (-0.148)	-2.228 (0.046)
STR02	-3.297 (0.463)	-2.457 (0.019)	-1.892 (0.080)	-2.329 (0.072)
STR03	-3.369 (0.483)	-2.622 (0.224)	-2.421 (-0.128)	-2.064 (0.039)
STR04	-3.358 (0.464)	-2.552 (0.217)	-2.399 (-0.130)	-1.981 (0.023)
STR05	-3.218 (0.483)	-2.434 (0.225)	-2.271 (-0.123)	-1.888 (0.036)

The VDD scheme is based on the calculated amount of electron density that flows to or from a certain atom due to bond formation through spatial integration of the deformation density over the atomic Voronoi cell, and thus is not explicitly dependent on the basis functions involved in a calculation. Consequently, VDD derived charge values are considered to provide chemically meaningful charge distributions values. Here, it may be noticed that lanthanides are having less positive or slightly negative charges; however, actinides are associated with slightly higher positive charge values. The orbital population i.e. distribution of electrons corresponding to *s*, *p*, *d* and *f* orbitals for the central metal atom of various encapsulated structures, calculated using NPA scheme are reported in Table 6.6.

Table 6.6 Calculated values of orbital populations for the central metal atom (M) in M@C₂₄ clusters using PBE functional in Turbomole.

Isomers		Pu@C ₂₄	Sm@C ₂₄	Gd ⁺² @C ₂₄	Cm ⁺² @C ₂₄
STR01	n(s)	4.334	4.323	4.372	4.335
	n(p)	11.997	12.002	11.999	11.997
	n(d)	11.881	12.621	12.536	11.879
	n(f)	9.311	7.836	9.318	10.332
STR02	n(s)	4.315	4.299	4.349	4.314
	n(p)	11.974	11.987	11.983	11.969
	n(d)	11.857	12.573	12.495	11.835
	n(f)	9.147	7.597	9.063	10.208
STR03	n(s)	4.324	4.309	4.358	4.323
	n(p)	11.982	11.989	11.988	11.978
	n(d)	11.882	12.602	12.514	11.864
	n(f)	9.178	7.72	9.202	10.253
STR04	n(s)	4.318	4.303	4.353	4.316
	n(p)	11.987	11.992	11.992	11.985
	n(d)	11.863	12.565	12.482	11.847
	n(f)	9.186	7.691	9.152	10.248
STR05	n(s)	4.308	4.294	4.342	4.307
	n(p)	11.971	11.981	1.975	11.963
	n(d)	11.875	12.611	12.513	11.847
	n(f)	9.061	7.547	9.055	10.151

Values for n(s) and n(p) follow a similar trend for all the encapsulated species whereas, a huge fluctuation is observed in the values of n(d) and n(f). It may be interesting to note that for the lanthanide encapsulated species n(d) populations are larger as compared to the actinide encapsulated species whereas, in case of n(f) population just opposite trend is observed. It may be due to the larger spatial extent of the 5f orbitals of actinides as compared to the 4f orbitals of lanthanides.

6.3.1.5 Effect of Spin-Orbit interaction

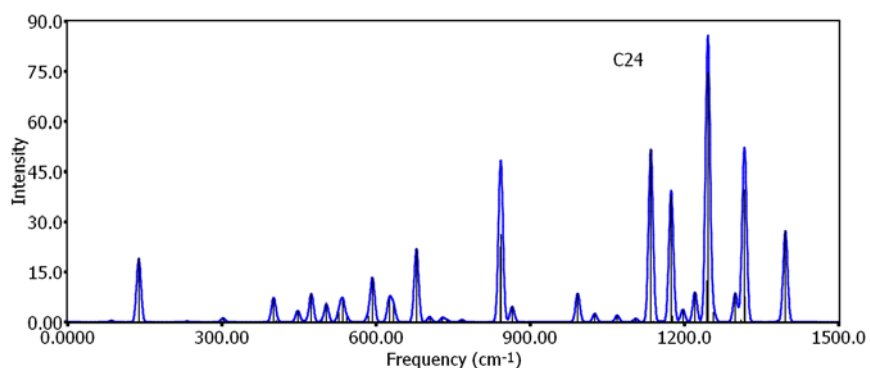
Spin-orbit effect is very much significant in presence of any heavy element within a chemical system. To assess the effect of spin-orbit interaction we have taken Pu@C₂₄ complex and made a systematic investigation. Inclusion of spin-orbit effect for the geometry optimization step leads to almost no change in bond length values as compared to the corresponding values obtained using relativistic scalar ZORA calculations. After inclusion of spin-orbit effect, an overall increase in stability by 2.68 eV (0.111 eV in terms of BE) is found as far as the total interaction energy corresponding to atomic dissociation is concerned. It may also be noted that there is an increase of 0.17 % in the steric component and 0.41 % in orbital component after incorporating spin-orbit effect.

Now, it is interesting to consider the spin-orbit effect on the orbital energy diagram. For all the valence orbitals, spin-orbit splittings are reported in Figure 6.3. The effect of spin-orbit interaction is not very significant for the systems studied here. It can be noticed that after inclusion of spin-orbit interaction, the HOMO-LUMO gap for the Pu@C₂₄ cluster calculated using scalar relativistic approach is decreased from 1.49 to 1.26 eV (using PBE functional). The extent of splitting of the molecular orbital levels are found to be rather small except for the 5e₁ mixed orbital, which shows significant splitting with a value of 0.70 eV. Thus, the effect of spin-orbit coupling is not that significant for the present systems. It may be attributed to the presence of C₂₄ cage, which reduces the effect of spin-orbit interaction.

6.3.1.6 Spectroscopic Analysis: C_{24} and $M@C_{24}$

Vibrational Spectra: A detailed IR spectroscopic analysis for the bare as well as the encapsulated structures has been carried out using Turbomole program. Harmonic vibrational spectra for the bare C_{24} (STR01) and $Pu@C_{24}$ (STR01) clusters are represented in Figure 6.6. In the case of bare C_{24} cage with C_2 point group, both the frequency values corresponding to the A and B symmetries are IR-active, whereas, for the $Pu@C_{24}$ (D_{6d} symmetry) cluster frequencies with B_2 and E_1 symmetries are IR-active. It has been found that in the case of vibrational spectra of the $Pu@C_{24}$ cluster, the Pu atom has strong influence on the spectrum.

(a)



(b)

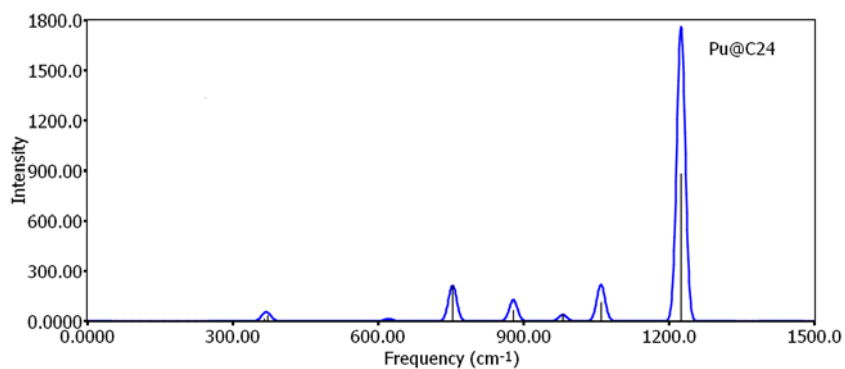


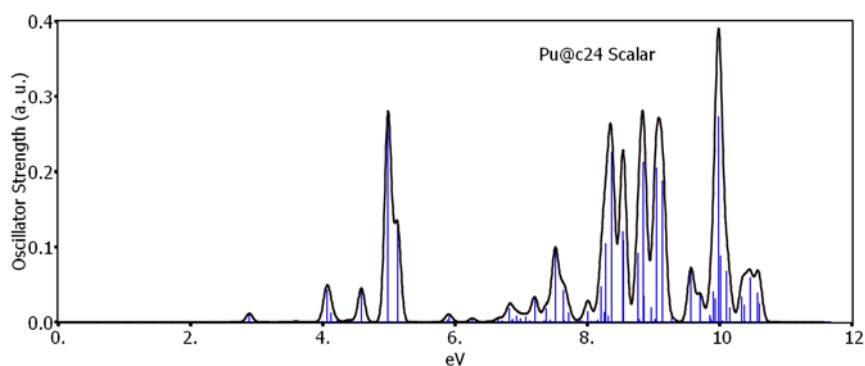
Figure 6.6 Simulated vibrational spectra of the (a) bare C_{24} cage and (b) $Pu@C_{24}$ cluster.

As a result, the peak positions and the corresponding intensities are changed drastically for the Pu encapsulated C_{24} cluster as compared to that in the bare C_{24} cage. It is interesting to note that the lowest and the highest frequency peaks in the C_{24} cage are shifted towards the blue and red regions, respectively. The first hump in the vibrational spectrum of the $Pu@C_{24}$ cluster is a combination of two peaks (366 cm^{-1} and 372 cm^{-1}), which can be ascribed to be associated with a combined motion of the encapsulated metal atom (Pu) and the C_{24} cage atoms. The highest frequency peak of 1225 cm^{-1} is also associated with highest intensity and it is also due to a combined motion of the Pu atom and the C_{24} cage atoms. Other non-zero intensity peaks are found to be at $621, 753, 879, 981, 1060\text{ cm}^{-1}$, where all the vibrational peaks arise because of the combined motion of Pu atom and the C_{24} cage atoms, except the 981 cm^{-1} peak. The 981 cm^{-1} peak is the result of the motion of the C_{24} cage only.

Electronic Spectra: Time-dependent density functional theory with ZORA approach has been adopted here for calculating the vertical electronic excited states to obtain UV-Vis. Spectra. For this purpose SAOP model functional in ADF program has been used to calculate the excitation energies corresponding to the singlet-singlet excitations. As far as the selection rule is concerned, only the transitions from the ground state D_{6d} structure of $Pu@C_{24}$ cluster to the e_1 and b_2 states have been found to be the dipole allowed transitions. The calculated spectra using scalar relativistic approach within the framework of ZORA as well as spin-orbit interaction are given in Figure 6.7 for the Pu encapsulated C_{24} cage structure. For the purpose of comparison we have also calculated the similar spectrum for the bare C_{24} cage as obtained using scalar relativistic approach, which is represented in Figure 6.8. From the figures it is

clear that the low intensity absorption maxima found at the visible region corresponding to the C_{24} cage (~ 1.5 eV) is shifted towards higher energy region (~ 2.95 eV) for $Pu@C_{24}$ cluster. High intensity peaks for the bare C_{24} cluster generally lie in the range 4.5-5.8 and 8.5-10.5 eV. After encapsulation of a Pu atom these high intensity peaks are found to be shifted slightly towards higher energy region.

(a)



(b)

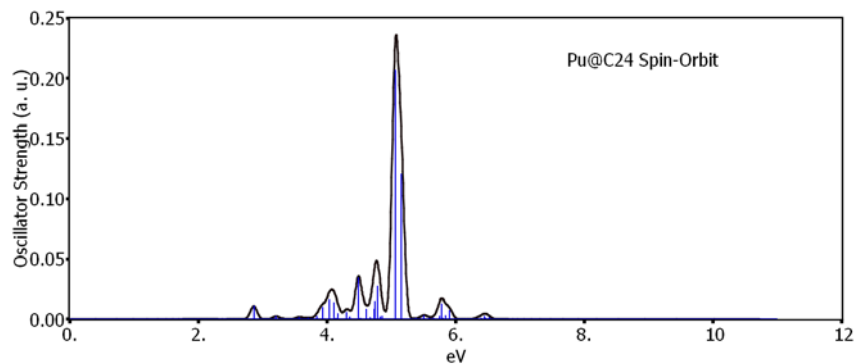


Figure 6.7 UV-Visible spectra for the $Pu@C_{24}$ cluster: (a) without and (b) with spin-orbit coupling.

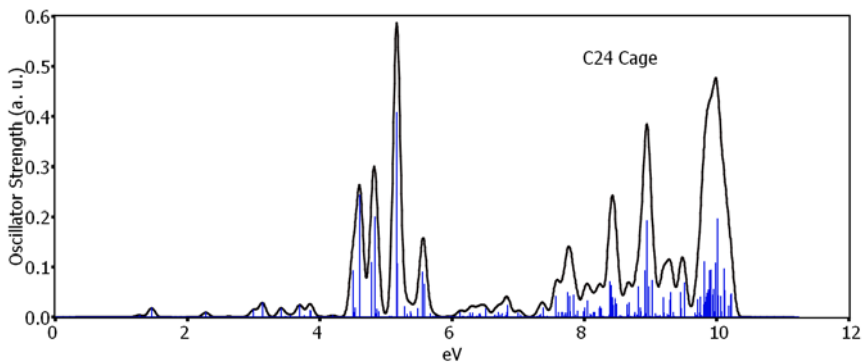


Figure 6.8 UV-visible spectra for the C₂₄ cage.

After inclusion of spin-orbit interaction in the Pu@C₂₄ cluster, the absorption peak observed at around 5 eV is found to be slightly blue shifted and this is the only high intensity peak that is retained after incorporation of spin-orbit effect. Overall intensity of the peaks also decreases after considering spin-orbit interaction. Here it may be noted that depending on the nature of the encapsulated metal atom/ion the metal-cage interaction would be changed. Consequently, spectrum nature may be strongly influenced by the metal species encapsulated in the fullerene cage.

6.3.2 Study of Ln/An encapsulated C₂₆ fullerene

6.3.2.1 Bare C₂₆ Cage

The ground state optimized geometry of sole classical isomer of C₂₆ is of D_{3h} symmetry and corresponds to ⁵A₁' state. It is an open shell quintet spin state system with two unpaired electrons in each e' and e'' orbitals as reported earlier.^{230,231} The C-C bond distances in C₂₆ cage have been calculated using B3LYP functional and found to be 1.410, 1.428, 1.450, 1.473 and 1.540 Å. The HOMO-LUMO gap for the bare C₂₆ cage with D_{3h} symmetry is found to be 1.62 and 1.56 eV using Turbomole and ADF programs, respectively, with B3LYP functional. The molecular orbitals 5a₂' and 11e''

are the HOMO and LUMO, respectively, similar to the previous report.²³⁰ We have found that the optimized structure of the singlet state bare C₂₆ cage with D_{3h} symmetry (reported earlier by Beate Paulus,¹⁵⁹ as the ground state) is associated with three imaginary frequencies, which is consistent with the results reported by An et. al.²³¹ recently. According to our calculations, singlet C₂₆ structure with no imaginary frequency is found to be of D₃ symmetry and energetically higher (~8 kcal/mol) than the D_{3h} quintet state. Moreover, geometry optimization of the singlet state with lower symmetry or even with no symmetry leads to a higher energy isomer as compared to the quintet state. In addition to the classical isomer, which is the ground state lowest energy structure of C₂₆ cluster, we have also considered the lowest energy non-classical isomer (triplet state), which contains one 4-membered ring surrounded by three hexagons and one pentagon. However, the non-classical isomer has been found to be energetically higher as compared to the classical one with an energy difference of 3 kcal/mol. Similar result has been reported earlier by Li and coworkers.²³¹

6.3.2.2 Optimized Structures of M@C₂₆ Clusters

The geometries of all the M@C₂₆ clusters have been optimized using Turbomole and ADF programs with PBE and B3LYP functionals in Turbomole, and BP86 and PBE functionals in ADF. The calculated vibrational frequencies have been found to be real for all the clusters, which indicate that these structures are true minima on their respective potential energy surfaces. Starting from various initial cage structures geometries of M@C₂₆ clusters have been optimized; however, in all the cases geometry optimization leads to the same closed shell D_{3h} structure. The optimized structures of bare C₂₆ and M@C₂₆ clusters are represented in Figure 6.9.



Figure 6.9 Optimized structures of a) bare C_{26} cage and b) $M@C_{26}$ cluster.

For the purpose of comparison we have also investigated the encapsulation of U within the lowest energy nonclassical C_{26} structure. However, this nonclassical $U@C_{26}$ is found to be energetically less stable by 27 kcal/mol as compared to the corresponding classical structure. Therefore, only the classical isomer has been considered for further investigations here. Now onwards we have discussed the results obtained using Turbomole program unless otherwise mentioned. Incorporation of metal atom/ion with 6 valence electrons into the C_{26} cage leads to the same D_{3h} structure (except Eu^{3+} and Gd^{3+}) for all the clusters. Eu^{3+} and Gd^{3+} encapsulated C_{26} systems are found to be of D_3 symmetry. Encapsulation of metal atom/ion within the C_{26} cage leads to an overall increase in cage size and as a result C-C bond lengths are found to increase except the largest one. For example, the calculated C-C bond lengths for the $U@C_{26}$ cluster are found to be 1.433, 1.480, 1.486, 1.514 and 1.531 Å, as compared to the corresponding values of 1.410, 1.428, 1.450, 1.473 and 1.540 Å for the bare C_{26} . The M-C bond lengths obtained from Turbomole and ADF using different functionals are reported in Table 6.7.

Table 6.7 Calculated values of M-C bond distance (R_{M-C} in Å) using different functionals with Turbomole and ADF Programs and binding energy per atom (BE) in eV with Turbomole program for all the $M@C_{26}$ clusters

Metal Atom/Ion (M)	R_{M-C} (Turbomole)		R_{M-C} (ADF)		BE ^b in eV (Turbomole)
	B3LYP	PBE	BP86	PBE	B3LYP
C_{26}^a	2.220/2.286/ 2.465/2.595	2.234/2.305/ 2.472/2.617	2.228/2.296/ 2.467/2.604	2.226/2.294/ 2.464/2.602	5.969
Pr^-	2.344/2.369/ 2.466/2.542	2.351/2.374/ 2.468/2.548	2.353/2.376/ 2.467/2.547	2.350/2.372/ 2.463/2.543	6.263
Pa^-	2.369/2.387/ 2.472/2.555	2.375/2.391/ 2.474/2.553	2.379/2.394/ 2.474/2.550	2.376/2.390/ 2.469/2.544	6.415
Nd	2.336/2.365/ 2.457/2.502	2.339/2.366/ 2.457/2.529	2.340/2.366/ 2.456/2.530	2.337/2.362/ 2.452/2.526	5.978
U	2.348/2.369/ 2.455/2.532	2.355/2.374/ 2.458/2.533	2.359/2.376/ 2.457/2.529	3.345/2.372/ 2.452/2.524	6.283
Pm^+	2.330/2.365/ 2.443/2.493	2.332/2.362/ 2.449/2.516	2.332/2.360/ 2.449/2.519	2.329/2.357/ 2.445/2.516	5.855
Np^+	2.335/2.359/ 2.444/2.512	2.342/2.364/ 2.447/2.519	2.345/2.366/ 2.447/2.516	2.342/2.362/ 2.442/2.512	6.197
Sm^{2+}	2.326/2.370/ 2.429/2.501	2.329/2.361/ 2.445/2.511	2.324/2.359/ 2.451/2.548	2.321/2.355/ 2.447/2.545	5.763
Pu^{2+}	2.328/2.355/ 2.436/2.499	2.334/2.359/ 2.442/2.512	2.336/2.360/ 2.441/2.509	2.333/2.356/ 2.436/2.505	6.127
Eu^{3+}	2.335/2.373/ 2.439/2.516	2.329/2.363/ 2.445/2.515	2.328/2.360/ 2.447/2.517	2.324/2.356/ 2.443/2.514	6.024
Am^{3+}	2.326/2.354/ 2.433/2.498	2.330/2.358/ 2.442/2.521	2.333/2.360/ 2.442/2.511	2.329/2.356/ 2.437/2.507	6.303
Gd^{4+}	2.336/2.374/ 2.445/2.526	2.336/2.374/ 2.445/2.526	2.330/2.364/ 2.452/2.525	2.326/2.361/ 2.449/2.522	6.830
Cm^{4+}	2.330/2.358/ 2.435/2.505	2.331/2.362/ 2.447/2.519	2.333/2.362/ 2.445/2.515	2.329/2.359/ 2.441/2.512	6.930

^aFor the bare C₂₆ cage, the distance between the cage center to the unique carbon atoms are reported.

^bFor a stable cluster we have considered positive sign for BE energy values.

From the calculated M-C bond length values it is clear that the bare C₂₆ cage becomes nearly spherical in shape on encapsulation with the metal atom/ion. For the bare C₂₆ cluster the largest and the smallest distances from the center dummy atom to the symmetry unique carbon atoms of the cage have been found to decrease and increase, respectively, to intermediate values after metal atom/ion encapsulation. The average B3LYP calculated M-C distance for U@C₂₆ cluster is found to be 2.396 Å as compared to 2.336 Å for the bare C₂₆ cage. Thus, the averages increase in the distance from the cage center to surface carbon atoms (0.06 Å) is comparable to that found in the M@C₂₈ system.¹⁵⁵ The M-C bond lengths calculated using different functionals are found to be almost the same for a particular metal atom/ion. The trends in the variation of the bond lengths along the lanthanide and the actinide series also remain the same. In general, from Pr to Sm in lanthanide and Pa to Am in the actinide series, M-C bond lengths have been found to decrease and then again increase. It is interesting to note that the calculated M-C bond lengths in M@C₂₆ systems are comparable to that in M@C₂₈ systems.¹⁵⁵

6.3.2.3 Molecular Orbital Ordering and Charge Distribution Analysis

The molecular orbital energy diagram for the U@C₂₆ system as calculated using B3LYP functional and ADF program is represented in Figure 6.10. The HOMO and the LUMO for this system have been found to be 9a₁' and 3a₁" molecular orbitals (MOs), respectively. However, it is to be noted that HOMO or LUMO state may differ

from one system to another depending on the encapsulated species. We have reported the calculated HOMO-LUMO gaps using different functionals in Table 6.8.

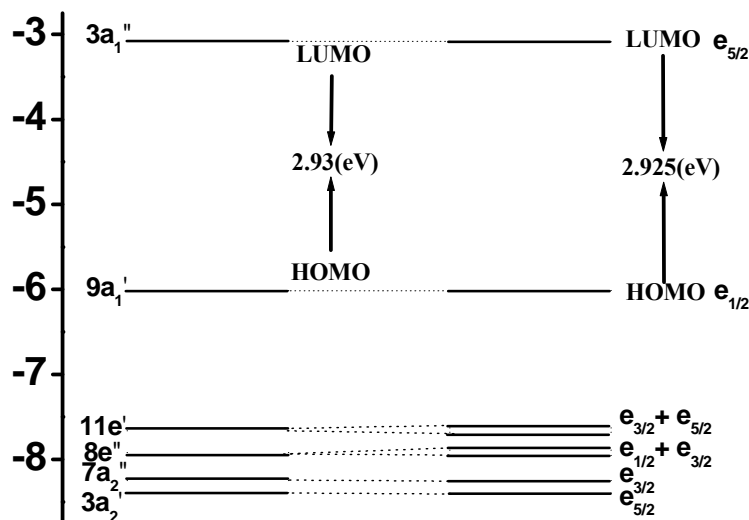
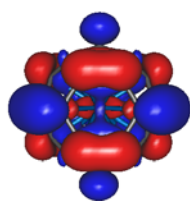


Figure 6.10 Molecular orbital diagram for the $U@C_{26}$ cluster without (left) and with (right) spin-orbit coupling.

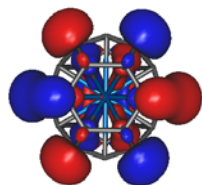
The calculated HOMO-LUMO energy gap values for all the $M@C_{26}$ systems are found to be considerably higher (e.g., 2.4-4.0 eV with B3LYP functional) as compared to that for the bare C_{26} (1.62 eV) cage using the same functional. In this context it may be noted that some of the highly stable clusters, reported recently, have been found to be associated with high HOMO-LUMO gaps.^{53,54,83,155,184-186,189-191} Consequently, calculated higher HOMO-LUMO gaps in case of $M@C_{26}$ can be correlated with the chemical stability gain after incorporation of the metal atom/ion into the C_{26} cage. Figure 6.11 depicts the pictorial representation of the valence molecular orbitals (MOs) of the $U@C_{26}$ cluster.

Table 6.8 The calculated values of HOMO-LUMO gap (in eV) as obtained using Turbomole and ADF programs for the M@C₂₆ clusters with different functional

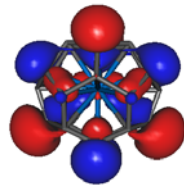
Metal Atom/Ion (M)	HOMO-LUMO gap		
	Turbomole		ADF
	B3LYP	PBE	B3LYP
Pr ⁻	2.71	1.57	2.61
Pa ⁻	2.61	1.57	2.60
Nd	3.03	1.14	2.90
U	2.94	1.82	2.93
Pm ⁺	3.35	0.84	3.16
Np ⁺	3.35	2.08	3.31
Sm ²⁺	3.14	0.78	3.31
Pu ²⁺	3.73	1.93	3.77
Eu ³⁺	2.74	1.69	2.82
Am ³⁺	3.81	1.69	3.86
Gd ⁴⁺	2.44	2.44	2.62
Cm ⁴⁺	3.99	1.59	3.95



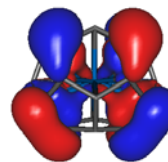
9a₁' [15a₁']



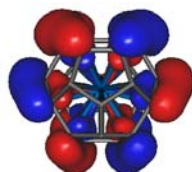
11e' [18e']



8e'' [12e'']



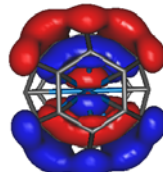
7a₂'' [11a₂'']



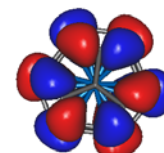
3a₂' [5a₂']



10e' [17e']



2a₁'' [3a₁''] (P)



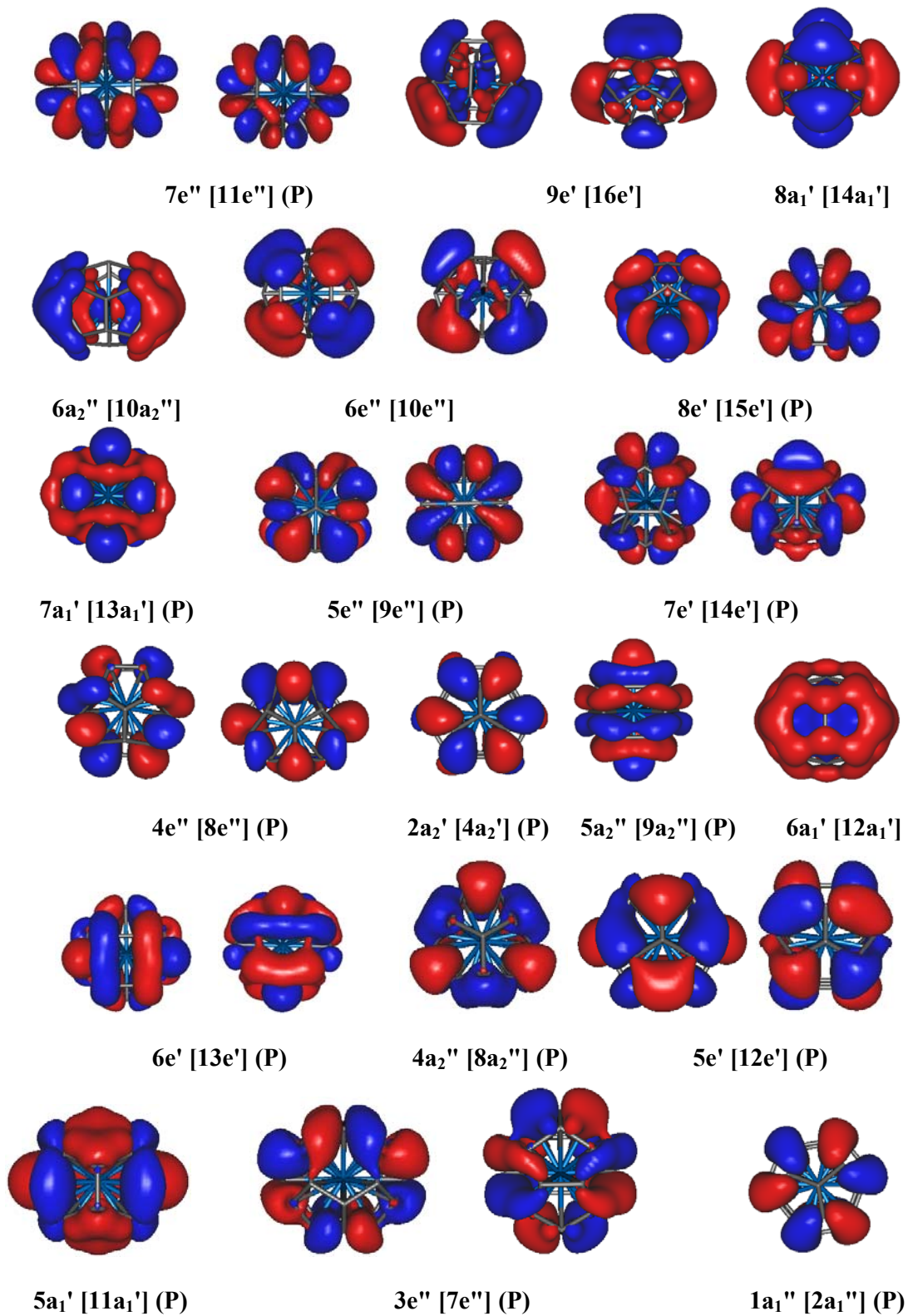


Figure 6.11 Valence molecular orbitals of $U@C_{26}$. Within the parentheses 'P' refers to the orbitals contributed by pure C_{26} cage only.

The atomic orbitals (AOs) from both metal atom/ion and carbon atoms are hybridized to form the $9a_1'$, $11e'$, $8e''$, $7a_2''$, $3a_2'$, $10e'$, $9e'$, $8a_1'$, $6a_2''$, $6e''$ and $6a_1'$ MOs with a total valence electron count of 32 for the central f-block element. The 6 valence electrons of the metal atom/ion and the 26 π electrons of the C_{26} cage cumulatively make a 32-electron system. Considerable amount of overlap has been found to be present between the metal and C_{26} cage orbitals for these MOs. Conversely, the $2a_1''$, $7e''$, $8e'$, $7a_1'$, $5e''$, $7e'$, $4e''$, $2a_2'$, $5a_2''$, $6e'$, $4a_2''$, $5e'$, $5a_1'$, $3e''$ and $1a_1''$ MOs correspond to pure carbon orbitals of C_{26} cage. The energy gap between the inner orbitals, viz., $1a_1''$ and $4a_1'$ MOs is calculated to be quite large, and starting from the HOMO to the inner $1a_1''$ MO, a cumulative number of 32 electrons are found to be present in the metal-cage hybrid orbitals. Thus, it is quite evident that the open shell C_{26} cage has been stabilized on encapsulation of a lanthanide and actinide atom/ion corresponding to 6 valence electrons, resulting into the close shell $M@C_{26}$ system, through fulfilling the 32-electron principle for the central metal atom/ion. Indeed, through metal atom/ion encapsulation within a cluster, only few highly stable chemical systems with 32 valence electrons have been predicted^{54,155,223} so far.

Now we focus on the charge distributions in the $M@C_{26}$ clusters. High negative charges on the metal centers as obtained from both natural population analysis (NPA) and Löwdin schemes (Table 6.9) are somewhat unrealistic. This problem of getting unrealistic charge values is very common for other metal cluster systems also.¹⁸⁶ Nevertheless, the calculated charge values using the above two schemes indicate that, with increase in the positive charge on the bare metal ion, the negative charge on the metal center in $M@C_{26}$ decreases almost monotonically, except few cases. In addition to the NPA and Löwdin schemes we have also

calculated the VDD charges (Table 6.9) that is based on the calculated amount of electron density that flows to or from a certain atom due to bond formation through spatial integration of the deformation density over the atomic Voronoi cell, and thus is not explicitly dependent on the basis functions involved in a calculation. Therefore, VDD derived charges are considered to provide chemically meaningful charge distributions values.^{186,195}

Table 6.9 Calculated natural, Löwdin and VDD charges on metal centers for the M@C₂₆ clusters using Turbomole and ADF programs with different functionals

Metal Atom/ion (M)	Natural Charges		Löwdin Charges		VDD	
	Turbomole				ADF	
	B3LYP	PBE	B3LYP	PBE	BP86	PBE
Pr ⁻	-2.331	-2.530	-1.355	-1.463	0.329	0.330
Pa ⁻	-2.284	-2.475	-2.444	-2.597	0.314	0.316
Nd	-2.291	-2.586	-1.301	-1.412	0.291	0.293
U	-3.242	-3.416	-2.231	-2.360	0.298	0.303
Pm ⁺	-2.192	-2.531	-1.229	-1.349	0.265	0.268
Np ⁺	-3.326	-3.433	-2.156	-2.257	0.244	0.251
Sm ²⁺	-2.005	-2.429	-1.182	-1.311	0.259	0.261
Pu ²⁺	-3.205	-3.279	-2.040	-2.120	0.492	0.500
Eu ³⁺	-1.441	-2.170	-1.071	-1.265	0.200	0.231
Am ³⁺	-2.510	-2.582	-1.677	-1.740	0.416	0.425
Gd ⁴⁺	-1.238	-1.949	-1.032	-1.217	-0.115	-0.110
Cm ⁴⁺	-2.282	-2.351	-1.636	-1.690	0.050	0.059

The calculated VDD charges (Table 6.9) lie in the range of 0.2-0.5. It is also interesting to get an idea about the distribution of electrons corresponding to the s, p, d, and f orbital occupations for the metal center in M@C₂₆ clusters. For this purpose

the NPA calculated orbital-wise population values for the metal center in $M@C_{26}$ clusters are reported in Table 6.10. For both the lanthanide and the actinide containing clusters, the occupations corresponding to the s and p orbitals remain almost the same. However, d orbital occupation, $n(d)$, has been found to be higher for a particular lanthanide as compared to the corresponding isoelectronic actinide system. This trend is found to be opposite in case of f orbital populations ($n(f)$), which may be due to a larger spatial extent of the 5f orbital of actinides as compared to the 4f orbital of lanthanides.

Table 6.10 Calculated values of orbital population for the central metal atom in $M@C_{26}$ clusters with B3LYP functional using Turbomole program

Metal Atom/Ion (M)	n(s)	n(p)	n(d)	n(f)
Pr ⁻	4.31	12.00	12.38	4.64
Pa ⁻	4.34	11.99	11.89	5.06
Nd	4.31	12.00	12.44	5.54
U	4.33	12.00	12.03	6.89
Pm ⁺	4.31	12.00	12.50	6.38
Np ⁺	4.33	12.00	11.96	8.04
Sm ²⁺	4.31	12.00	12.55	7.15
Pu ²⁺	4.32	12.00	11.97	8.93
Eu ³⁺	4.30	12.00	12.51	7.76
Am ³⁺	4.31	11.99	11.97	9.24
Gd ⁴⁺	4.30	12.00	12.53	8.50
Cm ⁴⁺	4.31	11.99	11.97	10.01

The calculated values of the percentage of atomic orbitals contributing to various MOs reported in Table 6.11 reveal that all the valence s, p, d and f orbitals of lanthanides and actinides are found to be involved in the hybridization with the C_{26} cage orbitals.

Table 6.11 The percentage contributions of the metal valance orbitals to the hybridized valance MOs as obtained using ADF

Metal Atom/Ion (M)	9a ₁ '	11e'	8e''	7a ₂ ''	3a ₂ '	10e'	9e'	8a ₁ '	6e''	6a ₂ ''	6a ₁ '
Pr ⁻	22.0 <i>f</i>	12.6 <i>f</i>	15.2 <i>f</i>	12.0 <i>f</i>	15.0 <i>f</i>	4.6 <i>p</i> 3.4 <i>d</i>	3.3 <i>p</i> 7.5 <i>d</i>	6.8 <i>d</i>	8.5 <i>d</i>	6.8 <i>p</i>	8.8 <i>s</i>
Pa ⁻	10.7 <i>f</i>	11.0 <i>f</i>	13.1 <i>f</i>	11.0 <i>f</i>	14.1 <i>f</i>	12.7 <i>p</i>	1.3 <i>p</i> 8.6 <i>d</i>	8.3 <i>d</i>	14.0 <i>d</i>	13.3 <i>p</i>	9.0 <i>s</i>
Nd	56.1 <i>f</i>	19.6 <i>f</i>	17.9 <i>f</i>	16.4 <i>f</i>	13.1 <i>f</i>	3.3 <i>p</i> 6.7 <i>d</i>	3.0 <i>p</i> 10.4 <i>d</i>	13 <i>d</i>	18.5 <i>d</i>	6.5 <i>p</i>	11.5 <i>s</i>
U	23.4 <i>f</i>	16.8 <i>f</i>	19.0 <i>f</i>	19.0 <i>f</i>	15.7 <i>f</i>	12.0 <i>p</i>	1.0 <i>p</i> 9.0 <i>d</i>	8.6 <i>d</i>	12.2 <i>d</i>	13.1 <i>p</i>	10.4 <i>s</i>
Pm ⁺	81.6 <i>f</i>	29.3 <i>f</i>	20.4 <i>f</i>	20.1 <i>f</i>	11.4 <i>f</i>	2.4 <i>p</i> 8.3 <i>d</i>	2.9 <i>p</i> 9.0 <i>d</i>	13.0 <i>d</i>	18.5 <i>d</i>	6.5 <i>p</i>	6.0 <i>s</i>
Np ⁺	42.3 <i>f</i>	24.2 <i>f</i>	25.2 <i>f</i>	21.3 <i>f</i>	22.7 <i>f</i>	10.5 <i>p</i> 1.6 <i>d</i>	1.52 <i>p</i> 11.4 <i>d</i>	12.3 <i>d</i>	15.0 <i>d</i>	12.2 <i>p</i>	9.0 <i>s</i>
Sm ²⁺	90.6 <i>f</i>	50.0 <i>f</i>	24.0 <i>f</i>	19.8 <i>f</i>	11.9 <i>f</i>	1.5 <i>p</i> 10.6 <i>d</i>	2.8 <i>p</i> 6.2 <i>d</i>	15.0 <i>d</i>	15.0 <i>d</i>	5.7 <i>p</i>	11.7 <i>s</i>
Pu ²⁺	61.2 <i>f</i>	32.4 <i>f</i>	31.1 <i>f</i>	27.1 <i>f</i>	24.9 <i>f</i>	9.1 <i>p</i> 1.1 <i>d</i>	1.8 <i>p</i> 9.3 <i>d</i>	15.1 <i>d</i>	10.5 <i>d</i>	11.2 <i>p</i>	11.9 <i>s</i>
Eu ³⁺	94.2 <i>f</i>	66.2 <i>f</i>	28.5 <i>f</i>	17.6 <i>f</i>	14.2 <i>f</i>	13.5 <i>d</i>	3.2 <i>p</i> 2.9 <i>d</i>	16.5 <i>d</i>	14.5 <i>d</i>	4.3 <i>p</i>	12.5 <i>s</i>
Am ³⁺	76.0 <i>f</i>	41.4 <i>f</i>	38.3 <i>f</i>	33.6 <i>f</i>	28.0 <i>f</i>	6.8 <i>p</i> 3.6 <i>d</i>	3.5 <i>p</i> 8.6 <i>d</i>	22.0 <i>d</i>	10.9 <i>d</i>	9.7 <i>p</i>	11.7 <i>s</i>
Gd ⁴⁺	94.9 <i>f</i>	79.8 <i>f</i>	38.0 <i>f</i>	16.0 <i>f</i>	16.5 <i>f</i>	18.5 <i>d</i>	3.5 <i>p</i> 2.0 <i>d</i>	20.0 <i>d</i>	20.5 <i>d</i>	4.5 <i>p</i>	13.7 <i>s</i>
Cm ⁴⁺	82.6 <i>f</i>	50.1 <i>f</i>	44.5 <i>f</i>	40.4 <i>f</i>	33.2 <i>f</i>	4.6 <i>p</i> 9.5 <i>d</i>	5.2 <i>p</i> 14.0 <i>d</i>	21.5 <i>d</i>	8.7 <i>d</i>	9.1 <i>p</i>	13.4 <i>s</i>

Moreover, the participation of 5f/4f atomic orbitals are maximum for the 9a₁', 11e', 8e'', 7a₂'', 3a₂' MOs with a cumulative 14 electrons, as obtained from the symmetrized fragment orbital analysis through ADF calculations. Subsequently, participation of

metal d and p orbitals is maximum for the $10e'$, $9e''$, $8a_1'$ and $6e''$ MOs with a total electron count of 16 corresponding to 10 d and 6 p electrons. The remaining 2 electrons of $6a_1'$ are contributed by metal s orbital along with carbon orbitals. For the actinide systems, the participation of the 5f-orbitals is fully reasonable and well accepted in the scientific community, however, there is some controversy regarding the contribution of 4f orbitals for the lanthanides in bonding, and participation of 5d orbitals is important in the case of lanthanides.²³² Nevertheless, for the presently investigated lanthanide systems strong f orbital participation is observed (Table 6.11).

6.3.2.4 Energetics and Thermodynamic Stability

The calculated binding energy per atom (BE) values for the $M@C_{26}$ clusters are reported in Table 6.7. It has been found that the BE values vary from 6.13 to 6.93 and 5.76 to 6.83 eV for the actinides and lanthanides, respectively. The calculated BE values for the actinides are higher than the corresponding lanthanides. It is important to note that the BE values for all the $M@C_{26}$ clusters are higher than the corresponding value for the bare C_{26} cage (5.97 eV) except for $Pm^+@C_{26}$ and $Sm^{2+}@C_{26}$ clusters.

In addition to the binding energy per atom, it is also interesting to know about the different energy components for an in-depth analysis of the nature of interactions involved in the formation of the $M@C_{26}$ complex from its constituent fragments. For this purpose we have reported the calculated values of different energy components and also the total interaction energy corresponding to the dissociation of $M@C_{26}$ into ($M + C_{26}$) in Figures 6.12 and 6.13, for the actinide and lanthanide systems, respectively. Interaction energies calculated using the ADF software are found to lie

in the range of -15 to -37 eV, which indicates that all the cluster studied here are very stable. The nature of the plots corresponding to the total interaction energy is found to be the same for both lanthanide and actinide series and becomes more negative with increase in positive charge. However, the other energy components differ widely for the two series. Both the orbital stabilization energy and the steric term are found to be the minimum for $\text{Pu}^{2+}@\text{C}_{26}$ and $\text{Sm}^{2+}@\text{C}_{26}$ clusters among all the actinides and lanthanides, respectively.

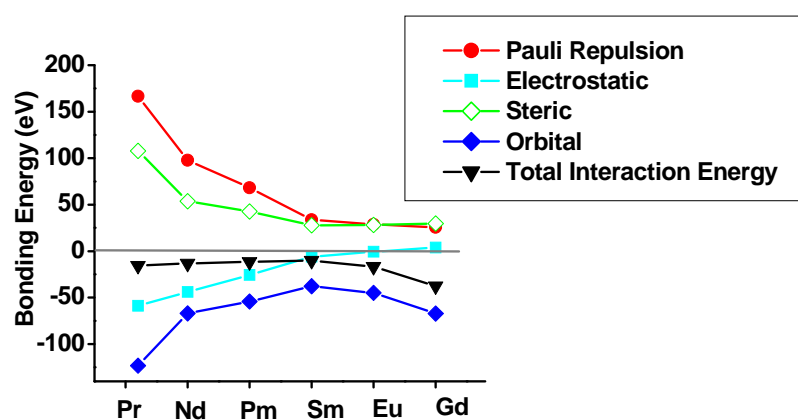


Figure 6.12 Interaction energy analysis for the $\text{M}@\text{C}_{26}$ clusters, where $\text{M} = \text{Pr}^-$, Nd , Pm^+ , Sm^{2+} , Eu^{3+} , Gd^{4+} .

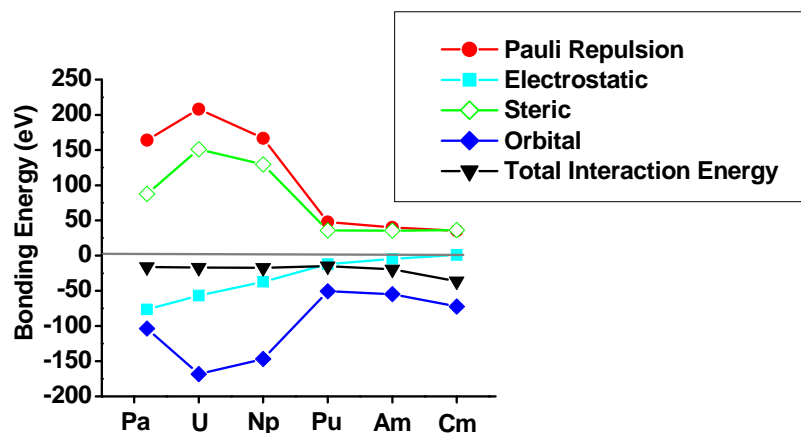


Figure 6.13 Interaction energy analysis for the $\text{M}@\text{C}_{26}$ clusters, where $\text{M} = \text{Pa}^-$, U , Np^+ , Pu^{2+} , Am^{3+} , Cm^{4+} .

Thermodynamic analysis have been carried out using Turbomole program for the reaction, $M + C_{26} \rightarrow M@C_{26}$. Thermodynamic parameters calculated using B3LYP functional ($T = 298.15 \text{ K}$, $P = 0.1 \text{ MPa}$) are reported in Table 6.12. Calculated values of Gibb's free energies (Δ_rG) and enthalpies (Δ_rH) of reaction are found to be negative for most of the cases, and reaction entropy (Δ_rS) are in the range of -180 to $-195 \text{ Jmol}^{-1}\text{K}^{-1}$. Negative Δ_rG values for all the actinides and few lanthanides suggest the spontaneity of the metal atom/ion encapsulation process into the C_{26} cage. In case of lanthanides Δ_rG values are less negative as compared to the actinides, however, the trends are similar in both the cases. Starting from Pr^-/Pa^- the negative Δ_rG values decrease up to $\text{Np}^{2+}/\text{Pu}^{2+}$ and then again increase. The trends in the variations of the calculated Δ_rH values are found to be the same. Calculated negative Δ_rH values for most of the clusters suggest the exothermic nature of the encapsulation process. It is interesting to note that the calculated Δ_rH value for a particular actinide-containing cluster is more negative as compared to the corresponding isoelectronic lanthanide ones.

Table 6.12 The calculated values of change in enthalpy (in kJmol^{-1}), Entropy (in $\text{Jmol}^{-1}\text{K}^{-1}$) and Free Energy (in kJ/mol) corresponding to the reaction $M + C_{26} \rightarrow M@C_{26}$ as Obtained from Turbomole Program using B3LYP Functional.

Metal Atom/Ion (M)	Δ_rH	Δ_rS	Δ_rG
Pr^-	-646	-182	-592
Pa^-	-1045	-187	-989
Nd	100	-184	154
U	-692	-191	-635
Pm^+	423	-187	478
Np^+	-460	-195	-402

Sm ²⁺	659	-183	714
Pu ²⁺	-275	-197	-217
Eu ³⁺	-18	-184	36
Am ³⁺	-732	-196	-674
Gd ⁴⁺	-2121	-180	-2067
Cm ⁴⁺	-2368	-195	-2310

The higher stability of M@C₂₆ with actinide metal atoms/ions may be due to the higher orbital interactions between the C₂₆ cage and the actinides with large 5f contribution. It is clearly due to the higher spatial extent of actinide 5f orbitals as compared to the 4f orbitals of lanthanides. Here we have also compared the stability of M@C₂₆ systems with some other experimentally observed endohedral metallofullerene systems such as U@C₂₈,^{51,154} Ti@C₂₈,¹⁵⁴ using the same level of theory. The calculated ΔG and ΔH values are found to be -673, -722 for U@C₂₈ and -541, -548 kJ/mol for Ti@C₂₈ systems, respectively. These values are comparable with the ΔG and ΔH values reported in the present work for most of the M@C₂₆ systems, indicating the feasibility of their possible existence. It is also interesting to consider the reaction, U@C₂₈ → U@C₂₆ + C₂, which is associated with a positive Δ_rG value (955 kJ/mol). So, this process is not energetically favorable. Therefore, (U@C₂₆ + C₂) system may be viewed as a metastable system with respect to U@C₂₈ system and the former one is bound within a local minimum with a sufficient energy barrier for its conversion into U@C₂₈. However, it is important to note here that this type of clusters are generally formed from the constituent atomic fragments in experiments (obtained by laser ablation of the corresponding solid materials); therefore, the binding energies of the clusters with respect to atomic fragments are more important as compared to the above process. Indeed, the calculated BE values for the U@C₂₆ and U@C₂₈ systems

(6.28 and 6.39 eV) are rather so close that a proper tuning of experimental parameters may lead to the observation of U@C₂₆ system experimentally.

It may be noted that the calculated value of basis set super position error for the complexation energy has been found to be 9.9 kcal/mol for the U@C₂₆ complex, which is rather negligible in comparison to the computed ΔG (-151.8 kcal/mol) and ΔH (-165.5 kcal/mol) values for the same complex.

6.3.2.5 Effect of Spin-Orbit Interaction

In general, effect of spin-orbit interaction is very important especially for the heavy elements. Therefore, to assess the spin-orbit interaction effect a systematic investigation has been performed on the U@C₂₆ complex. The structural parameters remain almost the same after inclusion of spin-orbit coupling within the ZORA approach. Similarly, detail bonding energy analysis considering spin-orbit effects leads to an increase of 0.02 % in the steric component and 0.18 % in the orbital component, with an overall increase in stability by 1.96 eV as far as the total interaction energy corresponding to atomic dissociation is concerned.

Although the effect of spin-orbit coupling is found to be rather negligible in the energetics, however, it is still interesting to assess its effect on the orbital energy levels. The calculated spin-orbit splittings for the valence orbitals reported in Figure 6.10 indicate that the HOMO-LUMO gap for the U@C₂₆ cluster calculated using scalar relativistic approach almost remains the same after inclusion of spin-orbit interaction, and thus spin-orbit interaction has no significant effect here, which may be due to the presence of the C₂₆ cage, which reduces this effect. In general, the splittings of the energy levels are found to be very small (~0.05 eV). Accordingly, ground state

molecular properties are rather insensitive to the spin-orbit coupling for the $M@C_{26}$ systems. Nevertheless, in the case of $M@C_{28}$ systems¹⁵⁵ this effect has been found to be slightly higher.

In recent years, the NICS index, which is well accepted in chemical community has been proven to be highly successful in predicting the aromaticity of a chemical system.¹⁹⁹⁻²⁰¹ A negative NICS value indicates the presence of diatropic ring current i.e. aromaticity, whereas presence of paramagnetic ring current or antiaromaticity is represented by a positive NICS value. Moreover, the concept of aromaticity is not just limited to conjugated organic molecules but also extended to inorganic molecules including metal clusters.²⁰² NICS calculations have been carried out at different positions for the C_{26} cage and the $M@C_{26}$ clusters in order to acquire an idea about the aromaticity of the systems. Three different positions viz. center of the cage or midpoint between the cage center and the center of a pentagon/hexagon located on the cage surface, surface of the cage (center of a pentagon/hexagon located on the cage surface) and 1 Å above the respective cage, have been chosen to calculate the NICS values for the C_{26} cage or $U@C_{26}$ cluster. The calculated NICS values for $U@C_{26}$ are -54.88, -28.57 and -8.29 ppm for the positions inside the cage, on the surface of the cage and above the cage, respectively, in the case of pentagon, while for the hexagon case the corresponding values are found to be -42.86, -27.91 and -6.93 ppm. All the calculated NICS values suggest a presence of aromatic character at all the positions considered here, and can be rationalized through the $2(N+1)^2$ rule of aromaticity²³³ corresponding to the presence of 32 valence electrons. The calculated NICS values for the bare C_{26} cage are 2.85, 2.92 (6.02) and 2.65 (5.03) ppm at the cage center, at a pentagon (hexagon) ring center on the surface and at 1 Å above the

respective ring centers outside the cage, respectively. All these calculated values indicate that aromatic character of the C_{26} cage is increased on encapsulation with U atom, which may be due to a significant electronic delocalization in the metallic center orbitals, mainly from the 5f orbitals. We have also evaluated the effect of spin-orbit interaction on the NICS values for the $U@C_{26}$ cluster and the calculated values of -51.23, -27.82 and 8.19 ppm at the positions, inside the cage, on the surface of the cage and above the cage, respectively (pentagon case) are very close to the corresponding scalar values. Similar trend is observed while considering the hexagon ring and corresponding values are found to be -42.44, -27.49 and -6.72 ppm. Here it may be interesting to discuss the changes in the bond lengths while considering the aromaticity from the viewpoint of structural/geometrical aspects. Thus, the calculated C-C bond lengths for $U@C_{26}$ cluster are found to be 1.433, 1.480, 1.486, 1.514 and 1.531 Å, as compared to the corresponding values of 1.410, 1.428, 1.450, 1.473 and 1.540 Å for the bare C_{26} . Thus, it is evident that the deviations in the C-C bond length values from the corresponding average value is more for the bare C_{26} cage (1.448 Å) as compared to that in $M@C_{26}$ cluster (1.481 Å), which indicate that $M@C_{26}$ cluster is associated with more aromatic character than the bare C_{26} cage.

6.3.2.6 Spectroscopic Properties of C_{26} and $M@C_{26}$ Clusters

Time-dependent density functional theory in conjunction with ZORA approach as implemented in ADF program has been used for the calculation of the vertical electronic excited states for the $U@C_{26}$ cluster. To obtain the excitation energies corresponding to the singlet-excited states, SAOP model functional has been employed here. The transitions from the ground state to the e' and a_2'' states have been

found to be allowed ones as far as the selection rule is concerned. Scalar relativistic approach has been adopted here for the calculation of the absorption spectra of the bare C_{26} cage. On the other hand, in the case of $U@C_{26}$ system both scalar as well as spin-orbit methods have been used. Graphical presentations of all the calculated spectra are reported in Figures 6.14 and 6.15.

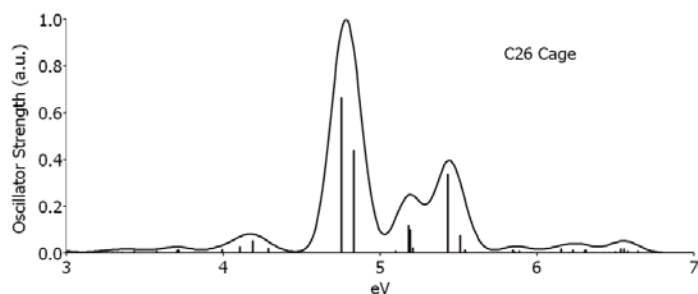
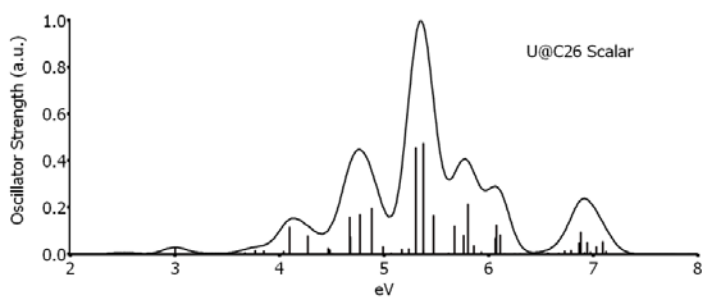


Figure 6.14 UV-visible spectra for the C_{26} cage.

a)



b)

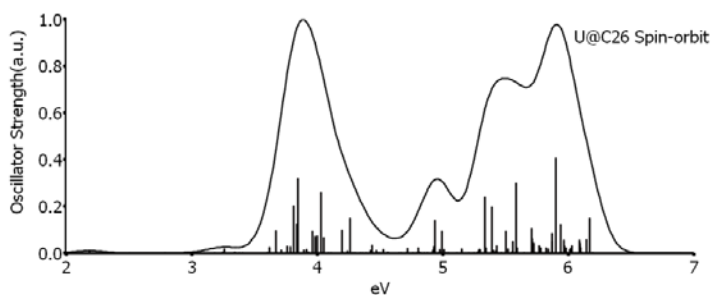


Figure 6.15 UV-visible spectra for $U@C_{26}$ cluster, a) without and b) with spin-orbit coupling.

For the bare C_{26} cluster two main absorption maxima corresponding to 4.80 and 5.44 eV are found. The absorption spectrum is also associated with small humps at around 4.18 and 5.14 eV. In the case of $U@C_{26}$ cluster, the first absorption peak is observed at around 3 eV, whereas the maximum intensity peak appeared at 5.36 eV is associated with few low intensity peaks around 4.86, 5.78 and 6.89 eV using scalar relativistic approach. In general, the HOMO-LUMO gap correlates well with the excitation energy of a chemical species.

In the present work, the HOMO-LUMO energy gap values for all the $M@C_{26}$ systems are found to be considerably higher as compared to that of the bare C_{26} cage. However, in the case of $U@C_{26}$, the first absorption peak is observed at around 3 eV, which is much lower than that of the bare C_{26} cage (4.80 eV). To explain the occurrence of the low intensity 3 eV peak in $U@C_{26}$ cluster, an excited state calculation has been performed for the free U atom and it has been observed that the first excitation peak appears at around 3 eV. Moreover, from the detail analysis of the low intense first excitation peak of $U@C_{26}$, involvement of U atom orbitals has been found to be significant, and this can be implicated as the origin of the 3 eV peak in $U@C_{26}$ cluster. After inclusion of spin-orbit effect two high intensity peaks have been observed corresponding to 3.85 and 5.88 eV associated with two humps at 4.92 and 5.58 eV.

6.4 Concluding Remarks

In this chapter, two new series of metal atom/ion encapsulated “superatoms” fulfilling the 32-electron principle have been proposed using the results obtained from density functional calculations.

In case of C_{24} fullerene, the non-classical C_2 symmetric isomer is the most stable one for the bare cluster, which is consistent with the previously published report.²²⁹ However, after encapsulation of an atom/ion with 8 valence electrons inside the bare C_{24} cage, the sole classical isomer achieve high symmetry (D_{6d}) and stability along with high HOMO-LUMO gap. The elevation of symmetry from C_2 to D_{6d} point group and gain in stability can be attributed through fulfilment of 32-electron principle for the central actinide/lanthanide metal atom/ion. The calculated results show that, $Pu@C_{24}$ (STR01) is the most stable metallofullerene among all the isomers studied here. The calculated relative energy ordering, binding energy per atom and thermodynamic data are found to be consistent with each other and indicate that the encapsulation of 8-valence actinide metal atom/ion is energetically more favorable as compared to encapsulation of 8-valence lanthanide metal atom/ion.

It has been found that the open-shell C_{26} cluster transforms to a closed-shell system on encapsulation with an actinide/lanthanide atom/ion with 6-valence electrons. A complete discussion of different aspects such as structural, electronic, bonding, aromatic and spectroscopic properties for all the clusters has been provided. Relativistic effects have been taken into account using both scalar as well as spin-orbit approaches within the framework of zeroth order regular approximations. High stability of the $M@C_{26}$ clusters for all the actinides and few of the lanthanides has been rationalized in terms of larger HOMO-LUMO gap, higher NICS values and higher binding energy per atom as compared to the same for the bare C_{26} cage. Calculated negative values of free energy and enthalpy of reaction suggest the formation of $M@C_{26}$ cluster from M and C_{26} species. Thus, the $M@C_{26}$ systems with

32 valence electrons occupying the metal-carbon hybrid orbitals, can be considered as highly stable clusters with magic number of electronic configuration.

Thus, in addition to the recently predicted Pu@Pb_{12} ,⁵⁴ M@C_{28} ¹⁵⁵ and the $[\text{U@Si}_{20}]^{6-223}$ systems, the new series of clusters reported in the present work strongly suggest that the 32-electron principle might have important implications in the chemistry of lanthanide and actinide compounds. Moreover, all the calculated structural, energetic and spectroscopic properties imply that it may be possible to identify the M@C_{24} and M@C_{26} species through proper tuning of the experimental parameters.^{51,154,217,218}

Chapter 7: Summary and Outlook

In this concluding chapter we summarize all the works discussed in the preceding five chapters as well as possible future perspectives of the work that can stem out from our previous discussions. In this thesis we have made an attempt to understand the electronic structure, properties and reactivity of a broad range of molecules and clusters. The study of chemical bonding and reactivity is of immense importance in diverse areas of chemistry and physics. In recent times computational chemistry has been proven to be a versatile tool in providing meaningful insights to explain the behavior of various chemical systems and processes. Thus, the selectivity of a particular ligand towards a particular metal ion can be rationalized in a better way through theoretical modeling studies. Although, accurate estimation of the bonding energies and measure of reactivity in small molecules can in principle be obtained through *ab-initio* quantum mechanical calculations, understanding this prediction in terms of simple chemical concepts is an equally important and interesting topic of investigation. The work presented in this thesis has been based on the density functional theory (DFT) which provides an alternative appealing framework for the quantum mechanical study of electronic structure and properties. Here we have attempted to provide theoretical insights towards the selective complexation and encapsulation of important metal ions/atoms with various ligands and clusters using *ab initio* DFT based methods. Few experiments have also been performed to validate some of our theoretical predictions.

In Chapter 2 we have proposed a modified concept related to selective complexation of actinides with either S or N donor ligands. Although actinide selective ligands with hard donor atom like O seems highly unusual, here we have

made an attempt to reply to this question affirmatively through introducing a new concept, 'intramolecular synergism', where electrostatic interaction predominates between the softer metal ion and hard donor atoms in presence of soft donor centers within the same ligand. For this purpose the complexation behavior of pre-organized 1,10-phenanthroline-2,9-dicarboxylic acid (PDA) based ligands with trivalent lanthanides and actinides have been studied using DFT. Through functionalization of the PDA ligand with soft donor atoms such as sulfur, new ligands viz. mono-thio-dicarboxylic acids and di-thio-dicarboxylic acids have been designed. This unusual aspect where softer actinide metal ion is bonded strongly with hard donor oxygen atoms has been explained using the popular chemical concepts, viz., HSAB principle and the Fukui reactivity indices.

The theoretical design of 1,10-phenanthroline-2,9-dicarboxylamide (PDAM) and prediction of its selectivity of towards Am(III) ion have been discussed in chapter 3. Since PDA ligand has very low solubility in both organic and aqueous medium, to improve its organic solubility we have switched from PDA to PDAM. Moreover, we further extended our calculation to explore different derivatives of PDAM with long alkyl chains e.g. N,N-di-isobutyl (PDAM-Isobutyl) and N-decyl (PDAM-Decyl). Subsequently, the amide derivatives have been synthesized and solvent extraction experiments have been carried out to validate our theoretical prediction.

Additionally, we have also theoretically investigated some conventional extractants to rationalize the experimentally observed trends. Chapter 4 provides an in-depth theoretical insight on the experimentally observed complexation behavior of the Am(III) and Eu(III) ions with Cyanex301 [bis(2,4,4-trimethyl-pentyl) dithiophosphinic acid], Cyanex302 [bis(2,4,4-trimethyl-pentyl) monothiophosphinic

acid] and Cyanex272 [bis (2,4,4-trimethylpentyl) phosphinic acid] ligands. A shorter Am-S bond distance, a higher percentage of orbital interaction energy and a higher degree of metal-ligand charge transfer leading to a greater degree of covalency in $\text{Am}(\text{Cyanex301})_3$ as compared to the $\text{Eu}(\text{Cyanex301})_3$ complex are in agreement with the experimentally observed selectivity trend.

Chapter 5 deals with the selective encapsulation of a metal atom or ion inside a small fullerene cage of different sizes. Smaller fullerenes are of special interest due to the presence of high curvature and huge strain energy owing to the presence of adjacent pentagonal rings, which lead to clusters with unusual intra and inter -molecular bonding and electronic properties. However, the smaller fullerenes, which are formed during the production of stable fullerenes, are difficult to isolate because of their extremely high chemical reactivity. Nevertheless, encapsulation of a proper dopant atom or ion (metal or nonmetal) into the smaller fullerenes may lead to highly stable clusters with fascinating properties. In Chapter 5 we have considered two smaller fullerenes, viz., C_{20} and C_{36} and study their possible stabilization through doping with a suitable lanthanide or actinide atom/ion.

The origin of the stability of a cluster can be considered as a manifestation of electronic or geometric shell closing. In general, 8- and 18- electron rules are observed for the compounds involving main group and transition elements, respectively, corresponding to fully occupied ns^2np^6 and $ns^2np^6(n-1)d^{10}$ orbitals. In addition to the 8- and 18-electron principles, possibility of 32 valence electron systems had been indicated by Langmuir in 1921. However, until recently, no chemical system with 32 valence electrons has been reported in the literature except PuPb_{12} , $\text{An}@C_{28}$, (An is an actinide atom/ion with 4 valence electrons) and $[\text{U}@Si_{20}]^{6-}$. In Chapter 6 we have

explored the possibility of stabilizing two small size fullerenes, viz., C₂₄ and C₂₆ through encapsulation of a suitable actinide/lanthanide metal atom or ion which satisfy valence 32 electron counts around the central metal atom/ion.

To conclude, we can say that the separations using mixed donor ligands are comparatively new so standardization of the experimental techniques followed by the plant scale establishment will be interesting as well as highly challenging task. Radio nuclide immobilization using carbon nano-clusters is also a new concept and till now only very few theoretical or experimental investigations have been done. Thus, this is also a very challenging and potential area of research for both theoreticians and experimentalists.

References

1. Kauffman, G.B. "Alfred Werner - Founder of Coordination Chemistry", Springer-Verlag, Berlin, Heidelberg, New York, **1966**; Kauffman, G.B. "Inorganic Coordination Compounds", Heyden & Son, Ltd., London, Philadelphia, Rheine, **1981**.
2. Schläfer, H. L.; Gliemann, G. "Basic Principles of Ligand Field Theory" Wiley Interscience: New York, **1969**.
3. Cotton, F. A. "Metal Atom Cluster Compounds", McGraw-Hill Yearbook of Science and Technology, McGraw Hill, New York, **1966**.
4. Hancock, R. D. *Chem. Rev.* **1989**, 89, 1875 and references in therein.
5. Diamond, R. M.; Street, K.; Seaborg, G. T. *J. Am. Chem. Soc.* **1954**, 76, 1461.
6. Baybarz, R. D.; Weaver, B. S.; Kinser, H. B. *Nucl. Sci. Engg.*, **1963**, 17, 457
7. Weaver, B.; Kappelmann, F. A. *J. Inorg. Nucl. Chem.*, **1968**, 30, 263
8. Hudson, M. J.; Hagström, I.; Spjuth, L.; Enarsson, Å.; Liljenzin, J. O.; Skålberg, M.; Iveson, P. B.; Madic, C.; Cordier, P.-Y.; Hill, C.; Francois, N. *Solv. Extr. Ion. Exch.*, **1999**, 178, 221
9. Cordier, P.Y.; Hill, C.; Baron, P.; Madica, C.; Hudsonb, M. J.; Liljenzin, J. O. *J. Alloys Compds*, **1998**, 738, 271.
10. Kolarik, Z.; Müllich, U.; Gassner, F. *Solv. Extr. Ion. Exch.*, **1999**, 17, 23.
11. Kolarik, Z.; Müllich, U.; Gassner, F. *Solv. Extr. Ion. Exch.*, **1999**, 17, 1155.
12. Geist, A.; Hill, C.; Modolo, G.; Foreman, M. R.; Weigl, M.; Gompper, K.; Hudson, M. J.; Madic, C. *Solv. Extr. Ion Exch.*, **2006**, 24, 463.
13. Modolo, G.; Odoj, R. *Solv. Extr. Ion Exch.*, **1999**, 17(1), 33.

14. Modolo, G.; Odoj, R.; Baron, P. *Proc. Global 99 (International Conference on Future Nuclear Systems)*, Jackson Hole, Wyoming, USA, August 29-September 3, **1999**
15. Madic, C.; Hudson, M. J.; Liljenzin, J. O.; Glatz, J. P.; Nannicini, R.; Facchini, A.; Kolarik, Z.; Odoj, R. EUR 19149, European Commission, Luxembourg **2000**.
16. Zhu, Y.; Chen, J.; Jiao, R. *Solv. Extr. Ion Exch.* **1996**, *14*, 61.
17. Popov, A. A.; Yang, S.; Dunsch, L. *Chem. Rev.* **2013**, *113*, 5989 and references in therein.
18. Kratschmer, W.; Lamb, L. D.; Fostiropoulos, K.; Huffman, D. R. *Nature* **1990**, *347*, 354.
19. Kroto, H. W.; Heath, J. R.; O'Brien, S. C.; Curl, R. F.; Smalley, R. E. *Nature* **1985**, *318*, 162; Heath, J. R.; O'Brien, S. C.; Zhang, Q.; Liu, Y.; Curl, R. F.; Tittel, F. K.; Smalley, R. E. *J. Am. Chem. Soc.* **1985**, *107*, 7779.
20. Mikawa, M.; Kato, H.; Okumura, M.; Narazaki, M.; Kanazawa, Y.; Miwa, N.; Shinohara, H. *Bioconjugate Chem.* 2001, *12*, 510–514; Bolskar, R. D.; Benedetto, A. F.; Husebo, L. O.; Price, R. E.; Jackson, E. F.; Wallace, S.; Wilson, L. J.; Alford, J. M. *J. Am. Chem. Soc.* **2003**, *125*, 5471.
21. Iezzi, E. B.; Duchamp, J. C.; Fletcher, K. R.; Glass, T. E.; Dorn, H. C. *Nano Lett.* **2002**, *2*, 1187.
22. Cagle, D.W., Kennel, S. J., Mirzadeh, S., et al. *Proc. Natl. Acad. Sci. U S A.* **1999**, *96*, 5182.

23. Ross, R. B.; Cardona, C. M.; Guldi, D. M.; Sankaranarayanan, S. G.; Reese, M. O.; Kopidakis, N.; Peet, J.; Walker, B.; Bazan, G. C.; Van Keuren, E.; Holloway, B. C.; Drees, M. *Nat. Mater.* **2009**, *8*, 208.
24. Rudolf, M.; Feng, L.; Slanina, Z.; Akasaka, T.; Nagase, S.; Guldi D. M. *J. Am. Chem. Soc.*, **2013**, *135*, 11165.
25. Hohenberg, P.; Kohn, W. *Phys. Rev.* **1964**, *136*, B864.
26. Kohn, W.; Sham, L. J. *Phys. Rev.* **1965**, *140*, A1133.
27. Born, M.; Oppenheimer, R. *Ann. Phys. (Leipzig)* **1927**, *84*, 457.
28. Slater, J. C. *Phys. Rev.* **1951**, *81*, 385.
29. Fock, V. *Z. Phys.* **1930**, *61*, 126.
30. Parr, R. G.; Yang, W. *Density Functional Theory of Atoms and Molecules*, Oxford University Press, New York **1989**.
31. Thomas, L. H. *Proc. Camb. Phil. Soc.*, **1927**, *23*, 542.
32. Fermi, E. *Rend. Accad. Naz. Linc.* **1927**, *6*, 602.
33. Fermi, E. *Z. Phys.* **1928**, *48*, 73.
34. Vosko, S. H.; Wilk, L.; Nusair, M. *Can. J. Phys.* **1980**, *58*, 1200.
35. Perdew, J. P.; Wang, Y. *Phys. Rev. B* **1992**, *46*, 12947.
36. Becke, A. D. *Phys. Rev. A* **1988**, *38*, 3098, Becke, A.D., *J. Chem. Phys.* **1993**, *98*, 1372.
37. Perdew, J. P. *Phys. Rev. B* **1986**, *33*, 8822.
38. Becke, A. D. *J. Chem. Phys.* **1993**, *98*, 5648.
39. Lee, C.; Yang, W.; Parr, R. G. *Phys. Rev. B* **1988**, *37*, 785.
40. Perdew, J. P.; Burke, K.; Ernzerhof, M. *Phys. Rev. Lett.*, **1996**, *77*, 3865.

41. Tsuneda, T.; Hirao, K. *Chem. Phys. Lett.* **1997**, 268, 510; Tsuneda, T.; Suzumura, T.; Hirao, K. *J. Chem. Phys.* **1999**, 110, 10664; Kamiya, M.; Tsuneda, T.; Hirao, K. *ibid.* **2002**, 117, 6010.
42. Piskoti, C.; Yarger, J.; Zettl, A. *Nature* **1998**, 393, 771.
43. Pearson, R. G. *J. Am. Chem. Soc.* **1963**, 85, 3533.
44. Sen, K. D. Ed.; *Chemical Hardness, Structure and Bonding*; Springer-Verlag: Berlin, Heidelberg, **1993**; Vol 80.
45. Parr, R. G.; Zhou, Z. *Acc. Chem. Res.* **1993**, 26, 256.
46. Geerlings, P.; De Proft, F.; Martin, J. M. L. in *Recent Developments and Applications of Modern Density functional Theory* (Theoretical and Computational Chemistry, Vol. 4, pp 773-809).
47. Sen, K. D.; Jørgensen, C. K. Eds. *Electronegativity, Structure and Bonding*; Springer-Verlag: Berlin, **1987**; Vol 66.
48. Iczkowski, R. P.; Margrave, J. L. *J. Am. Chem. Soc.* **1961**, 83, 3547.
49. Parr, R. G.; Pearson, R. G. *J. Am. Chem. Soc.* **1983**, 105, 7512.
50. Parr, R. G.; Yang, W. *J. Am. Chem. Soc.* **1984**, 106, 4049.
51. Guo, T.; Diener, M. D.; Chai, Y.; Alford, M. J.; Haufler, R. E.; McClure, S. M.; Ohno, T.; Weaver, J. H.; Scuseria, G. E.; Smalley, R. E. *Science* **1992**, 257, 1661.
52. Kaltsoyannis, N. *Chem. Soc. Rev.* **2003**, 32, 9.
53. Cui, L.-F.; Huang, X.; Wang, L.-M.; Li, J.; Wang, L.-S. *Angew. Chem. Int. Ed.* **2007**, 46, 742.
54. Dognon, J. P.; Clavaguéra, C.; Pyykkö, P. *Angew. Chem. Int. Ed.* **2007**, 46, 1427.

55. Cockrell, G. M.; Zhang, G.; VanDerveer, D. G.; Thummei, R. P.; Hancock, R. D. *J. Am. Chem. Soc.* **2008**, *130*, 1420.
56. Apostolidis, C.; Schimmelpfennig, B.; Magnani, N.; Lindqvist-Reis, P.; Walter, O.; Sykora, R.; Morgenstern, A.; Colineau, E.; Caciuffo, R.; Klenze, R.; Haire, R. G.; Rebizant, J.; Bruchertseifer, F.; Fanghänel, T. *Angew. Chem. Int. Ed.* **2010**, *49*, 6343.
57. Nash, K. L. *Solvent Extr. Ion. Exch.* **1993**, *11*, 729; Holder, J. V. *Radiochim. Acta* **1978**, *25*, 171.
58. Ahearne, J. F. Special issue: Radioactive wastes, *Physics Today* **1997**, *50*, 22; *Physics Today* **1997**, *50*, 24.
59. Crowley, K. D. *Physics Today* **1997**, *50*, 32-39; McCombie, C. *Physics Today* **1997**, *50*, 56.
60. Manna, D.; Ghanty, T. K. *Phys. Chem. Chem. Phys.*, **2012**, *14*, 11060.
61. Bhattacharyya, A.; Mohapatra, P. K.; Manchanda, V. K. *J. Radioanal. Nucl. Chem.*, **2011**, *288*, 709.
62. Bhattacharyya, A.; Mohapatra, P. K.; Manchanda, V. K. *Radiochim. Acta.*, **2010**, *98*, 141; Bhattacharyya, A.; Mohapatra, P. K.; Manchanda, V. K. *Sep. Sci. Technol.*, **2011**, *46*, 376.
63. Pearson, R. G. *Science*. **1966**, *151*, 172.
64. Pearson, R. G. *J. Am. Chem. Soc.* **1963**, *85*, 3533; Pearson, R. G. *J. Chem. Edu.* **1968**, *45*, 581; **1968**, *45*, 643.
65. Fukui, K. *Science* **1982**, *218*, 747.
66. Melton, D. L.; VanDerveer, D. G.; Hancock, R. D. *Inorg. Chem.* **2006**, *45*, 9306.

67. Dean, N. E.; Hancock, R. D.; Cahill, C. L.; Frisch, M. *Inorg. Chem.* **2008**, *47*, 2000.
68. Williams, N. J.; Balance, D. G.; Reibenspies, J. H.; Hancock, R. D. *Inorg. Chim. Acta.* **2010**, *363*, 3694.
69. Gephart, R. T.; Williams, N. J.; Reibenspies, J. H.; Sousa, A. S. D.; Hancock, R. D. *Inorg. Chem.* **2009**, *48*, 8201.
70. Vetere, V.; Roos, B.O.; Maldivi, P. Adamo, C. *Chem. Phys. Lett.*, **2004**, *396*, 452.
71. Vetere, V.; Maldivi, P.; Adamo, C. *J. Comput. Chem.* **2003**, *24*, 850.
72. Yang, W.; Mortier, W. *J. Am. Chem. Soc.* **1986**, *108*, 5708.
73. Roy, R. K.; Krishnamurti, S.; Geerlings, P.; Pal, S. *J. Phys. Chem. A* **1998**, *102*, 3746.
74. Roy, R. K.; Proft, F. De; Geerlings, P. *J. Phys. Chem. A* **1998**, *102*, 7035.
75. TURBOMOLE is program package developed by the Quantum Chemistry Group at the University of Karlsruhe, Germany, 1988: Ahlrichs, R.; Bär, M.; Häser, M.; Horn, H.; Kölmel, C. *Chem. Phys. Lett.* **1989**, *162*, 165.
76. Velde, G. te; Bickelhaupt, F.M.; Gisbergen, S.A. van; Fonseca Guerra, C.; Baerends, E. J.; Snijders, J. G.; Ziegler, T. *J. Comp. Chem.*, **2001**, *22*, 931.
77. Fonseca Guerra, C.; Snijders, J. G.; Velde, G. te; Baerends, E. J. *Theor. Chem. Acc.* **1998**, 391.
78. ADF2006.01, SCM, Theoretical Chemistry, Vrije Universiteit, Amsterdam, The Netherlands; <http://www.scm.com>.

79. Ziegler, T.; Rauk, A. *Theor. Chim. Acta* **1977**, *46*, 1; Bickelhaupt, F. M.; Baerends, E. J. in *Rev. Comput. Chem.*, edited by K. B. Lipkowitz, D. B. Boyd, Wiley-VCH, **2000**, vol. *15*, pp. 1–86.
80. Petit, L.; Adamo, C.; Maldivi, P. *Inorg. Chem.* **2006**, *45*, 8517.
81. Bhattacharyya, A.; Ghanty, T. K.; Mohapatra, P. K.; Manchanda, V. K. *Inorg. Chem.* **2011**, *50*, 3913.
82. Petit, L.; Daul, C.; Adamo, C.; Maldivi, P. *New J. Chem.* **2007**, *31*, 1738.
83. Dognon, J. P.; Clavaguéra, C.; Pyykkö, P. *C. R. Chimie* **2010**, *13*, 884.
84. Küchle, W.; Dolg, M.; Stoll, H.; Preuss, H. *J. Chem. Phys.* **1994**, *100*, 7535.
85. Cao, X.; Dolg, M.; Stoll, H. *J. Chem. Phys.* **2003**, *118*, 487.
86. Cao, X.; Dolg, M. *J. Mol. Struct. (THEOCHEM)* **2004**, *673*, 203.
87. Dolg, M.; Stoll, H.; Preuss, H. *J. Chem. Phys.* **1989**, *90*, 1730.
88. Cao, X.; Dolg, M. *J. Chem. Phys.* **2001**, *115*, 7348.
89. Cao, X.; Dolg, M. *J. Mol. Struct. (THEOCHEM)* **2002**, *581*, 139.
90. Dolg, M.; Stoll, H.; Preuss, H. *Theor. Chim. Acta* **1993**, *85*, 441.
91. Dolg, M.; Cao, X. *Chem. Rev.* **2012**, *112*, 403.
92. Clark, A. E.; Sonnenberg, J. L.; Hay, P. J.; Martin, R. L.; *J. Chem. Phys.* **2004**, *121* 2563.
93. Klamt, A.; Schüürmann, G. *J. Chem. Soc. Perkin Trans.* **1993**, *2*, 799.
94. Cao, X.; Heidelberg, D.; Ciupka, J.; Dolg, M. *Inorg. Chem.* **2010**, *49*, 10307.
95. Cosentino, U.; Villa, A.; Pitea, D. *J. Phys. Chem. B* **2000**, *104*, 8001.
96. Shannon, R. D. *Acta Cryst.* **1976**, *A32*, 751.
97. Zhu, Y.; Chen, J.; Jiao, R. *Solvent Extr. Ion. Exch.* **1996**, *14*, 61.

98. Bhattacharyya, A.; Mohapatra, P. K.; Manchanda, V. K. *Solvent Extr. Ion. Exch.* **2006**, *24*, 1.
99. Kolarik, Z. *Chem. Rev.* **2008**, *108*, 4208.
100. Miguiditchian, M.; Guillaneux, D.; Moisy, P.; Madic, C.; Jensen, M. P.; Nash, K. L. *Inorg. Chem.* **2005**, *44*, 1404.
101. Heitzmann, M.; Brevard, F.; Gateau, C.; Boubals, N.; Berthon, C.; Pécaut, J.; Charbonnel, M. C.; Delangle, P. *Inorg. Chem.* **2009**, *48*, 246.
102. Lewis, F. W.; Harwood, L. M.; Hudson, M. J.; Drew, M. G. B.; Desreux, J. F.; Vidick, G.; Bouslimani, N.; Modolo, G.; Wilden, A.; Sypula, M.; Vu, T.H.; Simonin, J. P. *J. Am. Chem. Soc.* **2011**, *133*, 13093.
103. Jensen, M. P.; Bond, A. H. *J. Am. Chem. Soc.* **2002**, *124*, 9870.
104. Petit, L.; Joubert, L.; Maldivi, P.; Adamo, C. *J. Am. Chem. Soc.* **2006**, *128*, 2190.
105. Ghanty, T. K.; Ghosh, S. K. *Inorg. Chim.* **1992**, *31*, 1951; Ghanty, T. K.; Ghosh, S. K. *J. Am. Chem. Soc.* **1994**, *116*, 3943; Ghanty, T. K.; Ghosh, S. K. *J. Am. Chem. Soc.* **1994**, *116*, 8801.
106. Ghanty, T. K.; Ghosh, S. K. *J. Phys. Chem.* **1996**, *100*, 12295.
107. Pal, S.; Chandrakumar, K. R. S. *J. Am. Chem. Soc.* **2000**, *122*, 4145.
108. Ghanty, T. K.; Ghosh, S. K. *J. Phys. Chem.* **2000**, *104*, 2975.
109. De, H. S.; Krishnamurty, S.; Pal, S. *J. Phys. Chem. C* **2010**, *114*, 6690.
110. Tian, G.; Martin, L. R.; Zhang, Z.; Rao, L. *Inorg. Chem.* **2011**, *50*, 3087.
111. Marie, C.; Miguiditchian, M.; Guillaumont, D.; Tosseng, A.; Berthon, C.; Guilbaud, P.; Duvail, M.; Bisson, J.; Guillaneux, D.; Pipelier, M.; Dubreuil, D. *Inorg. Chem.* **2011**, *50*, 6557.

112. Nilsson, M.; Nash, K. L. *Solv. Extr. Ion. Exch.* **2007**, *25*, 665.
113. Roy, L. E.; Bridgesb, N. J.; Martin, L. R. *Dalton Trans.*, **2012**, *42*, 2636.
114. Ogden, M. D.; Sinkov, S. I.; Nilson, M.; Lumetta, G. J.; Hancock, R. D.; Nash, K. L. *J Solution Chem.*, **2013**, *42*, 211.
115. D. Manna, S. Mula, A. Bhattacharyya, S. Chattopadhyay and T. K. Ghanty, *Dalton Trans.* (Submitted for publication)
116. Galletta, M.; Scaravaggi, S.; Macerata, E.; Famulari, A.; Mele, A.; Panzeri, W.; Sansone, F.; Casnati, A.; Mariani, M. *Dalton Trans.*, **2013**, *42*, 16930.
117. Bader, R. F. W. *Atoms in Molecules—A Quantum Theory*; Oxford University Press, Oxford, **1990**.
118. Biegler-könig, F. W.; Bader, R. F. W.; Tang, T. H. *J. Comput. Chem.* **1982**, *3*, 317–328.
119. Newkome, G. R.; Kiefer, G. E.; Puckett, W. E.; Vreeland, T. *J. Org. Chem.*, **1983**, *48*, 5114.
120. Mäkelä, M.; Zhang, L.; Zetterberg, K.; Hansson, S. *Syn. Commun.*, **1992**, *22*, 2811.
121. Merrill, D.; Hancock, R. D. *Radiochim. Acta*, **2011**, *99*, 161.
122. Gephart III, R. T.; Williams, N. J.; Reibenspies, J. H.; Sousa, A. S. De; Hancock, R. D. *Inorg. Chem.*, **2008**, *47*, 10342.
123. Arnold, P. L.; Turner, Z. R.; Kaltsoyannis, N.; Iekani, P.; Bellabarba, R. M.; Tooze, R. P. *Chem. Eur. J.*, **2010**, *16*, 9623.
124. Schnaars, D. D.; Gaunt, A. J.; Hayton, T. W.; Jones, M. B.; Kirker, I.; Kaltsoyannis, N.; May, I.; Reilly, S. D.; Scott, B. L.; Wu, G. *Inorg. Chem.*, **2012**, *51*, 8557.

125. Modolo, G.; Odoj, R. *J. Rad. Anal. Nucl. Chem.* **1998**, 228, 83.
126. Wei, Y.; Kumagai, M.; Takashima, Y.; Modolo, G.; Odoj, R. *Nucl. Tech.* **2000**, 132, 413.
127. Bhattacharyya, A.; Mohapatra, P. K.; Ansari, S. A.; Raut, D. R.; Manchanda, V. K. *J. Membr. Sci.*, **2008**, 312, 1.
128. Boehme, C.; Wipff, G. *Inorg. Chem.* **1999**, 38, 5734.
129. Boehme, C.; Wipff, G. *Chem. Eur. J.* **2001**, 7, 1398.
130. Bhattacharyya, A.; Mohapatra, P. K.; Ghanty, T. K.; Manchanda, V. K. *Phys. Chem. Chem. Phys.* **2008**, 10, 6274.
131. Chen, J.; Wang, F.; He, X.; Pan, D. *Progr. Chem.* **2011**, 23, 1338.
132. Guillaumont, D. *J. Phys. Chem. A* **2004**, 108, 6893.
133. Nash, K. L. *Solvent Extr. Ion. Exch.* **1993**, 11, 729.
134. Dolg, M.; Stoll, H.; Savin, A.; Preuss, H. *Theor. Chim. Acta* **1989**, 75, 173.
135. Moritz, A.; Cao, X.; Dolg, M. *Theor. Chem. Acc.* **2007**, 118, 845.
136. Moritz, A.; Cao, X.; Dolg, M. *Theor. Chem. Acc.* **2007**, 117, 473.
137. D. Manna, A. Bhattacharyya, and T. K. Ghanty, *Comput. Theor. Chem.*
(Submitted for publication)
138. Keith, J. M.; Batista, E. R. *Inorg. Chem.* **2012**, 51, 13.
139. Perdew, J. P.; Chevary, J. A.; Vosko, S. H.; Jackson, K. A.; Pederson, M. R.; Singh, D. J.; Fiolhais, C. *Phys. Rev. B*, **1992**, 46, 6671.
140. Ingram, K. I. M.; Tassell, M. J.; Gaunt, A. J.; Kaltsoyannis, N. *Inorg. Chem.* **2008**, 47, 7824.
141. Zhu, Y.; Chen, J.; Choppin, G. R. *Solv. Extr. Ion Exch.* **1996**, 14, 543.

142. Vetere, V.; Roos, B. O.; Maldivi, P.; Adamo, C. *Chem. Phys. Lett.* **2004**, *396*, 452.
143. Vetere, V.; Maldivi, P.; Adamo, C. *J. Comput. Chem.* **2003**, *24*, 850.
144. Perdew, J.P.; Ernzerhof, M.; Burke, K. *J. Chem. Phys.* **1996**, *105*, 9982.
145. Kovács, A.; Esterhuysen, C.; Frenking, G. *Chem. Eur. J.* **2005**, *11*, 1813.
146. Krapp, A.; Bickelhaupt, F. M.; Frenking, G. *Chem. Eur. J.* **2006**, *12*, 9196.
147. Takagi, N.; Krapp, A.; Frenking, G. *Inorg. Chem.* **2011**, *50*, 819.
148. Hopffgarten, M. V.; Frenking, G. *Comput Mol Sci.* **2012**, *2*, 43.
149. Heath, J. R. *Nature* **1998**, *393*, 730.
150. Fowler, P. W.; Mitchell, D.; Zerbetto, F. *J. Am. Chem. Soc.* **1999**, *121*, 3218.
151. Côte, M.; Grossman, J. C.; Cohen, M. L.; Louie, S. G. *Phys. Rev. Lett.* **1998**, *81*, 697.
152. Paquette, L. A.; Ternansky, R. J.; Balogh, D. W.; Kentgen, G. J. *J. Am. Chem. Soc.* **1983**, *105*, 5446.
153. Prinzbach, H.; Weiler, A.; Landenberger, P.; Wahl, F.; Wörth, J.; Scott, L. T.; Gelmont, M.; Olevano, D.; Issendorff, B. v. *Nature* **2000**, *407*, 60.
154. Dunk, P. W.; Kaiser, N. K.; Mulet-Gas, M.; Rodriguez-Forteza, A.; Poblet, J. M.; Shinohara, H.; Hendrickson, C. L.; Marshall, A. G.; Kroto, H. W. *J. Am. Chem. Soc.* **2012**, *134*, 9380.
155. Dognon, J. P.; Clavaguéra, C.; Pyykkö, P. *J. Am. Chem. Soc.* **2009**, *131*, 238-243.
156. Manna, D.; Ghanty, T. K. *J. Phys. Chem. C* **2012**, *116*, 16716.
157. Manna, D.; Ghanty, T. K. *J. Phys. Chem. C* **2013**, *117*, 17859.
158. An, W.; Geo, Y.; Bulusu, S.; Zeng, X.C. *J. Chem. Phys.* **2005**, *122*, 204109.

159. Paulus, B. *Phys. Chem. Chem. Phys.* **2003**, *5*, 3364.
160. Zhang, C.; Sun, W.; Cao, Z. *J. Chem. Phys.* **2007**, *126*, 144306.
161. Wu, J.; Sun, Z.; Li, X.; Ma, B.; Tian, M.; Li, S. *Int. J. Quantum Chem.* **2011**, *111*, 3786.
162. Grossman, J. C.; Côté, M.; Louie, S. G.; Cohen, M. L. *Chem. Phys. Lett.* **1998**, *284*, 344.
163. Halac, E.; Burgos, E.; Bonadeo, H. *Chem. Phys. Lett.* **1999**, *299*, 64.
164. Jagadeesh, M. N.; Chandrasekhar, J. *Chem. Phys. Lett.* **1999**, *305*, 298.
165. Ito, A.; Monobe, T.; Yoshii, T.; Tanaka, K. *Chem. Phys. Lett.* **2000**, *328*, 32-38.
166. Chen, Z.; Jiao, H.; Hirsch, A.; Thiel, W. *Chem. Phys. Lett.* **2000**, *329*, 47.
167. Yuan, L.; Yang, J.; Deng, K.; Zhu, Q. *J. Phys. Chem. A* **2000**, *104*, 6666.
168. Slanina, Z.; Uhlík, F.; Zhao, X.; Osawa, E. *J. Chem. Phys.* **2000**, *113*, 4933.
169. Varganov, S. A.; Avramov, P. V.; Ovchinnikov, S. G.; Gordon, M. S. *Chem. Phys. Lett.* **2002**, *362*, 380.
170. Fowler, P. W.; Heine, T. K.; Rogers, M.; Sandall, J. P. B.; Seifert, G.; Zerbetto, F. *Chem. Phys. Lett.* **1999**, *300*, 369.
171. Fowler, P. W.; Heine, T. *J. Chem. Soc., Perkin Trans.* **2001**, *22*, 487.
172. Corminboeuf, C.; Fowler, P. W.; Heine, T. *Chem. Phys. Lett.* **2002**, *361*, 405.
173. Xu, X. F.; Shang, Z. F.; Wang, G. C.; Cai, Z. S.; Pan, Y. M.; Wu, B. X.; Zhao, X. Z. *J. Mol. Struct.: THEOCHEM* **2002**, *589*, 265.
174. Yang, Z. Y.; Li, R. F.; Yang, X.; Wang, G. C.; Shang, Z. F.; Pan, Y. M.; Wu, B. X.; Zhao, X. Z. *Chem. J. Chin. Univ.-Chin.* **2002**, *23*, 1929.

175. Yang, Z. Y.; Wang, G. C.; Shang, Z. F.; Cai, Z. S.; Pan, Y. M.; Zhao, X. Z. *J. Mol. Struct.: THEOCHEM* **2001**, *549*, 243.
176. Li, J. Q.; Huang, X.; Wu, L.-M.; Zhang, Y.-F. *Acta Chim. Sin.* **2000**, *58*, 319.
177. Slanina, Z.; Chow, T. *J. Nanosci. Nanotechnol.* **2003**, *3*, 303.
178. Fowler, P. W.; Manolopoulos, D. E. *An Atlas of Fullerenes*; Oxford University Press: New York, U.S.A., 1995.
179. Hong, B.; Chang, Y.-F.; Qiu, Y.-Q.; Sun, H.; Su, Z.-M.; Wang, R.-S. *MP2 J. Chem. Phys.* **2006**, *124*, 144108.
180. Kang, H. S. *J. Phys. Chem. A* **2006**, *110*, 4780.
181. Małolepsza, E.; Witek, H. A. *J. Phys. Chem. A* **2007**, *111*, 6649.
182. Garg, I.; Sharma, H.; Kapila, N.; Dharamvir, K.; Jindala, V. K. *Nanoscale* **2011**, *3*, 217.
183. Lu, X.; Chen, Z. *Chem. Rev.* **2005**, *105*, 3643.
184. Pyykkö, P.; Runeberg, N. *Angew. Chem. Int. Ed.* **2002**, *41*, 2174.
185. Li, X.; Kiran, B.; Li, J.; Zhai, H.-J.; Wang, L.-S. *Angew. Chem. Int. Ed.* **2002**, *41*, 4786.
186. Autschbach, J.; Hess, B. A.; Johansson, M. P.; Neugebauer, J.; Patzschke, M.; Pyykkö, P.; Reiher, M.; Sundholm, D. *Phys. Chem. Chem. Phys.* **2004**, *6*, 11.
187. Khanna, S. N.; Jena, P. *Phys. Rev. Lett.* **1992**, *69*, 11.
188. Ghanty, T. K.; Chandrakumar, K. R. S.; Ghosh, S. K. *J. Chem. Phys.* **2004**, *120*, 11363.
189. Li, J.; Li, X.; Zhai, H.-J.; Wang, L.-S. *Science* **2003**, *299*, 864.
190. Johansson, M. P.; Sundholm, D.; Vaara, J. *Angew. Chem., Int. Ed.* **2004**, *43*, 2678.

191. Gao, Y.; Bulusu, S.; Zeng, X. C. *J. Am. Chem. Soc.* **2005**, *127*, 15680.
192. Karttunen, A. J.; Linnolahti, M.; Pakkanena, T. A.; Pyykkö, P. *Chem. Commun.* **2008**, 465.
193. Cui, L-F.; Huang, X.; Wang, L-M.; Boldyrev, A. I.; Li, J.; Wang, L-S. *J. Phys. Chem. A* **2006**, *110*, 10169.
194. Cui, L-F.; Huang, X.; Wang, L-M.; Zubarev, D. Y.; Boldyrev, A. I.; Li, J.; Wang, L-S. *J. Am. Chem. Soc.* **2006**, *128*, 8390.
195. Guerra, C. F.; Handgraaf, J. W.; Baerends, E. J.; Bickelhaupt, F. M. *J. Comput. Chem.* **2004**, *25*, 189.
196. Gritsenko, O. V.; Schipper, P. R. T.; Baerends, E. J. *Chem. Phys. Lett.* **1999**, *302*, 199.
197. Schipper, P. R. T.; Gritsenko, O. V.; van Gisbergen, S. J. A.; Baerends, E. J. *J. Chem. Phys.* **2000**, *112*, 1344.
198. Aikens, C. M. *J. Phys. Chem. A* **2009**, *113*, 10811; Aikens, C. M. *J. Phys. Chem. Lett.* **2010**, *1*, 2594.
199. Stener, M; Nardelli, A.; Fronzoni, G. *J. Chem. Phys.* **2008**, *128*, 134307.
200. Kamal, C.; Ghanty, T. K.; Banerjee, A.; Chakrabarti, A. *J. Chem. Phys.* **2009**, *131*, 164708.
201. Ghanty, T. K.; Banerjee, A.; Chakrabarti, A. *J. Phys. Chem. C* **2010**, *114*, 20; Banerjee, A.; Ghanty, T. K.; Chakrabarti, A.; Kamal, C. *J. Phys. Chem. C* **2012**, *116*, 193.
202. Schleyer, P. v. R.; Maerker, C.; Dransfeld, A.; Jiao, H.; Hommes, van Eikema N. J. R. *J. Am. Chem. Soc.* **1996**, *118*, 6317.

203. Wannere, C. S.; Corminboeuf, C.; Wang, Z.-X.; Wodrich, M. D.; King, R. B.; Schleyer, P. v. R. *J. Am. Chem. Soc.* **2005**, *127*, 5701.
204. Chen, Z.; Wannere, C. S.; Corminboeuf, C.; Puchta, R.; Paul von Rague' Schleyer, P. v. R. *Chem. Rev.* **2005**, *105*, 3842.
205. Boldyrev, A. I.; Wang, L. S. *Chem Rev.* **2005**, *105*, 3716.
206. Páez-Hernández, D; Murillo-López, J. A.; Arratia-Pérez, R; *J. Phys. Chem. A* **2011**, *115*, 8997.
207. van Leeuwen, R.; Baerends, E. J. *Phys. Rev. A* **1994**, *49*, 2421.
208. Grimme, S.; Antony, J.; Ehrlich, S.; Krieg, H. *J. Chem. Phys.* **2010**, *132*, 154104.
209. Grimme, S. *J. Comput. Chem.* **2006**, *27*, 1787.
210. Schwabe, T.; Grimme, S. *Phys. Chem. Chem. Phys.* **2007**, *9*, 3397.
211. Paier, J.; Marsman, M.; Kresse, G. *J. Chem. Phys.* **2007**, *127*, 024103.
212. Dai, X.; Cheng, C.; Zhang, W.; Xin, M.; Huai, P.; Zhang, R.; Wang, Z. *Sci. Rep.* **2013**, *3*, 1341.
213. Infante, I.; Gagliardi, Laura.; Scuseria, G. E. *J. Am. Chem. Soc.* **2008**, *130*, 7459.
214. Wu, X., Lu, X. *J. Am. Chem. Soc.* **2007**, *129*, 2171.
215. Skwara, B.; Robert W. Góra, R. W.; Zaleśny, R.; Lipkowski, P.; Bartkowiak, W.; Reis, H.; Papadopoulos, M. G.; Luis, J. M.; Kirtman, B. *J. Phys. Chem. A* **2011**, *115*, 10370.
216. Dunk, P. W.; Kaiser, N. K.; Hendrickson, C. L.; Quinn, J. P.; Ewels, C. P. Nakanishi, Y.; Sasaki, Y.; Shinohara, H.; Marshall, A. G.; Kroto, H. W. *Nature Commu.* **2012**, *3*, 855.

217. Diener, M. D.; Smith, C. A.; Veirs, D. K. *Chem. Mat.* **1997**, *9*, 1773.
218. Akiyama, K.; Zhao, Y. L.; Sueki, K.; Tsukada, K.; Haba, H.; Nagame, Y.; Kodama, T.; Suzuki, S.; Ohtsuki, T.; Sakaguchi, M. et. al. *J. Am. Chem. Soc.* **2001**, *123*, 181.
219. Knight, W. D.; Clemenger, K.; de Heer, W. A.; Saunders, W. A.; Chou, M. Y.; Cohen, M. L. *Phys. Rev. Lett.* **1984**, *52*, 2141.
220. Harbola, M. K. *Proc. Natl. Acad. Sci. (USA)* **1992**, *89*, 1036.
221. Langmuir, I. *Science* **1921**, *54*, 59.
222. Pyykkö, P. *J. Organomet. Chem.* **2006**, *691*, 4336.
223. Dognon, J. P.; Clavaguéra, C.; Pyykkö, P. *Chem. Sci.*, 2012, *3*, 2843.
224. Kemsley, J. N. *Chem. Eng. News* **2008**, *86*, 29.
225. Frenking, G.; Tonner, R. *Nature* **2007**, *446*, 276.
226. Manna, D.; Ghanty, T. K. *J. Phys. Chem. C* **2014**, *118*, 7211.
227. Manna, D.; Ghanty, T. K. *J. Phys. Chem. C* **2012**, *116*, 25630.
228. Brinkmann, G.; O. Delgado Friedrichs, Liskén. S.; Peeters, A.; Cleemput, N. Van *MATCH Commun. Math. Comput. Chem.*, **2010**, *63*, 533. URL: <http://www.math.uni-bielefeld.de/~CaGe>.
229. An, W.; Shao, N.; Bulusu, S.; Zeng, X. C. *J. Chem. Phys.* **2008**, *128*, 084301.
230. Balevičius, L. M.; Stumbrys, E.; Tamulis, A. *Fullerene Science and Technology* **1997**, *5*, 85.
231. An, J.; Gan, L-H; Zhao, J-Q, Li R; *J. Chem. Phys.* **2010**, *132*, 154304.
232. Xu, W.; Jin, X.; Chen, M.; Pyykkö, P.; Zhou, M.; Li, J. *Chem. Sci.* **2012**, *3*, 1548 and references therein.
233. Hirsch, A.; Chen, Z.; Jiao, H. *Angew. Chem., Int. Ed.* **2000**, *39*, 3915.